VENEZUELA-MEM/USA-DOE FOSSIL ENERGY REPORT IV-10

DOE/BC-98/1/SP
(DE98000459)

SUPPORTING TECHNOLOGY FOR ENHANCED OIL RECOVERY

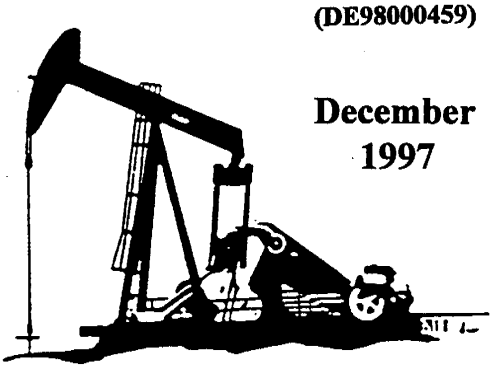

December
1997

EOR THERMAL PROCESSES

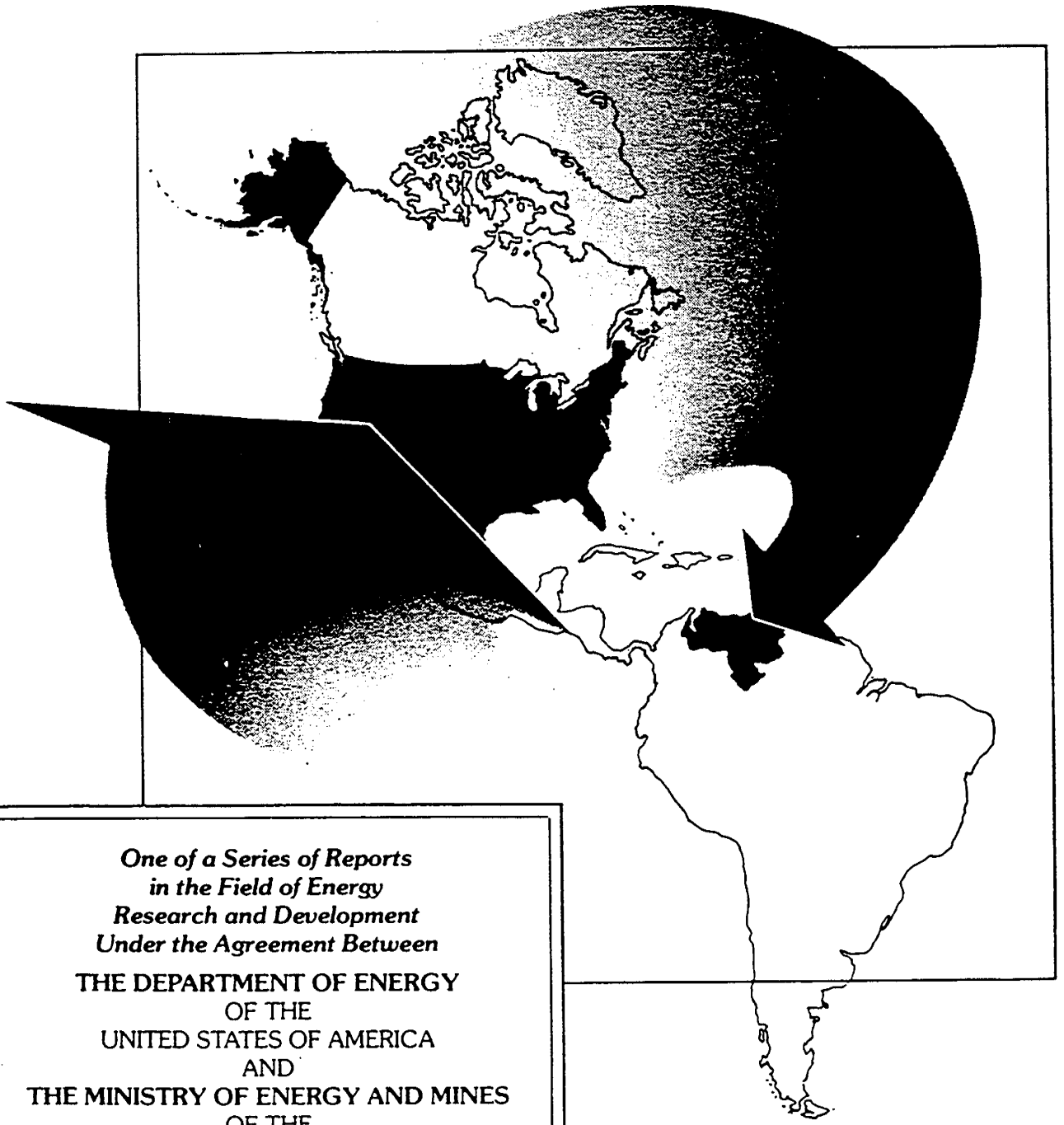

One of a Series of Reports
in the Field of Energy
Research and Development
Under the Agreement Between

THE DEPARTMENT OF ENERGY
OF THE
UNITED STATES OF AMERICA
AND
THE MINISTRY OF ENERGY AND MINES
OF THE
REPUBLIC OF VENEZUELA

DISCLAIMER

This report was prepared as an account of work sponsored by an agency of the United States Government. Neither the United States Government nor any agency thereof, nor any of their employees, makes any warranty, expressed or implied, or assumes any legal liability or responsibility for the accuracy, completeness, or usefulness of any information, apparatus, product, or process disclosed, or represents that its use would not infringe privately owned rights. Reference herein to any specific commercial product, process, or service by trade name, trademark, manufacturer, or otherwise does not necessarily constitute or imply its endorsement, recommendation, or favoring by the United States Government or any agency thereof. The views and opinions of authors expressed herein do not necessarily state or reflect those of the United States Government.

This report has been reproduced directly from the best available copy.

Available to DOE and DOE contractors from the Office of Scientific and Technical Information, P.O. Box 62, Oak Ridge, TN 37831; prices available from (615) 576-8401.

Available to the public from the National Technical Information Service, U.S. Department of Commerce, 5285 Port Royal Rd., Springfield VA 22161

DOE/BC-98/1/SP
(DE98000459)
Distribution Category UC-122

NINTH AMENDMENT AND EXTENSION TO

Annex IV–ENHANCED OIL RECOVERY THERMAL PROCESSES

THE DEPARTMENT OF ENERGY OF THE UNITED STATES OF AMERICA

And

THE MINISTRY OF ENERGY AND MINES OF THE REPUBLIC OF VENEZUELA

Submitted By:

Thomas B. Reid, Project Manager
Thermal Recovery
National Petroleum Technology Office
U.S. Department of Energy

Jesus Bolivar, Manager
Heavy/Extra Heavy Crude
INTEVEP, S. A.
Filial de Petroleos de Venezuela, S. A.

Approved By:

Thomas C. Wesson, Director
National Petroleum Technology Office
PO Box 3628
Tulsa, OK 74101

Simon Antunez, Assistant
to the Minister of Energy and Mines
Caracas 1010A, Venezuela

United States Department of Energy

PREFACE

An Agreement between the Department of Energy of the United States of America and the Ministry of Energy and Mines of the Republic of Venezuela to cooperate in Energy Research and Development was signed March 6, 1980. The object of cooperation under this DOE/MEMV Agreement was to promote a balanced exchange of energy technologies and to conduct joint projects in the areas of Petroleum, Solar Energy, Geothermal Energy, Hydroelectric Energy and Coal.

This Agreement supported the Agreement for Scientific and Technological Cooperation between the two countries which was signed by the Secretary of State of the U.S.A. and the Minister of Foreign Relations of Venezuela on January 11, 1980.

The original DOE/MEMV Agreement was supplemented by six annexes to describe specifically the work to be done. Over the past fourteen years additional annexes have been signed, resulting in a total of fifteen annexes as of November 30, 1994. The Agreement has been extended to September 8, 1998. The annexes are:

I. Joint Characterization of Heavy Crudes Oils
II. Supporting Research in the Area of Enhanced Oil Recovery
III. Evaluation of Past and Ongoing Enhanced Oil Recovery Projects in the U.S. and Venezuela
IV. Enhanced Oil Recovery Thermal Processes
V. Oil Drilling, Coring and Telemetry
VI. Residual Oil Saturation
VII. Petroleum Products Utilization and Evaluation
VIII. Coal Preparation, Combustion and Related Technology
IX. Subsidence Due to Fluid Withdrawal
X. On-Site Training of Petroleum Engineers
XI. Energy Conservation
XII. Geochemistry (Oil Generation, Migration and Accumulation)
XIII. Microbial Enhanced Oil Recovery
XIV. Exchange of Energy Related Personnel
XV. Oil Recovery Information and Technology Transfer
XVI. Oil and Petrochemical Ecology and Environmental Research
XVII. Drilling Technology

Each of these annexes has a document describing the work to be done as part of the cooperation. Amendments and Extensions to the Annexes are provided for in the Agreement.

Currently, seven annexes are active (Annexes I, IV, X, XIV, XV, XVI, and XVII); one annex is inactive (VIII); and nine annexes have been completed (Annexes II, III, V, VI, VII, IX, XI, XII, and XIII). The "Agreement" is in force until September 8, 1998.

CONTENTS

	Page
Preface	iii
Abstract	v
TASK 62 DOE-SUPRI Laboratory Research on Flow Properties, In-Situ Combustion, Steam Injection, Computerized X Ray Tomography, and Formation Evaluations Methods	62-1
TASK 63 INTEVEP - Studies to Optimize Heavy Oil Field Exploitation Using Horizontal Wells	63-1
TASK 64 DOE-NIPER - Laboratory Research and Field Projects on Light Oil Steam Flooding	64-1
TASK 65 INTEVEP - Modeling of Thermal Processes - Production Performance of Steam Stimulated Wells	65-1
TASK 66 DOE-LLNL - Laboratory Research and Field Projects on Electrical Imaging Using from Cross-Borehole and Surface-to-Borehole Electromagnetic Induction	66-1
TASK 67 INTEVEP - Laboratory and Field Research on H2S Inhibition During Steam Injection	67-1

APPENDIX A. Full text of the "Ninth Amendment to Annex IV of the Implementing Agreement Between the Department of Energy of the United States of America and the Ministry of Energy and Mines of the Republic of Venezuela in the Area of Enhanced Oil Recovery Thermal Processes."

APPENDIX B. Full text of the extension to the "Agreement Between Between the Department of Energy of the United States of America and the Ministry of Energy and Mines of the Republic of Venezuela in the Field of Energy Research and Development."

Signed on September 8, 1993 extending the Agreement for five years to September 7, 1998.

ABSTRACT

This report contains the results of efforts under the six tasks of the Ninth Amendment and Extension of Annex IV, Enhanced Oil Recovery Thermal Processes of the Venezuela/USA Agreement. The report is presented in sections (for each of the 6 tasks) and each section contains one or more reports prepared by various individuals or groups describing the results of efforts under each of the tasks.

A statement of each task, taken from the agreement, is presented on the first page of each section. The tasks are numbered 62 through 67. The first, second, third, fourth, fifth, sixth, seventh, eighth, and ninth reports on Annex IV, [Venezuela MEM/USA-DOE Fossil Energy Report IV-1, IV-2, IV-3, IV-4, IV-5, IV-6, IV-7, and IV-8 (DOE/BETC/SP-83/15, DOE/BC-84/6/SP, DOE/BC-86/2/SP, DOE/BC-87/2/SP, DOE/BC-89/1/SP, DOE/BC-90/1/SP) DOE/BC-92/1/SP, DOE/BC-93/3/SP, and DOE/BC-95/3/SP)] contain the results from the first 61 tasks. Those reports are dated April 1983, August 1984, March 1986, July 1987, November 1988, December 1989, October 1991, February 1993, and March 1995 respectively.

Task 62

DOE shall provide INTEVEP with results from the SUPRI research on heavy oil recovery mechanisms. This task includes experiments on flow properties, in-situ combustion, steam injection, and computerized X ray tomography. Mathematical and simulation results on the same topics as well as formation evaluation methods such as well testing or tracer surveys will be included.

1.1 EFFECTS OF TEMPERATURE ON MULTIPHASE RELATIVE PERMEABILITY

(S. Akin)

1.1.1 INTRODUCTION

Production of oil from petroleum reservoirs usually involves simultaneous flow of two or more immiscible fluids through a porous rock. Multiphase flow in porous media is a complex process that depends on a number of factors; including the absolute permeability, pressure drop, capillary pressure, fluid viscosities, and relative permeabilities of each phase. Of these, the relative permeability is probably the most important parameter in determining reservoir performance. For modeling thermal recovery processes for heavy oil recovery, one needs to know not only the relative permeabilities at the original reservoir temperature but also the effect of increasing temperature on the relative permeability curves. Over the past three decades, a number of experimental studies have reported contradictory temperature effects on two phase relative permeabilities in porous media. Most experiments were performed on consolidated rocks, and only a few studies used reservoir cores and crude oils.

The reasons for divergence among experimental multiphase relative permeability data may be summarized as follows:

1. Errors produced in saturation measurements.
2. Errors introduced by neglect of capillary pressure end effects.
3. Wettability variations caused by the usage of different oils and brines.
4. Assumptions made to develop experimental procedures or calculations.
5. Inadequacy of mathematical models to represent multiphase flow conditions.

It is clear that, unless the problems stated above are overcome, a better understanding of the effects of temperature on relative permeabilities will not be achieved. Therefore careful, unsteady state relative permeability experiments at different temperatures will be conducted and reported. Two phase saturation profiles along an unconsolidated core will be measured utilizing computerized tomography (CT) which is a reliable and accurate means of measuring local saturations. Johnson-Bossler-Naumann (JBN) technique (Johnson 1959) and a black oil simulator, coupled with a global optimization code will then be used to estimate two phase relative permeabilities. Experimental saturation profiles, differential pressure and recovery data will be used in a least squares manner in the numerical model. Possible heterogeneity effects will be considered in the simulations by using CT calculated porosity values along the core.

1.1.2 LITERATURE REVIEW

Relative permeability is the basis used to predict multiphase flow through porous media. It is an empirical concept which allows Darcy's Law to be generalized for multiple phases (Honarpour 1986). This is done by assuming that the absolute permeability, used in Darcy's Law, may be replaced by a term which contains both the absolute permeability and a "relative permeability", a function of the fluid saturation. For a two phase system (oil and water), the flow equations are given as:

$$u_o = -\frac{kk_{or}}{\mu_o}\left(\nabla p_o - \rho_o \, g/g_c\right) \tag{1}$$

$$u_w = -\frac{kk_{wr}}{\mu_w}\left(\nabla p_w - \rho_w \, g/g_c\right) \tag{2}$$

where u_i is the flow velocity, k is the absolute permeability, k_{ir} is the relative permeability, μ_i is the dynamic viscosity, ∇p_i is the gradient of the pressure, ρ_i is the density. In these equations, i represents oil or water, g is the gravitational acceleration, and g_c is the universal constant in Newton's Law. Three different absolute (base) permeabilities are commonly used: the absolute air permeability, the absolute water permeability, and the permeability to oil at reservoir connate water saturation.

Although the concept of relative permeability is very simple, the measurement and interpretation of relative permeability versus saturation is not. For example, there is evidence that relative permeability may be a function of many more parameters than fluid saturation (Honarpour 1986). Temperature, flow velocity, saturation history, wettability changes and the mechanical and chemical behavior of the matrix material may all play roles in changing the functional dependence of relative permeabilities on saturation. The best defined of these dependencies is the variation of relative permeability with saturation history; relative permeability curves show hysteresis between drainage processes (wetting phase decreasing) and imbibition processes (wetting phase increasing).

A common use of relative permeability data is in numerical simulators. These data are fundamental parameters necessary in all field simulations. However, numerical simulation of thermal recovery processes requires its temperature dependence. Often, relative permeabilities measured at ambient conditions are used to predict performance at higher temperatures which in turn may lead to erroneous results.

Over the last three decades a number of laboratory studies on the effects of temperature on relative permeability and residual oil saturation as well as irreducible water saturation, appeared in the literature. Edmondson (1965) found a reduction in residual oil saturation in Berea cores as the temperature increased. Using refined oils and an unsteady state experimental technique, he noted that the relative permeability ratio of oil to water shifted in the direction of 100% water saturation as the temperature increased.

Poston *et al.* (1970) investigated the effects of temperature on unconsolidated sand using refined oils. They reported that irreducible water saturation increased, and the residual oil saturation decreased with increasing temperature. Moreover, they concluded that both relative permeability to oil and water increased with increasing temperature.

Contradicting previous researchers, two studies (Sufi *et al.*, 1982 and Miller and Ramey, 1985) conducted in Stanford University have reported temperature independent relative permeability data obtained from unsteady state experiments in unconsolidated and Berea cores using refined oils. Miller and Ramey (1985) noted various artifacts such as material balance errors, viscous instability, clay migration problems, wettability alteration by miscible cleaning methods, and capillary pressure end effects, that may have affected former conclusions on the effect of temperature on relative permeability data.

Closmann *et al.* (1985) utilized the steady state technique to measure altered, unaltered and deasphalted tar and brine relative permeability at elevated temperature using frozen Peace River cores. They concluded that tar and water relative permeability curves shifted toward lower water saturations.

Maini and Batcyky (1985) conducted unsteady state experiments at temperatures ranging from room temperature to 522F using a frozen core from a heavy oil reservoir, and stock tank oil and formation brine from the same reservoir. They measured the absolute permeability to formation water using a transient pressure decay test, and used history matching calculations to obtain relative permeabilities. They concluded that, irreducible water saturation increased and residual oil saturation decreased with increasing temperature until an optimum temperature. Moreover, they reported that relative permeability to oil decreased and the relative permeability to water remained unchanged with increasing temperature.

Polikar *et al.* (1986) used the steady state technique to measure the relative permeability of Athabasca bitumen using unconsolidated Ottawa sand as the porous medium. Their results showed no significant effect of temperature as verified statistically on relative permeability and saturation data up to 392F.

Maini and Okazawa (1987) analyzed the unsteady state experiments conducted on an unconsolidated silica sand using Bodo stock tank oil and deionized water. They history matched production and differential pressure data to obtain relative permeability curves. They concluded that the most reliable data they obtained was at residual oil saturation after 3 pore volumes of fluid injected. They observed increasing relative permeability to water with increasing temperature.

Unlike the previous researchers, Watson and Ertekin (1988) studied the effect of temperature gradient on relative permeability measurements using the steady state technique. They found that the differences in the temperature gradient resulted in variations in both the irreducible water saturation and residual oil saturation which suggested that the fired Berea cores become increasingly water-wet and unfired cores become increasingly oil wet during imbibition and drainage. Moreover, they concluded that both relative permeability to oil and water decreased with increasing temperature. They also observed that the absolute permeability of fired Berea sandstone cores were unaffected by temperature.

Polikar *et al.* (1990) conducted both steady-state and unsteady-state relative permeability experiments to find out the effects of temperature on relative permeability. Using Athabasca bitumen and deionized water, they used JBN technique to analyze their results. They observed no significant temperature effects on relative permeability of either phase, non in the residual oil and irreducible water saturations. They attributed the small changes seen to the heterogeneity effect. Moreover, they reported that steady-state and unsteady-state techniques resulted in similar relative permeability curves with little differences.

More recently, Muqeem *et al.* (1993) conducted steady state two phase and three phase relative permeability experiments at 75C and 125C using an unconsolidated silica sand with refined oil, brine and nitrogen gas. The measured relative permeabilities showed no significant temperature effect.

Kumar and Inouye (1994) used the JBN technique to analyze unsteady state relative permeability experiments conducted at differing temperatures. They tried to obtain low

temperature analogue to high temperature relative permeability data. They concluded that relative permeability data obtained at ambient conditions can be used for high temperature ones as long as the viscosity ratio and the wettability for the two systems were similar. They also reported that residual oil saturation and irreducible water saturation is independent of temperature and is a function of viscosity ratio.

The results obtained from the aforementioned studies are summarized in Table 1. It can be observed that, because of the experimental duration and convenience, most of the researchers preferred to use unsteady state experiments. The relative permeability data were obtained by interpreting such experiments either with the JBN technique or by history matching. Moreover, most experiments were performed on consolidated rocks, and only a few studies used reservoir cores and crude oils.

The reasons for divergence of experimental multiphase relative permeability data may be summarized as follows:

1. Errors produced in saturation measurements.
2. Errors introduced by neglect of capillary pressure end effects.
3. Wettability variations caused by the usage of different oils, and brines.
4. Assumptions made to develop experimental procedures or calculations.
5. Inadequacy of mathematical models to represent multiphase flow conditions.

It is clear that, unless the problems stated above are overcome, a better understanding of the effects of temperature on relative permeabilities will not be achieved.

1.1.3 EXPERIMENTAL MATERIALS AND APPARATUS

High temperature relative permeability experiments necessitate the use of high temperature and high pressure resistant core holders and sleeves. The SUPRI CT laboratory now has a high temperature and high pressure core holder donated by Mobil as shown in Fig. 1. It consists of an aluminum outer shell with six plastic centralizers placed at equal angles near the top and bottom. The centralizers hold and centralize a high temperature and pressure, two inch inside diameter, and 16 inch long core sleeve made up of special plastics. The core sleeve can operate safely with temperatures up to 350°F and pressures up to 400 psi. With its current design the core holder is not suitable for CT monitored experiments because the end clamp design will not allow us to measure saturations near the ends, where capillary end effects would be important. Moreover, it is not possible to keep the core at constant temperature since it does not have any outer insulation. A possible solution may be to change the outer shell with a new one which enables CT scanning as well as constant temperature. In that way, it may also be possible to design a clamp that can be used to place the core holder in the positioning system located on the patient couch of the CT. Figures 2 through 6 give the details of core holder sleeve and the CT couch assembly parts that will be constructed and used with the positioning system. The pressure ports shown in Figure 6 will be used to ensure obtaining pressure data that is free of end effects.to design a clamp that can be used to place the core holder in the positioning system located on the patient couch of the CT. Figures 2 through 6 give the details of core holder sleeve and the CT couch assembly parts that will be constructed and used with the positioning system. The pressure ports shown in Fig. 6 will be used to ensure obtaining pressure data that is free of end effects.

Table 1. A summary of the Recent Experimental Investigations of Temperature Effects on Relative Permeability.

Reference	Experimental Technique	Fluids	Core	Temperature Range	Saturation Measurement	End Point Saturation	Relative Permeability
Edmondson, 1965	Unsteady State (Welge)	Refined Oils (No 5 & 15)	Berea (1382°F)	room-500°F	graduated cylinders	$S_{or}\downarrow$ T↑	shifted
Sufi et al., 1982	Unsteady State (JBN)	Refined Oil	Unconsolidated Ottawa (170-200)	room-250°F	photo cell + frequency counter	independent	independent
Miller & Ramey, 1985	Unsteady State (JBN)	Refined Oil (Blandol)	Unconsolidated Ottawa (100-200) + Berea (932°F)	room-300°F	separator + graduated cylinders	independent	independent
Closmann et al., 1985	Steady State	Altered-unaltered-deasphalted tar	Frozen Peace River Cores	385°F	electrical resistance	np	k_{rw} shifted to lower S_w
Maini & Batcyky, 1985	Unsteady State (History Matching)	Stock Tank Oil	Frozen Core from a Hvy Oil Res	room-522°F	separator + fractional collector	$S_{wirr}\uparrow$ T↑ $S_{or}\downarrow$ T↑ (until T_{opt} transverse)	$k_{ro}\downarrow$ T↑ $k_{rw}\rightarrow$ T↑
Polikar et al., 1986	Steady State	Athabasca Bitumen	Unconsolidated Ottawa (~200)	room-482°F	material balance	independent	independent below 392°F
Maini & Okazawa, 1987	Unsteady State (History Matching)	Bodo Stock Tank Oil+3.5% ether	Unconsolidated Silica Sand (140-170)	room-392°F	separator + fractional collector	np	$k_{rw}\uparrow$ T↑ $k_{ro}\downarrow\uparrow$ T↑
Watson & Ertekin, 1988	Steady State	Refined Oil (Soltrol 170)	Berea (1832°F) + unfired	room-300°F	material balance	$S_{wirr}\uparrow$ T↑	k_{ro}, $k_{rw}\downarrow$ T↑
Polikar et al., 1990	Steady & Unsteady State (JBN)	Athabasca Bitumen	Unconsolidated Silica Sand (170-230)	212°F-482°F	material balance	independent	independent
Muqeem et al. 1993	Steady State	Refined Oil+N2	Unconsolidated Silica Sand (140-200)	167°F&257°F	separator	np	independent
Kumar & Inouye, 1994	Unsteady State (JBN)	Refined Oil-Drakeol 19-G.E. Silicon Oil- San Joaquin Valley Hvy Oil-GulfLight+SJV	Unconsolidated preserved cores + Berea (925°F)	room-300°F	graduated cylinders	independent	shifted

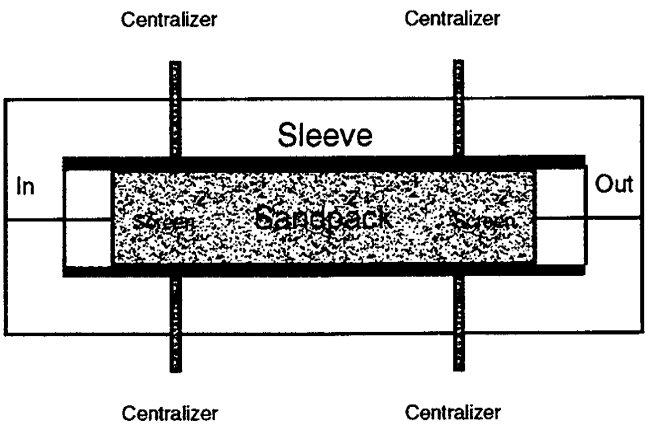

Figure 1. Schematic Diagram of Mobil Core Holder.

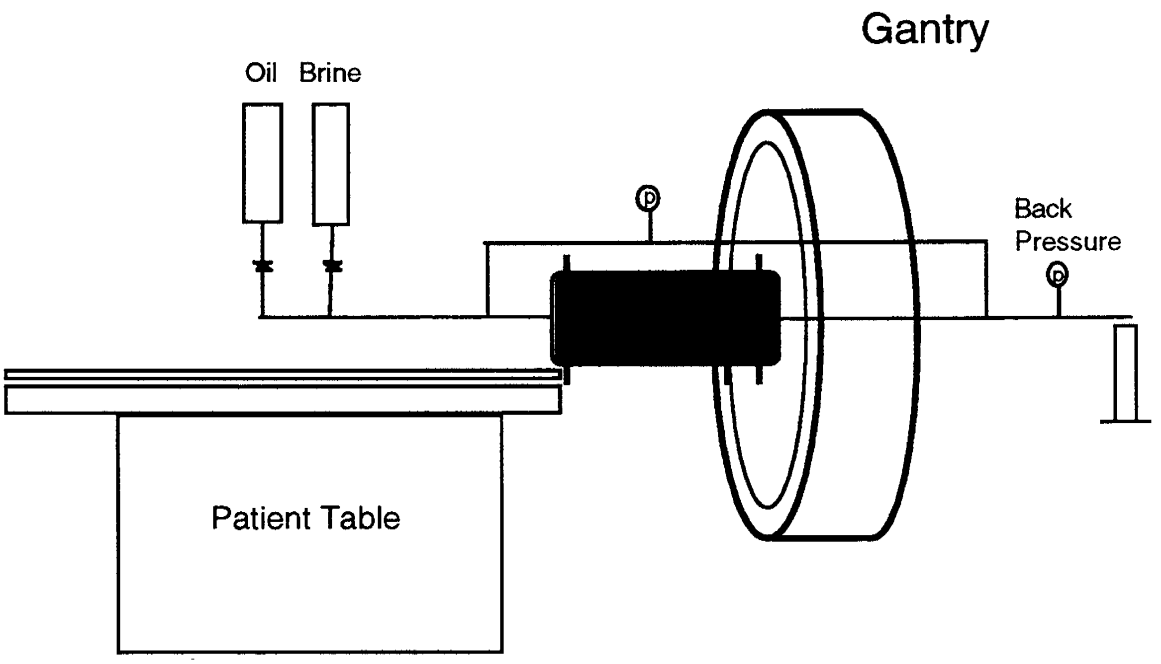

Figure 2. Schematic Diagram of the Experimental Setup Design.

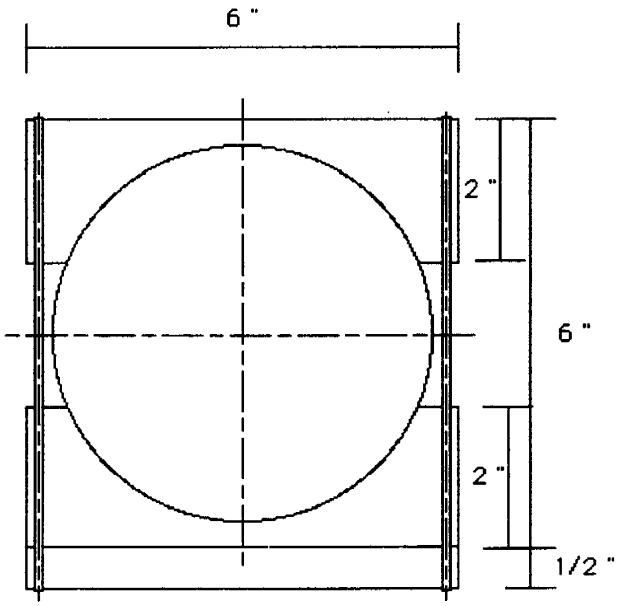

Figure 3. Front View of the Core Holder Partial Assembly.

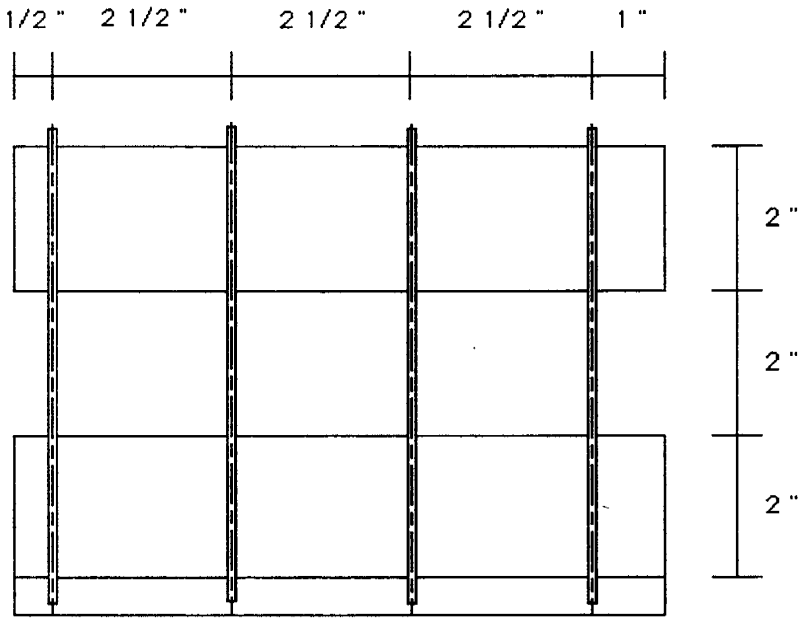

Figure 4. Side View of the Core Holder Partial Assembly.

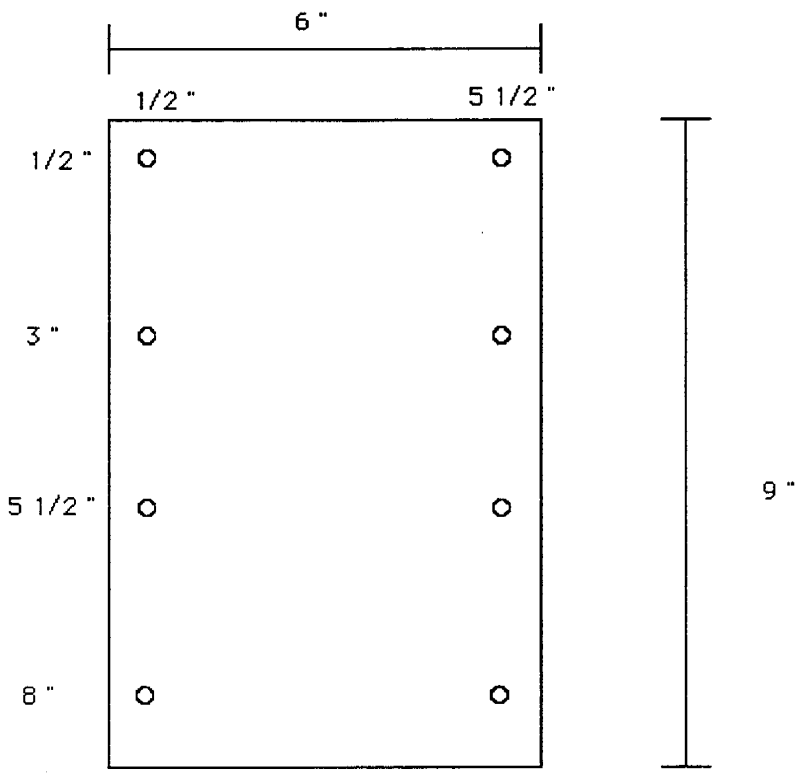

Figure 5. Top View of the Core Holder Partial Assembly.

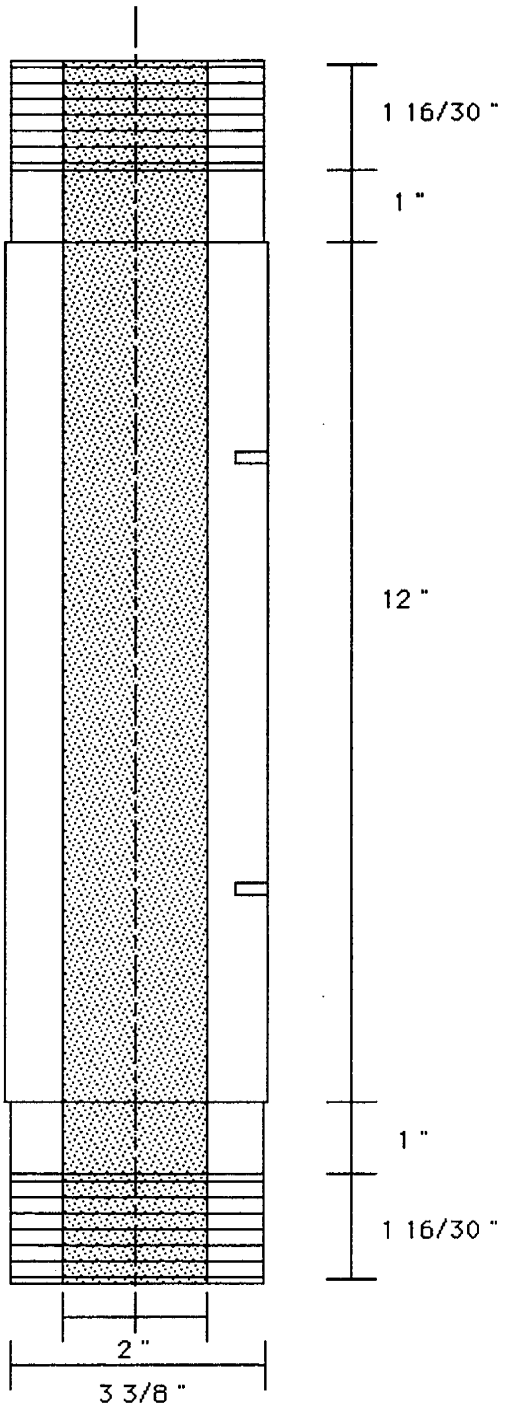

Figure 6. Schematic Description of the Core Sleeve.

1.1.4 METHOD OF SOLUTION

The production and pressure data recorded during the corefloods will be used to obtain relative permeabilities by using the well known JBN technique (Johnson *et al.* 1959) and by a history-match simulation approach (Akin 1997). The JBN technique is based on three equations given below:

$$f_o = \frac{1}{1+\frac{k_{rw}\mu_o}{k_{ro}\mu_w}} = \frac{dN_p}{dW_i} \tag{3}$$

$$S_{w2} = S_{wi} + N_p - W_i f_o \tag{4}$$

$$\frac{f_o}{k_{ro}} = \frac{d\left(\frac{1}{W_i I_r}\right)}{d\left(\frac{1}{W_i}\right)} \tag{5}$$

In these equations f is the fractional flow, k_{ro} and k_{rw} are the relative permeability to oil and water respectively, S_w is saturation of brine, N_p and W_i are the oil produced and brine injected in terms of pore volumes, and I_r is the relative injectivity. The data required are pressure drop across the core and produced volumes of fluids as functions of time.

To estimate relative permeabilities with the history matching or parameter estimation approach, an objective function is constructed as a weighted sum of squared differences between the measured data and the data calculated with a mathematical model of the experiment. For a typical displacement experiment, the measured data might consist of the pressure drop across the core sample, the cumulative volume of displaced phase recovered, and the internal saturation profiles. Then, the objective function, J, can be expressed as:

$$J = \sum_{i=1}^{N} W_{pi}\left(\Delta P_i^{obs} - \Delta P_i^{cal}\right)^2 + \sum_{i=1}^{N} W_{qi}\left(Q_{ti}^{obs} - Q_{ti}^{cal}\right)^2 + \sum_{k=1}^{M}\sum_{i=1}^{N} W_{si}\left(S_{i,k}^{obs} - S_{i,k}^{cal}\right)^2 \tag{6}$$

In the above equation, P is pressure, Q is production, S is saturation, and W_i' s are the inverses of the variances of the experimental measurement errors which will give the maximum-likelihood/minimum-variance estimates of the parameters (Akin, 1997).

A single set of data (i.e. pressure profiles) or more than one set of data (pressure, production, saturation profiles) may be used in history matching procedure. In this study, the numerical reservoir simulator utilized is the well known black oil code developed by DOE: BOAST (Fanchi *et al.*, 1987), and the optimization code is a version of the simulated annealing process developed by Goffe *et al.* (1994).

The BOAST program simulates isothermal, Darcy flow in three dimensions. It assumes reservoir fluids are three fluid phases (oil, gas, and water) of constant composition with physical properties that depend on pressure only. BOAST is a finite difference, implicit pressure - explicit saturation (IMPES) numerical simulator in which both direct and iterative solution techniques are implemented.

The computer code requires an input data file, and an output data file for execution. The input data file is divided into two parts: an initialization data section and a recurrent data section. The initialization data consists of model grid dimensions and geometry, distribution of porosity and permeability, PVT data, and initial pressure and saturation distributions, as well as the solution method and various run parameters. The recurrent data include well data and the time step control information.

In this study, the computer code is slightly modified and coupled with the simulated annealing code. The input data file is modified such that relative permeability and capillary pressure data are controlled within the optimization code as unknowns to be found. One other change with the simulator is the usage of extra output files that produce time dependent pressure and production data as well as saturation profiles. These data files are then used by the optimization code so that Eq. 6 can be utilized.

The structure of the simulated annealing computer code that will be utilized during the course of this study is given below:

1. Input and assess initial solution.
2. Estimate initial annealing temperature.
3. Generate new solution.
4. Assess new solution.
5. Accept new solution? (if no go to Step 7).
6. Update stores.
7. Adjust annealing temperature.
8. Terminate search? (if no go to Step 3).
9. Stop.
10.

Since the calculated quantities in the objective function are evaluated at each iteration, it is necessary that the parameter values at each step correspond to physically realistic relative permeability curves. For instance, if relative permeability curves that are negative or nonmonotonic are generated, evaluation of the calculated quantities becomes impossible, which may result in premature minima. This difficulty is overcome by incorporating inequality constraints in the minimization algorithm. An approach commonly used in developing optimizers is to first convert the constrained optimization problem into an equivalent unconstrained problem.

One method for converting a constrained optimization problem into an unconstrained problem is the penalty function method. In this method, a constrained problem in optimization is transformed to an unconstrained problem by associating a cost or penalty with all constraint violations. This cost is included in the objective function evaluation. In this study two sets of penalty functions were utilized. The first one handles negative and nonmonotonic relative permeabilities, and the second one penalizes insufficient number of data generated by the model which may develop because of improper relative permeabilities. The penalty functions and the conditions that require penalization are as follows (Akin 1997):

$$if \quad \left(k_{ri} \rangle k_{rj}\right) \quad then \quad J = J + \sum_{i=1}^{N} \sum_{j=i}^{N-1} N_{iter} \left(k_{ri} - k_{rj}\right)^2 N_{scale} \tag{7}$$

$$if \quad \left(N_{model} \langle N_{exper}\right) \quad then \quad J = J + \sum_{j=i}^{N} \left(N_{model} - N_{exper}\right) N_{scale} \tag{8}$$

Here N_{scale} refers to a scaling coefficient and is chosen depending on the problem.

1.1.5 NOMENCLATURE

Roman

f	:	Fractional flow
g	:	Gravitational acceleration
k	:	Relative permeability
u	:	Darcy velocity
I	:	Relative injectivity
J	:	Objective function
M	:	Number of grids
N	:	Production or number of data points
Q	:	volume of displaced phase recovered
p	:	Pressure differential across the core
p	:	Pressure gradient
S	:	Wetting phase saturation, fraction
W	:	Pore volumes injected or weighing factor

Greek

: Viscosity
: Density

Subscripts and superscripts

cal	:	Calculated
exper	:	Experimental
i, j, k	:	Indices
iter	:	Iteration
model	:	Model
o	:	Oil
obs	:	Observed
p	:	Produced
scale	:	Scale
w	:	Water
w2	:	End point

1.1.6 REFERENCES

1. Akin, S. : "Application of Computerized Tomography to the Determination of Three Phase Relative Permeabilities," Phd dissertation, Middle East Technical University, Ankara, Turkey (Jan. 1997).

2. Closmann, P. J., Waxman, M. H., and Deeds, C. T.: "Steady-State Tar/Water Relative Permeabilities in Peace River Cores at Elevated Temperature," paper SPE 14227, presented at 60th Annual Technical Conference and Exhibition of Society of Petroleum Engineers held in Las Vegas, (Sept. 22-25, 1985).

3. Edmondson, T. A.: "Effect of Temperature on Waterflooding," J. Cdn. Pet. Tech. (Oct. - Dec. 1965) 236-42.

4. Fanchi, J. F., Kennedy, J. E., and Dauben, D.: "BOAST II :A Three -Dimensional, Three-Phase Black Oil Applied Simulation Tool," Bartlesville Project Office, U. S. Department of Energy (Dec. 1987).

5. Goffe, Ferrier and Rogers : "Global Optimization of Statistical Functions with Simulated Annealing," Jour. of Econometrics, vol. 60, no. 1/2, Jan./Feb. 1994, 65-100.

6. Honarpour, M., Koederitz, L., and Harvey, A. H .:"Relative Permeability of Petroleum Reservoirs," CRC Press, Boca Raton , Florida, 1986.

7. Johnson, E.F., Bossler, D. P., and Naumann, V. O. :"Calculation of Relative Permeability From Displacement Experiments," Trans. AIME (1959) 216, 61-63.

8. Kumar, M., and Inouye, T. A.: "Low-Temperature Analogs of High-Temperature Water/Oil Relative Permeabilities," paper SPE 28616 presented at 69th Annual Technical Conference and Exhibition of Society of Petroleum Engineers , New Orleans, USA, (Sept. 25-28, 1994).

9. Maini, B. B., and Batycky, J. P.: "Effect of Temperature on Heavy-Oil/Water Relative Permeabilities and Vertically Drilled Core Plugs," JPT (Aug. 1985) 1500-1510.

10. Maini, B. B., and Okazawa, T.: "Effect of Temperature on Heavy Oil-Water Relative Permeability of Sand," J. Cdn. Pet. Tech. (May - June 1987) 33-41.

11. Miller, M. A., and Ramey, H. J. Jr.: "Effect of Temperature on Oil/Water Relative Permeabilities of Unconsolidated and Consolidated Sands," JPT (Dec. 1985) 945-953.

12. Muqeem, M., Bentsen, R., and Maini, B.: "Effect of Temperature on Three-Phase Water-Oil-Gas Relative Permeabilities of Unconsolidated Sands," paper 5593-03 presented at the 5th Petroleum Conference of the South Saskatchewan Section, the Petroleum Society of CIM, Regina, Canada (Oct. 18-20, 1993).

13. Polikar, M., Ali, F. S M., and Puttagunta, V. R.: 'High Temperature Relative Permeabilities for Athabasca Oil Sands," SPE Res. Eng. (Feb. 1990) 25-32.

14. Polikar, M., Ferracuti, F., Decastro, V., Puttagunta, V. R., and Ali, F. S. M.: 'Effect of Temperature on Bitumen-Water End Point Relative Permeabilities and Saturations," J. Cdn. Pet. Tech. (Sep. - Oct. 1986) 44-50.

15. Poston, S. W., Israel, S., Hossain, A. K. M. S., Montgomery III, E. F. and Ramey, H. J., Jr.: "The Effect of Temperature on Irreducible Water Saturation and Relative Permeability of Unconsolidated Sands," Soc. Pet. Eng. J. (June, 1970) 171-180.

17. Sufi A. H., Ramey, H. J., Jr., and Brigham, W. E.: "Temperature Effects on Relative Permeabilities of Oil-Water," paper SPE 11071 presented at 57th Annual Fall Technical Conference and Exhibition of Society of Petroleum Engineers, New Orleans (Sept. 26-29, 1982).

18. Watson, R. W., and Ertekin, T.: "The Effect of Steep Temperature Gradient on Relative Permeability Measurements,' paper SPE 17505 presented at the SPE Rocky Mountain Regional Meeting, Casper, WY (May 11-13, 1988).

1.2 TWO AND THREE-PHASE EXPERIMENTS IN FRACTURED POROUS MEDIA USING CT SCANNER

(E. Rangel-German)

Fractured porous media are usually divided into two systems: matrix system which contains most of the fluid storage, and fracture system where fluids can flow more easily.

1.2.1 INTRODUCTION.

Under this assumption, flow equations are written considering that recovery as dominated by the transfer of fluid from the matrix to the high conductivity fractures which are also often entirely responsible for flow between blocks and flow to wells.

The flow through this kind of medium depends on some mechanisms (e.g. imbibition, drainage, snap-off, piston like flow) that can be studied by means of both numerical analysis and experimental work. Although some people have already worked on the problem, no one knows exactly which mechanisms occur and how strong their effects are. We know that a better understanding of the physical mechanisms and the parameters that influence the flow through fractured porous media the more accurate will be the results from simulator calculations.

To get more data on parameters such as capillary pressure, fracture relative permeabilities and /or saturation distributions, we need further experimental work. The kind of work most commonly done is on artificial fractured models where we know the actual fracture distribution.

1.2.2 LITERATURE REVIEW.

Some authors have performed fine grid simulations to determine the relative effects of various parameters to develop better ways to represent the physical flow processes in dual porosity simulators. Most of the time these studies have relied on the sparce experimental data in the literature (Mattax and Kyte, 1962; Kleppe and Morse, 1974; Kazemi and Merrill; 1979) to verify their models.

The Mattax and Kyte data and the Kleppe and Morse data were obtained similarly. A solid core was placed in a core holder with sparcer along the sides of the core. The gaps were initially filled with oil and were displaced by water being injected form below. Oil recovery and ratios were reported vs time. The Kleppe and Morse experiments could measure saturations via resistivity measurements, but these data were not reported. Mattax and Kyte performed additional imbibition tests using two cores with all faces sealed but one. The two cores were mated spacers between the open faces. The mated cores were then immersed in water, and oil recovery and ratios were reported.

Kazemi and Merrill utilized cores cut in half for their experiments. Water was injected only into the fracture and displacement tests were run at various rates. Fine grid simulations were then used to match the recovery and data on rate vs pore volume injected. Matrix capillary pressure was the matching parameter that was adjusted, since it was noted that at low rates, imbibition dominates the flow. Successful matches were obtained at capillary pressures very close to the ones obtained on a whole core of the same material. Fracture capillary pressure was assumed to be "essentially zero". All but one of their tests were run with zero initial water saturation. Reported water-oil ratio

values had substantial fluctuations with increasing pore volumes injected, which did not occur in their test with an initial water saturation.

Recent experimental work has concentrated on understanding the physical processes going on when the primary flow mechanism is gravity drainge (Horie et al. 1988; Firoozabadi and Hauge, 1990; Labastie, 1990; Firoozabadi and Markeset, 1992). In all of these experiments, stacked cores containing oil were displaced with air. Production rates were modified and average block saturations were measured. The authors argue that matrix blocks are not isolated from each other as stated in many of the dual porosity model formulations, but must have some capillary continuity to obtain the observed performance. Capillary pressures in the fracture as high as 40 psi are reported (Firoozabadi and Hauge, 1990).

As the discussion above indicates, a more fundamental study of two-flow in fractured media is needed. Work sponsored under this program was initiated by Guzman an Aziz (1993) to study two-phase flow in fractured porous media. The initial purpose for this work was to attempt to measure relative permeabilities in the fracture. An experiment was designed to measure saturation distributions in two cores of identical material. One core would be a control, while the other could be cut in half and propped open with inert material to simulate a fracture. Oil and water would be injected into the cores at varying rates. Saturations will be measured by computarized tomographic (CT) scanning the core at various stages of the injection process. Fine grid simulations were then used to history match the experimental results. Fine grid simulations were performed to help in the design of the experimental procedure. An experiment was built but, unfortunately, problems which developed during single phase injection testing, precluded obtaining any useful results.

In general, several authors (Kazemi and Merrill (1979), Beckner (1990), Gilman *et al.* (1994)) have assumed that fracture capillary pressures are negligible. Other have shown experimentally capillary continuity becomes important when gravity provides a driving force (Horie *et al.* , 1988; Firoozabadi and Hauge, 1990; Labastie, 1990; Firoozabadi and Markeset, 1992a, 1992b; Kazemi, 1990) states his belief that capillary continuity is prevalent in the vertical direction and has suggested that, to reduce the number of equation to solve, fractured reservoir simulations should use the dual permeability formulation for the z direction and the dual porosity formulation for the x and y directions.

Hughes (1995) designed, constructed, and got results of an experiment that studies imbibition displacement in two fractured blocks.

1.2.3 EXPERIMENTAL DESIGN.

Three rectangular blocks of Boise sandstone were prepared for this work. The first is a compact (solid) core measuring 3-1/8 x 3-1/16 x 11 inches. The second and third cores consist of two 2-15/16 x 1-1/2 x 11 inch blocks. The second core system has a 1 mm thick spacer fastened in place with Epoxy 907 to provide a separation between the blocks to simulate a fracture. The third core system is constructed similarly but has no spacer between the blocks.

Due to the rectangular shape and the desire to measure in-situ saturations through the use of the CT scanner, conventional core holders could not be used. A core holder similar to the original designed by Guzman and Aziz (1993) was developed for each of the cores. It consists of an epoxy resin surrounding the core. Plexiglas end plates were constructed for the core holders with a piece of 3/8 inch Viton acting as a gasket between the core and the Plexiglas end plates. The Viton gaskets were held in place with automotive gasket material and Plexiglas rods as shown in Fig. 1.

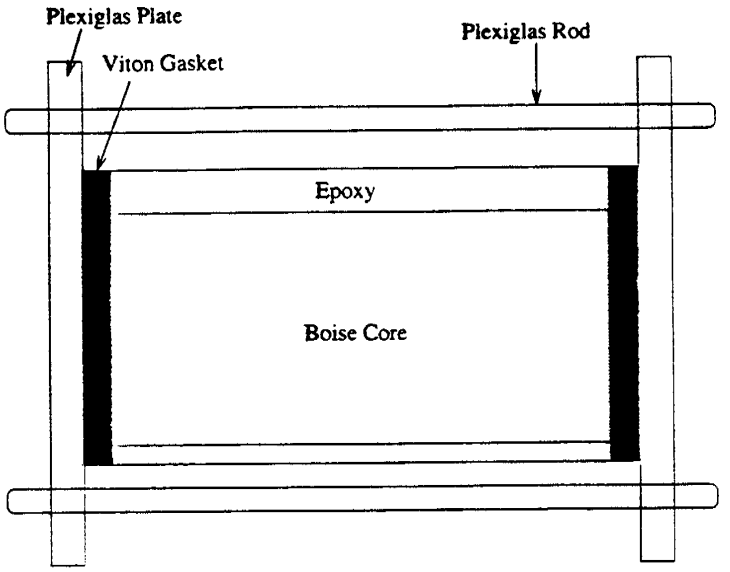

Figure 1. The core holder.

The design that Hughes used had two pressure taps on the top ant two on the bottom. In addition, a Plexiglas plate that was epoxied to the top surface of the core was removed in the new design. The plate was found to be unnecessary and a potential source for leaks.

Several different epoxy system were tested in addition to the system chosen. The Tap Plastics Marine Grade Epoxy system selected uses the #314 resin. The #143 Hardener was chosen because it provides a slower cure, yet remains its chemical resistance properties.

In addition to using a slower epoxy system, an aluminum mold was constructed to allow better heat dissipation.

The mold was tilted at a 45 degree angle and the poxy was poured in. During the consttruction of the compact core holder, heat expansion of the air inside the core caused air bubbles to form and rise the two subsequent cores, holes were drilled in the Plexigas end plates. This action alleviated the problem.

A piece of 3/8 inch Viton was then cut for each ed face of the core holder. A hole was cut in the Viton so that the core face would be exposed.

The pump could deliver 0.01 to 9.99 cm^3/min increments. To use the pumps the user sets the desired discharge rate, the minimum allowable pressure, and the maximum allowable pressure. Plumbing downstream of the pumps allows mixing of the fluids being discharged by each pump. This setup allows injection pressure to be monitored with a test gauge and recirculation to measure pump output rates.

All piping used for the experiment was Paraflex 1/8 inch diameter, 500 psi working pressure plastic tubing with stainless steel Swagelok fittings. This system allows fluids to be directed to any port or combination of ports in the experiment. It can be directed to test the calibration of the pressure transducers, inject from one end and produce dorm the opposite end, inject into one or more if the ports on the top and bottom of the core holder, or to bypass the core holder completely.

The production measurement system is an adaptation of a design first proposed by engineers at Conoco, Inc that was built by Ameri and Wang (1985) and modified by Qadeer (1194) Figure 2 shows the system.

1.2.4 REVIEW OF PREVIOUS RESULTS.

Hughes (1995) evaluated how water imbibed into an unsaturated core. Two items prevented a regular sequence of scan locations. The first was that stainless steel fittings were used for the ports on the top and bottom of the core holder. The second item that caused an irregular spacing of the scan locations was a large vug located 170 mm from the inlet face which we wanted to monitor throughout the experiment.

Migration of the water was monitored with the CT scanner. When approximately 0.06 pore volumes (PV) had been injected, a slight amount of water was seen crossing the fracture to the top block at both the 40 mm location and the 60 mm location. Hughes (1995) concluded from his experiments that the water crossed at those locations and then migrated towards the outlet face in the top and bottom blocks. The water also imbibes back toward the inlet face in the top block.

Despite the fact that water was being injected only into the bottom block, capillary imbibition pulled the water across the continuity and through the top block such that the top block actually broke through before the bottom block.

The experiment was run over the course of four days. Approximately 4.26 PV of water passed through the core. Once the experiment was terminated the valves leading to the core were closed and the core was allowed to sit for three months. The core was then scanned again. The changes that occured between the scans at the end of the injection and those three months later were most noticeable along the edges of blocks and the edges of the vug. According to Hughes (1995) these alterations could possibly be caused by positiong errors, since the core holder was removed from the scanning table during the three months wait.

Hughes (1995) found that the vug in his experiment has filled considerably with water but that there continued to be smal area in the upper left side of the vug that contained air. Those results suggested that, at least some of the changes seen are real, and are not positioning differences.

Hughes (1995) calculated the porosity using the Withjack (1988) expression

$$\phi = \frac{CT_{cw} - CT_{cd}}{CT_w - CT_a} \tag{1}$$

where CT_{cw} is the CT number for a water saturated core at a matrix location, CT_{cd} is the CT number for a dry core at a matrix location, CT_w is the CT number for water, and CT_a is the CT number for air. The CT number for water is 0, while the CT number for air is -1000.

Hughes (1995) found that the average value for porosity calculated from the scans at the end of the displacement experiment using the previous equation was 14.35% which differs from the average porosity measurements of 25.4% obtained by Guzman and Aziz (1993) and 29.3% obtained by Sumnu (1995). He also showed that his experiment had areas in the rock which had lower permeability.

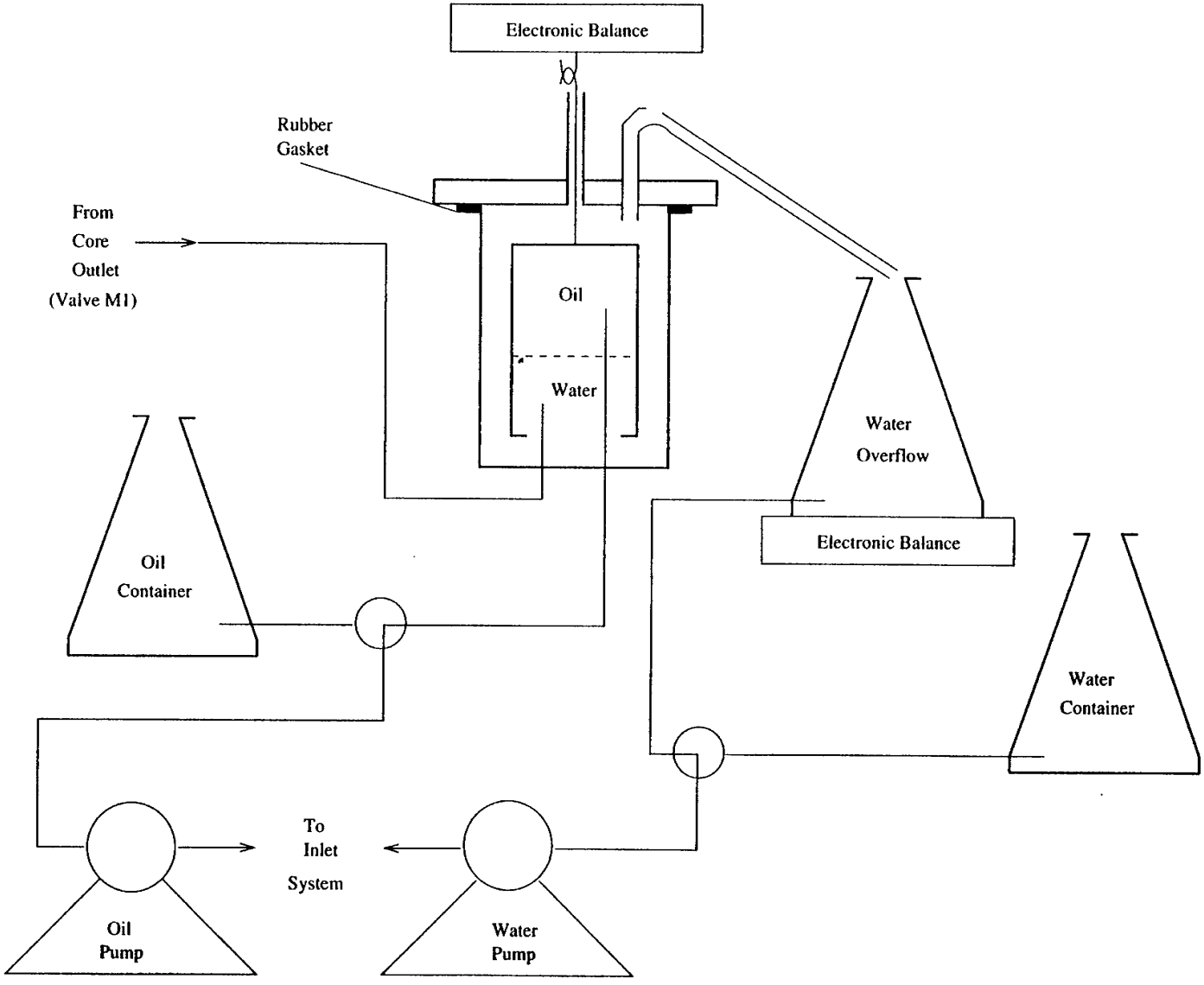

Figure 2. Production measurement system (Hughes, 1995).

The CT scans presented by Hughes (1995) confirmed that capillary continuity can occur in the vertical direction. This continuity pulls fluid in the opposite direction of gravity. The continuity works in any direction depending on the relative strengths of the capillary and Darcy terms in the flow equations.

1.2.5 PLANNED WORK.

The proposed research will continue along the same lines as the Hughes study plans. Detailed measurements of pressure, rate and saturation distribution, as the test are being performed, will be recorded and attempts will be made to measure phase distribution inside the fracture. This research should result in a much better handle on the physical processes that occur when two and three phases flow in a fractured system.

We will also review the criteria to fluids selection, apparatus testing and the apparatus modifications and adjustments (e.g. accommodate other possible boundary conditions, construct another cart for the model) required according to those works done after that, and the knowledge acquired in this kind of models after literature review. All this will provide more accurate results and will let us have a better understanding of how flow through fractured porous media is governed.

The experimental design of Hughes will be utilized, starting for fixing the equipment becuase it is not in right conditions since some "storage duties" made it lose capability. So, the very first step of this proposed research is make everything work as well as Hughes made it before.

Once the previous step is completed, I will start running the same experiments as Hughes(1995) in order to verify that new experiment is giving proper results.

The core holder had a gap corresponding to the width of the Viton gasket at both the inlet and outlet face of the core. Hughes ran it at an injection rate of 1 cm^3/min, the injected water simply dribbled down the inside of the Plexiglas inlet face plate and was imbibed into the bottom block. As the experiment progressed, the water began filling the gap between the Plexiglas plate and the core; however, it was very late in the experiment before the injection water got above the level of the fracture As third step I will fill the space between the Plexiglas plate and the core with filter paper or fine grained sand in order to get a more even distribution inlet or outlet condition. If the injection is to be limited to the fracture space, I will use a tubing configuration similar to that described in a study by Kazemi and Merrill (1979).

According to the recommendations that appear in Hughes(1995), I will put special attention when charging the core with oil, during the displacement experiments, and also during cleaning operations; since Hughes(1995) observed that the cores have areas in the rock which have lower permeability.

To use the CT scanner to monitor the migration of fluids when the core is being charged with oil, or when the core is being cleaned, I will also replace the stainless steel fittings with equivalent plastic fittings. According to Hughes(1995), artifacts in the CT numbers will still occur due to the fittings. So replacing the fittings will decrease them and will allow observations of saturation changes near the injection ports which are not possible with stainless steel fittings.

It remains unclear what causes the continuity between blocks in those experiments. Hughes(1995) states that the most likely explanation is that fine grained material from cutting the end pieces may not have been thoroughly cleaned form the fracture. Repeating those experiments I

will try to reveal whether this material caused the continuity across the fracture, or if there is some other mechanisms.

1.2.6 REFERENCES.

1. Beckner, B.L.: *Improved Modeling of Imbibition Matrix/Fracture Fluid Transfer in Double Porosity Simulators*, PhD dissertation, Stanford University (July 1990)

2. Firoozabadi, A. and Hauge, J.: "Capillary Pressure in Fractured Porous Media," JPT (June 1990) 784-791.

3. Firoozabadi, A. and Markeset, T.: "An Experimental Study of Capillary and Gravity Crossflow in Fractured Porous Media," SPE 24918, presented at the 67th SPE Annueal Technical Conference and Exhibition, Washington, D.C., October 4-7, 1992.

4. Firoozabadi, A. and Markeset, T.: "An Experimental Study of Gas-Liquid Transmissibility in Fractured Porous Media," SPE 24919, presented at th 67th SPE Annual Technical Conference and Exhibition, Washington, D.C., October 4-7, 1992.

5. Gilman, J.R., Bowzer, J.L. and Rothkopf, B.W.: "Application of Short-Radius Horizontal Boreholes in the Naturally Fractured Yates Field," SPE 28568, presented at the 69th SPE Annual Technical Conference and Exhibition, New Orleans, LA, September 25-28, 1994.

6. Guzman, R.E. and Aziz, K.: *Design and Construction of an Experiment For Two-Phase Flow in Fracuted Porous Media*, SUPRI TR-95, Stanford Petroleum Research Institute, Stanford, CA, (June 1993).

7. Horie, T., Firoozabadi, A. and Ishimoto, K.: "Capillary Continuity in Fractured Reservoirs," SPE 18282, presented at the 63rd SPE Annual Technical Conference and Exhibition, Houston, TX, October 2-5, 1988.

8. Hughes, R.G.: *CT Measurements of Two-Phase Flow in Fractured Porous Media,* Masters Report, Stanford University (December 1995).

9. Kazemi, H. and Merrill, L.S.: "Numerical Simulation of Water Imbition in Fractured Cores," SPEJ (June 1979) 175-182.

10. Kazemi, H.: *Naturally Fractured Reservoirs,* Third International Forum on Reservoir Simulation, Baden, Austria (1990).

11. Kleppe, J. and Morse, R.A.: "Oil Production from Fractured Reservoirs by Water Displacement," SPE 5084 presented at the 49th Annual Meeting of the Society of Petroleum Engineers, Houston, TX, Oct. 6-9, 1974.

12. Labastie, A.: "Capillary Continuity Between Blocks of a Fractured Reservoir," SPE 20515 presented at the 65th SPE Annual Technical Conference and Exhibition, New Orleans, LA, September 23-26, 1990.

13. Mattax, C.C. and Kyte, J.R.: "Imbibition Oil Recovery from Fractured, Water-Drive Reservoir," SPEJ (June 1962), 177-184.

1.3 IMBIBITION IN LOW PERMEABILITY MEDIA

(J. Schembre)

1.3.1 INTRODUCTION

The increasing depletion of oil reservoirs requires developing additional crude reserves and implementing efficient recovery techniques for oil to maintain the growing global demand for energy. Fractured petroleum reservoirs contain a substantial fraction (over 20%) of the world's oil reserves (Saidi, 1983). Nonetheless, the efficiency of recovery processes in such reservoirs remains difficult to evaluate because of the lack of general understanding of multiphase flow through fractured porous media.

The existence of fractured reservoirs in siliceous shales such as diatomite, imposes a need for better understanding of the factors influencing hydrocarbon recovery from such rocks. In the Diatomites, fractures are both natural and manmade, and spontaneous imbibition is of critical importance to oil recovery from fractured reservoirs as the rate of imbibition is primarily dependent on the porous media, the fluids, and their interactions. Therefore, a detailed knowledge of the behavior of this process in diatomite is necessary.

Diatomite is a hydrous, noncrystalline form of silica or opal composed of the remains of microscopic shells of diatoms, which are single-celled aquatic plankton plants (Stosur and David, 1975). Reservoir rock is assumed to be water or intermediate wet. Diatomites have a very high porosity (it frequently exceeds 50 percent), and high initial oil saturation (35-70 percent). Unfortunately, they have an exceptionally low permeability (0.1-10 mD) which makes efficient oil production very difficult by conventional means.

Imbibition is an immiscible displacement process, whereby a non-wetting fluid which is within the porous medium is spontaneously expelled by wetting fluid which surrounds the medium and is drawn into the medium by capillary suction. This phenomenon is caused by the differential attraction forces between the pores' walls and the fluids.

In this work, our main focus is the study of one-dimensional spontaneous imbibition in diatomites. We will compare these results with those obtained for a typical sandstone. Thus, we will illustrate the effects of pore structure, permeability, and porosity on imbibition.

The project has been divided in two stages. In the first stage, studies of imbibition in gas-water systems and other properties related to imbibition will be performed for Boise Sandstone. Some understanding of the behavior of water-oil-rock systems may be obtained from studies of the simpler water-air-rock-systems (Handy, 1960). A well defined one-dimensional geometry (Fig.1) is chosen to avoid counter-current imbibition and multidimensional effects. The theoretical understanding and experimental practice obtained in this first stage will be useful in the second stage, where the same properties and mechanisms will be studied for a diatomite outcrop sample. Both rocks are water wet.

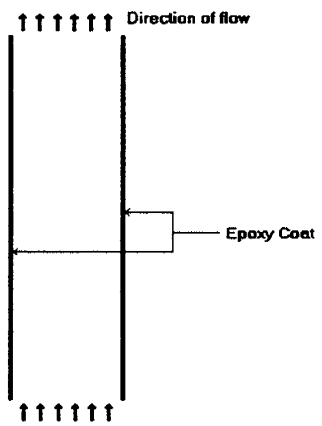

Figure 1. Schematic representation of flow path through the core (one-dimensional flow).

1.3.2 LITERATURE SURVEY

In spite of the importance of imbibition processes in low-permeability fractured rocks, very little work is reported for diatomites.

As defined previously, imbibition is that process by which one fluid displaces another from a porous medium as a result of capillary forces only. An equation that describes the movement of water into dry soils has been derived (Kirkham, 1949 and Cruz, 1992) and the authors noted similarity of the equation obtained to the diffusion equation. From this analogy, it is predicted that the volume of water imbibed would yields a straight line versus the square root of the time and this prediction was confirmed by experimental results.

However, the diffusion-type equation may be questionable for some cases. An alternative equation assuming piston-like displacement can be derived which leads to the same dependence of volume imbibed on the square root of time (Handy, 1960).

If imbibition occurs vertically upward, the flow equation is

$$v_\omega = \frac{k_\omega}{\mu_\omega}\left(\frac{p_c}{x} - \Delta\rho g\right) \tag{1}$$

where

p_c = capillary pressure(atm)

v_w = flow rate($cm^3/cm^2/sec$)

k_w = effective water permeability (Darcy)

w = water viscosity (cp)

$\Delta\rho$ = density difference for water and air(gm/cc)

g = acceleration due to gravity(cm/sec^2)

x = position of front (cm).

In Eq. 1, p_c is assumed to be constant. Assuming piston-like displacement,

$$v_\omega = \phi\, S_w \frac{\partial x}{\partial t} \tag{2}$$

where

ϕ = fractional porosity

S_w = fractional water content of the pore space

x = distance(cm)

t = time(sec)

Substituing Eq. 2 in Eq. 1 results in,

$$\frac{\partial x}{\partial t} = \frac{k_\omega}{\phi \mu_\omega S_\omega}\left(\frac{p_c}{x} - \Delta\rho g\right) \tag{3}$$

Integrating Eq. 3, one obtains,

$$x + \frac{p_c}{\Delta\rho g}\ln\left(1 - \frac{\Delta\rho g x}{P_c}\right) = -\frac{k_\omega \Delta\rho g}{\phi S_\omega \mu_\omega} t \tag{4}$$

For $\frac{\Delta\rho g x}{p_c} << 1$, gravity forces are much less than capillary forces and Eq. 4 reduces

to,

$$x^2 = \left(\frac{2p_c k_\omega}{\phi S_\omega \mu_\omega}\right)t \tag{5}$$

Since $x^2 = \frac{Q_\omega}{\phi A S_\omega}$ where Q_W equals total volume of water imbibed,

$$Q_\omega^2 = \left(\frac{2p_c k_\omega \phi A^2 S_\omega}{\mu_\omega}\right)t \tag{6}$$

where A = cross-sectional area of sample.

The rate of imbibition is a function of the product of the effective water permeability and the capillary pressure of the porous medium. There have been many studies where this non-linear relation has been tested for consolidated porous media, while studies of such a mechanism in low-permeability rocks have been poorly performed. Thus, previous studies of sandstones will be useful, in the first stage of the research, to calibrate and improve our equipment, and simultaneously, acquire detailed knowledge about the mechanism of imbibition.

1.3.3 EXPERIMENTAL DESIGN

The first stage of the research was begun in October, 1996, and has not been completed. At the present time, one-dimensional experiments in Boise Sandstone are still being conducted. Our objective is obtain the change of the average water saturation with time, the time rate of imbibition, and to calculate the permeability-capillary pressure properties from the slope of the average water saturation versus the square root of time.

1.3.3.1 Preparation of Samples

The samples to be used in this first stage are Berea and Boise sandstones. The Berea core is square shaped with dimensions of 14x2.5x2.5 cm, a porosity of 25%, and a permeability of 300 md.

To obtain the samples of Boise Sandstone, a block of sandstone measuring 30x30x30 cm was cut into six smaller blocks of equal dimensions. Cuts were made along the bedding plane to obtain homogeneous permeability along every block. Cylindrical cores were then drilled in the laboratory. The diameter in the samples is 2.0 cm, the length is 11.0 cm, and the permeability and porosity will be measured.

The sample is fired at 450°C for 12 hours to remove the effect of clay swelling and migration during the imbibition process. The cores are then sealed with epoxy on the cylindrical sides to obtain one-dimensional imbibition.

1.3.3.2 Description of Experimental Apparatus and Procedure

The scheme of the experimental setup is shown in Fig. 2. The sample core is suspended by means of an acrylic and steel frame from a weighing balance in an acrylic

container. The reading of the dry weight of the dry core provides the reference in the measurement of weight change during the experiment.

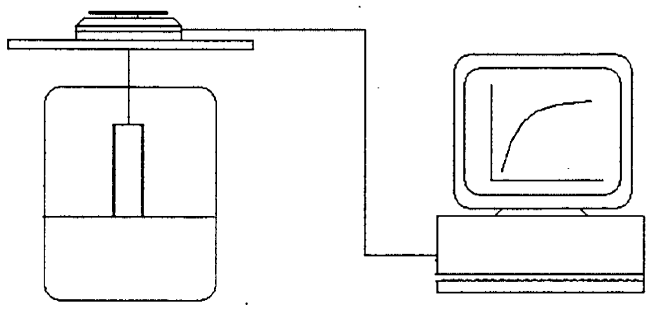

Figure 2. Schematic representation of experimental design.

The water level in the container is regulated manually throughout the experiment so as to just touch the bottom of the core. Thus, the influence of buoyancy forces on the weight change of the core is minimized.

In the experiment performed, the sample used was the Berea core, sample weight was recorded every 10 seconds for 3 hours. After this time, no change was observed in the weight of the sample.

1.3.4 RESULTS

Data obtained from the imbibition experiment for the Berea core was converted into the weight of water imbibed into the core in order to measure the rate of change of water saturation in the core with time. The plot of the weight gain versus the square root of time for the core is shown in Fig. 3. Note that the amount imbibed versus the square root of time is linear consistent with Eq. 16.

Previous studies [Kirkham and Feng (1949), Handy (1960), Garg *et al.* (1996)] show similar results to that obtained in the experiment performed. Hence, we conclude that our apparatus and techniques are appropriate and accurate.

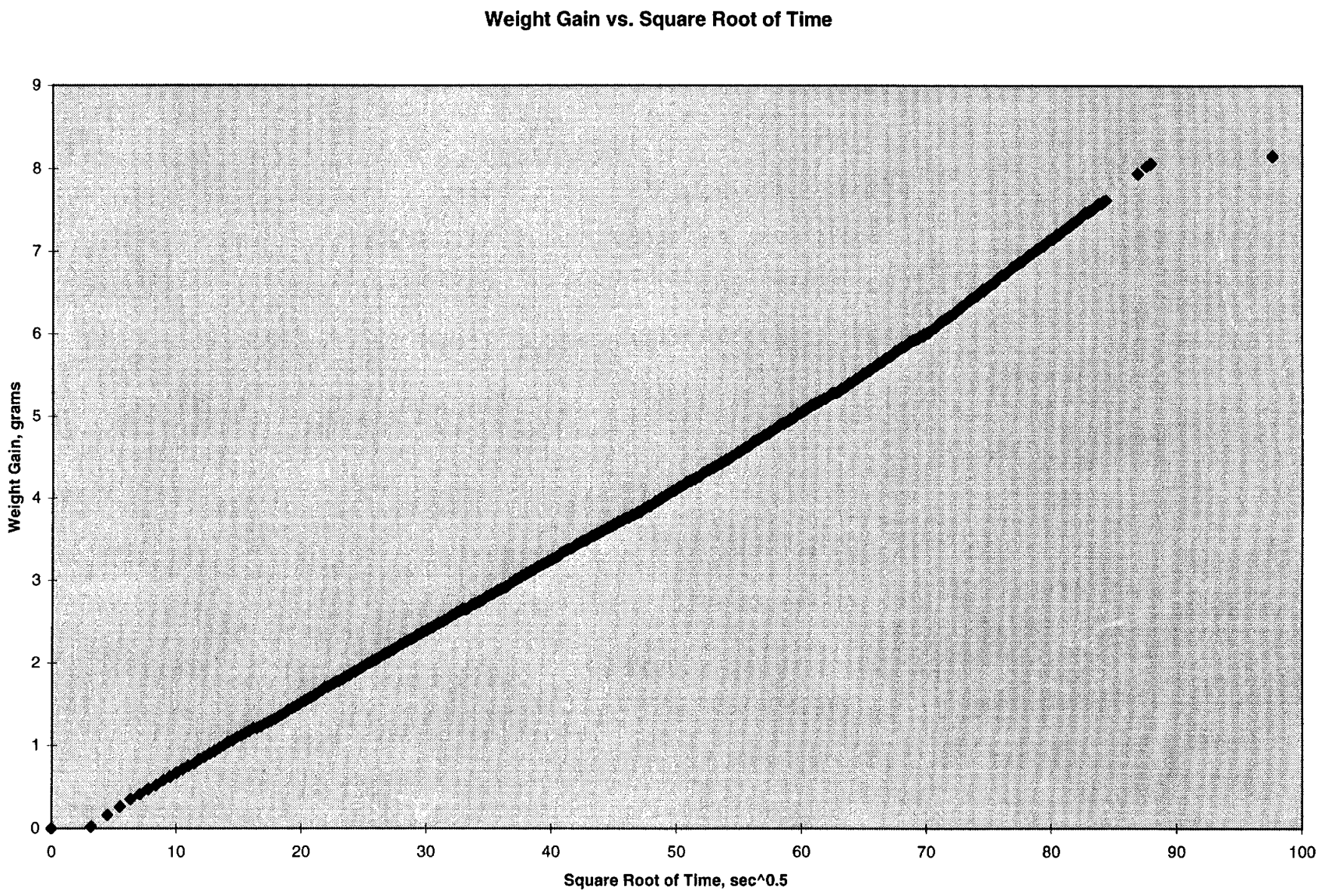
Weight Gain vs. Square Root of Time
Weight Gain, grams
Square Root of Time, sec^0.5
0
1
2
3
4
5
6
7
8
9
0
10
20
30
40
50
60
70
80
90
100

Fig. 3

1.3.5 FUTURE PLANS

The experimental apparatus is being improved at the present time so that the acquisition of the data will be by means of a computer to improve the accuracy and frequency of data reading. Further testing with the Boise samples will be perfomed.

As mentioned before, the next step in this work is to conduct experiments with diatomite at the same conditions to obtain a better understanding of the effects of pore structure, permeability , and porosity on imbibition in low-permeability rocks.

This study is a preamble to the understanding of the mechanism of imbibition in diatomite. For example, we will be able to study the scaling rules for this type of rock and compare these to those obtained for sandstones (Xiaoyun, Norman and Xhouxiang, 1995).

Furthermore, we also intend to extend this work to the imaging of fluid distributions during imbibition. The Petroleum Engineering Department's CT scanner will be used here. Experiments will be performed with both gas-water and oil-water systems.

1.3.6 SUMMARY

Fractured petroleum reservoirs contain a substantial fraction of world's oil reserves, and estimating the efficiency of recovery processes in such reservoirs remains difficult because of the lack of complete understanding of multiphase flow through fractured porous media.

Spontaneous imbibition is of critical importance to oil recovery from fractured reservoirs. However, imbibition processes in low-permeability fractured rocks are not fully understood, and very little work is reported for diatomites. In previous studies for sandstones, it was predicted that the volume of water imbibed versus the square root of time would give a straight line, which was confirmed by experimental results. In this work, our main focus is the study of one-dimensional spontaneous imbibition in diatomites, so that we can compare the results with those reported for a typical sandstone.

The project has been divided in two stages. In the first stage, studies of imbibition in gas-water systems and other properties related to this mechanism will be performed for Boise sandstone. The understanding and practice obtained in this first stage will be useful in the second stage, where the same properties and mechanisms will be studied for a diatomite outcrop sample.

At the present time the project is at the first stage, where experiments are being performed for air-water systems in sandstones, improving both the experimental apparatus and procedure. The future plans include experiments with diatomite for air-water and oil-water systems, the study of scaling rules for such rocks, and the use of an X-ray CT scanner during experiments.

1.3.7 REFERENCES

1. Cruz, J. and Perez, C.: "Imbibition as a Dispersion Process," SPE 23748, paper presented at the Second Latin American Petroleum Engineering Conference, II LAPEC, Caracas, Venezuela (March 8-11, 1992).

2. Garg, A., Kovscek, A.R., Nikravesh, M., Castanier, L.M. and Patzek, T.W.: "CT Scan and Neural Network Technology for Construction of Detailed Distribution of Residual Oil Saturation During Waterflooding," SPE 35737, paper prsented at the Western Regional Meeting, Alaska (May 22-24, 1996).

3. Handy, L.L.: "Determination of Effective Capillary Pressures for Porous media from Imbibition Data," *Trans. AIME* 219 (1960).

4. Kirkham, Don and Feng, C.L.: Soil Science 67 (1949) 29.

5. Saidi, A.M.: "Simulation of Naturally Fractured Reservoirs," SPE 12270, paper presented at the SPE Symposium on Reservoir Simulation, San Francisco (Nov. 16-18, 1983).

6. Stosur, J.J. and David, A.: "Petrophysical Evaluation of the Diatomite Formation of the Lost Hills Field, California," SPE 5501, paper presented at the SPE-AIME 50th Annual Fall Technical Conference and Exhibition, Dallas (Oct. 1975).

7. Xiaoyun, Z. Morrow, N. and Xhouxiang, M.: "Experimental Verification of a Modified Scaling Group for Spontaneous Imbibition," SPE 30762, paper presented at the SPE Annual Technical Conference and Exhibition, Dallas (Oct. 22-25, 1995).

PROJECT 2: IN-SITU COMBUSTION

To evaluate the effect of different reservoir parameters on the in-situ combustion process. This project includes the study of the kinetics of the reactions.

2.1 In-Situ Combustion

(L.M. Castanier)

Although no work has been done this academic year on in-situ combustion, we have a keen interest in this recovery method. Indeed, in-situ combustion can be economically used in reservoirs where no other improved oil recovery technique is possible. We intend to maintain our effort in this research direction.

As soon as we find the appropriate student we plan to continue work on the catalytic effects of metallic salts on the combustion reactions of crude oils. This will involve both kinetic experiments and tube runs. Of special interest will be a study of possible in-situ upgrading of heavy crudes by combustion. Based on comments from industry at various technical meetings, a need for research exits in this direction. Preliminary work appears very promising, both in the areas of sulfur and heavy metals reduction, and in terms of API gravity improvement. We plan to collaborate with interested companies during this project.

The experimental equipment is in working order. Modeling of the reactions using the results from both kinetics apparatus and tube runs will be continued. This effort should ultimately lead to predictive models for in-situ combustion field projects.

PROJECT 3: STEAM WITH ADDITIVES

To develop and understand the mechanisms of the process using commercially available surfactants for reduction of gravity override and channeling of steam.

3.1 STEAM INJECTION IN FRACTURED POROUS MEDIA

(S. Shang)

This work will be published separately as a technical report and will be sent to DOE for publication.

3.1.1 SUMMARY

Steam injection is the most widely used enhanced oil recovery (EOR) technique and the most successful one for heavy oil recovery in unfractured reservoirs. Field tests indicate that steam injection is also feasible for fractured reservoirs which are estimated to contain a large fraction of the world's oil supply. However, the mechanisms involved in fluid and heat transfer between the matrix and the fracture during steam injection processes are not well understood. The aim of this project is in situ measurement of three phase saturations during steam injection in a fractured model, and to understand the physical processes involved in such systems. The plan was to continue the work of Sumnu (1995) by conducting steam injection experiments in the presence of oil using the existing fractured model. However, preliminary experiments revealed some problems associated with the existing model. Simple modifications were then made to the model, and steam injection experiments were performed. For most of the steam injection runs, steam was not observed in the matrix blocks. In one of the runs, however, steam was observed in the matrix and this was found to be due to the partial blockage of the production well. Attempts to saturate the model with oil proved to be difficult with the configuration of the model.

Numerical simulations of the steam injection experiments were performed using a commercial thermal simulator (STARS). The effects of injection steam quality, steam/water relative permeability and fracture capillary pressure on steam saturation in the matrix were investigated in the simulation study.

This report describes the steam injection experiments and reports the simulation results conducted in 2D. It also outlines the problems associated with the fractured models used in this work. Recommendations for a possible new design for a fractured model are also presented.

3.2 STEAM DRIVE IN DIATOMITE

(S.K. Bhat)

3.2.1 ABSTRACT`

There are large petroleum deposits in low permeability diatomaceous rocks. These oil deposits form a substantial part of original oil trapped in the San Joaquin Valley, California. Water flooding and steam drive with hydraulically fractured injectors and producers are possible ways of recovering oil from such deposits. Water flooding in diatomaceous rocks has not been widely effective, primarily due to the low mechanical strength of the rock. The brittle formation fractures easily and fracturing leads to injector/ producer linkage. Steam injection on the other hand shows better prospects of performance in these reservoirs. Since diatomite is primarily silica, steam injection into a diatomite reservoir could cause some changes in reservoir rock characteristics due to dissolution, transport and re-precipitation of silica. This study is aimed at modeling mathematically this dissolution process and predicting the dissolution and precipitation rates by developing a simulator code that predicts the physics of these processes. The simulator results will be compared with available experimental results. The mathematical model will then be updated to include the effect of this dissolution mechanism on the reservoir properties, such as permeability with duration of steam injection.

3.2.2 INTRODUCTION

A large number of diatomaceous petroleum reservoirs are found in Kern County, California. For example, these fields include South Belridge, North Belridge , Cymric, Midway Sunset and Lost Hills diatomite. Collectively they contain an estimated 10 billion barrels of original oil in place (OOIP). This figure is roughly comparable to the OOIP for Prudhoe Bay, Alaska (Kovscek *et al*, 1996).

Diatomite is a hydrous, non-crystalline form of silica or opal composed of microscopic shells of diatoms. Diatoms are the remains of single celled microscopic aquatic plankton. The diatomite reservoirs are typically of high porosity (25-65%) and high internal surface area, but have very low permeability ranging from 0.01 mD to 10 mD (Stosur, 1976). In addition, diatomaceous rocks have low mechanical strength. The low mechanical strength and low permeability of these rocks has resulted, generally, in low primary recovery and unpredictable performance of water flooding even with hydraulically fractured injectors and producers.

Steam flooding pilots have been more successful, and in general, thermal methods hold great promise. But, steam injection into diatomite has its own complications. One factor influencing this process is the reactivity of diatomite with steam. During steam injection the hot aqueous condensate might dissolve the diatomite which is principally SiO_2, and this dissolved silica could be carried forward by the moving water condensate. As the condensate travels, its temperature drops, and thus, the dissolved silica tends to precipitate at other places within the reservoir. This process can cause permeability redistribution within the reservoir, which is already relatively impermeable. Likewise, silica dissolution might cause cavities in the formation around injection wells. Thus, the understanding of kinetics of silica dissolution and precipitation will form an important facet of planning a good steam recovery project in diatomite reservoirs.

3.2.3 LITERATURE SURVEY

Many reports are available in the literature regarding silica dissolution in alkaline flooding. Most studies have focused on dissolution mechanisms and rates. One notable reference relates particularly to diatomite. Koh *et al.* (1996) have studied the problem of permeability damage in diatomaceous reservoirs due to condensate flow. They performed experiments to find the behavior of a diatomite core as hot saturated silica solution was injected into it. They compared their experimental results with a mathematical model that assumed silica dissolution and precipitation both follow a first- order kinetic equation. While modeling permeability damage, they also assumed a simple empirical model of permeability decrease due to porosity decrease,

$$k(x,t) = k_0\left(\frac{\phi}{\phi_0}\right)^{\gamma} \qquad (1)$$

where k_0 and k are permeabilities at porosities f_0 and f respectively; g is assumed to be a constant . They evaluated g to be 9.0 for the conditions of their experiment.

The model assumed by *et al.* for kinetics of silica dissolution and precipitation is simplistic. The following aspects possibly need to be investigated in order to successfully model diatomite dissolution and precipitation and their effect on permeability.

1. The kinetics of silica dissolution and precipitation reactions at high temperatures, the factors that influence these reactions, and ultimately their effect on the solubility of diatomite in water.

2. The relationship between permeability, porosity, and particle size distribution of a porous medium. The change of porosity and particle size distribution with diatomite dissolution and precipitation, and consequently, the evolution of permeability with throughput and temperature history.

3. The impact of high temperature and pressure conditions on the permeability of diatomite.

The system that we are examining is at a high temperature and is slightly alkaline (pH in the range of 7.5-8.0). Various people have tried experimentally to model silica dissolution and precipitation kinetics. Bunge *et al.* (1982) proposed kinetic models based on a irreversible first order reaction in an alkaline medium. Deghani (1983), based on experiments with sandstone, concluded that the dissolution of silica can be represented as a first order reaction only for pH's in the range of 8. Similar conclusions were reached by Mohnot (1984). Thornton (1985) *et al* later showed that silica dissolution rate decreases as the solubility limit of silica at the prevailing temperature is reached. These findings rule out first order kinetics for silica dissolution in an alkaline atmosphere near the solubility limit of silica in water.

Secondly, the effect of high temperatures on permeability of siliceous reservoirs has been studied experimentally. Weinbrandt *et al.* (1975), Aruna (1976), Danesh (1978) all performed experiments that suggest that there is a considerable permeability decrease at high temperatures and pressures in porous media comprised mainly of silica, whereas non-siliceous porous media, like limestone, show no permeability decrease. Udell *et al.* (1989)

postulated that this decrease in permeability of siliceous porous media is due to stress-induced silica dissolution. They argued that there is a linear relationship between surface chemical potential and surface stress. The surface stress is highest at contact points in a porous medium under pressure. Thus, the surface chemical potential, too is highest at these points. This high potential causes the solubility of silica in water to be higher at these location compared to locations with lower stresses, like the main pore body . The difference in solubility causes a silica concentration gradient between high stress locations and the rest of the medium. Due to the concentration gradient, silica migrates from contact points to the main pore fluid by diffusion along the surface. The pore fluid is already saturated at a level consistent with surface potential of unstressed pore surface. The addition of silica by diffusion, results in super saturation of silica in the main pore body. This results in precipitation of silica on the unstressed pore-body surface . This phenomenon causes permeability reduction.

3.2.4 MODELING

Our effort is to model mathematically a system undergoing the process of silica dissolution and precipitation with associated impact on permeability, and then compare the results of the model with the experimental data generated by Koh *et at* (1996), for hot water flow through diatomite.

Our modeling study will consists of two parts. The first is flow modeling, and the second is to model how dissolving and precipitating silica alters the rock porosity and permeability.

3.2.4.1 Flow Modeling

The flow modeling is essentially the mass conservation principle. Initially, a model for single-phase flow (hot water) through diatomite is considered. Once our model accurately describes the dissolution process and the permeability alterations for condensate flow through diatomite, we will update this model to multiphase (steam) flow.
The equations used for flow modeling are the following.

Silica Mass Balance Equation

$$-\frac{\partial(C_{si} u_w \rho_w)}{\partial x} + q_{si} = \frac{\partial(C_{si} \phi \rho_w)}{\partial t} \qquad (2)$$

where C_{si} is the silica concentration in moles of silica per unit mass of water, u_w is Darcy velocity of water in length per unit time, r_w is the liquid density at the location, x, and time, t. The term q_{si} is silica generation at location, x, and time, t, in moles of silica per unit time per unit rock volume and f is the porosity.

Rock Mass Balance Equation

$$q_r = \frac{\partial((1-\phi)\rho_r)}{\partial t} \qquad (3)$$

where q_r is rock generation in mass per unit time per unit rock bulk volume and r_r is the rock density. The rock generation term in the mass balance equation will be due to silica dissolution/ precipitation.

Energy Balance Equation

$$-\frac{\partial(u_w \rho_w c_{pw} T)}{\partial x} + q_h = \frac{\partial((\phi \rho_w c_{pw} + (1-\phi)\rho_r c_{pr})T)}{\partial t} \qquad (4)$$

where T is temperature change from base temperature, and c_{pw} and c_{pr} stand for specific heat capacity of liquid and rock respectively. The term q_h is the term for any heat source or sink.

Darcy's Law

$$u_l = \frac{k}{\mu}\frac{dp}{dx} \qquad (5)$$

where k is permeability, m is viscosity and p is the pressure.

Water Balance Equation

$$-\frac{\partial(u_w \rho_w)}{\partial x} = \frac{\partial(\phi \rho_w)}{\partial t} \qquad (6)$$

where it is assumed that there is no water generation.

3.2.4.2 Silica Kinetics Modeling

The second term on the left hand side of Eq. 2 and on the right hand side of Eq. 3 is the term for net silica dissolution. Initially we assume that Darcy velocities are low and hence the residence times are large such that silica dissolution and precipitation attain equilibrium. The equilibrium silica concentration attained as a function of temperature is given by a polynomial of the form (Bruton, 1996),

$$C_{si} = a_0 + a_1 T + a_2 T^2 + a_3 T^3 + a_4 T^4 \qquad (7)$$

where a_i are constants and T is the temperature in ^{0}C.

In case the assumption of local equilibrium proves to be invalid, (i.e., the dissolution process is not able to attain equilibrium), we will derive a kinetic model for silica dissolution.

The model would rely on the fact that silica which is primarily SiO_2 is like any other mineral oxide. So, its dissolution would occur via hydrolysis of active sites on the surface through the formation of an intermediate complex (Saneie *et al.*, 1986). This complex exists in equilibrium with silicic acid in the solution. The dissolution of the silica can be represented as a first-order reaction only for sufficiently low alkali concentrations and low temperatures. The reaction is not decidedly first order at moderately high pH and high temperatures. Most importantly, the dissolution phenomenon is a surface reaction.

Experiments (Saneie *et al.*, 1986) suggest that silica solubility in terms of total dissolved silica, increases with temperature only for moderate initial pH (less than 10) and it is practically insensitive to temperature changes for high initial pH values (in the range of 11 onwards).

The silica dissolution mechanism is a two step process.

1. formation of the intermediate complex

2. dissolution (desorption) by bond breaking.

The first step is a rapid step while the second step is slow, and thus rate limiting. There are experimental instances to prove the existence and formation of such a complex in the silica dissolution process (Saneie *et al.*, 1986).

An alkaline environment has effects on the silica dissolution rate and equilibrium concentration since it is hydrolysis of a mineral oxide. In an alkaline environment, there exist ionic silicic species other than $Si(OH)_4$ and none of these participate in the back reaction of Step b, (i.e. precipitating back on the surface). For a given amount of silica leaving the surface, the formation of ionic species other than $Si(OH)_4$ causes lower concentration of $Si(OH)_4$ in the solution and therefore tends to shift equilibrium (between the dissolution from surface and deposition on the surface) more towards dissolution. This leads to a higher reaction rate. Thus higher pH enhances the dissolution rate.

There is also an effect of the ionic species present in the system (like NaCl). Since the sites available for silica complex formation are also sites available for ion exchange, there is a competition between these sites and this fact must be taken into account when formulating the rate equation.

3.2.4.3 Permeability Modeling

For modeling permeability, instead of the simple power-law permeability-porosity relationship illustrated in Eq. (1), we will use a permeability relationship depending additionally on the particle size distribution. The permeability of an unconsolidated medium depends on porosity f, tortuosity t, mean grain size $D_{p,m}$, standard deviation s, and skewness g of the pore size distribution. For unconsolidated sands, for example, the permeability expressed in these terms is (Panda and Lake, 1994),

$$k = \frac{D_{p,m}{}^2 \phi^3}{72\tau(1-\phi)^2}\left[\frac{(\gamma V_{Dp}{}^3 + 3V_{Dp}{}^2 + 1)^2}{(1+V_{Dp}{}^2)}\right] \qquad (8)$$

where $V_{Dp} = s / D_{p,m}$ is the coefficient of variation of pore size distribution. For homogeneous media V_{Dp} is zero.

This model of permeability and porosity is good for a medium having permeability up to 1 mD. For media having permeability lower than 1 mD, this equation predicts results which are higher than observed. Since diatomite permeability falls below 1 mD limit, certain type of a suitable equation would be needed ultimately.

Based on the formulated mathematical model and the equations developed, we are solving the equations numerically using standard reservoir simulation techniques.

3.2.5 CONCLUSIONS

We are in the first stages of simulating a steam drive process for diatomite reservoirs. The system is currently, for single-phase flow with the assumption, that residence times are low enough, such that equilibrium is reached in the dissolution mechanism. If our assumptions are correct, the model would agree with the available experimental data. In case it is not, we will modify the flow model to take into account non equilibrium of the dissolution mechanism. After a dissolution model is validated, the simulation model will be updated to include permeability changes. Ultimately, we will attempt to model three-phase flow under reservoir conditions which would also include effects on permeability.

3.2.6 REFERENCES

1. Aruna M.: "The Effect of Temperature and Pressure on Absolute Permeability of Sandstone," (1976).

2. Aziz K. and Settari A.: "Petroleum Reservoir Simulation," (1979).

3. Bunge A. L., Radke, C. J.: "Migration of Alkaline Pulses in Reservoir Sands," (1982).

4. Bruton, C.: Private Communication, Lawrence Livermore National Laboratory (1996).

5. Danesh A., Ehling-Economides, C., and Ramey, H. J., Jr.: " Effect of Temperature Level on Absolute Permeability of Unconsolidated Silica and Stainless Steel," (1978).

6. Deghani K.: "Caustic Consumption by Reservoir Rock at Elevated Temperatures," (1983).

7. Koh, C. J., Dagenais, P. C., Larson D. C., and Murer A. S. : "Permeability Damage in Diatomite Due to In-situ Silica Dissolution/ Precipitation," (1996).

8. Kovscek, A. R., Johnston R. M., and Patzek T. W.: "Interpretation of Hydrofracture Geometry During Steam Injection Using Temperature Transients I. Model and Verifications (1996).

9. Stosur J. J.: "Petrophysical Evaluation of the Diatomite Formation of the Lost Hills Field, California," (1976).

10. Mohnot, S. M., Bae, J. H. and Foley L.: "A Study of Mineral Alkali Reactions. (1984).

11. Panda, M. and Lake, L. W.: "Estimation of Single Phase Permeability from Parameters of Particle Size Distribution," (1994).

12. Saneie, S. and Yortsos, Y.C.: "Kinetics of Silica Dissolution and Hydroxyl Ion Consumption in Alkaline flooding," (1986).

13. Thornton, S. D.: "Dissolution and Condensation Kinetics of Crystalline and Amorphous Silica in Alkaline Solutions," (1985).

14. Udell, K. S. and Lofy J. D.: "Permeability Reduction of Unconsolidated Media Caused by Stress Induced Silica Dissolution," (1989).

15. Weinbrandt, R. M., Ramey H. J., Jr., and Casse F.J.: "The Effect of Temperature on Relative and Absolute Permeability of Sandstones," (1975).

3.3 OIL-FOAM INTERACTIONS IN A MICROMODEL

(N. Sagar)

3.3.1 INTRODUCTION

This report describes the work done on Oil-Foam interaction visualization using micromodels. We first start out by a general introduction of micromodel studies and why they are important. After defining the micromodel characteristics which were used in our experiments, the experimental procedure is described followed by a discussion on the results and future research.

3.3.1.1 Why We Need Micromodel Studies

Different approaches have been used in the past to scale up foam properties to the reservoir scale. They represent different levels of ambition in describing the physics of confined foam. One approach, a purely empirical one, relies on calibrating a flexible simulator by selected laboratory data which are measured on a conventional core-sample scale and believed to represent those foam effects which are most critical. The empirical foam model implemented in STARS, a pseudo-compositional reservoir simulator is probably the best example of this approach. The other approach to scaling up foam properties, the mechanistic approach, attempts to extract information about the physical flow mechanisms as actually observed on the pore level, and construct mathematical relationships between experimental parameters that can be used to translate foam properties to different scales. The simulator best known for this approach was developed at the University of California at Berkeley. The physical mechanisms in this model are based strongly on observations of foam flow in etched-glass micromodels.

Micromodels representing the geometric structure of a rock pore network while allowing direct visual observation of the flow phenomenon, have proven useful for viewing pore-level events in several reservoir flow processes. Currently accepted theories on foam flow are largely built on the basis of pore-model observations.

3.3.1.2 Design on the Micromodels

Initially micromodels were etched in glass. The first type consisted of regular, straight or constricted channels, made into an interconnected lattice. They are useful in comparing experimental observation with theories of fluid flow in regular systems and provide a useful conceptual link to other media such as capillary tubes. Later the designs were improved upon to include images of actual rock pores. Three dimensional continuity was a natural loss.

For glass micromodels, the reaction kinetics of acid etching makes it necessary to enlarge the pore sizes of typical sandstone by a factor of 5 to 50 compared to the original size. This turns out to be a limitation in studying processes that depend critically on capillary forces. Acid etching also introduces a degree of surface roughness to the pore walls.

The micromodels used in our experiments comprise the next generation of pore-models. The design replicates the pore structure of Berea sandstone on a silicon wafer. The

fabrication technique is a direct adaptation of the etching techniques used by the computer industry. The pore cavities are created photochemically, a process which is not rate-limited such as acid etching. These high resolution silicon micromodels offer 1:1 scaling of the Berea sandstone pores and throats.

3.3.1.3 Foam Studies Using Micromodels

Considerable literature exists on foam work done with glass pore-models. The silicon-micromodel design and fabrication is covered in great detail by Hornbrook *et al.* Foam flow experiments using the silicon pore-models have been done (Hornbrook *et al.*). Figures 1 and 2 show their equipment. Ours is essentially the same. The work presented in this report outlines three experiments which were done with two different kinds of foam in the presence of oil. Foam propagation and stability in the presence of oil has always been a concern. By working with different foams and oils we have tried to expand on the knowledge on oil-foam interactions and the conditions required for lamella stability.

3.3.2 MICROMODEL CHARACTERISTICS

Two different types of micromodels were used in the study. The characteristics of these models are outlined below.

- Σ 500 micron repeat pattern repeated 10,000 times on a 5 sq. cm silicon wafer
  Etch depth 15 to 35 microns.
- Σ Porosity 35%
- Σ Permeability: 1 millidarcy.
- Σ Pore Sizes : 1-150 mm
- Σ Throats : 0.5-10 mm

<u>Specific Characteristics of 'Model A (old)'</u>

- Σ Bonding at 200-400 C & 600 Volts
- Σ Etch depth of 15 mm
- Σ Flow Channels only near the inlet and outlet ports.

<u>Specific Characteristics of 'Model B (new)'</u>

- Σ Bonding at 450 C a& 1500 Volts.
- Σ Etch depths of 15, 25 and 35 mm.
- Σ Flow Channels extended to the length of the sides near the inlet and outlet ports.

Model B (new) was used for Experiments 1 and 2. Model A (old) was used for Experiment 3. Figures 3-6 show details of the models.

3.3.3 EXPERIMENTAL SET-UP

All the experiments were done at constant pressure. Fluid injection (Carbon Dioxide, Surfactant, oil, water etc.) was facilitated by using pressure bottles (connected by the pressurized lines). The various equipment used are outlined below. All the tubing used was made of Teflon with a diameter of 1/16".

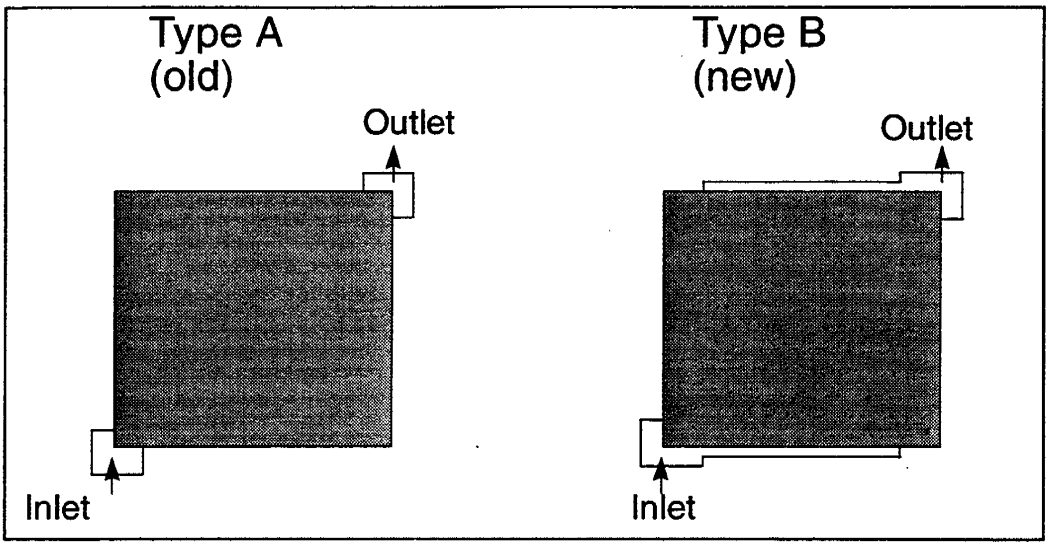

Figure 1: Flow Channels in the two silicon Micromodels

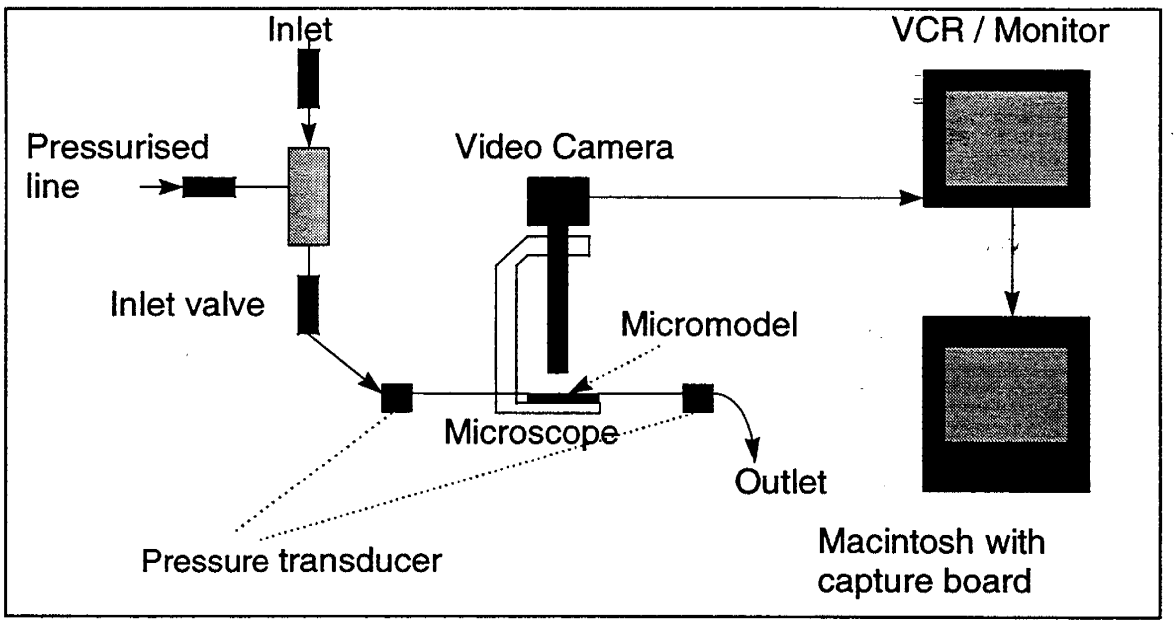

Figure 2: Line diagram of the experimental set-up.

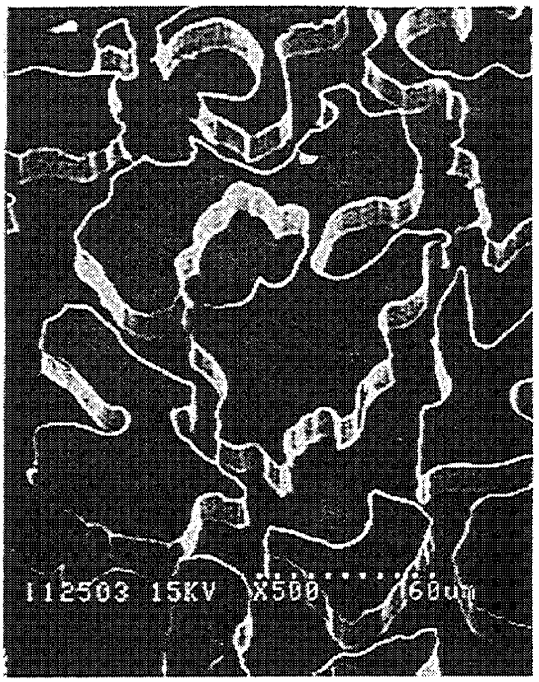

Figure 3: SEM of model A (old)

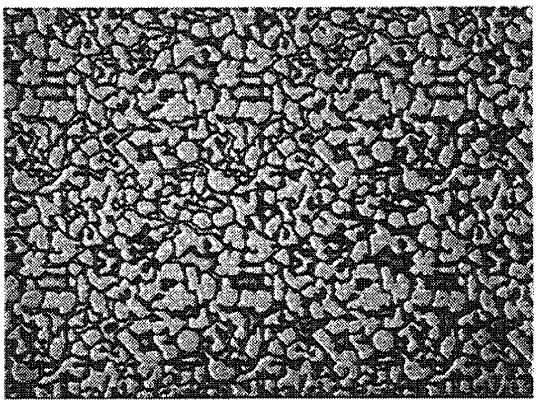
Figure 4: Photograph of the repeat etch pattern on the silicon wafer

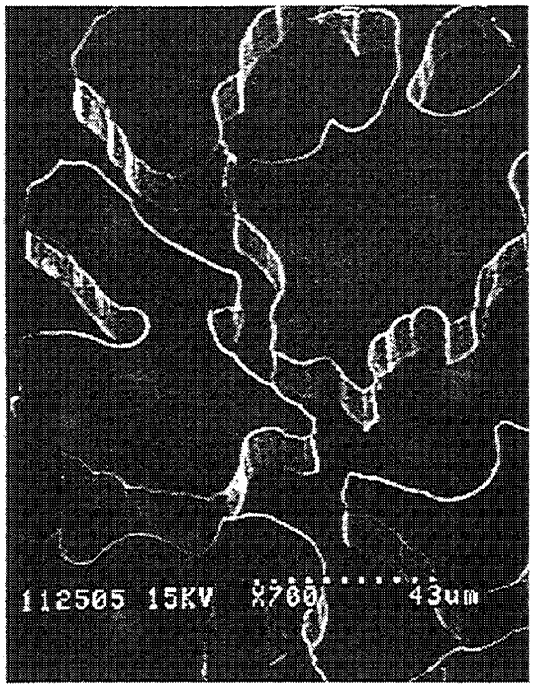

Figure 5: SEM of model A (old)

Figure 6: SEM of model B (new) showing the melted glass on the etched pattern due to bonding of the wafer with Pyrex at extreme conditions

. **Microscope**: A Nikon Optiphot-M with a photo tube allowing for video imaging was used. The Objective lenses used along with their properties are as outlined:

Table 1: Properties of Objective Lenses

Model	Magnification	Working Distance (mm)	Numerical Aperture	Viewable Diameter (mm)
5X	5X	20.0	0.1	3000
0.4LWD	20X	6.0	0.4	800
0.5ELWD	40X	10.1	0.5	375

Working distance is the distance between the tip of the lens and the focal plane of the objective. Numerical Aperture relates to the light gathering ability and is a dimension less number between 0 and 1. Higher the value, better the light gathering.

2. **Video Camera**: A Sanyo closed circuit television camera was used to convert the images through the microscope into electric impulses. An attached photo tube allowed image viewing.

3. **Video Cassette Recorder**: The image from the video camera was recorded on a Mitsubishi NTSC format video cassette recorder. Its NTSC format allowed recording and playback at a speed of thirty frames per second.

4. **Television Monitor**: In order to view the recorded pore-level events, the VCR was connected to a high definition Sony Color Monitor.

5. **Macintosh**: The images from the VCR were captured with the aid of a Spigot II tape video capture board in an Apple Macintosh computer. Image enhancement was done using Adobe Photoshop.

6. **Transducer**: A Celesco differential pressure transducer with a fifty psi pressure plate was used to measure fluid pressure differential across the silicon model.

7. **Demodulator**: A Celesco carrier demodulator was used to convert the electrical signals from the transducer into pressure units.

8. **Chart Recorder**: A Soltec strip chart recorder was used to plot the differential pressure as recorded by the transducer.

3.3.4. EXPERIMENTAL PROCEDURE

All the experiments were performed using the following generic procedure.

1. CO_2 Flood
2. Water / Brine flood to dissolve all CO_2.
3. Oil flood to connate water saturation.

4. Water / Brine flood to residual oil saturation.
5. Surfactant flood.
6. Gas Injection to generate foam
7. Surfactant flood (Higher concentration)
8. Gas Injection to generate foam

Steps 5 and 6 were repeated (as shown in 7 and 8) for higher concentrations of surfactant. Before beginning each experiment, the models were cleaned using water and methanol. The outlet was at atmospheric pressure and the inlet pressure was measured. All fluids entering the micromodel were filtered to 0.22 mm. The experimental set-up is as shown in Fig. 2. A soluble dye was used to color the surfactant so that it could be visualized better. The dye used was an ethyl-oil soluble dye: benzene-azo-2-Napthol.

Experiments Performed

The experiments conducted are tabulated in Table 2.

Table 2. Experiments Conducted.

Experiment	Surfactant	Concentration	Oil	Model Type
1.	AOS 1618	0.001% 0.01%	Oseberg Crude	B
2.	Nansa (AOS)	0.001% 0.01% 0.1% 1%	Kerosene	B
3.	FC 740 (In Kerosene)	0.01% 0.1% 1%	Kerosene	A

For Experiments 2 & 3, brine was used as the aqueous phase instead of water. The following table lists the brine formulation. This formulation is based on actual North Sea water. The brine was filtered with a 0.45 Milli-Pore filter.

Table 3. Composition of Brine (Wetting Phase in Experiments 2 & 3).

Chemical	Grams/ Liter
NaCl	24.79
MgCl2.6H2O	11.79
KCl	0.80
CaCl2.2H2O **	1.60 **
SrCl2.6H2O	0.021
Na2SO4	4.14
NaHCO3	0.206
Formaldehyde (1000ppm)	2.7

** CaCl2.2H2O was not added because of anticipated precipitation problems.

3.3.5 RESULTS

The results of the three experiments performed are discussed separately under individual headings.

3.3.5.1 Experiment 1

Experiment 1 was the only experiment in which crude oil (Oseberg) was used as the non-wetting phase. The surfactant used was an Alpha Olefin Sulfonate AOS 1618 and the gas used for foam generation was carbon dioxide. The aqueous (wetting) phase was water and the model used was 'B'. The following observations were of significance in Experiment 1 (Figs. 7 to 13).

1. Oseberg crude formed oil in water emulsions in the presence of AOS surfactant.

2. No foam lamella were observed.

3. An emulsion forming sequence was observed.

4. Asphaltene deposits clogged the micromodel disabling us from proceeding to higher surfactant concentrations.

5. Flow through the model was extremely slow in spite of a deeper etch depth of 35 mm.

3.3.5.2 Experiment 2

In Experiment 2, the surfactant used was again an Alpha Olefin Sulfonate (Nansa) with the gas for foam generation was carbon dioxide. The wetting phase was brine and the non-wetting phase was kerosene. The model type used was 'B'. The following were the main observations of Experiment two: (Figs. 14-19)

1. Emulsions were seen in the presence of kerosene and surfactant.

2. No foam was observed.

3. Emulsions were seen to be more stable at higher concentrations.

4. Very little oil was required for forming the emulsions.

5. Flow through the model was extremely slow.

3.3.5.3 Experiment 3

In Experiment 3, we formed an oil-foam. The surfactant was a Fluoro-Carbon, FC 740, diluted in kerosene. The wetting phase was Brine and the non-wetting phase was kerosene. Carbon Dioxide was used to generate the foam in-situ. The model type used was 'A'. The following were the main observations of Experiment 3 (Figs. 20 -25).

EXPERIMENT 1

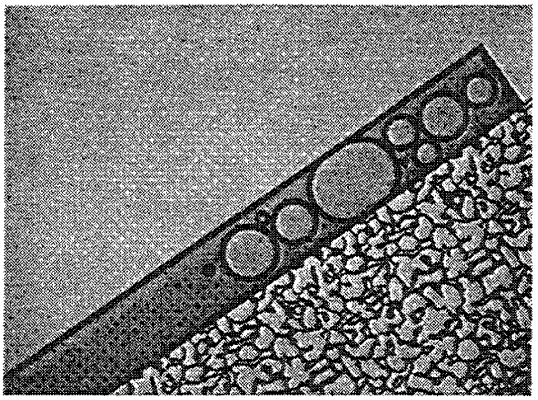

Figure 7: CO_2 bubbles flowing in the outlet channel during CO_2 flood. Flow is top to bottom diagonally.

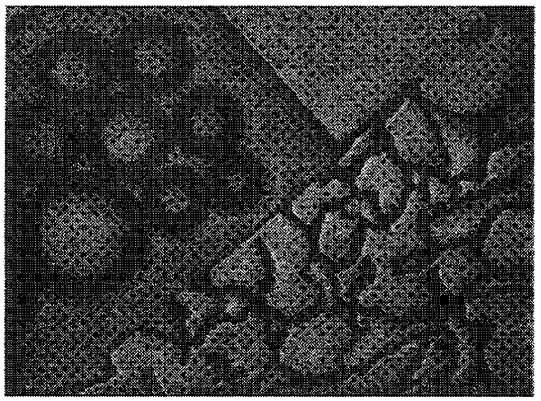

Figure 8: CO_2 bubbles have just emerged from the porous network into the outlet channel.

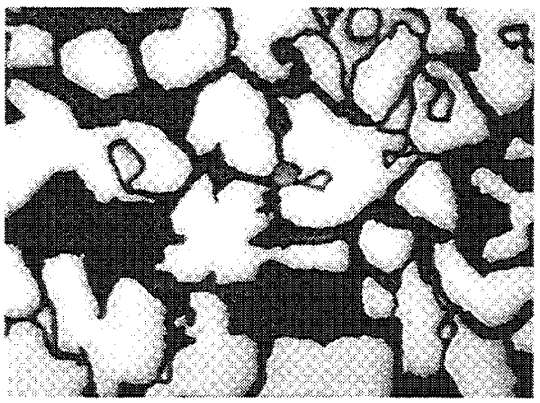

Figure 9: Crude oil emulsions seen in the large pores in the model after 0.01% surfactant flood.

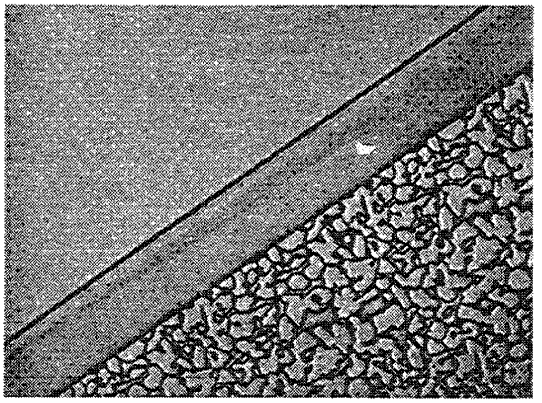

Figure 10: Water films in the outlet port during water flooding. The water contains dissolved CO_2 gas.

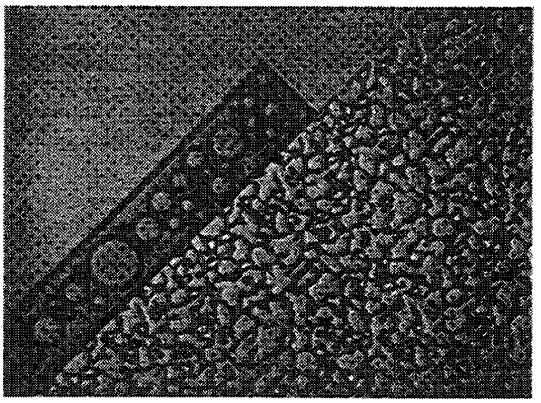

Figure 11: The CO_2 bubbles are generated near the corner. Flow is from top to bottom diagonally. The bubbles coalesce to form bigger bubbles almost instantly.

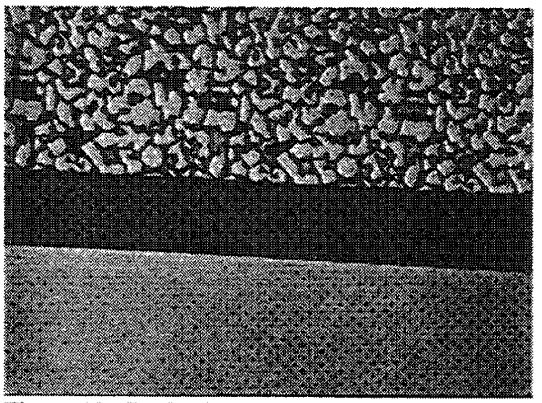

Figure 12: Crude oil invading the inlet channel. It can be seen that the oil does not fill the model uniformly.

EXPERIMENT 1

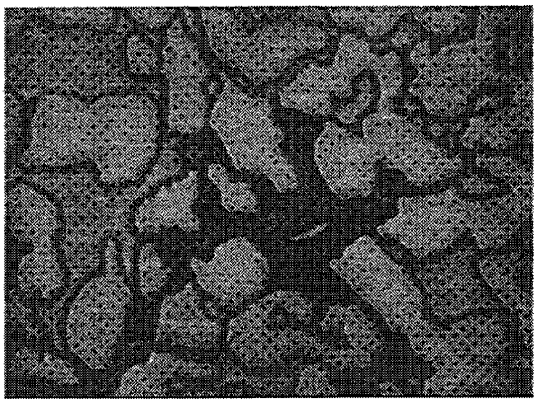

Figure 13(a)

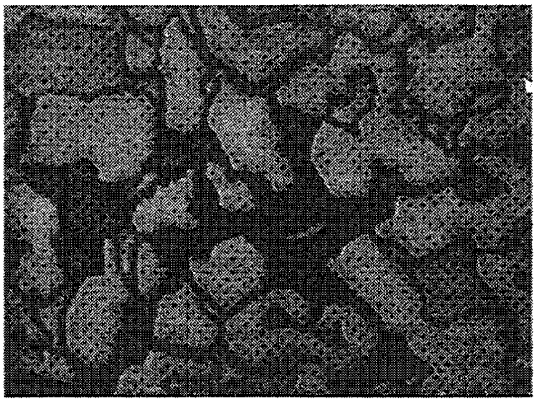

Figure 13 (d)

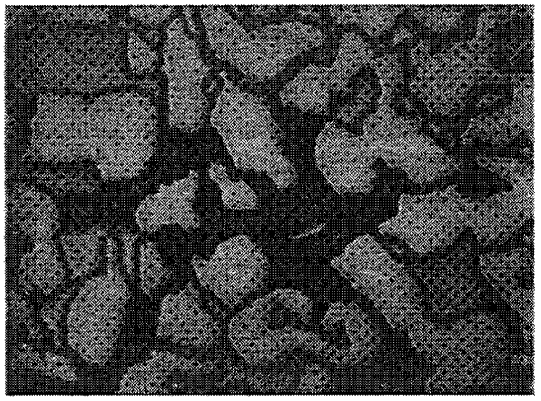

Figure 13(b)

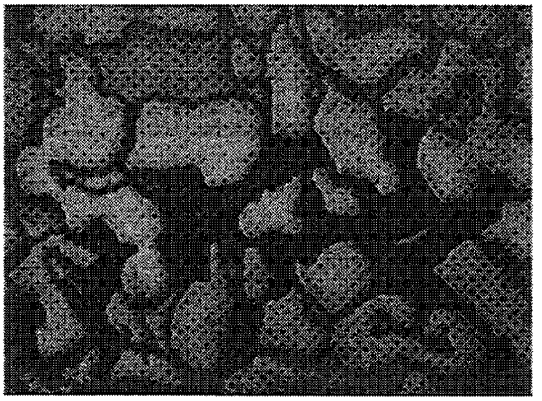

Figure 13 (e)

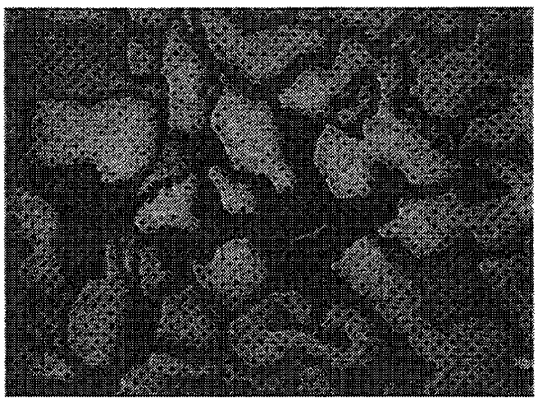

Figure 13 (c)

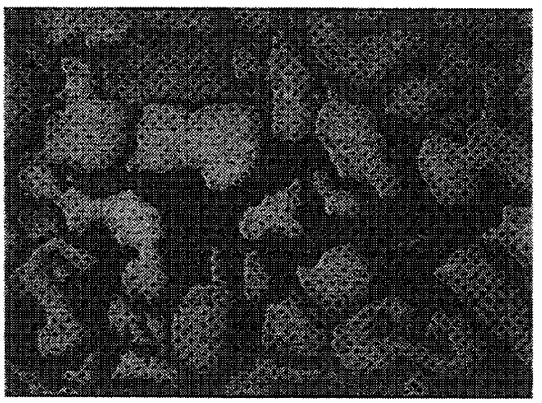

Figure 13(f)

Figure 13: Emulsion forming sequence observed with crude oil in the presence of AOS.

EXPERIMENT 2

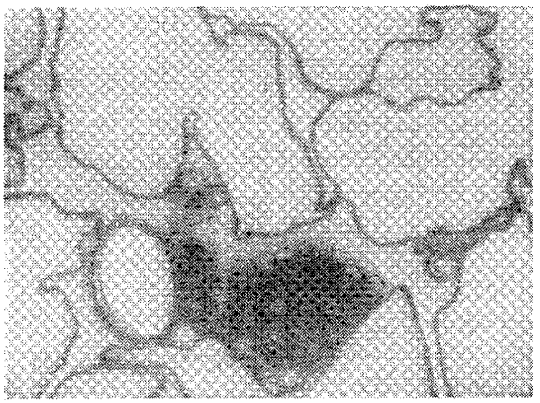

Figure 14: First emulsions seen with the higher magnification lens (40 X) at 0.001% surfactant flood.

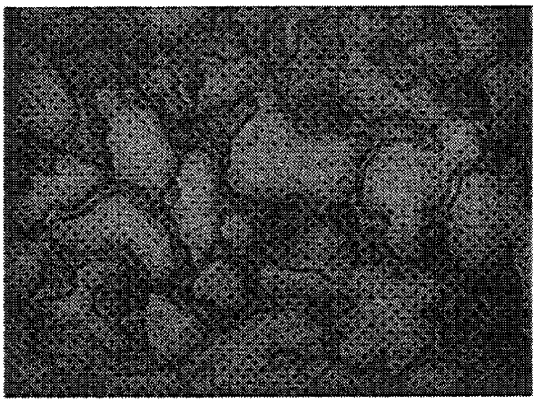

Figure 15: Emulsions seen after 0.01% surfactant flood.

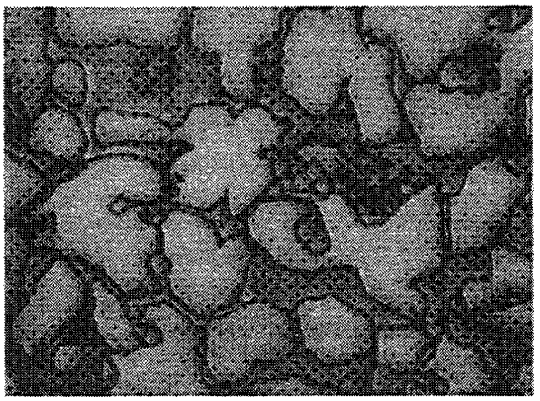

Figure 16: Emulsions seen after 0.1% surfactant flood.

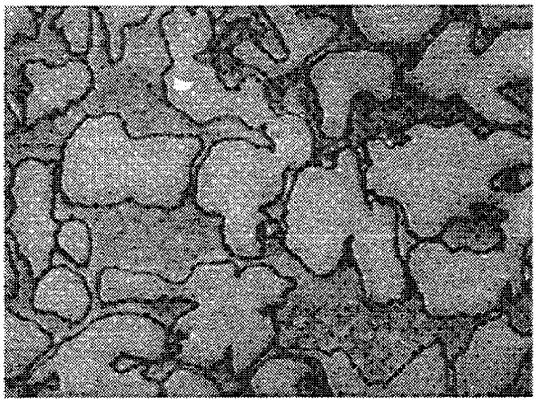

Figure 17: Emulsions seen after 1% surfactant flood. Three different kinds of emulsions are seen.

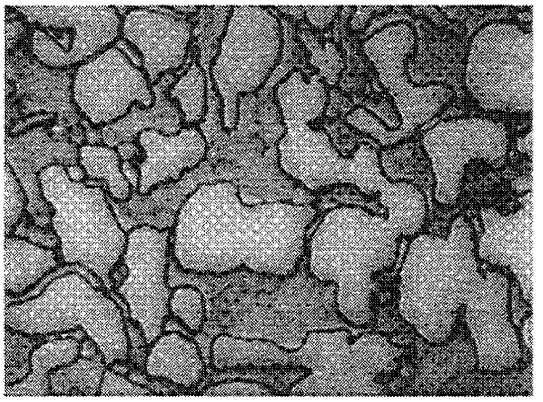

Figure 18: Emulsions as seen after 1% surfactant flood.

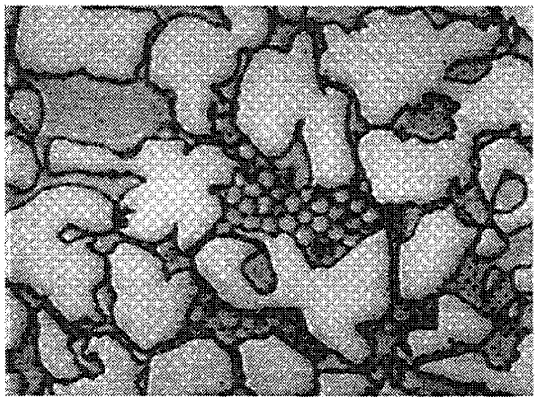

Figure 19: Very stable emulsions seen at the end of the experiment (after 1% surfactant flood).

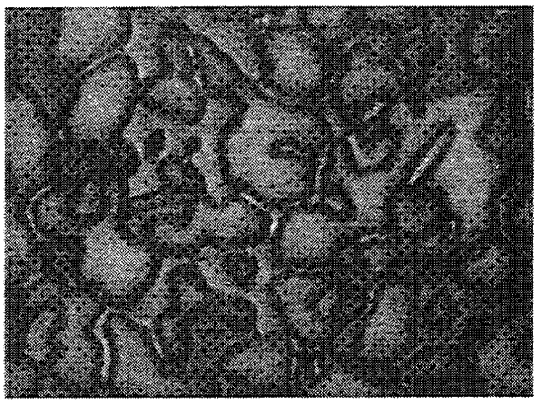

Figure 20: Water can be seen residing in the narrow throats.

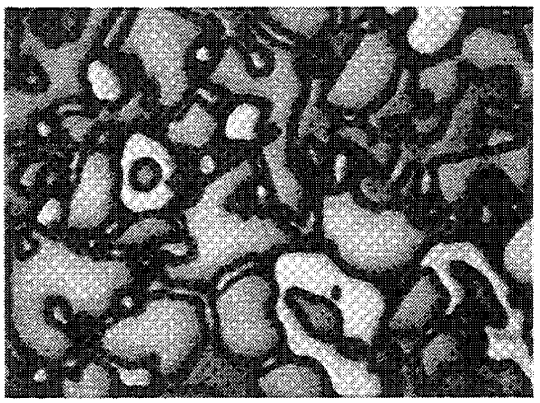

Figure 21: A lot of small CO_2 bubbles coated with surfactant film seen. The CO_2 phase is not continuous any more. Seen after 0.1% FC740 surfactant flood.

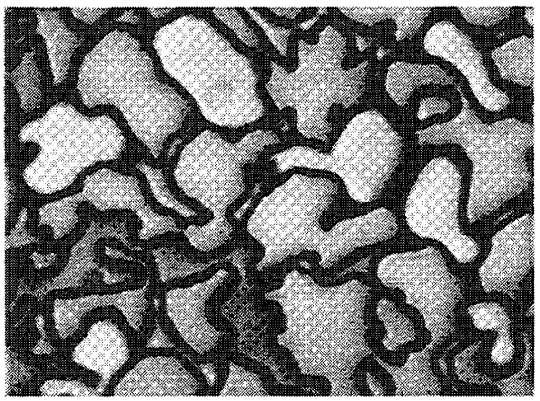

Figure 22:Stable foam lamellae seen after 0.1% FC740 surfactant flood.

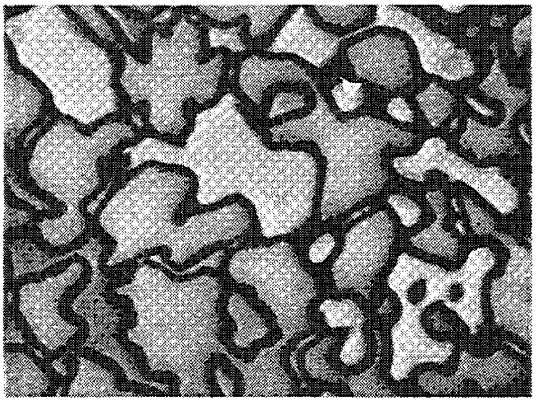

Figure 23: Stable lamellae seen after 0.1% FC740 surfactant flood.

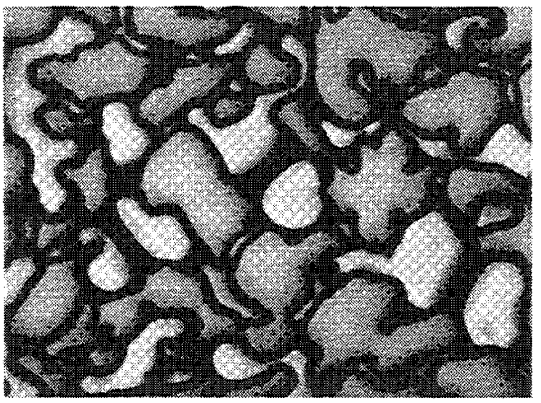

Figure 24: Stable lamellae after 1% FC740 surfactant flood

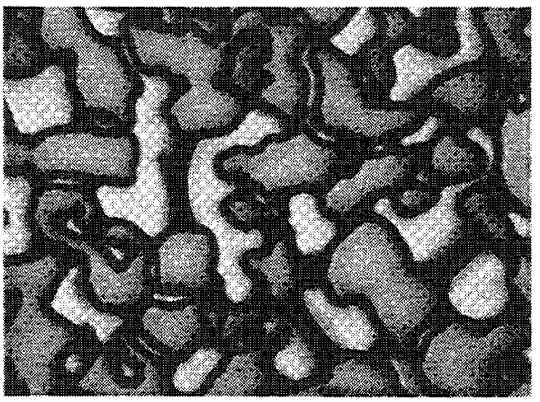

Figure 25: The biggest stable lamella seen during the experiment : after 1% FC740 surfactant flood.

1. Water was clearly seen residing in the narrow throats.

2. Stable foam lamellae were seen beginning at 0.01% surfactant concentration.

3. No significant increase in the number of foam lamellae were seen from 0.1% to 1.0% surfactant concentration, in spite of a noticeably higher gas blockage.

4. Certain pore geometry was more conducive to foam lamella formation than others, such as the big pores seen in Fig. 24.

5. Flow through the model was much faster.

Interfacial tension between the surfactant solution and the oil (kerosene) was measured for Experiments 2 and 3 and is listed below. No significant difference in the interfacial tension was observed because of the presence of the soluble dye.

Table 4. Interfacial Tension Measurement.

Surfactant	**Concentration**	**Interfacial Tension (dynes/cm)**
Nansa (AOS)	1%	1.4
	0.1%	0.71
	0.01%	1.63
	0.001%	7.9
FC740 (in Kerosene)	1%	14.928
	0.1%	8.868
	0.01%	19.686

3.3.6 CONCLUSIONS

Conclusions are categorized under three separate headings: The AOS surfactant, Oil-Foam and the micromodels.

3.3.6.1 For AOS Surfactant

From Experiments 1 and 2, no stable foam lamellae were observed with the AOS surfactant in the presence of oil indicating its non-tolerant behavior. Also, it could be concluded that the emulsion formation in the micromodel could be the reason for observations of delayed foam forming in the literature.

3.3.6.2 For Oil-Foam

Strong foam was generated by the Fluoro- surfactant both in oil saturated and oil free zones. Also, generation sites for the foam lamellae were definitely seen to be controlled by pore geometry and by local saturation. However no obvious link could be found with the number of films observed and the strength of gas blockage.

3.3.6.3 For the Micromodels

The SEM study shows that in the new micromodels (Model B), extreme conditions used in anionic bonding of the pyrex glass on to the silicon wafer: 450° C and 1500 volts, led to melting of the glass on to the silicon, leading to blockage of the flow paths in the pore network (Figs. 3, 5 and 6). This explains the extremely low permeability of the pore-models in Experiments 2 and 3.

3.3.7. CONTINUING RESEARCH

The following areas are being worked on:

1. New Micromodel fabrication to include thin sections of sandstone other than Berea. Also, a procedure to make the etched silicon wafer transparent, so that better flow visualization can be achieved is being considered.

2. Further work on the behavior of emulsions and how they effect foam properties in porous media is being studied. Specific work on foam destabilization by emulsified droplets is also being looked into.

3.3.8 SELECTED BIBLIOGRAPHY

1. Bikerman, J.J. *Foams*; Springer-Verlag, New York, 1973.

2. Hanssen, J.E. and Dalland, M.: "Foam Barriers for Thin Oil Rims : Gas Blockage at Reservoir Conditions, paper presented at the Sixth European Symposium on Improved Oil Recovery, Stavanger (May 21-23, 1991).

3. Hanssen, J.E. and Dalland, M.: "Foams for Effective Gas Blockage in the Presence of Crude Oil., SPE 20193, SPE/DOE Enhanced Oil Recovery Symposium, Tulsa (April 1990).

4. Hornbrook, J.W., Pettit, P. and Castanier, L.M.: "Foam/Oil in a New, High Resolution, Sandstone Replica Micromodel," SUPRI TR-86 (August 1992) [DOE/BC/14600-32].

5. Marsden, S.S.: "Foams in Porous Media," SUPRI TR-49 (May 1986).

6. Meling, T. and Hanssen, J.E.: "Gas Blocking Foams in Porous Media: Effects of Oil and Surfactant Hydrophobe Carbon Number, *Prog.Colloid Sci.* 82 (1990) 140-154.

7. Owete, O.S., Castanier, L.M., and Brigham, W.E.: "A Micromodel Study of Foam Flow Through Porous Media, " SUPRI TR-37 (July 1984) [DOE/SF/11564-6].

8. Schramm, L.L.: Foams: Fundamentals and Applications in the Petroleum Industry, American Chemical Society, Washington, D.C. (1994).

9. Woody, F., Blunt, M., and Castanier, L.M.: "Pore Level Visualization of Foam Flow in a Silicon Micromodel," SUPRI TR-100 (January 1996) [DOE/BC/14899-32].

3.4 EFFECT OF SURFACTANT CONCENTRATION ON FOAM FLOW IN POROUS MEDIA

(O. Apaydin)

3.4.1 INTRODUCTION

The decreasing trend of discovery of new oil reservoirs increases the importance of and potential for enhanced oil recovery (EOR) processes. Gas drives are a common means of improving oil recovery. Fluids that are used in gas drives such as carbon dioxide, steam, enriched hydrocarbons and nitrogen have high mobility compared to water and oil because they are less viscous and are less dense compared to the fluid originally in the reservoir. These two characteristics lead the gas drive fluids to channel through high permeability zones, and to rise to the top of the reservoir by gravity segregation and override the oil. As a result sweep efficiency decreases and the amount of oil left behind increases (Liu and Brigham, 1992; Kovscek and Radke, 1994).

Foam is suggested by many investigators to overcome the mobility problem of gas drive fluids. Foam is formed by a combination of surfactant solution and gas (for example, steam, nitrogen or carbon dioxide) either by consecutive injection or by co-injection of gas and surfactant solution into the reservoir. With this process, the gas phase is generally discontinuous and the liquid phase is continuous.

Bond and Holbrook (1958) introduced foam in porous media to the literature and suggested that if foam is generated by consecutive injection of surfactant solution and gas into reservoirs, it improves the sweep efficiency; and in Fried (1961) showed that foam reduces the gas-oil mobility ratio and acts as a gas blocking agent. Since then, the rheology and flow mechanism of foam as well as modes of foam generation and destruction have been investigated by many researchers.

Foam changes gas mobility in two ways. The first, has to do with moving bubbles. Confined foam bubbles transport as bubble trains in gas occupied channels. Hirasaki and Lawson (1985) worked on bubble and lamellae trains flowing in aqueous surfactant solutions. They used cylindrical capillary tubes for their experiments and showed that during flow the front bubble interface expands in the direction of the capillary wall while the rear interface contracts in the direction of capillary centerline. Surfactant depletes at the front and accumulates at the rear of a moving bubble. This process increases the surface tension gradient and slows the bubble motion and so increases the effective viscosity. Of course this process requires multiple lamellae, that is keeping the gas bubbles disconnected, to be stable. This stability is ensured by disjoining pressure between two foam bubbles. Aronson, Bergeron, Fagan and Radke (1994) showed that disjoining pressure is directly dependent on the concentration of surfactants and salt that are used for foam flow in porous media (Khatib, Hirasaki and Falls, 1988).

As a second mechanism, foam decreases the mobility of gas by a trapping process. Gas, as a non-wetting fluid, tends to flow through the high permeability and high porosity zones. The wetting phase occupies the smallest pore channels, and foam as a flowing phase occupies the largest pore channels. Trapping occurs in the intermediate-sized pores (Kovscek and Radke, 1994). The surfactant that is in the environment causes the lamella formation as a thin surfactant film between the bubbles. This leads to a disjoining pressure between two gas bubbles which keep them apart. This pressure prevents the connection of two bubbles in two neighboring pores and causes the gas to be trapped in these relatively

bigger pore spaces. Friedmann *et al.* (1991). showed that at constant fractional flow, the fraction of trapped gas changed slightly as a function of gas velocity. Gillis and Radke (1990) using sulfur hexafluoride and methane simultaneously as tracers, reported that there was no consistent trend of trapped fraction with liquid or gas velocity. When they injected gas into the Berea sandstone core, they observed that 85-99 % of the gas the remained trapped.

During the flow of gas in the reservoir, where the wetting phase is aqueous surfactant solution, foam generation and coalescence occurs continuously. Snap-off is the most significant mechanism of foam formation. It is a mechanical process that occurs continuously for multiphase flow in the reservoir, regardless of surfactant presence. As gas flows through the reservoir pores, when it reaches a throat that is initially filled with wetting fluid, capillary pressure and curvature increases to the entry value. When the front of the interface proceeds and enters the pore space, wetting fluid remains in the corners and local capillary pressure at the gas front decreases with the expansion. This leads to a pressure gradient in the wetting fluid between the pore throat and body. Liquid flows to the throat and separates the gas to form a gas bubble. If the wetting fluid is surfactant then a lamella forms (Kovscek and Radke, 1994).

Foam coalescence occurs by a stretching and squeezing process. While foam is flowing though pores and throats it expands and compresses simultaneously. Surfactant thin films (lamellae) separating the bubbles also stretch and squeeze by the movement of foam. When these thin films break, foam coalescence occurs. The strength of these lamellae depends on the capillary pressure and disjoining pressure, which are directly related to concentrations of surfactant and salt.

Changes in surfactant concentration have a significant effect on foam longevity in porous media. Chiang *et al.* (1980) showed that foam generation generally increases with increasing surfactant concentration until the critical micelle concentration (CMC) is reached, and changing surfactant concentration has little effect above the CMC. Likewise, Marsden and Khan (1966) found that the apparent viscosity increases with increasing surfactant concentration.

Beyond these observation, it is important to determine the optimum concentration of surfactant that should be used to form foam for field applications, because it has direct effect on the economics of a project. Also, foam displacement processes within reservoirs are inherently transient. Although a fixed surfactant concentration is usually injected, transient characteristics dominate foam flow during a significant portion of the project life. We require an understanding of how the reservoir responds with changing surfactant concentration.

In this work, the transient behavior of foam is observed with respect to changing surfactant concentrations. We will also explore transient flow in heterogeneous rocks and sands.

3.4.2 EQUIPMENT AND PROCEDURES

A sand pack was prepared to run the experiments (Fig. 1). A 64 cm long acrylic tube with 2.54 cm. inner diameter was packed with dry sand in an upright position. The sand used in the sand pack was 100-120 mesh Ottawa sand. Stainless steel screens were used on each end of the sand pack to prevent sand migration. To ensure good settling, pneumatic vibrators were used while packing the tube. During water and surfactant injection a Du Pont

Instruments Chromatographic pump was used. A Matheson mass flow meter (Model 8240) was used to inject the gas at a constant rate.

To measure absolute pressures along the sand pack, 8 pressure taps were used. Figure 1 details their location. Four differential pressure transducers calibrated to 25 psi (Validyne Model DP15), were used between taps 1,3,5,7 and the sand pack outlet. From the known outlet pressure, and pressure drops between taps, absolute pressures can be calculated. The differential pressure transducers were connected to transducer modulators (Fig. 1). Electrical signals obtained from transducer modulators were then transferred to an HP data acquisition/control unit (Model 3497A) that was connected to a PC. Transducers were also calibrated, and the transducer demodulators were adjusted before each experiment by using a voltmeter.

To saturate the sand pack with water, CO_2 was injected from the top of the sand pack to flush the medium. After CO_2 injection, distilled water was introduced from the bottom and the medium was saturated with water. The use of CO_2 allows the water to build to 100 % saturation, since any residual CO_2 is dissolved by the flushing water.

An X-ray CT (Computerized Topography, Picker International Synerview 1200SX) scanner was used to determine the value and homogeneity of porosity along the sand pack and saturation profiles during fluid flow in the porous media.

The sand pack was scanned by using the CT scanner. It was observed that the porosity profile is almost homogeneous and porosity was determined to be 32.3% (Fig. 2). The permeability of the sand pack was determined from the pressure drop data that were obtained for different injection rates (0.15, 0.3, 0.45 sccm.) of distilled water into the core. The permeability of the core was found to be 6.5 Darcys.

The endpoint permeability to nitrogen at gas-flood residual water was determined by injecting nitrogen gas at a flow rate of 0.8 sccm into the core, which was first saturated with distilled water. To measure more accurately pressure drop data, an additional 1 psi differential pressure transducer was added to the system between Taps 3 and 7. Stabilized pressure drop data after breakthrough were used to calculate the endpoint permeability value, and it was found to be 1.043 Darcy. During these experiments the sand pack was in the vertical position. Residual water saturation was calculated to be 40 %.

The surfactant used for the experiments was Shell AOS C1416. Table salt (NaCl) was used to form the surfactant solutions, because it does not contain trace amounts of organic solvents. For the foam experiments, surfactant solutions were prepared with different concentrations: 0.001, 0.01, 0.1 and 1 wt %. Solutions were all 0.5 wt % salt.

Before each experiment, the medium, which was in a vertical position, was flushed with CO_2 from the top until it became dry. Then the fluid that was going to be used for that experiment was injected from the bottom. The gas, which accumulated within the connection tubes between the sand pack and transducers during CO_2 flushing, was purged.

3.4.3 FOAM EXPERIMENTS

The sand pack was saturated completely with the desired solution before each experiment. The same sand pack has been used for repeated experiments. To cover the possible effect of not completely removing surfactant from the core, the experiments were started with the 0.001 % surfactant solution and larger concentrations followed subsequently.

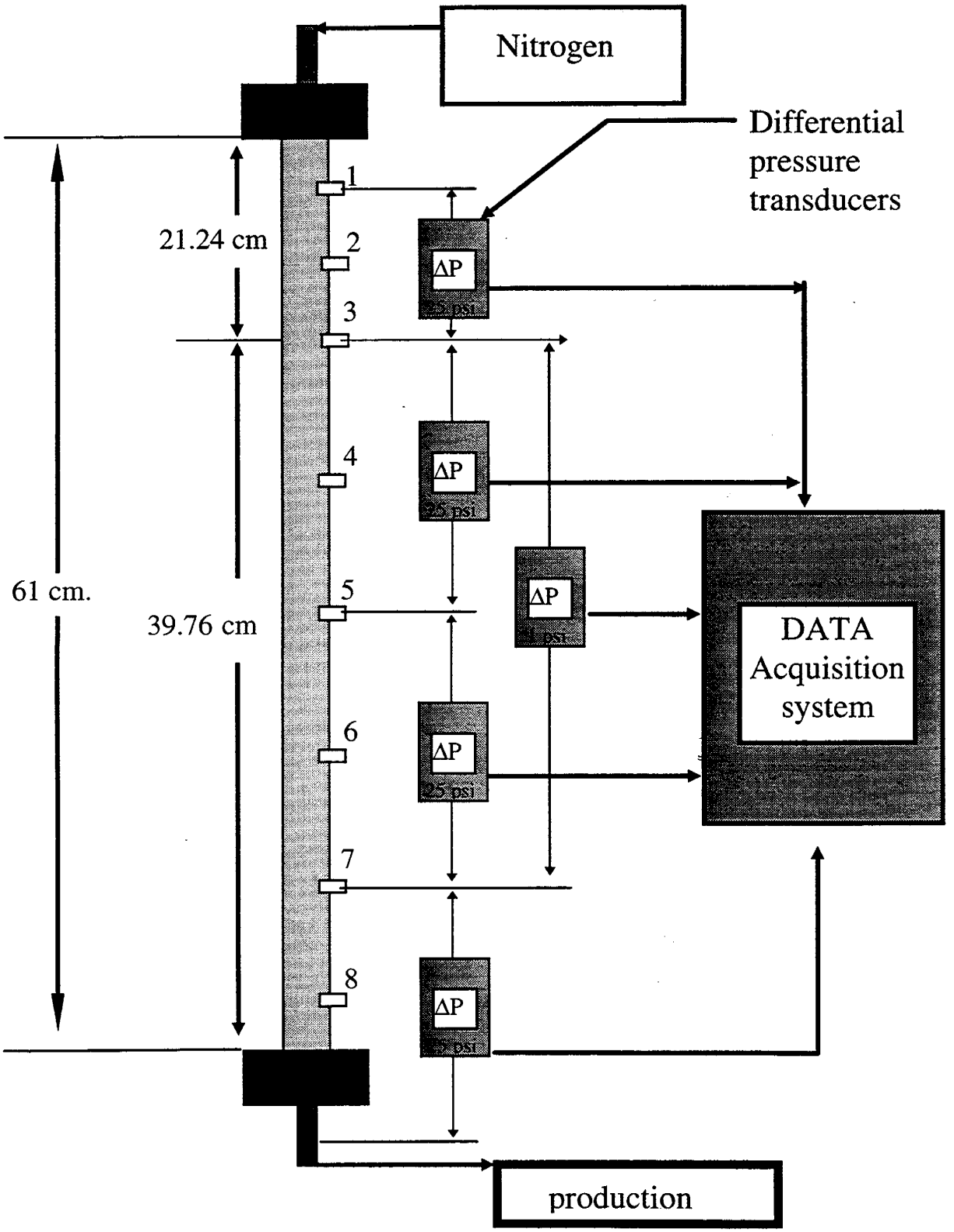

Figure 1. Experimental System Diagram

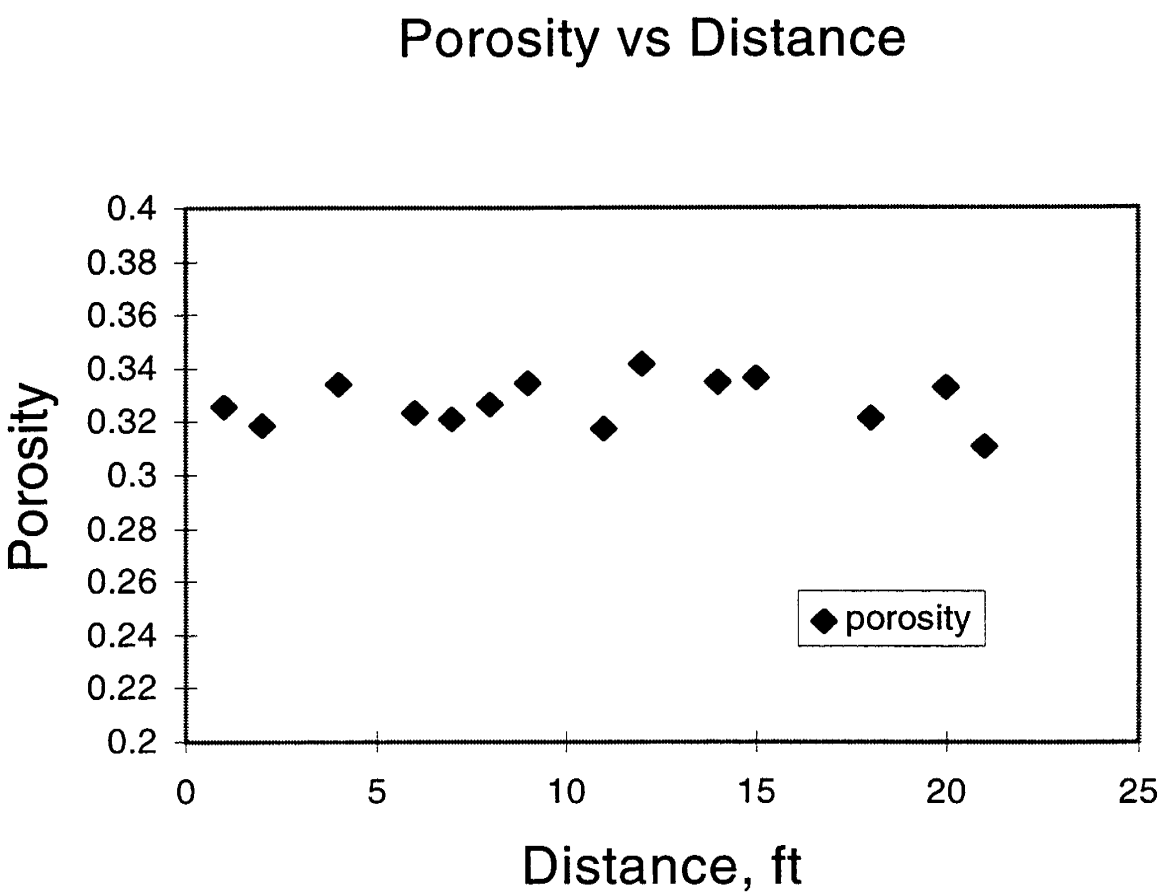

Figure 2. Porosity profile along the sand pack.

Concentrations of 0.001 wt % and 0.01 wt % surfactant solutions were used to run the experiments while the core was positioned vertically. Pressure drop and recovery data were obtained for both solutions. Gas injection rate was set to be 0.8 sccm. It was observed that 0.001 wt % surfactant concentration has negligible effect on water recovery. Here, gravity drainage dominates. Over 60 % of the water was recovered, which is the same as with gas injection. But with 0.01 wt % surfactant concentration, recovery increased to 93 % (Table 1). The time to gas breakthrough time was also increased, as was expected, with the higher surfactant concentration. Breakthrough times were dependent on the injection flow rate of gas. Because back pressure was not applied during the experiments, the injection flow rates decreased as the injection pressure increased. Hence exact breakthrough pore volumes could not be determined accurately. These flow rates are marked with an asterisk in Table 1.

The pressure drop data that were obtained for both surfactant solutions were not as reliable as expected. Due to foam generation in the core, an increase in the pressure drop was expected compared to the gas injection experiment. As it is seen in Fig. 3 for 0.01 wt % surfactant solution, pressure drop values are changing between 0 and 0.2 psi which is the same as gas injection experiments. Although recovery was increased by more than 30 % compared to gas injection, pressure drop values remained the same. In the figure it's also seen that after 15000 sec., which is breakthrough time, the transducers 3 and 4 give negative pressure drop values. These results are not logical and might be due to the transducers' inability to transfer the data well.

The second set of experiments were run with 0.01 wt % and 0.1 wt % surfactant solutions by fixing the sand pack in a horizontal position. Pressure-drop data were not recorded. A back pressure of 25 psi was put at the outlet of the mass flow controller to reduce the flow rate variation problem during injection. Recovery was measured by collecting liquid as a function of time at a fixed gas injection flow rate. When a back pressure of 25 psi was set at the sand pack outlet, leakage was observed through the pressure taps. The back pressure was then released. For 0.01 % surfactant solution a gas rate of 1.35 sccm. was used, and for 0.1 % surfactant solution, the gas injection rate was 0.85 sccm. As can be seen from Figs. 4 and 5, recovery has increased from 80 % to 90 % with increasing surfactant concentration. Also in Table 1, a summary of the recovery of all experiments can be seen.

At the moment, saturation profiles, with foam in the core, are being determined by using the CT scanner. The sand pack is set in the CT gantry on a moving table, different surfactant solutions are injected, this is followed by gas injection, and the changing saturation is measured.

3.4.4 FUTURE PLANS

The first objective is to solve problems in obtaining pressure drop data and get valuable results. Transducers will be cleaned, and re-calibrated, and tested under flow conditions. After that, heterogeneous porous media will be made from sandstone and sand. Experiments will illustrate the effect of permeability on foam flow. Both non communicating and communicating layered systems will be prepared and the same kind of experiments will be performed for these cores. Figures 6a and 6b show proposed geometries for these experiments. These appear to be the simplest to construct heterogeneous media.

Table 1. Total recoveries for foam experiments

Run No.	Surfactant concentration, wt %	Injection Flow rate, sccm	Total Recovery, %	Position
1*	0.001	0.8	60	Vertical
2*	0.01	0.8	93	Vertical
3	0.01	1.35	82	Horizontal
4	0.1	0.85	97	Horizontal

* Flow rates are not exact

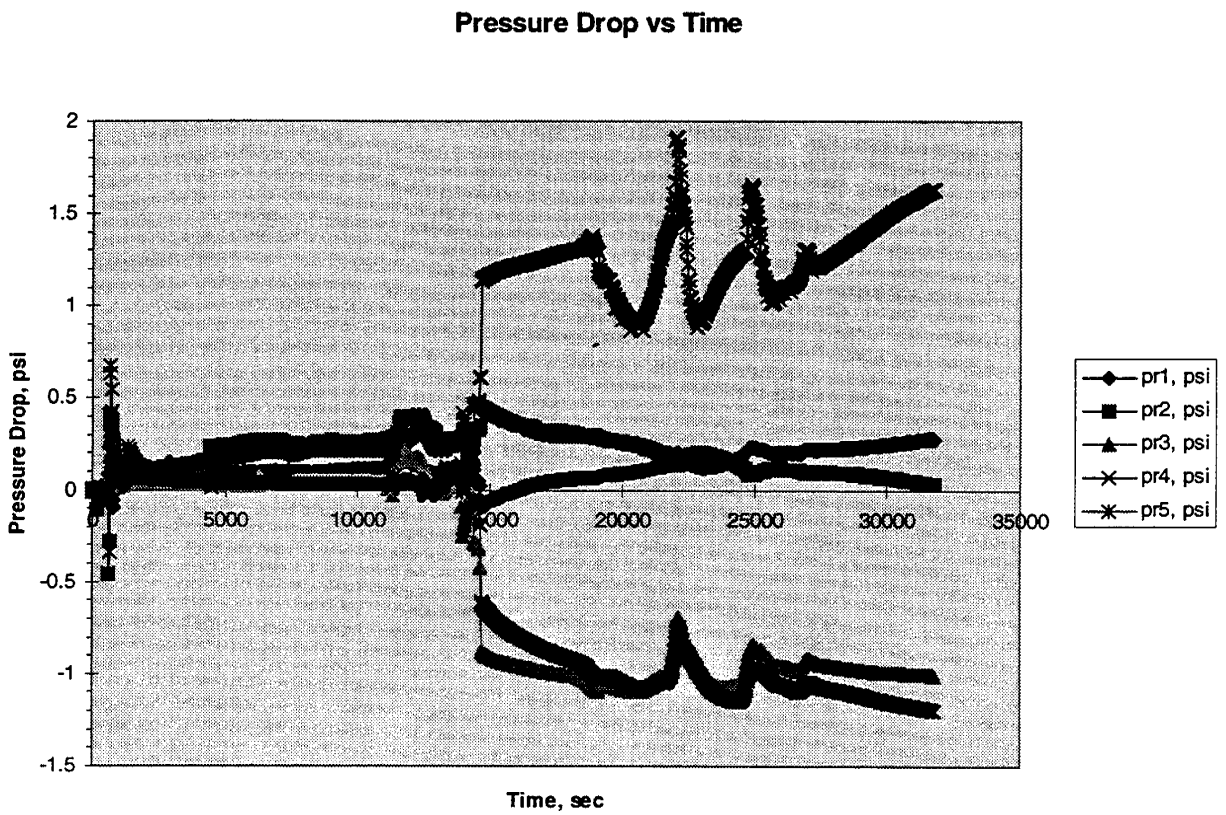

Figure 3. Pressure drop histories for 0.01 wt % surfactant solution. Gas injection rate is 0.8 sccm.*

* Not exact.

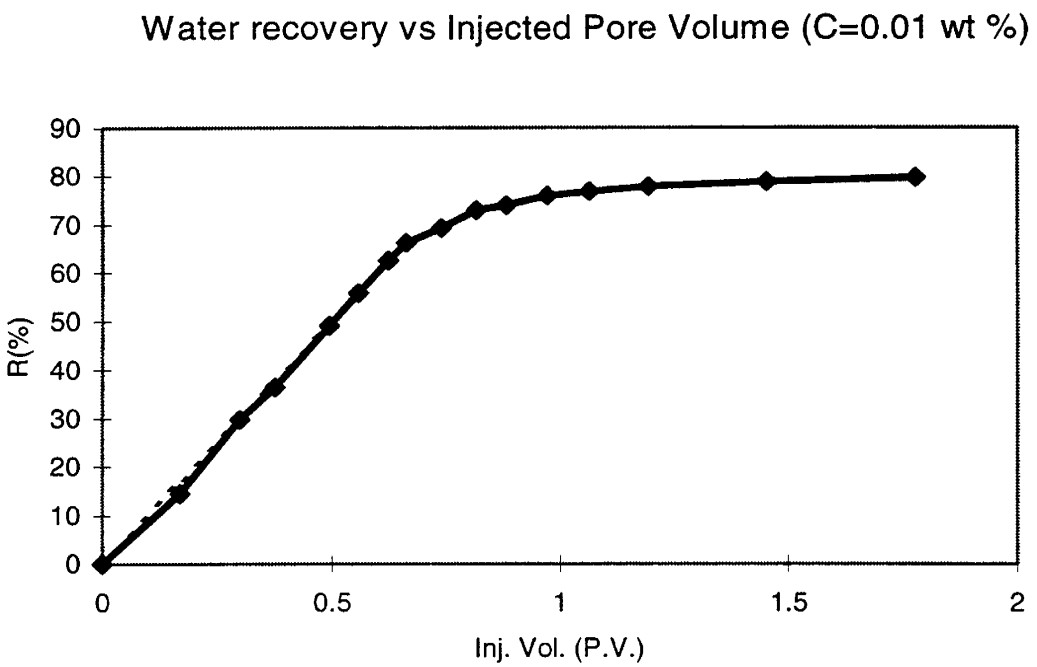

Figure 4. Water recovery for 0.01 wt % surfactant solution.*

* Position: Horizontal

Gas injection flow rate: 1.35 sccm.

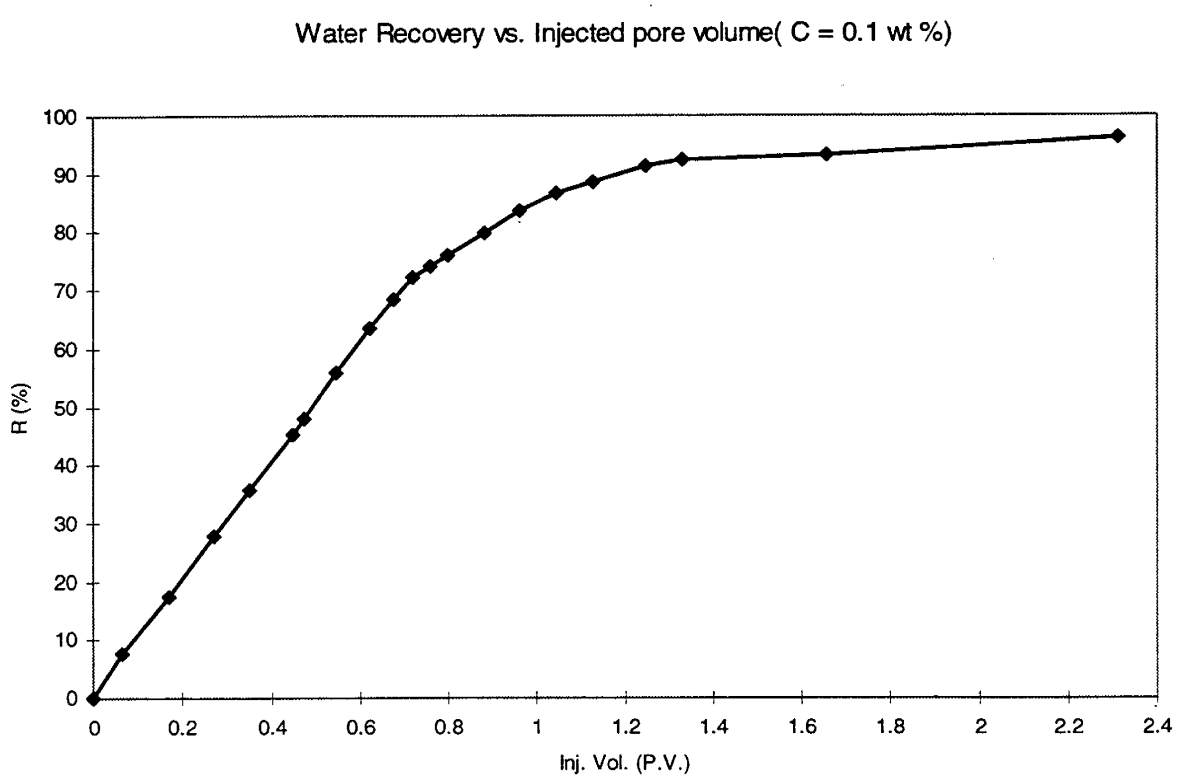

Figure 5. Water recovery for 0.1 wt % surfactant solution.*

* Position: Horizontal

Gas injection flow rate: 0.85 sccm.

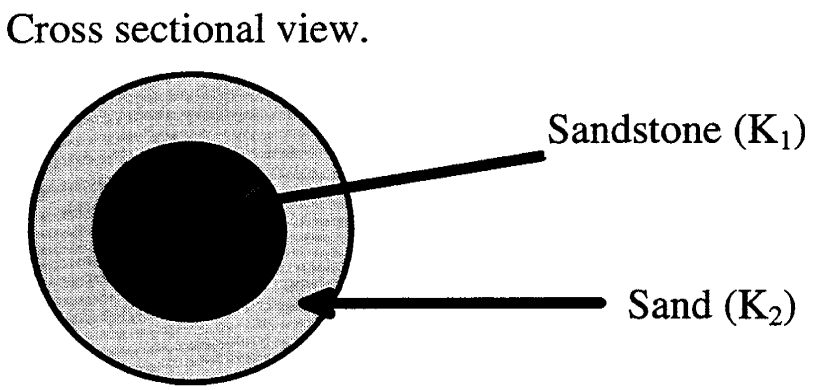

Figure 6a. Cross sectional view of communicating heterogeneous system.

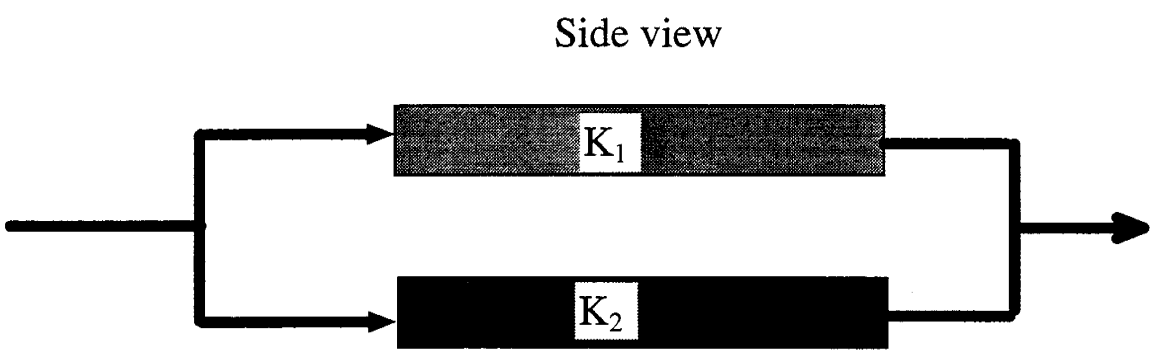

Figure 6b. Side view of non communicating heterogeneous system.

3.4.5 SUMMARY

In this work a sand pack was prepared and properties of this core such as porosity, permeability were determined. With a sand pack, a variety of porous media can be prepared rapidly for experiments. The sand pack was saturated with different surfactant concentrations and nitrogen was injected into the core for displacement experiments. It was observed that with increasing surfactant concentration water recovery increased. Foam was generated in the system with surfactant concentration above 0.01 wt %. There have been problems in obtaining pressure drop data with current pressure transducers. Since back pressure was not used due to leakage problem, difficulties have occurred while fixing the flow rate.

3.4.6 REFERENCES

1. Aronson, A. S., Bergeron, V., Fagan, M.E. and Radke, C.J.: "The Influence of Disjoining Pressure on Foam Stability and Flow in Porous Media," Colloids and Surfaces A. 83 (1994) 109-120.

2. Bond, D.C. and Holbrook, O.C.: "Gas Drive Oil recovery Process," U.S. Patent No. 2,866,507 (1958).

3. Chiang, J. C., Sanyal, S.K., Castanier, L.M., Brigham, W.E., and Sufi, A.: "foam as a Mobility Control Agent in steam Injection Processes," paper SPE 8912 presented at the 50th Annual California Regional Meeting, Los Angeles (April, 9-11, 1980).

4. Fried, A.N.: "The Foam Drive Processes for Increasing the Recovery of Oil," No. Report of Investigations 5866, USBM (1961).

5. Friedmann, F., Chen, W.H. and Gauglitz, P. A.: "Experimental and Simulation Study of High-Temperature Foam Displacement in Porous Media," Soc. Pet. Eng. Res. Eng. 6(1) (1991) 37-45.

6. Hirasaki, G. J. And Lawson, J. B.: "Mechanisms of Foam Flow in Porous Media: Apparent viscosity in Smooth Capillaries," Soc. Pet. Eng. J. (April 1985) 176-190.

7. Khatib, Z. I., Hirasaki, G. J. And Falls, A. H.: "Effects of Capillary Pressure on Coalescence and Phase Mobilities in Foams Flowing Through Porous Media," Soc. Pet. Eng. J. (August 1988) 919-926.

8. Kovscek, A. R. And Radke, C. J.: "Fundamentals of Foam Transport in Porous Media," in *Foams: Fundamentals and Applications in the Petroleum Industry* edited by American Chemical Society (1994) Chapter 3.

9. Liu, D. and Brigham W.E.: "Transient Foam Flow in Porous Media with CAT Scanner," No U.S. DOE Report No. DE-92001022, Stanford University Petroleum Research Inst., Stanford, CA (March 1992).

10. Marsden, S.S. and Khan, S.A.: "The Flow of Foam Through Porous Media and Apparent Viscosity measurments," Soc. Pet. Eng. J. (March 1966) 17-25.

11. Radke, C. J. And Gillis J. V.: "A Dual Gas Tracer Technique for Determining Trapped Gas Saturation During Steady Foam Flow in Porous Media," paper SPE 20519 presented at the 65th SPE Annual Technical Conference, New Orleans, LA (Sept. 1990).

3.5 SIMPLIFIED FOAM FLOW SIMULATION

(H. Bertin*)

3.5.1 ABSTRACT

Gas injection in reservoir can be used to increase oil recovery. However, the viscosity and density differences between the injected and displaced fluids can lead to a low sweep efficiency. To overcome mobility control problems, gas can be injected in the form of foam to increase its apparent viscosity and improve the reservoir sweeping. Foams are also used in several petroleum engineering applications such as matrix acidization, gas blocking agent for profile control or drilling operations.

For all of these applications numerical simulation of foam flow in porous media is a problem of central importance that is not simple to handle due to the complex rheological behavior of the foam itself. Several models are described in the literature from a simple modification of the gas mobility to a complete population balance model, taking into account the generation and destruction of lamellae.

In this paper we present a simple correlation, based on experimental observations performed at different scales, expressing the evolution of foam texture during transient foam flow in homogeneous porous media.

The results are compared with experiments performed in different conditions, agreement is satisfactory.

3.5.2 INTRODUCTION

Gas drive fluids are used during Enhanced Oil Recovery Processes (injection of hydrocarbons gas, nitrogen, carbon dioxide, steam ...). The low viscosity of the injected gas and high density contrast with the displaced fluid is, in many practical situations, the cause of low sweep efficiency due to unstable displacement (viscous fingering) and gravity override. Natural heterogeneity of the reservoir may emphasize these effects. To avoid those gas can be injected in the form of foam in order to increase its apparent viscosity and therefore, achieve a better mobility control during a displacement process.

Foams are used also in several petroleum engineering applications such as matrix acidization (Zhou and Rossen, 1992; Zerhboub *et al.*, 1994), gas blocking for profile control (Hanssen and Haugun, 1991) or drilling operations.

Foams are gas bubbles separated by thin liquid films called lamellae, i. e, the liquid phase is continuous while the gas phase is not. Foams in porous media are distinct of common bulk foams in the sense that when gas enters in the porous structure, the formed bubbles have almost the same characteristic length than the pore throats.

*Permanent address: LEPT-ENSAM, U. of Bordeaux I, Espl. Arts et M`etiers, 33405 TALENCE CEDEX, FRANCE

There is a wide literature on foams in petroleum engineering (see for example the volume edited by L. Schramm, 1994). Many authors tried to understand and describe foam from the point of views of generation, stability, rheology and propagation. Experimental studies performed with capillary tubes (Hirasaki and Lawson, 1985) showed the pseudoplastic behavior of foam. Microscopic phenomena could be observed using micromodels. Owete and Brigham (1987) using silicon plates, observed the displacement of aqueous surfactant solutions by air as a network of interconnecting films. They showed evidence that liquid and air were trapped in some pores. Chambers and Radke (1991) showed clearly that foam in porous media is not continuous.

Foam displacement in porous media has been extensively studied. Several authors focused their attention on the steady-state determination of relative permeability curves. The main conclusion is that relative permeability to water is almost independent of the presence of surfactant, however, relative permeability to gas is significantly decreased in presence of surfactant. This effect is attributed to the wetting nature of water and to the large trapped gas saturation. This trapped gas saturation has been measured using gas-phase tracer techniques (Gillis and Radke, 1990, Friedmann *et al.*, 1991). The authors have shown that it could be a very high value (more than 80%). The effect of flow rate on foam in porous medium has been described by Friedmann and Jensen (1986). The authors report experimental results showing the pronounced effect on foam texture, i.e., faster flow rates can produce smaller bubbles than slower flow rates do.

During IOR processes, the flow is obviously time dependent and, from our point of view, it is necessary to determine the unsteady-state relative permeability curves. Kovscek and Radke (1993) reported experimental results that could be described satisfactorily by a mechanistic model including a population balance equation.

Our study deals with the simulation of transient foam flow in porous media using a simple expression of foam texture based on experimental observations performed at different scales.

3.5.3 FOAM TEXTURE

The description of foam nature and the way it flows in porous media require the definition of several observation scales:

* The pore scale corresponds to a scale where it is possible to observe the porous medium geometry and the individual lamellae that compose foam.

* The darcy's scale (local scale), where the porous medium is assumed to be homogeneous.

* The large scale that include some heterogeneities, *e.g.*, the well vicinity.

* The megascopic scale (the reservoir).

We will focus our attention on the two first scales.

3.5.3.1 Pore Scale

The experiments described in the literature deals with direct observations using micromodels and rheological studies using capillary tubes.

Dealing with foam nature in porous media, it is clearly established that bubble formation is the result of gas injection in a liquid solution containing enough surfactant molecules to stabilize the thin films separating the gas bubbles, called lamellae. Experiments performed on micromodels, that are representative of a real porous medium, show that the characteristic length of bubbles is of the same order of magnitude than the pore size. It means that, where gas is present, we have almost one bubble per pore.

The main bubble generation mechanism, snap-off, depends on the gas velocity to the power 1/3.

When foam flows in the porous medium, only a small amount of the gas (a few %) participates to the flow.

The rheology of the foam in capillary tubes has been studied by Hirasaki and Lawson (1985). In addition to the non Newtonian behavior of the foam, they clearly show that foam viscosity depends on a parameter, called texture, that can be simply represented by the flowing bubble density, and on the gas velocity to the power -1/3. From this study we can express the foam viscosity as follows,

$$\mu_f = \mu_g + \frac{\alpha n_f}{V_g^{1/3}} \tag{1}$$

where μ_f et μ_g are foam and gas viscosities, n_f is the flowing bubble (or lamellae), V_g is the interstitial gas velocity α, a viscosity parameter function of the surfactant and its concentration.

3.5.3.2 Local Scale

There are several studies reported in the literature dealing with foam flow in porous media consolidated or not, reporting results on the influence of several physical parameters (permeability, flow rate, surfactant nature, concentration, pressure, temperature, oil presence, ...). Experiments dealing with relative permeability measurements were performed both on steady or unsteady state.

The main results obtained for transient gas-liquid displacement can be summarized in the following way :

- Strong non Newtonian behavior
- Piston like displacement before the breakthrough,
- Large trapped gas saturation during the flow.

The trapped gas saturation has been measured experimentally by Friedmann *et al.* (1988) and Gillis and Radke (1990), they both found low values of the flowing gas saturation (between 5 and 25 %).

3.5.4 MODELING

As reported in the literature, foam experiments performed at different scales of observation, pore-scale with micro-models, core-scale with homogeneous porous media, demonstrate clearly that foam texture is an important parameter that will govern foam mobility. Therefore, in order to model foam displacement in porous media it is necessary to take into account an external parameter into the generalized Darcy's laws, namely foam texture. Foam texture will be characterized by the number of gas bubbles or lamellae, taking into account that all bubbles generated in the porous medium are not mobile. This can be achieved by using a population balance for the lamellae that incorporates the mechanisms that generate or destroy the lamellae moving into the porous medium. Those mechanisms are, in the absence of oil, capillary snap-off, leave-behind and lamellae division for foam generation, and gas-diffusion and film breaking (bubble coalescence) for foam destruction.

$$\langle \text{Accumulation} \rangle + \langle \text{Convection} \rangle = \langle \text{Generation} \rangle - \langle \text{Destruction} \rangle \qquad (2)$$

Patzek (1988), Friedmann *et al.* (1988), Kovscek and Radke (1993), and Fergui *et al.* (1995) incorporated the population balance model (PBM) into conventional generalized Darcy's law models using experimental correlations to describe bubbles generation and coalescence.

There are several other models in the literature dedicated to foam modeling in porous media. The simplest way consists in drawing up an experimental correlation between the gas mobility and the physical parameters influencing it, namely the surfactant concentration, the gas velocity, the saturation and the permeability. Then the flow is simulated using a conventional simulator (Islam and Farouq-Ali, 1990). Fisher *et al.* (1990). Zhou and Rossen (1992) have developed models based on the concept of limiting capillary pressure, meaning that foam can be stable only if capillary pressure does not exceed a critical value allowing the existence of a stable thin film. In this approach the limiting capillary pressure gives the corresponding saturation, and then the system of equations can be solved using the fractional flow theory.

There is a major difference between these models and the population balance model which deserves some discussions. The population balance model does not presuppose the existence of a bijection between foam texture and the relevant parameters, namely surfactant concentration, velocity. Since it is usually acknowledged that mobility depends on the foam texture, the capability of models that do not contain this parameter to correctly model foam displacement is in general questionable. Their relative success may be due to the fact that correlations are determined and used in a limited parameter range for which extrapolations are valid. In principle, a population balance model has some advantage since foam texture is part of the system description. However, the balance equation for lamellae density requires the introduction of several correlations describing foam generation and coalescence. In addition, other parameters in the momentum balance equations must be non-linear function of the lamellae density. While this has been recognized as the major and

fundamental advantage of the population balance model, its practical implementation is not straightforward since the experimental determination of lamellae densities is not an easy task.

We plotted in Fig. 1 the evolution of the computed flowing bubble density obtained by a simulator including a population balance equation (Fergui *et al.*, 1995).

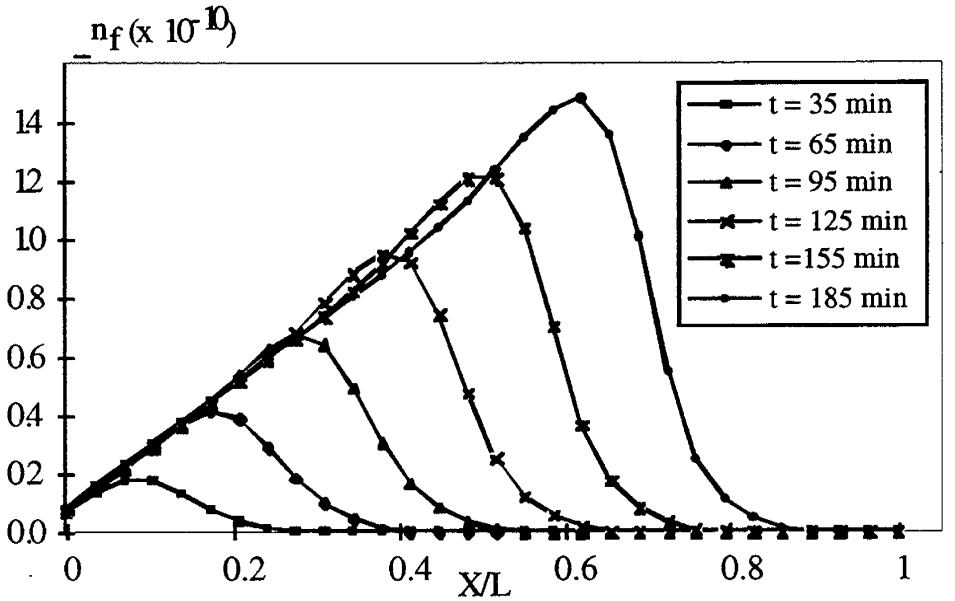

Figure 1. Flowing bubble density as a function of time.

This result corresponds to the modeling of an experiment described in Fergui et al. (1995), nevertheless, the behavior can vary from one experiment to an other one depending on several parameters,

- porous medium physical properties and geometry,
- surfactant type and concentration,
- boundary conditions (co-injection of surfactant solution and gas, gas injection after surfactant slug, gas injection in porous medium saturated by laden surfactant solution).

The flowing bubble density is a very important parameter to the description of the foam viscosity, however it is not possible to compare the numerical results with experimental measurement due to experimental difficulty.

Even if the physical description of the foam flow by the population balance model is satisfactory, the introduction of new parameters, namely generation and destruction parameters, is a major disadvantage for the development of this model in reservoir simulator.

3.5.5 PROPOSITION

Taking into account the literature results, at the different scales described before, and the restrictions on the use of the population balance model, we propose a simplified evaluation of the foam texture in the following way.

The foam viscosity is determined by the product αn_f that is a function of several parameters,

αn_f = F(porous medium, surfactant, gas saturation, flowing gas fraction, location)

We can separate the effects of the surfactant type and concentration that will be integrated in the viscosity coefficient α, we obtain,

$$n_f = G(K, \Phi, S_g, X_f, x/L) \tag{3}$$

where K is the permeability, Φ the porosity, S_g, X_f, are the gas saturation and flowing gas fraction, x is the location and L the length of the porous medium.

This can be written in the following way,

$$n_f = n_s \,.\, S_g \,.\, X_f \,.\, f(x/L) \tag{4}$$

where n_s is the number of sites where lamellae can be generated.

Equation 3 is the simple expression of the fact that we have a bubble in a site where gas is present, among all the bubbles, a few participate to the flow (X_f), moreover, as shown by the population balance model simulation, the bubble density increase as a function of the distance.

3.5.5.1 Number of Sites

In the following part we assume that the porous medium is made of spherical calibrated grains. In such a porous medium, if we have cubic packing, the sites number is equal to the grains number. Using the Kozeny-Carman equation to determine the grain average diameter, we obtain,

$$n_{pores} = \text{coeff} \,.\left(\frac{180(1-\Phi)^2}{\Phi^3} \,.\, K\right)^{-3/2} \tag{5}$$

In this equation only the physical properties of the porous medium are taken into account. The coefficient coeff. is a function of the packing type, its value, for simple packings, is close to 1.

According to the literature cited before, we took the value $X_f = 0.1$.

The function f(x/L) has been chosen in the simplest way

$$n_f = n_s \,.\, S_g \,.\, X_f \,.\, x/L \tag{6}$$

therefore

$$n_f = \left(\frac{180(1-\Phi)^2}{\Phi^3}.\,K\right)^{-3/2} .\, S_g \,.\, X_f \,.\, x/L \tag{7}$$

with

$$\mu_f = \mu_g + \frac{\alpha n_f}{V_g^{1/3}} \tag{8}$$

The complete equation system to be solved is the following one,

Balance Equations

$$\frac{\partial}{\partial t}\left(\varepsilon S_w \rho_w\right) + \nabla.\left(\mathbf{u}_w \rho_w\right) = 0 \tag{9}$$

$$\frac{\partial}{\partial t}\left(\varepsilon S_g \rho_g\right) + \nabla.\left(\mathbf{u}_g \rho_g\right) = 0 \tag{10}$$

Darcy's equations

$$\mathbf{u}_w = -\frac{k_{rw}}{\mu_w}\mathbf{K}.(\nabla P_w - \rho_w \mathbf{g}) \tag{11}$$

$$\mathbf{u}_g = -\frac{k_{rg}}{\mu_g}\mathbf{K}.(\nabla P_g - \rho_g \mathbf{g}) \tag{12}$$

Capillary pressure relationship

$$P_c = P_g - P_w \tag{13}$$

Relative permeabilities are expressed in the Corey's form and the capillary pressure relationship is the classical Leverett function.

Boundary conditions are :

$$q_g = q_0 \text{ at } x = 0 \tag{14}$$

$$P_c = 0 \text{ en } x = L \tag{15}$$

The equation system is solved numerically using a simple IMPES method with a computation, at each time step, of the flowing bubble density and the foam viscosity.

3.5.6 COMPARISON WITH EXPERIMENTAL RESULTS

The objective of this part is to describe experiments using only one fitting parameter, namely α, the viscosity coefficient.

3.5.6.1 Fergui *et al.* (1995)

The experiment consisted of nitrogen injection in an unconsolidated square cross section porous medium saturated by a surfactant solution. Pressure drop along the porous medium and water saturation were measured. This experiment could be satisfactorily described using the population balance model. Here below we compare the results obtained with the simple expression of the foam texture, Eq. (7), with the PBM results.

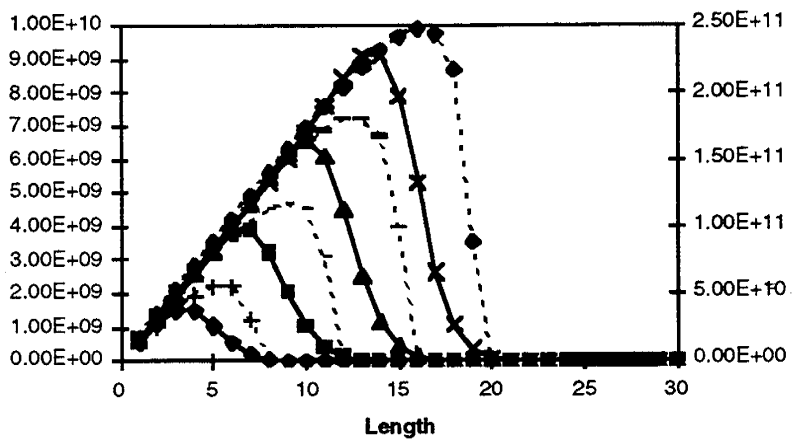

Figure 2. Flowing bubble density (every 30 min.) computed by PBM (solid lines) and using Eq. (7) (dashed lines).

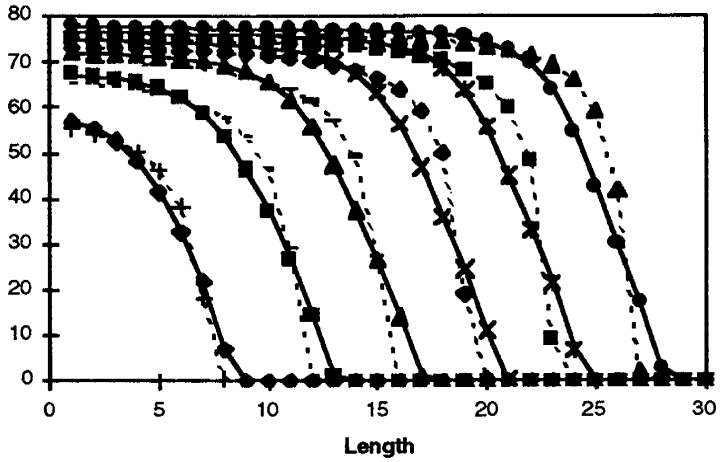

Figure 3. Saturation profiles (every 30 min.) computed by PBM (solid lines) and using Eq. (7) (dashed lines).

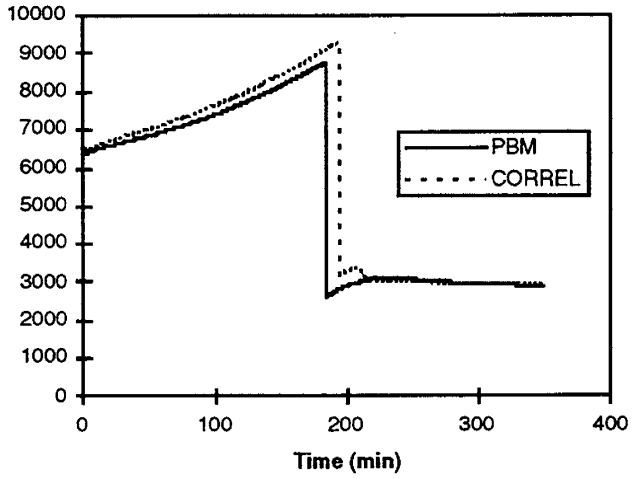

Figure 4 . Pressure drop computed by PBM (solid lines) and using Eq. (7) (dashed lines).

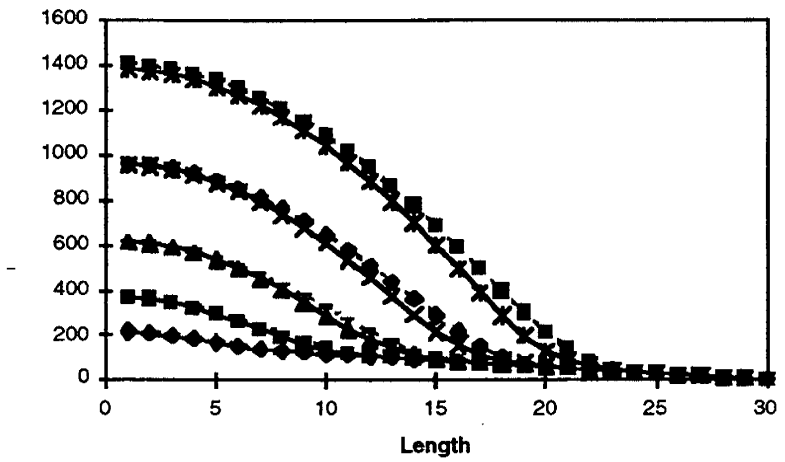

Figure 5 . Pressure profiles computed by PBM (solid lines) and using Eq. (7) (dashed lines).

Even if the profiles are similar, the bubble number density computed using the correlation is higher than the number computed by the PBM, this is due to the choice of generation and destruction terms in the initial PBM. This difference is finally corrected by the viscosity coefficient.

The saturation profiles are quite similar while we fit correctly both the whole pressure drop and the pressure drop profiles along the core.

3.5.6.2 Liu and Brigham (1992)

The porous medium was made of calibrated sand packed in two cylindrical core holders of 0.6 m and 1.2 m lengths. The core holders were equipped with pressure taps along them.

To describe correctly this experiment, we modified the function of location in the correlation to take better into account the fact that the porous medium is longer. The experiments of Fergui *et al.* (1995) was performed on a relatively short porous medium (0.17 m) and a linear increase of the texture is able to describe satisfactorily the behavior. When the porous medium is longer the linear evolution of the texture is not physically correct, therefore we choose a negative exponential of the geometrical location.

$$f(x/L) = 1 - e^{(-x/L)} \tag{16}$$

therefore

$$n_f = \left(\frac{180(1-\Phi)^2}{\Phi^3} . K\right)^{-3/2} . S_g . X_f \; 1 - e^{(-x/L)} \tag{17}$$

The comparison between experimental and simulated results is given in the following figures.

L = 1.2 m

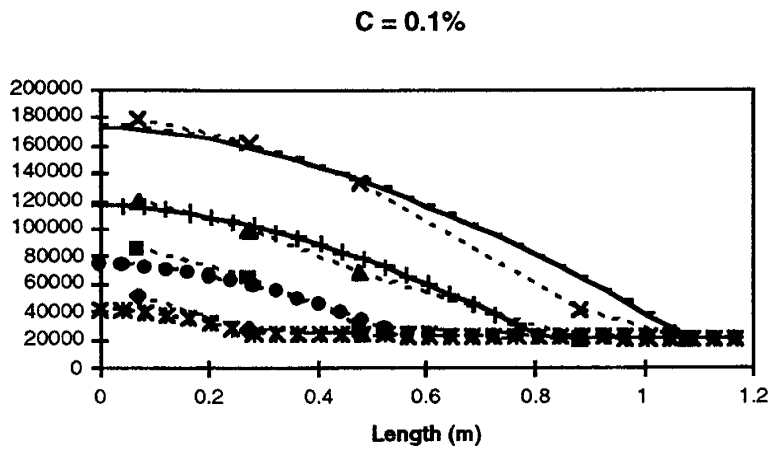

Figure 6. Comparison between experimental results (dashed lines) and simulation (solid lines).

These results have been obtained with a viscosity coefficient $\alpha = 4.5\ 10^{-15}$

L = 0.6 m

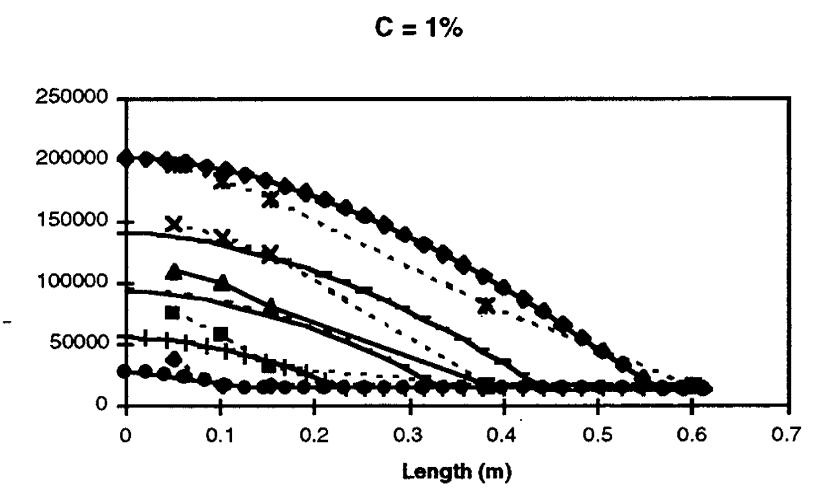

Figure 7. Comparison between experimental results (dashed lines) and simulation (solid lines).

These results have been obtained with a viscosity coefficient $\alpha = 1.3\ 10^{-14.}$

The comparison of the two fitted viscosity coefficients shows clearly the effect of the surfactant concentration on the foam viscosity.

3.5.7 CONCLUSION

The model presented in this paper, based both on experimental results obtained at different scales and on the description of the flowing bubble density obtained by the population balance model, use a simple expression of the foam texture that takes into account the porous medium physical properties. The effects of surfactant type, concentration and salinity is described by the viscosity coefficient.

Several experiments performed on different porous media with different geometry have been simulated satisfactorily.

3.5.8 REFERENCES

1. Chambers K.T. and Radke C.J.: "Capillary Phenomena in Foam Flow Through Porous Media," Interfacial Phenomena in Petroleum Recovery, Morrow N. R. Ed., Marcel Dekker Inc., New York, 1991.

2. Fergui, O., Quintard M., Bertin, H. and Defives D: "Transient Foam Flow in Porous Media: Experiments and Simulation." Proceedings of the 8th European IOR Symposium, Vienna, Austria (May 1995).

3. Fisher A.W., Foulser R.W.S. and Goodyear S.G.: "Mathematical Modeling of Foam Flooding," SPE 20195, paper presented at the SPE/DOE Enhance Oil Recovery Symposium, Tulsa (April 22-25, 1990).

4. Friedmann F. and Jensen J.A.: "Some Parameters Influencing the Formation and Propagation of Foams in Porous Media," SPE 15087, paper presented at the 56th Cal. Reg. Meeting of the SPE, Oakland (April 2-4, 1986).

5. Friedman F., Chen W.H. and Gauglitz P.A.: "Experimental and Numerical Study of High Temperature Foam Displacement in Porous Media," SPE 17357, paper presented at the SPE/DOE Enhance Oil Recovery Symposium, Tulsa (April 17-20, 1988).

6. Friedmann F., Chen W. H. and Gauglitz P.: "Experimental and Simulation Study of High Temperature Foam Displacement in Porous Media," SPE Res. Engng. (February 1991) 37-45.

7. Gillis J. V. and Radke C J.: "A Dual Gas Tracer Technique for Determining Trapped Gas Saturation During Steady Foam Flow in Porous Media," SPE 20519, paper presented at the 65th Annual Technical Conference, New Orleans (1990).

8. Hanssen J.E. and Haugun P.: "Gas Blockage by Non-aqueous Foams," SPE 21002, paper presented at the international Symposium on Oilfield Chemistry, Anaheim (Feb. 20-22, 1991).

9. Hirasaki G.J.and Lawson J.B.: "Mechanisms of Foam Flow Through Porous Media : Apparent Viscosity in Smooth Capillaries," SPE J. (April, 1985) 176-190.

10. Islam M.R. and Farouq-Ali S.M.: "Numerical Simulation of Foam Flow in Porous Media, " J. Can. Petrol. Technol. (July-August, 1990) 47-51.

11. Kovscek A.R. and Radke C.J.: "A Comprehensive Description of Transient Foam Flow in Porous Media," Paper presented at the DOE/NIPER Symposium on Field Application of Foams for Oil Production, Bakersfield (February 11-12, 1993).

12. Liu D. and Brigham W.E.: "Transient Foam Flow in Porous Media with CAT Scanner, SUPRI TR 19 (1992) [DOEBC14600-19].

13. Owete S.O. and Brigham W.E.: "Flow Behavior of Foam : A Porous Micromodel Study," SPE Res. Engng. (August 1987), 315-323.

14. Patzek T.W.: "Description of Foam Flow in Porous Media by the Population Balance Method," Surfactant Based Mobility Control Progress in Miscible Flood Enhanced Oil Recovery, Smith D.H. Ed., ACS Symposium Series N° 373 (1988) 326-341 .

15. Schramm L.L.: Ed., Foams : Fundamentals and Applications in the Petroleum Industry, Adv. In Chem. Series, ACS 242 (1994).

16. Zerhboub M., Ben-Naceur K., Touboul E.m and Thomas R.: "Matrix Acidizing: A Novel Approach to Foam Diversion," SPE Prod. and Facilities (May, 1994) 121-126.

17. Zhou Z.H.and Rossen W.R.: "Applying Fractional Flow Theory to Foam Processes at Limiting Capillary Pressure," SPE 24180, paper presented at the 8th SPE/DOE Symposium on Enhanced Oil Recovery, Tulsa (April 22-24, 1992).

3.6 MECHANISTIC FOAM FLOW SIMULATION IN HETEROGENEOUS AND MULTIDIMENSIONAL POROUS MEDIA

(A. R. Kovscek, T. W. Patzek, and C. J. Radke)

This work was supported by the Assistant Secretary for Fossil Energy, Office of Oil, Gas, and Shale Technologies of the U. S. Department of Energy, under contract No. DE-ACO3-76FS00098 to the Lawrence Berkeley National Laboratory of the University of California, U.S. Department of Energy, under contract No. DE-FG22-96BC14994 to Stanford University, and SUPRI-A.

3.6.1 ABSTRACT

Gases typically display large flow mobilities in porous media relative to oil or water, thereby impairing their effectiveness as displacing fluids. Foamed gas, though, is a promising agent for achieving mobility control in porous media. Because reservoir-scale simulation is a vital component of the engineering and economic evaluation of any enhanced oil recovery (EOR) project, efficient application of foam as a displacement fluid requires a predictive numerical model. Unfortunately, no such model is currently available for foam injection in the field where flow is multidimensional and porous media are heterogeneous.

We have incorporated a conservation equation for the number density of foam bubbles into a fully implicit, three-dimensional, compositional, and thermal reservoir simulator and created a fully functional, mechanistic foam simulator. Because foam mobility is a strong function of bubble texture, the bubble population balance is necessary to make accurate predictions of foam-flow behavior. Foam generation and destruction are included through rate expressions that depend on saturations and surfactant concentration. Gas relative permeability and effective viscosity are modified according to the texture of foam bubbles. In this paper, we explore foam flow in radial, layered, and heterogeneous porous media. Simulations in radial geometries indicate that foam can be formed deep within rock formations, but that the rate of propagation is slow. Foam proves effective in controlling gas mobility in layered porous media. Significant flow diversion and sweep improvement by foam are predicted, regardless of whether the layers are communicating or isolated.

3.6.2 INTRODUCTION

Field application of foam is a technically viable enhanced oil recovery (EOR) process as demonstrated by steam-foam field studies (Patzek and Koinis, 1990; Djabbarah *et al.*, 1990; Friedmann *et al.*, 1994; Mohammadi *et al.*, 1989) and recent nonthermal application of foam in the Norwegian sector of the North Sea (Svorstøl *et al.*, 1996; Aare *et al.*, 1995). Foam can mitigate gravity override of oil-rich zones and/or selective channeling through high permeability streaks, thereby improving volumetric displacement efficiency .

For example, Patzek and Koinis (1990) report that two different pilot studies in the Kern River Field (Kern Co., California) showed major incremental oil-recovery response after about two years of foam injection. They report increased production of 5.5 to 14% of the original oil in place (OOIP) over a five year period. Djabbarah *et al.* (1990) report

improved vertical and areal sweep efficiency in the South Belridge Field (Kern Co., California) and an incremental oil production of 183,000 B from two, contiguous, ten-acre, inverted, nine-spot patterns following a foam injection period of about 1 year. Friedmann *et al.* (1994) report more even injection profiles with steam foam, *in-situ* foam generation, and foam propagation in rock formations.

Efficient application and evaluation of candidates for foam EOR processes, though, requires a predictive numerical model of foam displacement. A mechanistic model would also expedite scale-up of the process from the laboratory to the field. No mechanistic, field-scale model for foam displacement is currently in use.

The population-balance method for modeling foam in porous media (Falls, *et al.*, 1988; Patzek, 1988) is mechanistic and incorporates foam into reservoir simulators in a manner that is analogous to energy and species mass balances (Falls, *et al.*, 1988; Patzek, 1988). Accordingly, a separate conservation equation is written for the concentration of foam bubbles. This simply adds another component to a standard n-component compositional simulator.

Until recently, the population balance method has only been used to model steady-state results in glass beadpacks (Falls *et al.*, 1988) and Berea sandstone (Ettinger, 1992) or to predict transient flow (Chang *et al.*, 1990; Friedmann *et al.*, 1991) , but not both. Previously, we presented the results of an extensive experimental and simulation study of transient and steady foam flow in one-dimensional porous media (Kovscek and Radke, 1994; Kovscek *et al.*, 1995). This initial work detailed the development of a mechanistic model for foam displacement that was easily implemented, fit simply into the framework of current reservoir simulators, and employed a minimum of physically meaningful parameters. Propagation of foam fronts within Boise sandstone was tracked experimentally and simulated successfully under a variety of injection modes and initial conditions (Kovscek *et al.*, 1995; Kovscek *et al.*, 1993).

This paper extends our foam displacement model to multidimensional, compositional, and nonisothermal reservoir simulation. For numerical stability and to accommodate the long time steps necessary for successful reservoir-scale simulation, a fully implicit backward-differencing scheme is used. The simulator employs saturation and surfactant concentration dependent rate expressions for lamella formation and destruction. Lamella mobilization is similarly included.

Our objectives are to show that not only is population-balance-based simulation of foam displacement possible in multidimensional heterogeneous porous media, but also highly instructive in regard to the physics of foam displacement. We only consider isothermal, oil-free systems. This allows easy comparison with our previous experimental and simulation results (Kovscek and Radke, 1994; Kovscek *et al.*, 1995). Numerous verification exercises are performed to discover the role foam plays in gas displacement through zones of contrasting permeability and to highlight the interplay of foam-bubble texture and gas mobility.

3.6.2.1 Foam in Porous Media

Foam microstructure in porous media is unique (Chambers and Radke, 1991). Accordingly, to model gas mobility it is important to understand foamed-gas microstructure (Kovscek and Radke, 1994). In water-wet porous media, the wetting surfactant solution remains continuous, and the gas phase is dispersed. Aqueous liquid

completely occupies the smallest pore channels where it is held by strong capillary forces, coats pore walls in the gas-filled regions, and composes the lamellae separating individual gas bubbles. Only minimal amounts of liquid transport as lamellae. Most of the aqueous phase is carried through the small, completely liquid-filled channels. Gas bubbles flow through the largest, least resistive pore space while significant stationary bubbles reside in the intermediate-sized pore channels where the local pressure gradient is insufficient to sustain mobilized lamellae.

Foam reduces gas mobility in two manners. First, stationary or trapped foam blocks a large number of channels that otherwise carry gas. Gas tracer studies (Friedmann, *et al.*, 1991; Friedmann *et al.*, 1991; Gillis and Radke, 1990) show that the fraction of gas trapped within a foam at steady state in sandstones is quite large and lies between 85 and 99%. Second, bubble trains within the flowing fraction encounter significant drag because of the presence of pore walls and constrictions, and because the gas/liquid interfacial area of a flowing bubble is constantly altered by viscous and capillary forces (Hirasaki and Lawson, 1985; Falls *et al.*, 1989). Hence, foam mobility depends strongly on the fraction of gas trapped and on the texture or number density of foam bubbles.

Bubble trains are in a constant state of rearrangement by varied foam generation and destruction mechanisms (Chambers and Radke, 1991). Individual foam bubbles are molded and shaped by pore-level making and breaking processes that depend strongly on the porous medium (Ettinger, 1992; Chambers and Radke, 1991). To account for foam texture in a mechanistic sense, foam generation and coalescence must be tracked directly. Additionally, bubble trains halt when the local pressure gradient is insufficient to keep them mobilized, and other trains then begin to flow. Bubble trains exist only on a time-averaged sense. More detailed summaries of the pore-level distribution of foam, and the mechanisms controlling texture are given in Chambers and Radke (1991) and Kovscek and Radke (1994).

3.6.3 MODELING FOAM DISPLACEMENT

A variety of empirical and theoretical methods for modeling foam displacement are available in the literature. These range from population balance methods (Falls, *et al.*, 1988; Patzek, 1988; Chang, *et al.*, 1990; Friedmann *et al.*, 1991; Kovscek *et al.*, 1995; Ettinger, R.A., 1989; Fergui *et al.*, 1995)to percolation models (Rossen, 1990; Rossen, 1990; Rossen, 1990; Rossen and Gauglitz, 1990; Chou, 1990) and from applying so-called fractional flow theories (Rossen *et al.*, 1991; Zhou, and Rossen, 1992) to semi-empirical alteration of gas-phase mobilities (Patzek and Koinis, 1990; Fisher, *et al.*, 1990; Liu and Brigham, 1992; Patzek and Myhill, 1989; Mohammadi *et al.*, 1993; Mohammadi and Coombe, 1992; Marfoe and Kazemi, 1987; Mahmood *et al.*, 1986). Of these four methods, only the population balance method and network or percolation models arise from first principles.

3.6.3.1 Population Balance Method

The power of the population balance method lies in addressing directly the evolution of foam texture and, in turn, reductions in gas mobility. Gas mobility is assessed from the concentration or texture of bubbles. Further, the method is mechanistic in that well-documented pore-level events are portrayed in foam generation, coalescence, and constitutive relations. Most importantly, the population balance provides a general

framework where all the relevant physics of foam generation and transport may be expressed.

We chose the population balance method because of its generality and because of the similarity of the equations to the usual mass and energy balances that comprise compositional reservoir simulation. Only a brief summary of the method is given here as considerable details of our implementation are available in the literature (Kovscek, and Radke, 1994; Kovscek *et al.*, 1995; Kovscek *et al.*, 1993). The requisite material balance on chemical species i during multiphase flow in porous media is written as,

$$\frac{\partial}{\partial t}\left[\varphi\sum_j\left(S_jC_{i,j}+\Gamma_{i,j}\right)\right]+\sum_j\nabla\bullet\vec{F}_{i,j}=q_{i,j} \tag{1}$$

where S is the saturation of phase j, C is the molar concentration of species i in phase j, Γ is the adsorption and absorption losses of species i from phase j in units of moles per void volume, $\vec{F}$ is the vector of combined convective and diffusive flux of species i in phase j, and q is a rate of generation of i in phase j per unit volume of porous medium. To obtain the total mass of species i, we sum over all phases j.

In the foam bubble population balance, $S_f n_f$ replaces $S_i C_{i,j}$ where n_f is the number concentration or number density of foam bubbles per unit volume of flowing gas and S_f is the saturation of flowing gas. Hence, the first term of the time derivative is the rate at which flowing-foam texture becomes finer or coarser per unit rock volume. Since foam partitions into flowing and stationary portions, Γ becomes $S_t n_t$ where S_t and n_t are the saturation of the stationary gas and the texture of the trapped foam per unit volume of trapped gas, respectively. Thus, the second term of the time derivative gives the net rate at which bubbles trap. Trapped and flowing foam saturation sum to the overall gas saturation, $S_g = S_f + S_g$. The second term on the left of Eq. (1) tracks the convection of foam bubbles where the flux, $\vec{F}$, is given by $\vec{u}_f n_f$, and $\vec{u}_f$ is the Darcy velocity of the flowing foam. Finally, q becomes the net rate of generation of foam bubbles. Within the above framework, foam is a component of the gas phase and the physics of foam generation and transport become amenable to standard reservoir simulation practice.

The net rate of foam generation:

$$q_f=\varphi S_g\left[k_1\,|\vec{v}_w|\,|\vec{v}_f|^{1/3}-k_{-1}\,|\vec{v}_f|\,n_f\right] \tag{2}$$

is written per unit volume of gas. In the simulations to follow, we do not inject pregenerated foam and so we do not require a source/sink term for bubbles. Interstitial velocities, *i.e.*, $\vec{v}_i=\vec{u}_i/\varphi S_i$, are local vector quantities that depend on the local saturation and total potential gradient, including gravity and capillary pressure. Foam generation is taken as a power-law expression that is proportional to the magnitude of the flux of surfactant solution multiplied by the 1/3 power of the magnitude of the interstitial gas velocity. The liquid-velocity dependence originates from the net imposed liquid flow through pores occupied by both gas and liquid, while the gas-velocity dependence arises from the time for a newly formed lens to exit a pore (Kovscek and Radke, 1996) Snap-off is sensibly independent of surfactant properties consistent with its mechanical origin (Chambers and Radke, 1991). The proportionality constant reflects the number of foam germination sites. Intuitively, the number of snap-off sites falls with decreasing liquid

saturation. However, k_1 is taken as a constant here. The generation rate expression does vary implicitly with liquid saturation through the gas and liquid velocities.

To prevent coalescence of newly formed gas bubbles, a surfactant must stabilize the gas/liquid interface. Foam lamellae form given sufficient suction capillary pressure and a stabilizing surfactant. However, too large of a suction-capillary pressure will overcome the stabilizing influence of surfactant and collapse a lamella (Chambers and Radke, 1991). A flowing lamella is vulnerable to breakage in termination sites as it flows into a divergent pore space where it is stretched rapidly. If sufficient time does not elapse for surfactant solution to flow into a lamella and heal it, coalescence ensues (Jiménez and Radke, 1989).

Equation (2) shows that foam lamellae are destroyed in proportion to the magnitude of their interstitial flux, $\bar{v}_f n_f$, into such termination sites. The coalescence rate constant, k_{-1}, varies strongly with the local capillary pressure and surfactant formulation. It is given by

$$k_{-1} = k_{-1}^{o}\left(\frac{P_c}{P_c^* - P_c}\right)^2 , \tag{3}$$

where the scaling factor, k^0_{-1} is taken as a constant and P^*_c is the limiting capillary pressure for foam coalescence (Khatib *et al.*, 1988)

The "limiting capillary pressure," P^*_c, as identified by Khatib *et al.* (1988) refers to the characteristic value of capillary pressure that a porous medium approaches during strong foam flow. It is set primarily by surfactant formulation and concentration. Highly concentrated foamer solutions and robust surfactants lead to high a P^*_c. In situations where surfactant transport is transient, we expect P^*_c to vary locally with surfactant concentration. The experimental work of Aronson *et al.* (1994) suggests the following functional form for P^*_c versus surfactant concentration of robust foamer solutions:

$$P_c^* = P_{c,\max}^*\left(\frac{C_s}{C_s^o}\right) \tag{4}$$

where $P^*_{c,max}$ is a limiting value for P^*_c and C^0_s is a reference surfactant concentration for strong net foam generation.

In the simulations of heterogeneous porous media to follow, we assume that P^*_c is independent of absolute permeability. Foam-lamella coalescence is determined mainly by the rupture capillary pressure of isolated lamellae which, in turn is set by the concentration and type of surfactant, and not the nature the porous medium (Jiménez and Radke, 1989). Equations (3) and (4) correctly predict that at high capillary pressures or for ineffective foamer solutions k_{-1} is quite high (Khatib *et al.*, 1988; Aronson *et al.*, 1994). The foam coalescence rate approaches infinity as the porous medium capillary pressure approaches P^*_c. We also assume geometric similarity between layers of differing permeability. Thus, for a uniform liquid saturation in the heterogeneous medium, foam is more vulnerable to breakage in the low permeability zones because P_c scales inversely as the square root of the absolute permeability according to the Leverett J-function (Leverett, 1941).

In addition to bubble kinetic expressions, the mass balance statements for chemical species demand constitutive relationships for the convection of foam and wetting liquid phases. Darcy's law is retained, including standard multiphase relative permeability functions. However, for flowing foam, we replace the gas viscosity with an effective viscosity relation for foam. Since flowing gas bubbles lay down thin lubricating films of wetting liquid on pore walls, they do not exhibit a Newtonian viscosity. We adopt an effective viscosity relation that increases foam effective viscosity as texture increases, but is also shear thinning

$$\mu_f = \mu_g + \frac{\alpha n_f}{|\vec{v}_f|^{1/3}} \tag{5}$$

where α is a constant of proportionality dependent mainly upon the surfactant system. In the limit of no flowing foam we recover the gas viscosity. This relation is consistent with the classical result of Bretherton (1961) for slow bubble flow in capillary tubes (Hirasaki and Lawson, 1985; Falls *et al.*, 1989; Wong *et al.*, 1995; Wong *et al.*, 1995).

Finally, stationary foam blocks large portions of the cross-sectional area available for gas flow and, thus, must be accounted for to determine gas flux. Since the portion of gas that actually flows partitions selectively into the largest, least resistive flow channels, we adopt a "Stone-type" relative permeability model (Stone, 1970) that, along with effective viscosity, specifies gas-phase flow resistance. Because wetting aqueous liquid flows in the smallest pore space, its relative permeability is unaffected by the presence of flowing and stationary foam in accordance with the experimental results of Bernard *et al.* (1965), Holm (1968), Sanchez *et al.* (1989), DeVries and Wit (1990). Since flowing foam partitions selectively into the largest pore space, the relative permeability of the nonwetting flowing gas is a function of only S_f. Consequently, gas mobility is much reduced in comparison to an unfoamed gas propagating through a porous medium, because the fraction of gas flowing at any instant is quite small (Friedmann *et al.*, 1991; Gillis and Radke, 1990).

3.6.4 COMPOSITIONAL FOAM SIMULATOR

Our starting point for multidimensional foam simulation is M^2NOTS (Multiphase Multicomponent Nonisothermal Organics Transport Simulator), a nonisothermal, n-component, compositional simulator capable of handling three-phase flow in response to viscous, gravity, and capillary forces (Adenekan *et al.*, 1993). It is a compositional extension of TOUGH2 (Pruess, 1991; Pruess, 1987).

The integral finite difference method (IFDM) is employed to discretize the flow domain (*cf.*, Narasimhan and Witherspoon, 1976). Spatial gradients are calculated in a manner identical to the classic block-centered finite difference method. Flow mobilities are upstream weighted except for the absolute permeability between blocks of differing permeability. These are based on harmonic weighting. Time derivatives are approximated by first-order finite differences with a fully implicit treatment of all flow terms. Time-step size is controlled automatically. Newton-Raphson iteration solves the discretized system of nonlinear algebraic equations. A robust thermophysical package is encorporated. A cubic equation of state represents the thermodynamic properties of the gas phase, which for N_2 at the temperatures and pressures simulated here reduces to an ideal gas. The method of corresponding states describes the oil phase. The International Steam Tables

provide the properties of the aqueous phase (International Formulation Committee, 1967). The simulator has been used successfully to model the deposition and clean up of petroleum hydrocarbons from soils and groundwater (Adenekan *et al.*, 1993).

We treat foam bubbles as a nonchemical component of the gas phase. Thus, the additional transport equation for foam-bubble texture described above is added to the mass balances for water, gas, and n organic components. The discretized foam-bubble equation is fully implicit with upstream weighting of the gas-phase mobility consistent with all other chemical species. In each grid block, the magnitude of the vectors representing the interstitial gas and liquid velocities are used to compute foam generation and coalescence rates from Eq. (2). The magnitude of each velocity is obtained by first summing the flow of each phase into and out of a grid block in the three orthogonal directions. Then the arithmetic average for each direction is calculated and the magnitude of the resultant vector used to calculate foam generation and coalescence rates. The gas velocity is similarly computed for the shear-thinning portion of the foam effective viscosity.

Numerical values of the population balance parameters are determined from steady-state measurements in one-dimensional linear flow. Steady-state flow trends, saturation, and pressure drop profiles are matched. These can all be obtained within one experimental run. The suite of foam displacement parameters do not need to be adjusted to accommodate different types of transient injection or initial conditions. Parameter values used here are taken from Kovscek *et al.* (1995) and apply specifically to very strong foams in the absence of oil and under isothermal conditions.

3.6.5 NUMERICAL MODEL RESULTS

Because there are many initial conditions, types of injection, and multidimensional geometries of interest, we present the results from several carefully chosen illustrative examples. First, we compare simulator predictions against experimental results for the simultaneous injection of nitrogen and foamer solution into a linear core presaturated with surfactant solution. Second, foam flow in heterogeneous, noncommunicating and communicating linear layers is considered. The layers are again assumed to be presaturated with surfactant. Next, we simulate the one-dimensional radial flow of foam and consider media that are initially unsaturated and saturated with surfactant solution. Here, we focus on the evolution of gas mobility as foam flows outward radially. Finally, we present simulations of surfactant and gas coinjection into a 2.5-acre five-spot pattern and the resulting foam generation. To avoid confusion between foam formation, surfactant propagation and adsorption, foam-oil interaction, and partitioning of surfactant into the oil phase, we choose a porous medium that does not adsorb surfactant and never contains any oil. In all simulations, the rock is initially filled with the aqueous phase, $S_W = 1$. Nitrogen and foamer solution are coinjected simultaneously. Thus, we focus attention on foam formation, coalescence, transport, and reduction of gas mobility.

3.6.5.1 Linear Core

In the first example, nitrogen is injected continuously into a linear core of length 0.60 m at a rate of 0.43 m/day relative to the exit pressure of 4.8 MPa. Foamer solution is also injected continuously at 0.046 m/day to give a quality or gas fractional flow of 0.90 at the core exit. The medium is initially filled with surfactant solution. These flow rates and initial conditions correspond exactly to our previous experiments conducted in a 1.3-μm^2 Boise sandstone with a length of 0.60 m (Kovscek and Radke, 1994; Kovscek and Radke,

1995). The foamer was a saline solution (0.83 wt% NaCl) with 0.83 wt% active AOS 1416 (C_{14-16} alpha olefin sulfonate, Bioterg AS-40, Stepan).

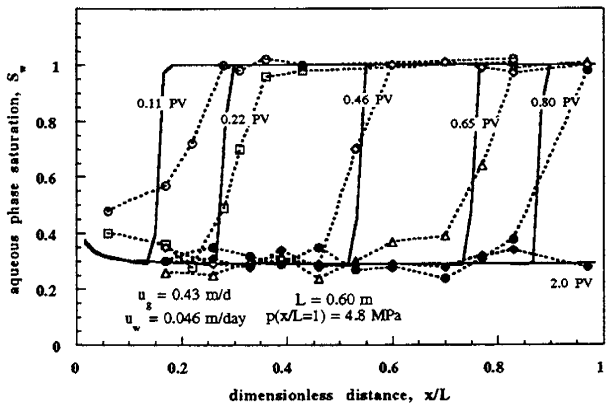

Fig. 1—Experimental and model transient aqueous-phase saturation profiles for 1-d displacement.

Figures 1 and 2 display the transient experimental and simulated saturation and pressure profiles, respectively. Figure 3 displays the foam texture profiles. Theoretical results are represented by solid lines. Dashed lines simply connect the individual data points. Elapsed time is given as pore volumes of total fluid injected, that is, as the ratio of total volumetric flow rate at exit conditions multiplied by time and divided by the core void volume.

Steep saturation fronts are measured and predicted at all time levels in Fig. 1 whereby aqueous-phase saturation upstream of the front is roughly 30% and downstream it is 100%. Model fronts are somewhat steeper and sharper than those measured experimentally, but the theoretical saturation profiles track experimental results very well. From the saturation profiles it is apparent that foam moves through the core in a piston-like fashion. Note that the simulation displays little numerical dispersion.

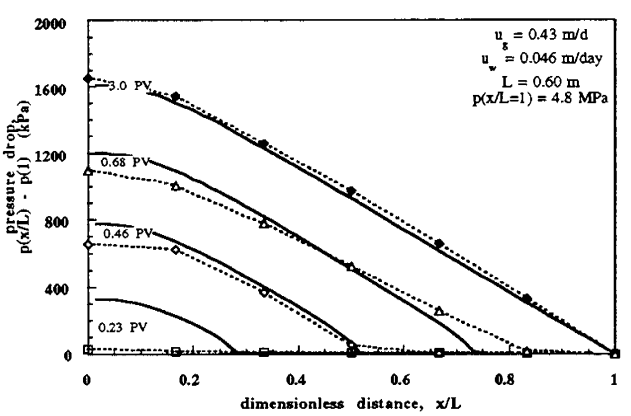

Fig. 2—Experimental and model transient pressure profiles for 1-d displacement.

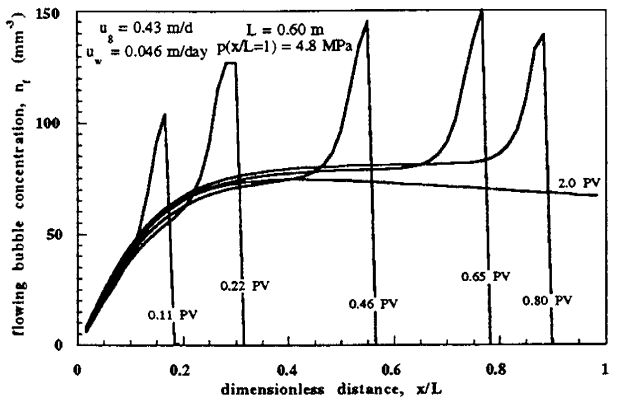

Fig. 3—Model transient flowing-foam texture profiles for 1-d displacement.

Even though nitrogen and surfactant solution are injected separately, rapid foam generation and liquid desaturation occur at the core inlet. A region of net foam generation near the inlet is clearly evident in the transient pressure profiles of Fig. 2. Both the experiments and calculations show that pressure gradients near the inlet are shallow, indicating that flow resistance is small and foam textures are coarse consistent with the injection of unfoamed gas. Steep gradients are found downstream of the inlet region. These steep gradients confirm the existence of a strong foam piston-like front moving through the core.

Figure 3 reports the predicted foam texture as a function of dimensionless distance and time. We find a coarsely textured foam near the inlet, but beyond the first fifth of the core, foam texture becomes very fine and nearly constant at each time level. High pressure gradients and fine foam textures are seen where liquid saturation is low and *vice versa.* No method currently exists to measure *in situ* foam texture directly. However, the predicted effluent bubble textures do match the bubble size of foams exiting a similar Berea sandstone (Ettinger and Radke, 1992; Ettinger, 1989).

One interesting feature of Fig. 3 is the elevation of foam texture near the foam front above that in steady-state and also that immediately upstream of the foam front. Foam texture is fine at the foam front because the aqueous-phase saturation increases from roughly 0.30 to 1. For high aqueous-phase saturation, Eq. (3) gives a very low foam coalescence rate. At the same time, interstitial liquid and gas rates are high resulting in a large rate of net foam generation. Setting Eq. (2) to zero and solving for the value of the local equilibrium foam texture indeed shows that texture can be quite high at the foam front. Because this intensive foam generation is confined to a very small region, pressure gradients at the foam front are affected negligibly, as displayed in Fig. 2. Further, as this result appears to be physical, we make no attempt to suppress it.

Gas compressibility effects are also found in Fig. 3. At steady state, the foam texture decreases along the latter portion of the of the core. As they flow downstream, the small compressible foam bubbles find themselves out of equilibrium with the lower pressure. Consequently, bubbles expand increasing their velocity. This increased velocity triggers increased foam coalescence and a more coarsely textured foam. Gas compressibility similarly accounts for foam textures finer than the steady-state texture upstream of the foam fronts at time levels of 0.65 and 0.80 PV.

In addition to good agreement with experiment, the model results in Figs. 1-3 agree quite well with our previous calculations generated by a one-dimensional simultaneous solution method with explicit upstream weighting of the flow mobilities (Kovscek and Radke, 1995) . Again, the foam displacement parameters employed are identical in both numerical methods. In the remaining simulations, we assume that the fraction of gas flowing in the presence of foam is a constant equal to 0.10. This shortens the computation time required for multidimensional calculations by decreasing the stiffness of the equations. The impact of the increase in foam texture at the foam front on gas mobility is also moderated.

3.6.5.2 Heterogeneous Noncommunicating Linear Layers.

In this section, we consider the case of two linear layers with different permeabilities and without cross flow. Both layers are initially filled with foamer solution as in the previous case. This geometry applies to a reservoir with continuous impermeable shale breaks and to parallel core experiments in the laboratory. The high permeability layer is assigned a permeability of 1.3 μm^2 which is identical to the permeability of the Boise sandstone cores used in our laboratory (Kovscek and Radke, 1994; Kovscek *et al.*, 1995).

The permeability of the second layer is made a factor of 10 smaller, 0.13 μm^2. Each layer is assumed to be geometrically similar and is given the same porosity, Leverett J-function (Leverett, 1941) and relative permeability functions. Initially, both layers are saturated with aqueous surfactant solution. Superficial velocities maintained in these simulations are the same as in the linear corefloods portrayed in Figs. 1 - 3. The system length is set at 0.60 m to allow direct comparison with these corefloods. Continuity of pressure is maintained at the inlet and outlet. Otherwise, each layer accepts whatever portion of the injected fluids it desires.

It is useful to begin by considering the effect that foam has on reapportioning the production from each layer. Figure 4 displays as solid lines the fraction of the original water displaced from each layer as a function of the time. The small amounts of surfactant solution injected with the gas are not included in the produced volume. Time is again given nondimensionally by the total pore volumes injected. Also, injection of nitrogen at 0.48 m/day in the absence of surfactant is shown with dashed lines as a reference case. For the unfoamed gas injection, little liquid is produced from the low permeability layer. Although the displacement of water from the high permeability layer is initially rapid, gas quickly moves through the 1.3-μm^2 layer and the production rate declines after only 0.2 PV. Nitrogen is very mobile relative to water making it an exceptionally poor displacement fluid. Foaming the nitrogen has a dramatic effect. Production from both layers is maintained for about a pore volume of injection indicating that foam provides efficient displacement in both the high and low permeability layers. Production plateaus at 1 PV because the displacement is essentially complete in 1 PV.

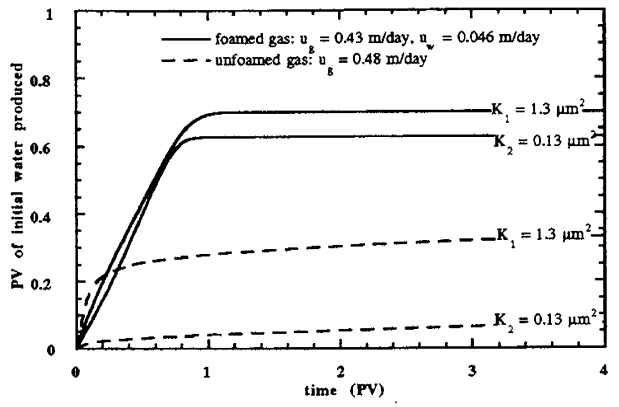

Fig. 4—Fraction of the initial water displaced by foamed gas and unfoamed gas as a function of time from two isolated layers.

The improvement of diversion with foam is seen quite strikingly in Fig. 5 which gives the simulated saturation profiles in each layer as a function of time. In the high-permeability-layer saturation profile shown in Fig. 5a, the foam front initially moves more quickly than in the low permeability layer as illustrated in Fig 5b. However, at 0.44 PV the foam displacement fronts in each layer are positioned at approximately x/L equal to 0.55. By examining the displacement fronts at 0.66 PV, we find that the front in the low permeability layer is actually ahead of the front in the high permeability layer. Foam breakthrough occurs first in the low permeability layer. Again, these are very efficient displacements because we began with the porous medium saturated with surfactant solution and use strong foam displacement parameters characteristic of AOS 1416 in oil-free porous media.

Another interesting feature of Fig. 5 is the steady-state aqueous-phase saturation in each layer. Because the layers are isolated, the strong foam generated in each layer causes the capillary pressure of each layer to approach P^*_c. The aqueous-phase saturation at steady state in each layer is thus set by P^*_c, and the steady-state saturations are related by P^*_c through the Leverett J-function (Leverett, 1941). Hence, the 0.13-μm^2 layer only desaturates to an S_W of about 0.38 before the limiting capillary pressure is approached, whereas in the 1.3-μm^2 layer, the S_W at steady state is 0.30.

Saturation profiles in Fig. 5 are best understood by considering the foam texture in each layer. A finely textured foam forms in the high permeability layer, as portrayed in Fig. 6a leading to substantial flow resistance. Conversely, the foam that is generated in the lower permeability layer shown in Fig. 6b, is over an order of magnitude coarser. Accordingly, the low permeability layer presents an overall flow resistance comparable with that of the high permeability layer. Roughly half of the entire gas flow is diverted to the 0.13-μm^2 layer.

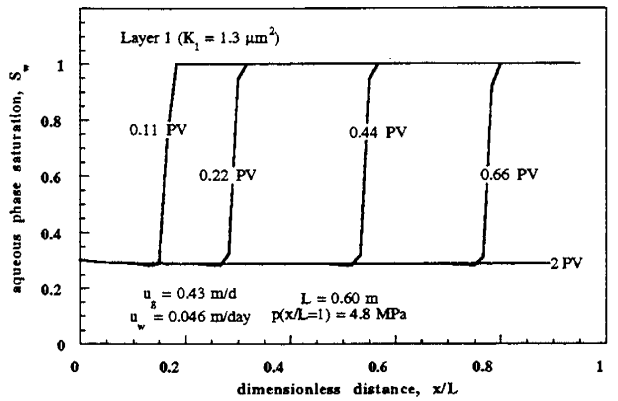

(5a)

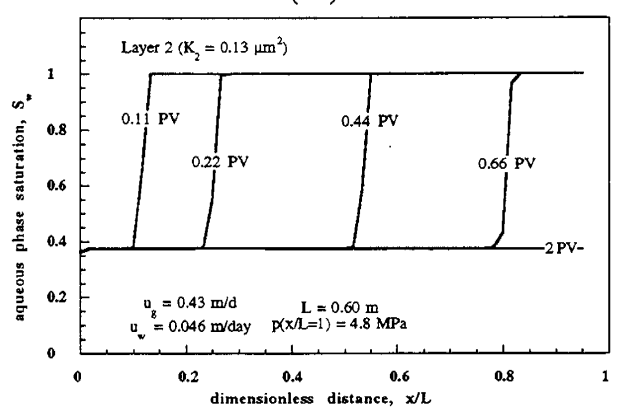

(5b)

Fig. 5—Transient aqueous-phase saturation profiles for displacement from two isolated layers.

Figure 7 presents the companion pressure-drop information for simultaneous injection of nitrogen and foamer solution into isolated layers of differing permeability. Pressure gradients build quickly in both layers consistent with the rapid foam generation displayed in Fig. 6. Interestingly, the total system pressure drop is only 2/3 of that found in the one-dimensional linear flow of Fig. 2 at these same superficial velocities. Because the foam texture in both layers of Fig. 6 is substantially less than that predicted in Fig. 3 for one-dimensional flow, flow resistance and pressure drop are significantly less.

Comparison of Fig. 7 with the saturation and bubble texture profiles in Figs. 5 and 6 shows that saturation, bubble texture, and pressure fronts track exactly as they did in one-dimensional linear flow. Where foam texture is large, S_W is low, pressure gradients are large, and *vice versa*.

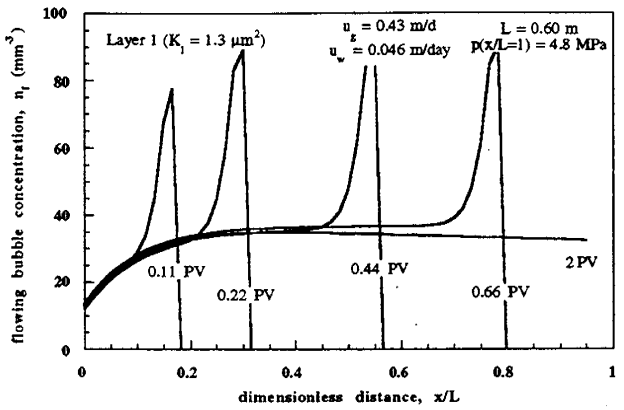

(6a)

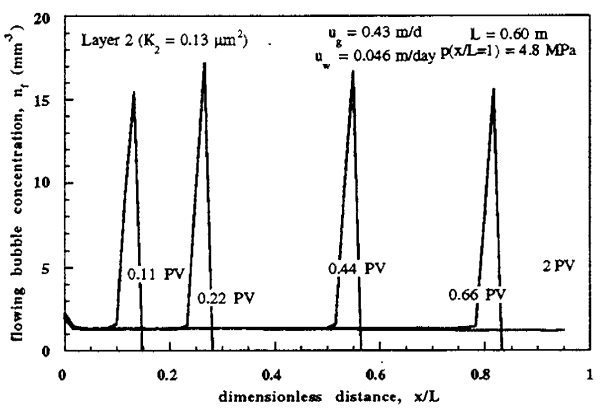

(6b)

Fig. 6—Transient flow-foam textures for displacement from two isolated layers.

3.6.5.3 Heterogeneous Communicating Linear Layers

The geometry, initial conditions, and flow rates employed here are identical to those for the noncommunicating linear layer case. However, cross-flow between the layers is allowed. Figure 8 contrasts production of the original aqueous-phase fluid from each layer when foam is both present (solid lines) and absent (dashed lines). Again, we find that foam induces significant production from the low permeability zone compared to gas injection. Displacement in both layers is quite efficient.

Figure 9 shows that sharp saturation fronts propagate at equal rates in both layers. Since the layers are communicating, gas at the foam front minimizes its flow resistance. For example, when the local flow resistance in the 1.3-μm^2 layer rises, some portion the foamed gas diverts into the 0.13-μm^2 layer, and *vice versa* yielding equal propagation rates in each layer. Saturation fronts in each layer are, thus, bound together by the necessity to maintain the minimum flow resistance. Likewise, this is true for unfoamed gas. The striking feature of Fig. 9 is the efficiency of displacement in each layer.

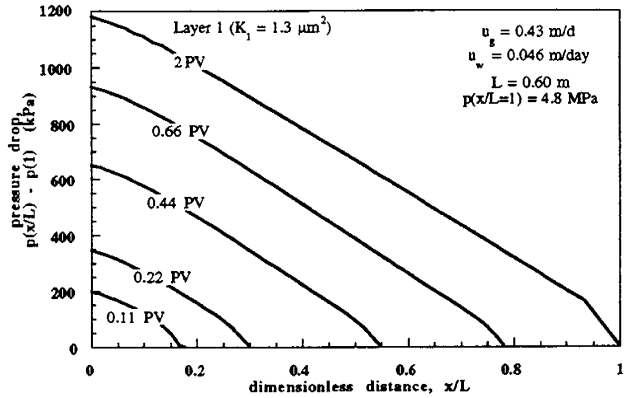

(7a)

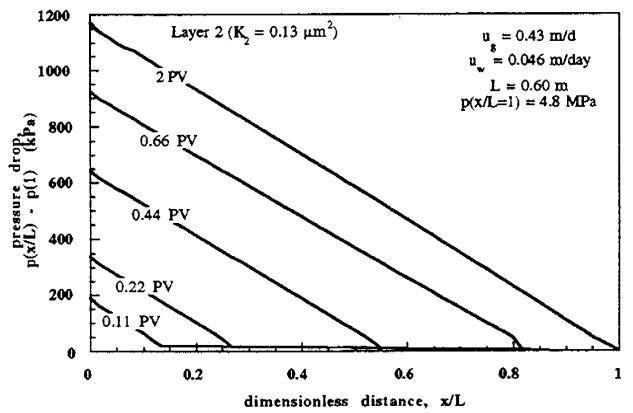

(7b)

Fig. 7—Transient pressure profiles for displacement from two isolated layers.

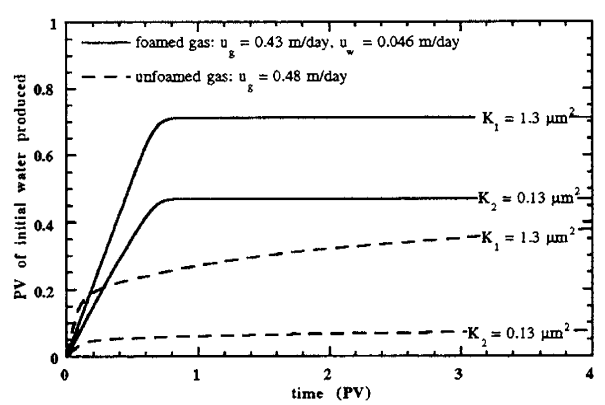

Fig. 8— Fraction of the initial water displaced by foamed gas and unfoamed gas as a function of time from two isolated layers.

Prior to foam breakthrough, S_w upstream of the saturation front in the low permeability, 0.13-μm^2 layer is larger in Fig. 9b than it is in Fig. 5b for noncommunicating layers. During foam propagation, each layer attempts to come to the S_w corresponding to the limiting capillary pressure. Because there is cross-flow and capillary connection between the layers, water is drawn into the low permeability layer maintaining S_w at slightly higher levels than in the noncommunicating layers of Fig. 5b.

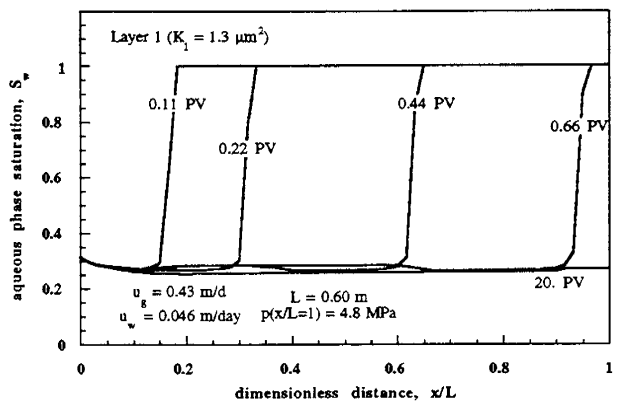

(9a)

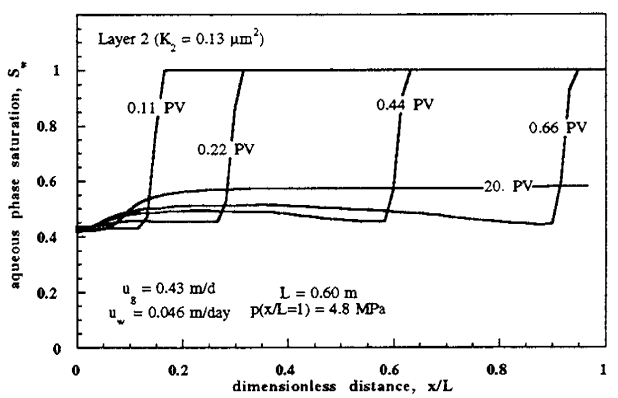

(9b)

Fig. 9—Transient aqueous-phase saturation profiles for displacement from two communicating layers.

Foam breakthrough occurs just after 0.66 PV. After breakthrough, the aqueous-phase saturation in the high permeability layer remains constant at about 0.27. In the low permeability layer, however, S_w slowly increases over time. At 20 PV the average aqueous phase saturation downstream of the inlet is 0.58. The lower permeability layer is slowly refilling with water in an attempt to come into capillary equilibrium with the high permeability layer where the capillary pressure is much lower. Equilibrium will be achieved when S_w reaches roughly 0.87 everywhere in the low permeability layer.

Refilling of the 0.13-μm^2 layer with foamer solution has a dramatic effect on the foam texture over time, as shown in Fig. 10b. Prior to foam breakthrough, foam textures

are comparable with those found in the previous cases. At 0.22 PV the bubble density in the low permeability layer averages about 30 mm^{-3} in the foam-filled region. After breakthrough as the layer refills with water in order to reduce its capillary pressure, the rate of foam coalescence decreases with decreasing capillary pressure as indicated by Eq. (3). Consequently, the net rate of foam generation increases according to Eq. (2) as does the flowing bubble texture. The average bubble texture between 0.66 PV and 10 PV increases by a factor of nearly 3.5. Increasing textures indicate increasing flow resistance. As flow resistance increases, the gas flow rate and also the foam coalescence rate decrease exacerbating the growth in foam texture. The texture in the high permeability layer shown in Fig. 10a is relatively coarse in obedience with the large foam coalescence rates caused by the high capillary pressure there and the relatively high gas flow rates. The texture becomes coarser with time because the high permeability layer carries increasingly more gas that in turn increases foam coalescence in the 1.3-μm^2 layer. In the meantime, the lower permeability layer fills with foam. The refilling effect is unlikely to be encountered in practical application of foam since it only occurs after many PV of foam injection.

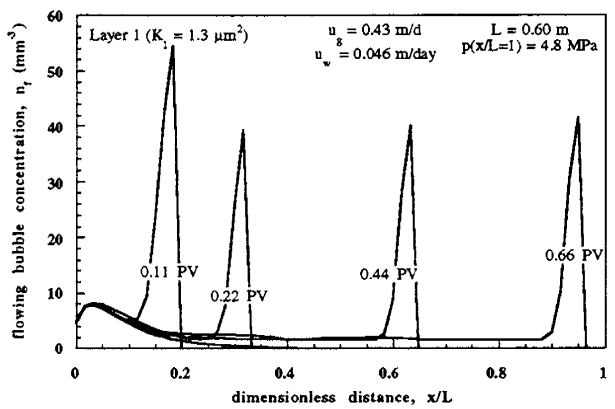

(10a)

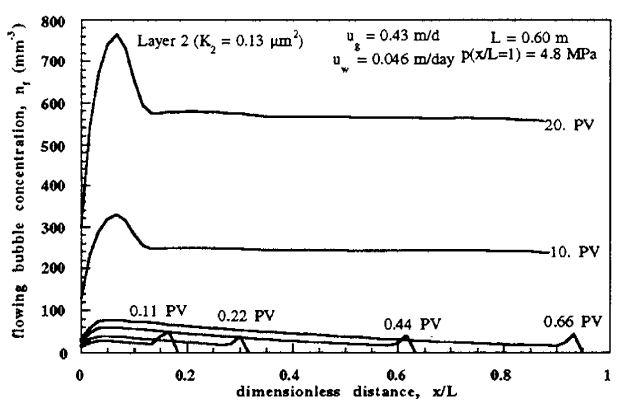

(10b)

Fig. 10— Transient flow-foam textures for displacement from two communicating layers.

The pressure drop profiles shown in Fig. 11 contain several additional interesting features. First, note the magnitude of the pressure drops. The maximum pressure drop

displayed is roughly 200 kPa (22 psi), whereas the identical flow rate conditions in Fig. 2 yielded a steady state pressure drop of a little more than 1600 kPa (230 psi). The flow resistance in the 1.3-μm^2 layer is small because foam is coarsely textured there and because the gas superficial velocity is large exploiting the shear-thinning foam rheology. This commands a smaller net flow resistance than that found in the linear one-dimensional and noncommunicating layer cases. Second, the pressure drop declines in time as the foam coarsens in the high permeability layer. The system pressure drop at 0.66 PV is nearly 190 kPa while at 20 PV it has declined to 140 kPa.

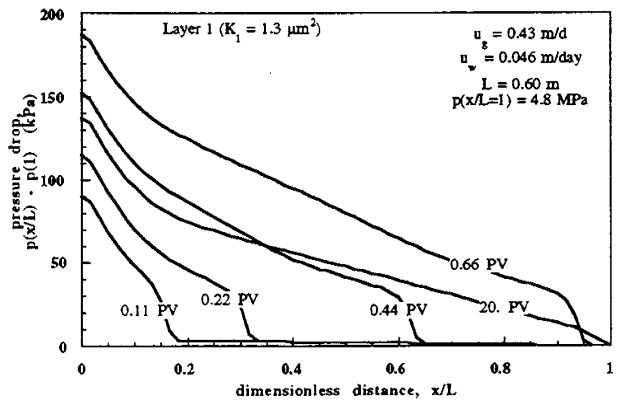

(11a)

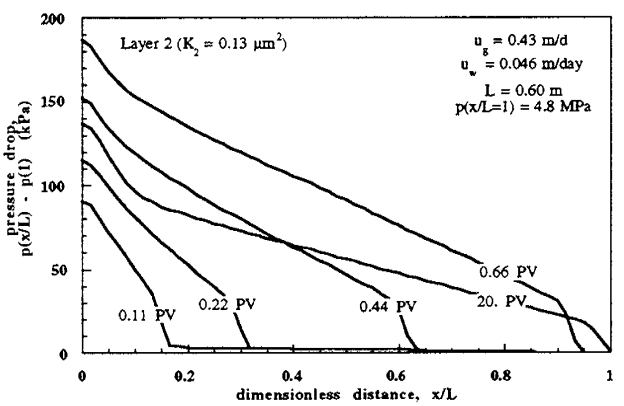

(11b)

Fig. 11—Transient pressure profiles for displacement from two communicating layers.

3.6.5.4 Radial Flow

Next, we consider simultaneous injection of nitrogen and foamer solution into a radial, one-dimensional, homogeneous porous medium that is 1 m thick with a radius, R, of 71.5 m and a permeability of 1.3 μm^2. The medium is initially saturated with surfactant-free brine. Volumetric injection rates are 0.165 m^3/day of surfactant solution and 3.14 m^3/day of nitrogen relative to the 4.8 MPa backpressure to give a gas fractional flow of 0.95.

Figure 12 displays the radial aqueous-phase saturation profiles as a function of time. Dimensionless radial distance is simply $r' = (r - r_{well})/R = 0$. At short times (*e.g.*, 0.1 PV), two saturation fronts exist. The front that has propagated farthest into the medium corresponds to unfoamed gas. For the 0.1 PV saturation profile, this first front is at roughly $r' = 0.7$. Little liquid is displaced by this front because gas mobility is high in the absence of foam. The trailing front is quite steep, sharp, and indicates efficient displacement. It arises because of foam generation and propagation. Behind these strong foam fronts, S_w is only about 5 saturation units above connate saturation. The velocity of both fronts slows as they move outward radially, as expected. Further, foam front propagation is slow because it can move only as quickly as surfactant propagates.

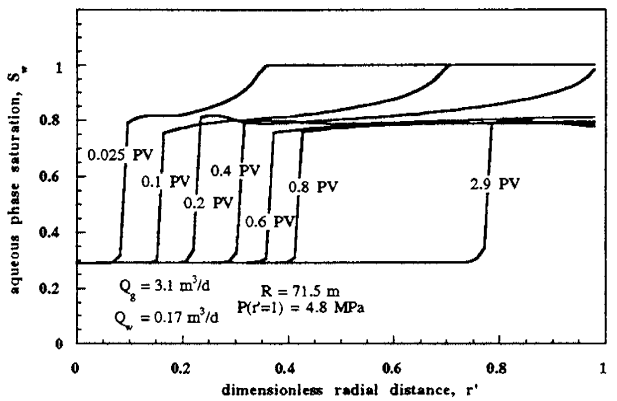

Fig. 12—Transient aqueous-phase saturation profiles for the radial flow of foam and surfactant.

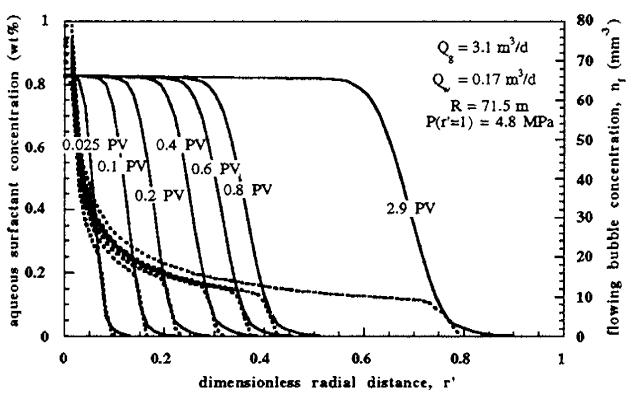

Fig. 13—Transient flowing-foam texture profiles superimposed upon surfactant concentration profiles for the radial flow of foam.

This point is better illustrated in Fig. 13 which presents the transient bubble concentration profiles superimposed over the surfactant concentration profiles. Foam texture is presented with a dashed line and bubble concentrations are located on the right y-axis. Surfactant concentration in weight percent is given with a solid line and values are found on the left y-axis. Foam texture is fine close to the injector, but texture falls off quickly as foam moves out radially and the gas and liquid velocities fall off as 1/r. Foam texture falls off

abruptly where the surfactant concentration falls to zero, because P^*_c falls to zero in the absence of surfactant and the foam coalescence rate approaches infinity. Ahead of the surfactant front, a continuous channel of unfoamed gas exists. It is interesting to compare the bubble profiles in Fig. 13 with the previous three cases, Figs. 3, 7, and 10. In the earlier examples, foam textures immediately behind the foam fronts are elevated above the steady-state value and above the textures found farther upstream. Since there was ample surfactant at the front due to presaturation, stable foam films were generated; since the capillary pressure at the front is relatively low, the foam coalescence rate is low. In the radial case shown in Fig. 13, there is no elevation in the foam texture immediately behind the foam front. Here, the foam coalescence rate is relatively high. The surfactant concentration decreases to zero across the foam front leading to low P^*_c at the front according to Eq. (4) and large foam coalescence rates according to Eq. (3).

Figure 14 shows the radial pressure profiles as a function of time on a semi-logarithmic scale. Pressure drop initially builds quickly in time as foam generates and fills the region around the injection well. The rate of pressure increase declines with time as the foam propagation rate slows in outward radial flow. Pressure gradients near the injection point are shallow just as they are for linear flow in Fig. 2. Because the radial grid is relatively coarse (72 grid blocks) compared to the radial distance spanned (*i.e.*, 72 m), the change in pressure gradient near r' equal to 0.02 is abrupt. Little foam is present in the first grid block making flow resistance small. Away from the inlet region, the pressure gradient declines as 1/r similar to a Newtonian fluid. Apparent Newtonian behavior is maintained because foam texture falls off as foam flows in the r-direction as shown in Fig. 13.

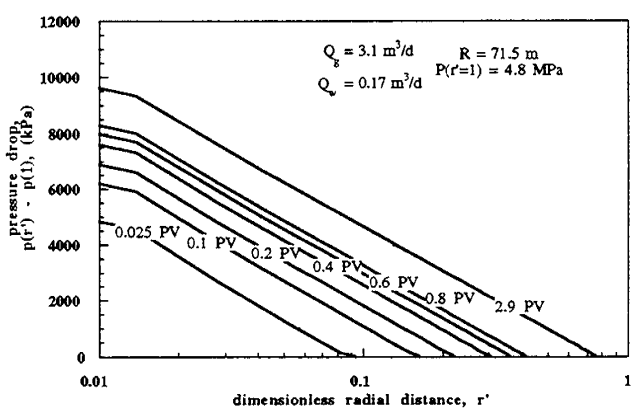

Fig. 14—Transient pressure profiles for the radial flow of foam and surfactant.

Tremendous pressure drops are predicted in Fig. 14, consistent with the foam-displacement parameters used to match our linear core floods (Fig. 2). These are incredibly strong foams reflecting the high limiting capillary pressures of AOS 1416 at concentrations around 1 wt% in the absence of oil. Practical field implementation of foam requires careful selection of the foaming agent and concentration (Patzek, 1996). Recall, that Figs. 6 and 11 predict that pressure drops should decrease in heterogeneous environments.

Patzek and Koinis (1990) reported mobility reduction factors (MRF = gas mobility / foam mobility) inferred from the Kern River steam-foam pilots, that decreased steadily

with increasing distance from the injection well (Patzek and Koinis, 1990). Figure 15 shows this same trend for our foam simulations. The predicted MRF decreases with increasing radial distance from the injector. Although the foam displacement simulated here is shear thinning at constant texture, we find that the MRF must decrease consonant with the decreasing foam textures of Fig. 13. In radial flow, the decrease of foam texture with increased distance has a greater effect on gas mobility than shear-thinning in Eq. (5). Again, high MRF is predicted because we employ parameters and initial conditions in the foam displacement simulator that give strong, efficient foams. In the steam-foam field tests, gas fractional flow was very high and gravity override was significant leading to dry foams that were very vulnerable to coalescence forces and hence much more coarse in texture. Additionally, heat losses that cause steam condensation, surfactant losses due to adsorption and precipitation, and foam coalescence due to the presence of oil were significant. All of these factors lessen the impact that foam has on gas mobility.

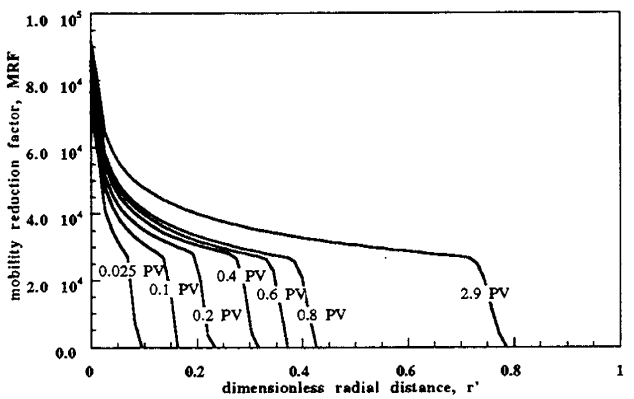

Fig. 15—Transient mobility reduction factors for the transient flow of foam and surfactant.

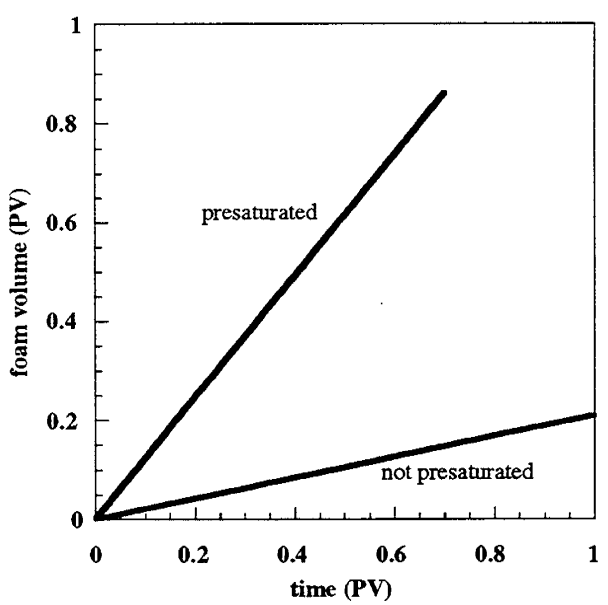

Fig. 16—Volume of foam in place versus total fluid injection (compare to Fig. 13 of Patzek and Koinis, 1990)

Another interesting comparison to the results reported by Patzek and Koinis (1990) is given in Fig. 16. Radial foam growth rate is displayed by plotting *in-situ* foam volume in PV as a function of the total cumulative fluid injection, relative the system backpressure of 4.8 MPa. Results garnered from the present case are presented as well as those from a radial simulation at identical injection rates and conditions except that the medium has been preflushed with surfactant. Both curves reveal that the PV of foam in place increases linearly with the total injected PV. Qualitatively, this trend agrees with that observed in steam-foam field studies where foam propagated in proportion to the injected PV of surfactant solution. The slope of the presaturated case demonstrates how efficient foam displacement might be in the absence of rock adsorption and foam-oil interaction under conditions of coinjection of gas and foamer solution.

3.6.5.5 5 Spot

The final case is simultaneous injection into one quarter of a confined 5-spot pattern. Hence, we simulate diverging/converging flow. The formation is assumed to be 20 m thick, the injector to producer spacing is 72 m, and the formation is not dipping. These dimensions correspond roughly to the conditions of the Mecca steam-foam pilot so that we may continue our qualitative, and superficial, comparisons to actual field results. The simulation assumes that the formation is homogeneous with a permeability of 1.3 μm^2, is initially filled with brine, and is bounded by impermeable layers. Injection occurs across the bottom 1/8 of the formation, while the producer is completed across the entire interval and is maintained at a pressure of 4.8 MPa. We will present saturation, bubble texture, and surfactant concentration in the vertical cross section between injector and producer. Grid spacing is 2 m in the horizontal direction and 1 m in the vertical direction.

To provide contrast with the highly efficient foam displacement to follow, we first ran simulations of unfoamed gas injection. Gas saturation contours in the vertical cross section are presented in Fig. 17 at 50, 100, 200 and 300d. The gray-scale shading indicates the gas saturation. Unshaded portions of the graph refer to an S_g of zero, and progressively darker shading corresponds to larger S_g. Without foam, areas contacted by gas are poorly swept. Buoyancy quickly drives injected gas to the top of the formation, a gas tongue forms, and gas breakthrough at the producer occurs quite rapidly. After breakthrough, little desaturation occurs because pressure gradients are low and buoyancy prevents gas from contacting areas along the lower horizontal boundary. This is classical gravity override.

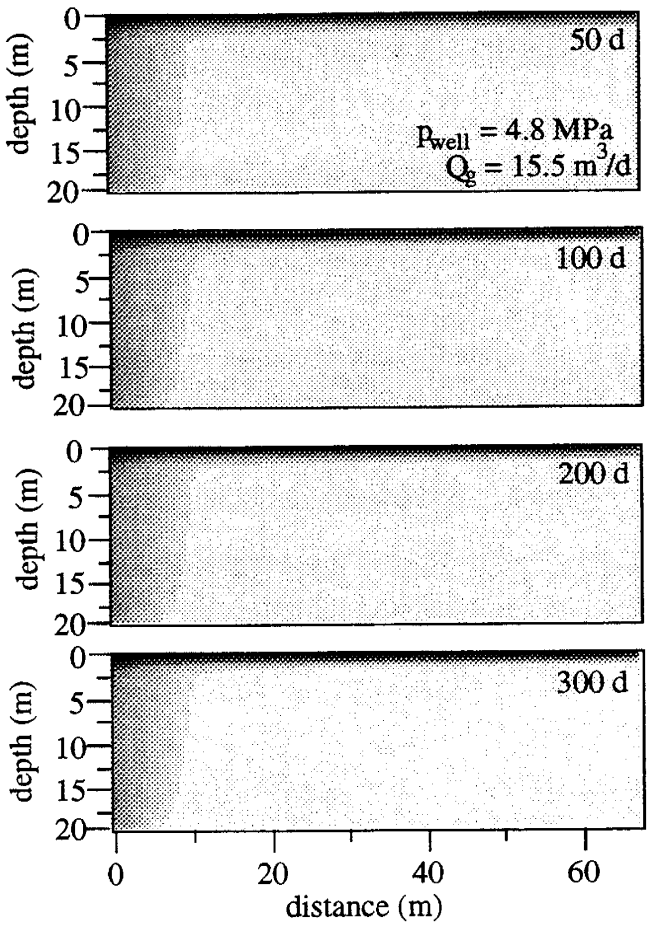

Fig. 17—Gas saturation profiles for unfoamed gas injection into a confined 5 spot.

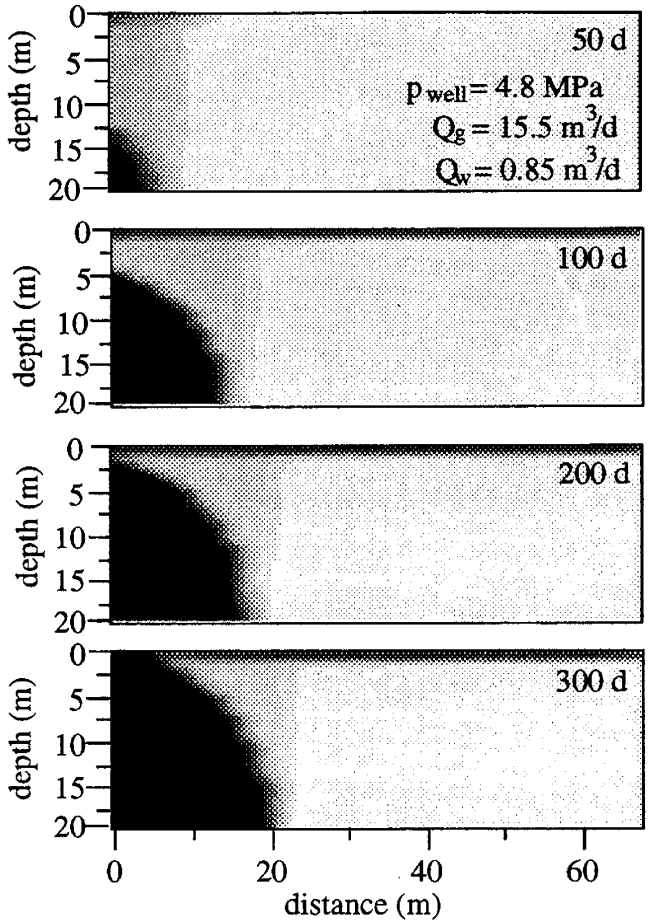

Fig. 18—Gas saturation profiles for the simultaneous injection of gas and foamer solution into a confined 5 spot.

With simultaneous injection of N_2 and 0.83 wt% foamer solution, foam generates where surfactant and gas are present, and the results are dramatically different. Figures 18, 19, and 20 present S_g, n_f, and C_s, respectively, in the vertical cross section at times of 50, 100, 200, and 300 days. The gas fractional flow is identical to the radial case, 0.95. Injection rates for N_2 and aqueous solution are 15.5 and 0.85 m^3/d, respectively. In Fig. 18, the gas saturation contours indicate that both a strong displacement by foam is occurring and a weak displacement by the unfoamed gas ahead of the foam front in a fashion similar to the radial displacement in Fig. 12. Near the injector, the high gas saturation region associated with the foamed gas assumes a semi-spherical shape. The contours at later times in Fig. 18 illustrate that spherical growth and efficient displacement continue. The darkly shaded region immediately below the upper impermeable boundary indicates a tongue of unfoamed gas that forms due to gravity override. Although not depicted, areal sweep is also good where foam is present.

Figure 19 illustrates foam texture as a function of time. The foamed regions correspond exactly with zones of high gas saturation. The bubble textures associated with black shading are 100 mm^{-3}, and the light-gray shading at the foam front is roughly 20 mm^{-3}. Interestingly, and in agreement with Fig. 13, the most finely textured foams are found adjacent to the well bore where gas and liquid flow velocities are largest.

The most provocative result of this simulation is found in Fig. 20: surfactant is actually lifted in the formation above its injection point. Black shading indicates a concentration of 0.83 wt%. Foamed gas effectively desaturates the zone around the injector. Although the aqueous-phase relative permeability function is unchanged in the presence of foam, the low S_w results in low relative permeability and highly resistive flow for the aqueous phase. The flow of surfactant-laden water is rerouted and surfactant is pushed upward in the formation. In this example, gravity override has been effectively negated.

When foam reaches the upper boundary of the layer, displacement continues from left to right in the horizontal direction in a piston-like fashion that expels the resident liquid phase. Propagation is slow until the flow begins to converse.

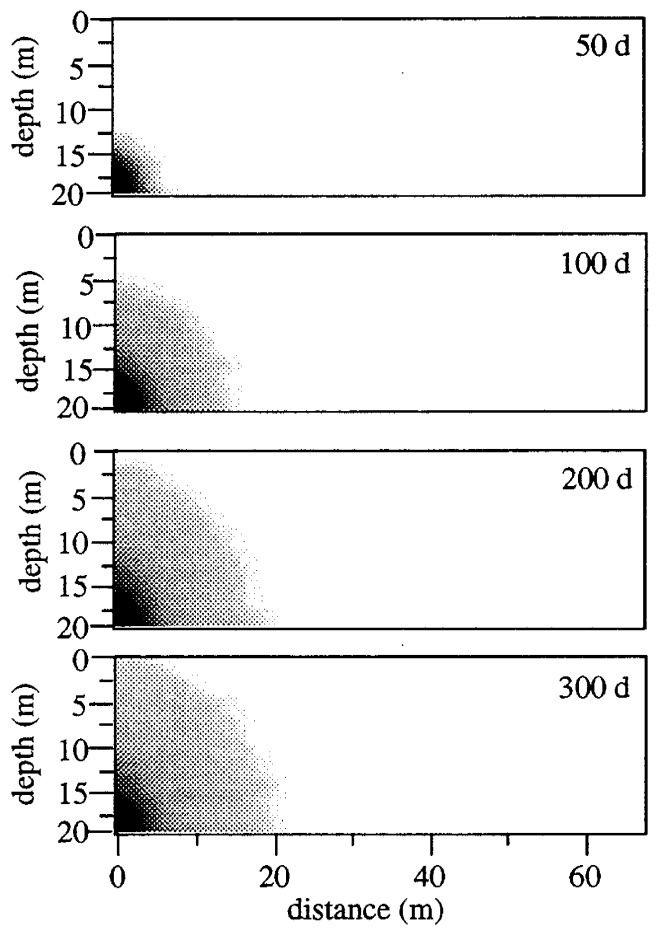

Fig. 19—Foam texture profiles for the simultaneous injection of gas and foamer solution into a confined 5 spot.

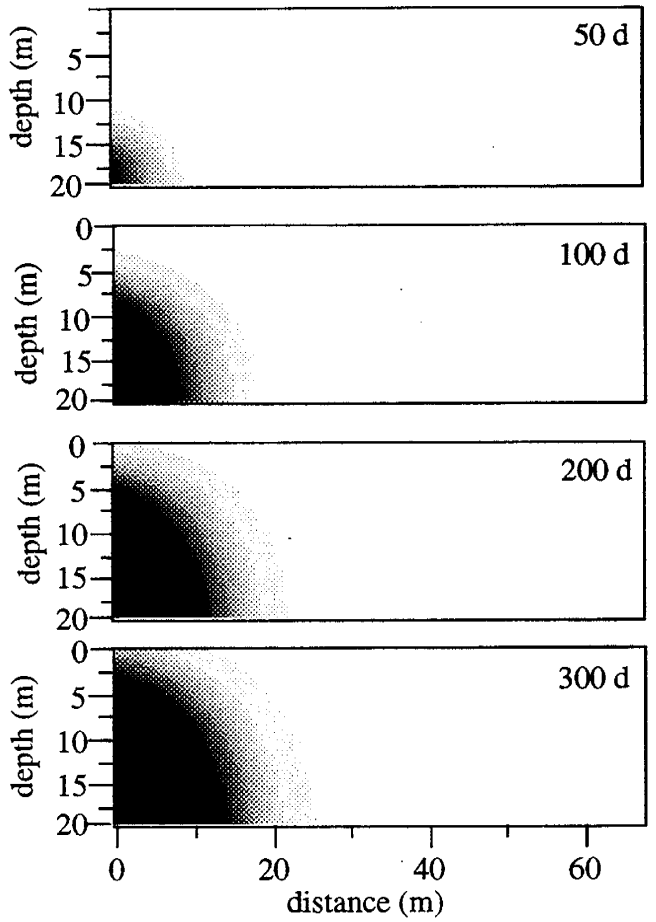

Fig. 20—Surfactant concentration profiles for the simultaneous injection of gas and foamer solution into a confined 5 spot.

3.6.6 DISCUSSION

Recently, Rossen and coworkers (Rossen *et al.*, 1991; Zhou and Rossen, 1992) presented a fractional flow theory for foam displacement in porous media. Their approach is notable since they consider gas diversion by foam among layers of differing permeability. Beginning with the steady-state experimental observations that aqueous-phase relative permeability is unchanged from the foam-free case (Bernard et al., 1965; Holm, 1968; Sanchez et al., 1986; Huh and Handy, 1989; DeVries and Wit, 1990; Friedmann and Jensen, 1986) and that aqueous-phase saturation is virtually constant (Ettinger and Radke, 1992; Persoff *et al.*, 1991), they used Darcy's law as illustrated by Khatib *et al.* (1988) and Persoff *et al.* (1991) to obtain a fractional flow theory for gas mobility in the presence of foam. This method does not explicitly account for the role that foam texture plays in reducing gas mobility. Additionally, the method is not readily applied to two- and three-dimensional flow. It does address, however, radial flow, diversion among isolated layers of differing permeability, and layers in capillary equilibrium.

Our simulations of layered porous media presaturated with surfactant solution reveal that significant flow diversion and production from low permeability layers occurs regardless of whether the layers communicate or not. For practical applications, the extent

of diversion into low permeability layers predicted by our population balance model is quite different than the prediction of the fractional flow theory of Rossen *et al.*, 1991; Zhou and Rossen; 1992). Because the fractional-flow model sets the capillary pressure in each layer equal to P^*_c at all times, it predicts strong foams in the low permeability layer and diversion into the high permeability layer. This asymptotic behavior is seen in Fig 10b as finely textured foam evolves in the low permeability layer because of the low coalescence rate at high water saturation and low P_C there. However, this behavior occurs only after more than 1 PV of foam has been injected, an occurrence unlikely to happen in the field. We should caution here that the foam textures predicted after many pore volumes of injection in Fig. 10b are exceptionally fine. When bubbles become so closely spaced, we expect foam generation by snap-off to cease as the close spacing of the bubbles prevents sufficient liquid accumulation for snap-off (Falls *et al.*, 1988)

For radial flow, our population balance method predicts that foam texture and, consequently, MRF falls with increasing distance from the injection well in both steady and unsteady flow consistent with field observations of gas mobility (Patzek and Koinis, 1990). The fractional flow model for foam, though, predicts that MRF is independent of radial distance. In the fractional flow model, all of the effects of foam on gas mobility are inferred from the wetting liquid mobility which is nearly constant for foam flow at the limiting capillary pressure. Since we explicitly account for the coarsening of foam texture as foam flows radially and the effect that texture has on gas mobility, we are able to obtain trends qualitatively similar to those observed in the field.

The case of simultaneous foamer and gas injection into a 5-spot geometry also permits some comparison with field trends. Firstly, we are able to simulate the propagation of foam far into the reservoir and improved vertical sweep (Patzek and Koinis, 1990; Mohammadi *et al.*, 1989). Secondly, there is some evidence for spherical growth of the foam zone, such as that shown in Fig. 19, in the Kern River steam-foam pilots[1]. We predict a constant growth rate of the foam zone, just as was found in the field. Likewise, temperature observations collected at the pilots indicate foam zones with roughly spherical shape.

The calculations presented in this paper represent only a small fraction of the interesting cases possible. Since we specified that all porous media were initially free of oil, we discovered the effect that foam might have if strong foam generation occurred *in situ*. We have not included coalescence terms for the interaction of foam with oil. Although our simulator is fully capable of modeling steam injection, we have not simulated such cases. Additionally, there is speculation of a minimum pressure gradient required to propagate foams under field conditions (Friedmann *et al.*, 1994; Rossen, 1990; Rossen, 1990; Rossen, 1990; Rossen and Gauglitz, 1990). We have not simulated foam including such a mobilization pressure gradient.

Only the effects of strong foam were simulated here. By simulating a surfactant system with a smaller P^*_c it is possible to simulate weak foams that can display even more interesting diversion behavior. For example, if P^*_c is less than the capillary entry pressure of a porous medium, foam will not form (Khatib *et al.*, 1988) Hence, stable foam may be generated in high permeability layers where the capillary entry pressure is slightly lower than P^*_c but not at all in low permeability layers. Flow resistance in the high-permeability layer will thus be significant and will divert substantial gas flow into the foam-free low-permeability layer. Further, gravitational effects and the interplay with heterogeneity should be considered more closely. Gravity might cause the top of a reservoir to be so dry that only very weak foams subject to rapid coalescence can form or the rock may be so dry

that no foam formation is possible. Finally, we need to simulate steam foams for which condensation is important.

Hence, we caution that the results shown here are not general. Foam displacement in porous media depends strongly on bubble texture which is influenced through the limiting capillary pressure by foamer formulation including the type of surfactant, surfactant concentration, the concentration and type of ions in solution, as well as the temperature. In all cases presented here, displacements begin with the formation full of water. High water saturation and low capillary pressure are conducive to foam formation. Different initial and injection conditions might change the effectiveness of foam as a displacement agent. Likewise, our knowledge of foam trapping is not sufficient to predict whether trapping occurs to the same degree, and in the same fashion, in high and low permeability rocks, even if geometrically similar.

3.6.7 SUMMARY

We have shown that it is practical to model foam displacement mechanistically in multidimensions. Beginning with an n-component compositional simulator, the bubble population balance equations are successfully incorporated within the simulator's fully implicit framework. The mechanistic population balance approach allows us to insert the physics of foam displacement directly into a reservoir simulator. Foam is treated as a nonchemical "component" of the gas phase and the evolution of foam texture is modeled explicitly through pore-level foam generation and coalescence equations. As foam mechanisms become better understood, this framework allows for their inclusion.

For both noncommunicating and communicating linear heterogeneous layers, foamed gas efficiently diverts to low permeability layers when the layers are initially saturated with surfactant solution in the absence of gravity. For communicating layers, the foam propagation rate is equal in both layers. In this instance, foam dramatically evens out injection profiles.

For one-dimensional radial flow, we find that foam pressure drop scales as 1/r similar to a Newtonian fluid. The gas mobility reduction factor for radial foam flow falls off as foam moves outward radially from the injector because the foam coarsens. This decline in mobility reduction factor in radial flow is consistent with previous field observations of steam-foam propagation (Patzek and Koinis, 1990).

For simultaneous injection of gas and foamer solution into a confined 5-spot pattern, we clearly see two displacement fronts. Unfoamed gas moves upward through the formation due to buoyancy and is ineffective in displacement. The second front tracks with surfactant propagation and the generation of foam. The strong foam desaturation front takes a semi-spherical shape for short times with the origin of the sphere at the injector. Importantly, it is found that gravity override can be effectively negated.

These predictions are a result of the direct approach taken to model foam displacement. Since gas mobility in the presence of foam depends strongly on foam texture, it is necessary to account for foam-bubble evolution to model gas mobility generally and correctly.

3.6.8 NOMENCLATURE

C= concentration
$\vec{F}$ = component vector flux,
k= rate constant
K= permeability
L= length of linear porous medium
MRF = mobility reduction factor
n= number density of foam
p= pressure
P_C= capillary pressure
PV= pore volume (injected or in place)
q= generation rate and source/sink term
r= radial distance
R= radial extent of porous medium
S= phase saturation
t= time
u= Darcy velocity
v= interstitial velocity

Greek Letters

a= proportionality constant for foam effective visosity
$\nabla \bullet$ = divergence operator
j= porosity
μ = viscosity
G = absorption or partition coefficient

Subscripts

1= generation rate constant
-1= coalescence rate constant
f= flowing foam
g= gas phase
i= phase (*i.e.*, aqueous, gas, or oil)
j= chemical species
s= surfactant
t= stationary foam
w= water or wetting phase
wc= connate water saturation
well= denotes well radius

Superscripts

o= denotes reference value
*= value correponds to the limiting capillary pressure
'= denotes normalized radial distance

3.6.9 REFERENCES

1. Aare, M.G. and A. Skauge: "A Foam Pilot Test Aimed at Reducing Gas Inflow in a Production Well at the Oseberg Field.," in Proceedings of the 8th European IOR Symposium, Vienna, Austria (May 1995).

2. Adenekan, A.E., T.W. Patzek, and K. Pruess: "Modeling of Multiphase Transport of Multicomponent Organic Contaminants and Heat in the Subsurface: Numerical Model Formulation," *Water Resources Research*, **29**(11) (1993) 3727-3740.

3. Aronson, A.S., V. Bergeron, M.E. Fagan, and C.J. Radke: "The Influence of Disjoining Pressure on Foam Stability and Flow in Porous Media," *Colloids and Surfaces A: Physicochemical Eng. Aspects*, **83**(1994) 109-120.

4. Bernard, G.G., L.W. Holm, and L.W. Jacobs: "Effect of Foam on Trapped Gas Saturation and on Permeability of Porous Media to Gas," *SPEJ*, **5**(4) (1965) 295-300.

5. Bretherton, F.P.: "The Motion of Long Bubbles in Tubes," *J. Fluid Mech.*, **10**(1961) 166-188.

6. Chambers, K.T. and C.J. Radke: "Capillary Phenomena in Foam Flow Through Porous Media", in *Interfacial Phenomena in Petroleum Recovery*, N.R. Morrow, Editor. , Marcel Dekker Inc., New York, (1991) p. 191-255.

7. Chang, S.H., L.A. Owusu, S.B. French, and F.S. Kovarik: "The Effect of Microscopic Heterogeneity on CO2-Foam Mobility:Part 2--Mechanistic Foam Simulation," SPE/DOE 20191, in Proceedings of the SPE/DOE 7th Symposium on Enhanced Oil Recovery, Tulsa, Oklahoma (April, 1990).

8. Chou, S.I.: "Percolation Theory of Foam in Porous Media," SPE/DOE 20239, in Proceedings of the 7th SPE/DOE Symposium on Enhanced Oil Recovery, Tulsa, OK (April, 1990).

9. DeVries, A.S. and K. Wit: "Rheology of Gas/Water Foam in the Quality Range Relevant to Steam Foam," *Soc. Pet. Eng. Res. Eng.*, **5**(2) (1990) 185-192.

10. Djabbarah, N.F., S.L. Weber, and D.C. Freeman: "Laboratory Design and Field Demonstration of Steam Diversion with Foam," SPE 20067, in Proceedings of the 60th California Regional Meeting, Ventura, CA (April 1990).

11. Ettinger, R.A.: "Foam Flow Resistance in Berea Sandstone," MS. Thesis , University of California, Berkeley (1989).

12. Ettinger, R.A. and C.J. Radke: "Influence of Foam Texture on Steady Foam Flow in Berea Sandstone,"*SPERE*, **7**(1) (1992) 83-90.

13. Falls, A.H., G.J. Hirasaki, T.W. Patzek, P.A. Gauglitz, D.D. Miller, and T. Ratulowski: "Development of A Mechanistic Foam Simulator: The Population Balance and Generation By Snap-Off," *SPERE*, **3**(3) (1988) 884-892.

14. Falls, A.H., J.J. Musters, and J. Ratulowski: "The Apparent Viscosity of Foams in Homogeneous Beadpacks," *SPERE.*, **4**(2) (1989) 155-164.

15. Fergui, A., M. Quintard, H. Bertin, and D. Defives: "Transient Foam Flow in Porous Media: Experiments and Simulation," Proceedings of the 8th European IOR Symposium, Vienna Austria (May 1995).

16. Fisher, A.W., R.W.S. Foulser, and S.G. Goodyear: "Mathematical Modeling of Foam Flooding," SPE/DOE 20195, in Proceedings of the 7th SPE/DOE Symposium on Enhanced Oil Recovery, Tulsa, OK (April 1990).

17. Friedmann, F., W.H. Chen, and P.A. Gauglitz: "Experimental and Simulation Study of High-Temperature Foam Displacement in Porous Media," *SPERE*, **6**(1) (1991) 37-45.

18. Friedmann, F. and J.A. Jensen: "Some Parameters Influencing the Formation and Propagation of Foams in Porous Media," SPE 15087, in Proceedings of the SPE California Regional Meeting, Oakland, CA (April, 1986).

19. Friedmann, F., M.E. Smith, W.R. Guice, J.M. Gump, and D.G. Nelson: "Steam-Foam Mechanistic Field Trial in the Midway-Sunset Field," *SPERE*, **9**(4) (1994) 297-304.

20. Gillis, J.V. and C.J. Radke: "A Dual-Gas Tracer Technique for Determining Trapped Gas Saturation During Steady Foam Flow in Porous Media," SPE 20519, in Proceedings of the 65th SPE Annual Technical Conference, New Orleans, LA (September, 1990).

21. Hirasaki, G.J. and J.B. Lawson: "Mechanisms of Foam Flow in Porous Media: Apparent Viscosity in Smooth Capillaries," *SPEJ*, **25**(2) (1985) 176-190.

22. Holm, L.W.: "The Mechanism of Gas and Liquid Flow Through Porous Media in the Presence of Foam," *Soc. Pet. Eng. J.*, **8**(4) (1968) 359-369.

23. Huh, D.G. and L.L. Handy: "Comparison of Steady- and Unsteady-State Flow of Gas and Foaming Solution in Porous Media," *Soc. Pet. Eng. Res. Eng.*, **4**(1) (1989) 77-84.

24. International Formulation Committee, I.F.: "A Formulation of the Thermodynamic Properties of Ordinary Water Substance," report, Düsseldorf, Germany (1967).

25. Jiménez, A.I. and C.J. Radke: "Dynamic Stability of Foam Lamellae Flowing Through a Periodically Constricted Pore", in *Oil-Field Chemistry: Enhanced Recovery and Production Stimulation*, J.K. Borchardt and T.F. Yen, Editors. , American Chemical Society, Washington, D.C., (1989) p. 460-479.

26. Khatib, Z.I., G.J. Hirasaki, and A.H. Falls: "Effects of Capillary Pressure on Coalescence and Phase Mobilities in Foams Flowing Through Porous Media," *SPERE*, **3**(3) (1988) 919-926.

27. Kovscek, A.R., T.W. Patzek, and C.J. Radke: "A Mechanistic Population Balance Model For Transient and Steady-State Foam Flow in Boise Sandstone," *Chem. Eng. Science*, **50**(23) (1995) 3783-3799.

28. Kovscek, A.R., T.W. Patzek, and C.J. Radke: "Simulation of Foam Transport in Porous Media," SPE 26402, in Proceedings of the the 68th Annual Technical Conference of SPE, Houston, TX (October 1993).

29. Kovscek, A.R. and C.J. Radke: "Fundamentals of Foam Transport in Porous Media", in *Foams in the Petroleum Industry*, L.L. Schramm, Editor., American Chemical Society, Washington, D.C., (1994) p. 115-163.

30. Kovscek, A.R. and C.J. Radke: "Gas Bubble Snap-Off Under Pressure Driven Flow in Constricted Noncircular Capillaries," *Colloids and Surfaces A: Physicochemical and Engineering Aspects*, **117**(1996) 55-76.

31. Leverett, M.C.: "Capillary Behavior in Porous Solids," *Trans., AIME*, **142**(1941) 152-169.

32. Liu, D. and W.E. Brigham: "Transient Foam Flow in Porous Media With the Cat Scanner," . , U.S. D.O.E. (March, 1992).

33. Marfoe, C.H. and H. Kazemi: "Numerical Simulation of Foam Flow in Porous Media," SPE 16709, in Proceedings of the 62nd SPE Annual Meeting, Dallas, TX (September, 1987).

34. Mahmood, S.M., S.M. Tariq, and W.E. Brigham: "A Model for Prediction of Recovery and Pressure History for 2-D Displacement of Oil Through Porous Media by Gas/Surfactant," SPE 15076, in Proceedings of the the SPE California Regional Meeting, Oakland, CA (April 1986).

35. Mohammadi, S.S. and D.A. Coombe: "Characteristics of Steam/Foam Drive Process in Massive Multi-Zone and Thin Single Zone Reservoirs," SPE 24030, in Proceedings of the SPE California Regional Meeting, Bakersfield, CA (April 1992).

36. Mohammadi, S.S., D.A. Coombe, and V.M. Stevenson: "Test of Steam-Foam Process for Mobility Control in S. Casper Creek Reservior," *J. Can. Pet. Tech.*, **32**(10) (1993) 49-54.

37. Mohammadi, S.S., D.C. Van Slyke, and B.L. Ganong: "Steam-Foam Pilot Project in Dome-Tumbador, Midway-Sunset Field," *SPERE*, **4**(1) (1989) 7-16.

38. Narasimhan, T.N. and P.A. Witherspoon: "An Integrated Finite Difference Method for Analyzing Fluid Flow in Porous Media," *Water Resources Research*, **12**(1) (1976) 57-64.

39. Patzek, T.W.: "Description of Foam Flow in Porous Media by the Population Balance Approach", in *Surfactant-Based Mobility Control: Progress in Miscible-Flood Enhanced Oil Recovery*, D.H. Smith, Editor. , American Chemical Society, Washington, D. C., (1988) p. 326-341.

40. Patzek, T.W.: "Field Application of Steam Foam for Mobility Improvement and Profile Control," *SPERE* **May**(1996) 79-85.

41. Patzek, T.W. and M.T. Koinis: "Kern River Steam-Foam Pilots," *JPT*, **42**(4) (1990) 496-503.

42. Patzek, T.W. and N.A. Myhill: "Simulation of the Bishop Steam Foam Pilot," SPE 18786, in Proceedings of the SPE California Regional Meeting, Bakersfield, CA (April 1989).

43. Persoff, P., C.J. Radke, K. Pruess, S.M. Benson, and P.A. Witherspoon: "A Laboratory Investigation of Foam Flow in Porous Media at Elevated Pressure," *SPERE*, **6**(3) (1991) 365-371.

44. Pruess, K.: "TOUGH Users's Guide," Rep NUREG/CR-4 645 , Nucl. Reg. Commision, Washington D.C. (1987) .

45. Pruess, K.: "TOUGH2--A general-purpose simulator for multiphase fluid and heat flow," Rep. LBL-29400 , Lawrence Berkeley Lab. (September 1991).

46. Rossen, W.R.: "Theory of Mobilization Pressure Gradient of Flowing Foams in Porous Media: I. Incompressible Foam," *J. Coll. Interface. Sci.*, **136**(1) (1990) 1-16.

47. Rossen, W.R.: "Theory of Mobilization Pressure Gradient of Flowing Foams in Porous Media: II. Asymmetric Lamella Shapes," *J. Coll. Interface. Sci.*, **136**(1) (1990) 38-53.

48. Rossen, W.R.: "Theory of Mobilization Pressure Gradient of Flowing Foams in Porous Media: II. Effect of Compressibility," *J. Coll. Interface. Sci*, **136**(1) (1990) 17-37.

49. Rossen, W.R. and P.A. Gauglitz: "Percolation Theory and Mobilization of Foams in Porous Media," *Am. Inst. Chem. Eng. J.*, **37**(8) (1990) 1176-1188.

50. Rossen, W.R., Z.H. Zhou, and C.K. Mamum: "Modeling Foam Mobility in Porous Media," SPE 22627, in Proceedings of the 66th SPE Annual Technical Conference, Dallas, TX (October 1991).

51. Sanchez, J.M., R.S. Schechter, and A. Monsalve: "The Effect of Trace Quantities of Surfactant on Nitrogen/Water Relative Permeabilities," SPE 15446, in Proceedings of the 61st SPE Annual Technical Conference, New Orleans, LA (October, 1986).

52. Stone, H.L.: "Probability Model for Estimating Three-Phase Relative Permeability," *J. Pet. Tech.*, **22** (2) (1970) 214-218.

53. Svorstøl, I., F. Vassenden, and K. Mannhardt: "Laboratory Studies for Design of a Foam Pilot in the Snorre Field," SPE 35400, in Proceedings of the SPE/DOE 10th Symposium on Improved Oil Recovery, Tulsa, OK (1996).

54. Wong, H., C.J. Radke, and S. Morris: "The Motion of Long Bubbles in Polygonal Capillaries: I. Thin Films," *J. Fluid Mech.*, **292** (1995) 71-95.

55. Wong, H., C.J. Radke, and S. Morris: "The Motion of Long Bubbles in Polygonal Capillaries: II. Drag, Fluid Pressure, and Fluid Flow," *J. Fluid Mech.*, **292**(1995) 95-110.

56. Zhou, Z. and W.R. Rossen: "Applying Fractional Flow Theory to Foam Processes at the Limiting Capillary Pressure," SPE/DOE 24180, in Proceedings of the SPE/DOE 8th Symposium on Enhanced Oil Recovery, Tulsa, OK (April 1992).

PROJECT 4: RESERVOIR DEFINITION

To develop and improve techniques of formation evaluation such as tracer tests and pressure transient tests.

4.1 USING STREAMLINES AND INVERSE APPROACHES FOR EFFICIENT TRACER FLOW INTERPRETATION

(Y. Wang)

4.1.1 INTRODUCTION

Sufficient information about reservoir rock properties, such as permeability and heterogeneity, is essential for predicting reservoir performance. Tracer flow evaluation is a useful tool to obtain this information.

Methods for analyzing tracer flow include initial qualitative studies and quantitative analyses. The latter can further be subdivided into two categories: analytical solutions and numerical solutions.

It is obvious that analytical solutions can be obtained only for very simple cases, both simple and regular geometries and uniform reservoir properties. Therefore the analytical solutions are very limited in practical use.

The traditional approach to analyzing field tracer data generally involves a history-matching procedure that is time consuming and frequently results in a non-unique solution (Gupta *et al.,* 1994). Also, the conventional modes of simulation apply finite difference methods and, as described below, are much slower than the streamline methods which will be employed in this study.

From what is discussed above, it is important that we seek a way that will predict tracer flow data accurately. For complex cases, using tracer flow data to infer reservoir properties can be very time consuming, and therefore a rapid calculation method is desired, and sometimes required.

Therefore, the objective of this study is to apply a streamline method and a stochastic inverse approach to infer reservoir properties. The uncertainty in the interpretation of the tracer flow data will also be studied.

4.1.2 LITERATURE SURVEY

Well-to-well tracer flow has been mainly used to infer the reservoir properties, especially permeability and heterogeneity. Applications include identifying high permeability channels which may strongly affect sweep efficiency in oil recovery. Useful synopses of progress in tracer flow interpretation are provided by Abbaszadeh-Dehghani and Brigham (1982) and Datta-Gupta *et al.* (1994).

At the beginning of tracer flow studies, inference of reservoir properties was made by qualitatively analyzing tracer breakthrough data. Later, analytical solutions to the differential equations, which describe the tracer flow, were applied to simple cases with regular geometry and uniform permeability. This approach, though quantitative, is limited in its applications.

In the last two decades, engineers have resorted to numerical approaches to tracer flow studies. At the beginning, constrained by the capability of computer memory and computational speed, this method was still limited to quite simple cases. The rapid development of computer technology gave rise to relatively fast and accurate reservoir

simulation, and numerical solutions to tracer flow in complicated cases is no longer so serious a problem. This approach rapidly maps the tracer flow given the rock properties of the reservoir. However, to infer the properties of the reservoir using tracer flow, the inverse problem is not as fast or straightforward, and still needs much research.

4.1.2.1. The Streamline Method

A fast way to interpret tracer flow data is required in complicated cases. Usually, we infer the properties of a reservoir in the following way. Given some initial values of those properties based on other information such as geostatistics, solve the flow field. Then compare the calculated history with observed tracer flow data, and modify the values. Repeat this process until it yields a good match to the field data.

Therefore, we need a good way to solve the flow field. Thiele *et al.* (1996) successfully applied the streamline method to simulation of water-flooding. The streamline approach allows us to decouple the physics describing the displacement from the size of the grid used to model the reservoir geology. Consequently, this method is much faster and more accurate than the conventional finite difference methods. When mapping approximate analytical solutions along streamlines, the streamline method uses two to five orders of magnitude less computation time than conventional simulation. When mapping numerical solutions, this method gives a more accurate result than that by conventional methods (i.e., less numerical dispersion), and is still up to 600 times faster (Thiele *et al.*, 1996).

Figures 1-4 illustrate typical results with the streamline method. The figures present water saturation distributions as a function of time for water injection into one quarter of a 5-spot pattern. The grayscale shading indicates water saturation. Black shading corresponds to an aqueous phase saturation of 1, whereas white corresponds to connate water saturation. The dark solid lines are streamlines. Water is injected in the lower left corner of each panel and production occurs from the upper right corner. The effect of increasing the oil to water viscosity ratio is given in Figs. 1 to 3 for ratios of 1:1, 10:1, and 40:1, respectively. As the oil to viscosity ratio increases the time for water breakthrough at the production well decreases. In Fig. 1, injected water reaches the production well between 0.58 and 0.87 PV of injection. For the 10:1 oil to water viscosity ratio summarized in in Fig. 2 breakthrough occurs between 0.29 PV and 0.58 PV. For the largest oil to water ratio, water breaks through in less than 0.29 PV.

In the current implementation of the streamline method both analytical and numerical solutions can be mapped along streamlines. The advantage of the numerical solution is the ability to handle complex initial and time-varying boundary conditions. Figures 3 and 4 contrast the difference between numerical and analytical solutions for a 40:1 oil to water viscosity ratio. Figure 4, where analytical solutions are mapped, displays no numerical dispersion compared to Fig. 3; however, the saturation maps are only approximate. The pressure field evolves substantially during injection, because of the difference in phase viscosities. Hence, the streamlines evolve also. It is difficult to interpolate results from an old streamline onto an updated streamline. Instead of mapping solutions from the last time step onto updated streamlines, the analytical solution is mapped from time zero along the updated streamline. Refer to Thiele *et al.* (1996) and Batycky *et al.* (1996) for more detail.

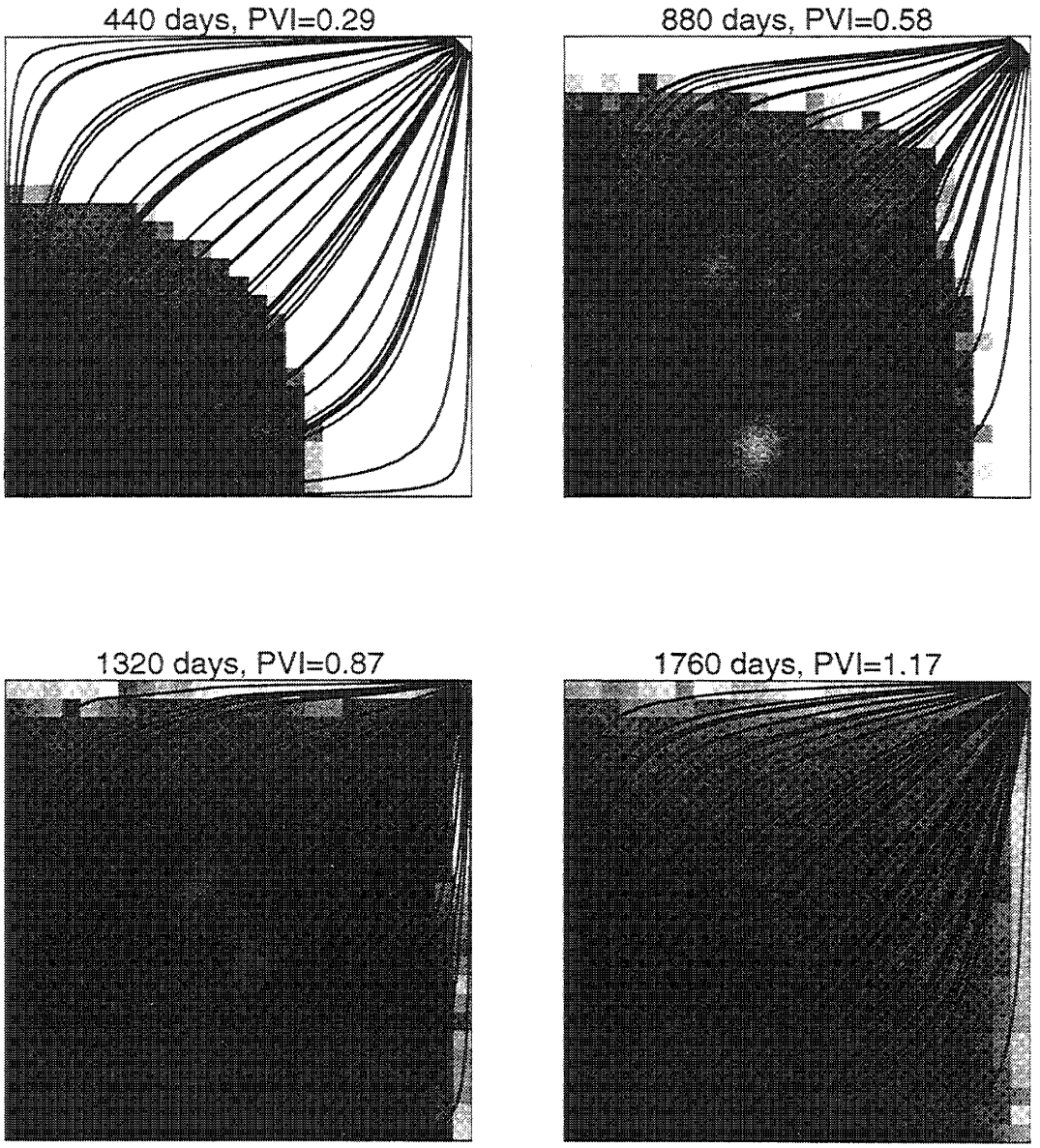

Figure 1 Water flooding--one quarter of five-spot pattern

Mapping numerical solutions
Viscosity: water 1cp, oil 1cp

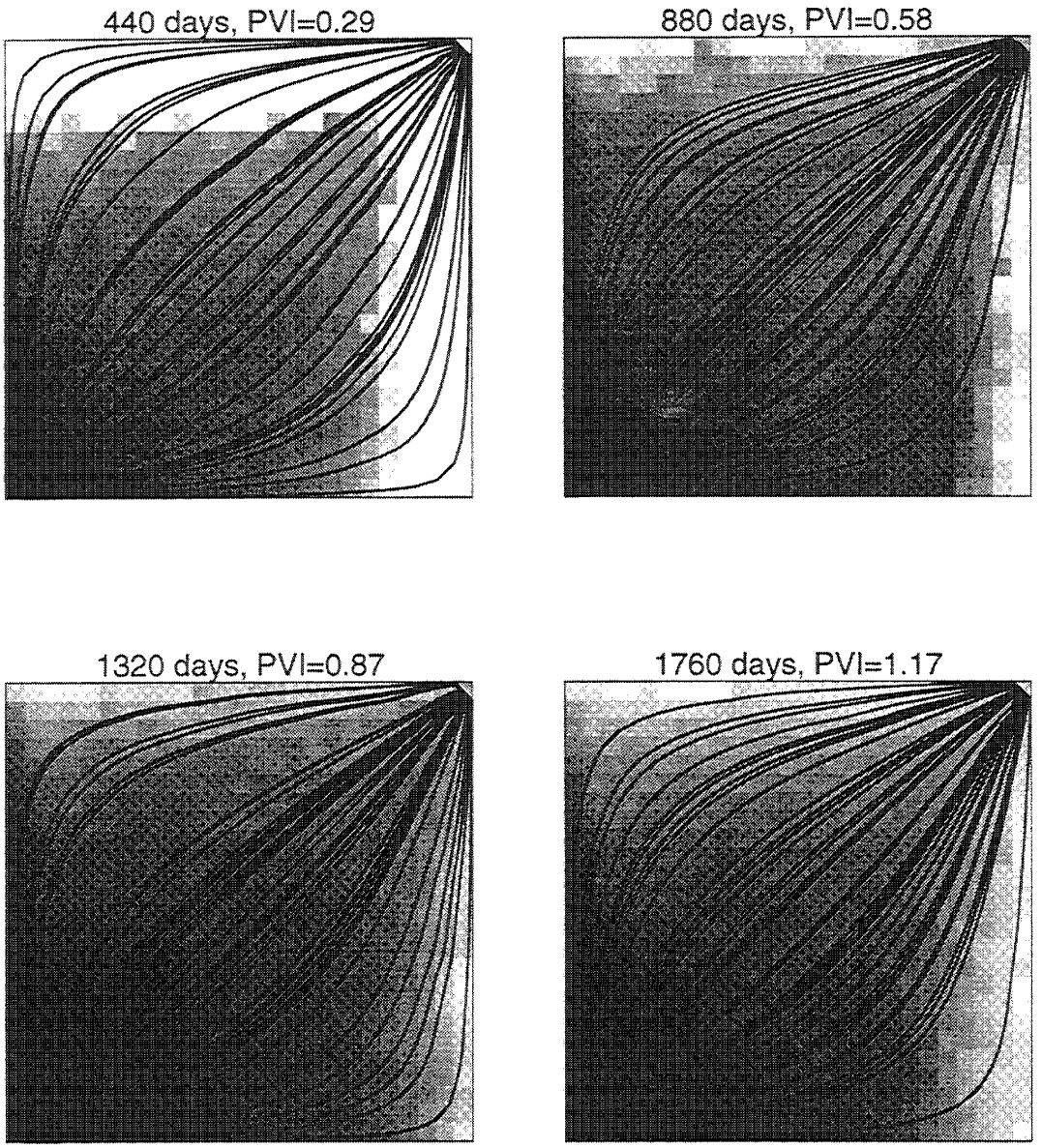

Figure 2 Water flooding--one quarter of five-spot pattern

Mapping numerical solutions
Viscosity: water 1cp, oil 10cp

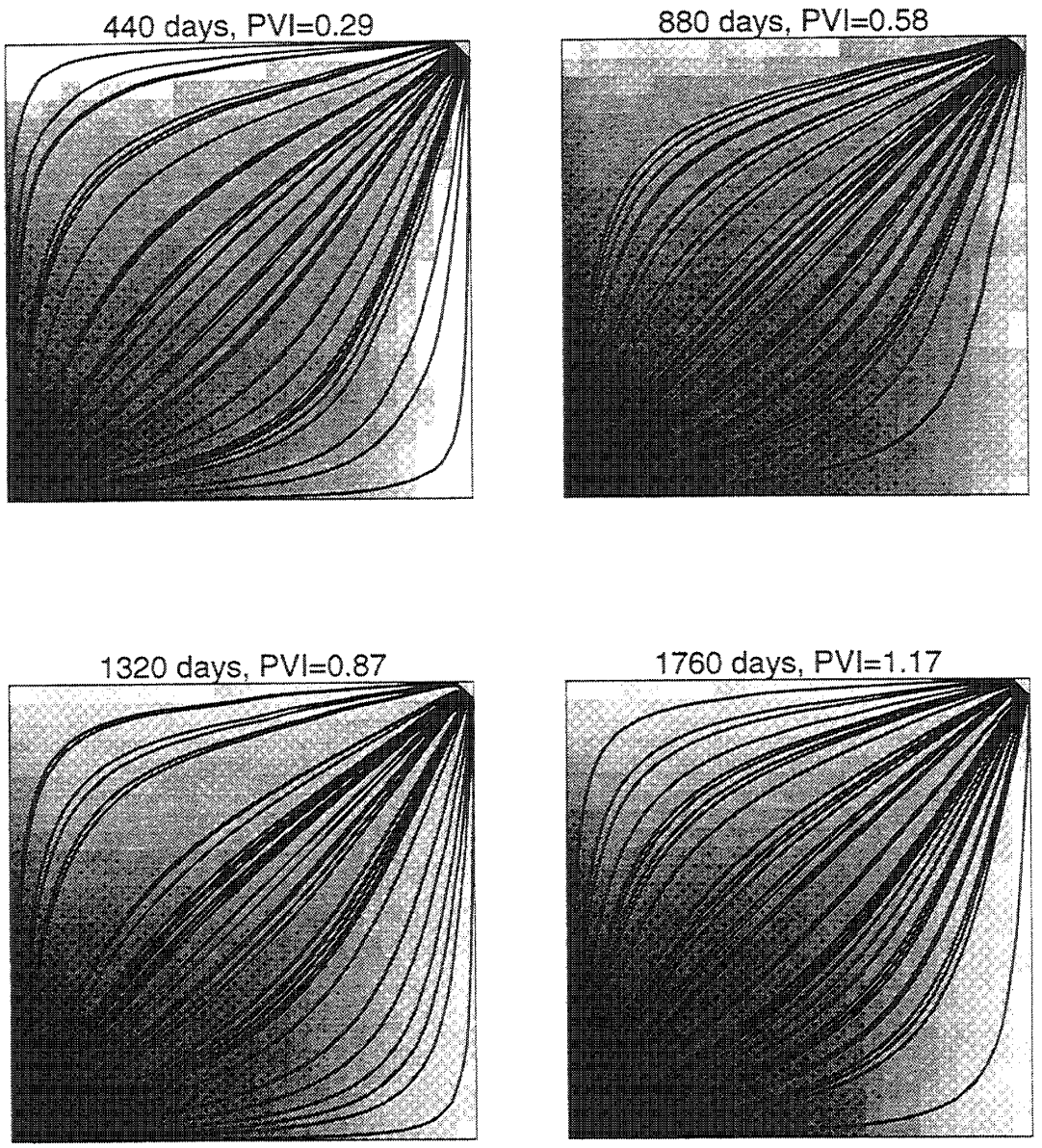

Figure 3 Water flooding--one quarter of five-spot pattern

Mapping numerical solutions
Viscosity: water 1cp, oil 40cp

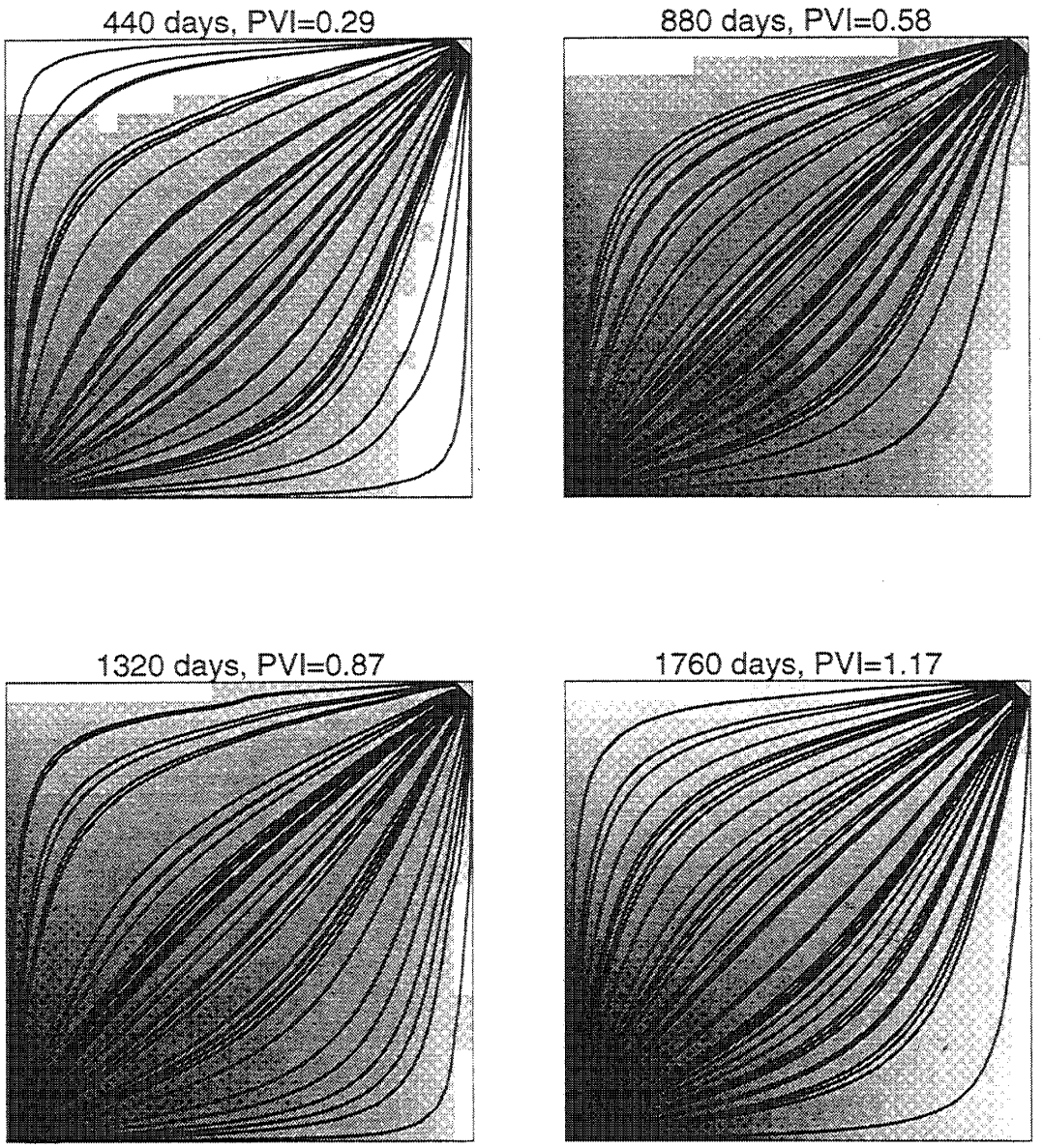

Figure 4 Water flooding--one quarter of five-spot pattern

Mapping analytical solutions
Viscosity: water 1cp, oil 40cp

4.1.2.2 Stochastic Inverse Approaches

In inverse modelling, flow fields and formation properties are inferred from observed data. Essentially, this is automatic history matching. Gupta *et al.* (1994) used stochastic inverse approaches to characterize the fracture connectivity and transmissibility of a fractured limestone formation. They presented two models. The first is called "equivalent discontinuum" that conceptualizes the fracture network as a partially filled lattice of conductors that are locally connected or disconnected to reproduce the observed hydrological behavior. The second "variable aperture lattice" represents the fracture system as a fully filled network composed of conductors of varying aperture.

For the first model, the algorithm proceeds by choosing a lattice element at random and if the element is present or "on," it is turned off and vice versa. The change in misfit, that is the difference between the actual and numerical data, is computed due to the perturbation. If the misfit decreases, then the perturbation is accepted; otherwise the perturbation is accepted with a certain probability.

The second approach consists of randomly selecting an element and assigning an aperture sampled from a log-normal distribution of apertures. The difference between the actual history and the computed history is computed as above and simulation parameters are adjusted similarly. This approach generates preferential flow paths by selectively placing high apertures and thus creates a set of variable aperture channels. Both methods appear to be well suited to the general reservoir inverse problem.

The results obtained by inverse approaches are generally non-unique. Gupta *et al.* (1994) also discussed an approach to generating and describing a collection of models that fit the data in some sense and deducing properties which are shared by the ensemble of acceptable models. Although the method of Gupta el al. was developed for fractured systems, it is likely that these ideas can be applied generally to any porous medium.

4.1.3 OBJECTIVES AND APPROACHES

As mentioned above, I will focus my research on applying a combination of the streamline method and inverse approaches to infer reservoir properties. Here is the general picture of this project:

1. Obtain initial values of the permeability field (or other reservoir properties such as initial fluid distribution) through an appropriate method(e.g., geostatistics).

2. Compute tracer breakthrough curves and compare with observed tracer flow data.

3. Modify the permeability field.

4. Repeat Steps 2 and 3 until a good match to the field data is found.

4.1.3.1. Applying the Streamline Method to Infer Reservoir Properties

For each repetition of the above steps, we need to solve the flow field once. It is essential to use a fast method to solve the flow field if we deal with a complicated reservoir because a large number of modifications is required to match the observed data with tolerable accuracy. Also, we need an efficient approach to modify the parameters so that

the number of iterations is minimized before acceptable results are obtained. This issue will be discussed in the next section.

The streamline method provides solutions to the flow problem much more rapidly than conventional simulation methods. For tracer flow, mobility ratio is normally near one, and the pressure field can be solved with one run. Then we can map the analytical solution to get tracer saturation distributions with time and distance. For this application, the streamline method is two to five orders of magnitude faster than a conventional finite difference method. However, we still need to verify the accuracy and speed of the streamline method as it is applied to tracer flow.

I also need to modify the code to meet the requirements of any case study. The modifications will include adding subroutines for mapping tracer concentrations along streamlines.

4.1.3.2 Methods of Modifying Permeability Field

The approach I will employ in this study can be described as follows. We assume property values in each grid block. The assumed values can be an estimated average or just an initial guess. Then the streamline method will be used to solve the flow field and breakthrough data. The computed data will be compared with the observed date, and modifications will be made to the properties to improve the fit. The problem will be solved again and the properties will be modified as necessary until the misfit is minimized or acceptable.

It is advisable to relate the above modifications to the types and values of the misfits to avoid modifying the properties randomly. By doing so, it will save computational time. Working a method for modifications is a main objective of this study.

I may apply one of the following approaches to modify the reservoir properties:

1. Stochastic approach

2. Sensitivity study - weighting

3. Genetic algorithm (GA) or micro GA (Goldberg, 1989)

The first approach has been described above. The second approach, sensitivity study, is to study the sensitivity of the error to the changing property value of specific grid blocks. By doing so, we know how thedegree of misfit is related to the properties in each block. Therefore we will able to find an efficient way to modify the value and minimize the computational time.

Genetic algorithms are good at dealing with uncertainties. The basic idea is that we produce a population where each individual carries an attritibute. In this study, attributes are the combination of reservoir property values, one such attribute might be permeability. Then, based on some criteria, we decide which property values survive and pass on to the next generation. The criteria is the fit or the degree to which the computed and actual histories agree. If we range the fit from 0 to 1 (1 is for good match and 0 is for bad), then an individual that has some value, say 0.5, higher than others, is chosen to survive. Or if an individual has some value lower than the others, it is erased and a new guess for the value made. The way to reproduce the next generation can be cross over and mutation. In

crossover, the good attributes of two individuals are combined to make a new individual in the next generation, whereas in mutation, the good attributes of a single individual survives and its bad attributes will mutate.

The differences between GA and micro GA are the size of the population and the way of reproduction. For GA, we can have a large population. For micro GA, we usually have a population of five. Also, we usually do not use mutation to produce the next generation in micro GA.

We may also choose to refine the grid gradually. This means that we may use a coarse grid at the beginning, do the field match for this coarse grid and then refine the grid. We use less computational time for coarse grids. With the results of the coarse grid as the initial value, we use fewer iterations for the finer grids to match the field data. We will study whether this approach can reduce the computational time.

By combining the streamline method and effective ways of modifying the permeability field or other properties, we expect we will be able to interpret tracer flow data intelligently.

To deal with the uncertainty, the approach described above by Gupta *et al.* (1994) may also be applied to combine all reasonable results and generate an ensemble model.

4.1.4 SUMMARY

It is important to interpret tracer flow data as intelligently and as accurately as possible. The interpretation usually involves a large amount of numerical computation. Therefore, a fast numerical solution is essential. In this study, the streamline method will be employed, because it is two to five orders of magnitude faster than conventional simulation methods.

Minimizing the number of times that a property value must be modified is a key issue of this study. I will apply one of the following approaches: (1) Stochastic approach; (2) Sensitivity study; and (3) Genetic algorithm or micro GA.

To infer the reservoir rock properties by interpreting field tracer flow data is an inverse problem, thus the results may be non-unique. The uncertainty of the inferred property distribution is also an issue of this study. To combine a collection of models that "fit the data" in some sense, and to deduce inferences about properties which are shared by the ensemble of acceptable models is a possible solution to this issue, and is hence proposed.

In conclusion, inverse methods to infer rock property distributions in a reservoir usually involve extensive numerical computation. Minimizing computational time is an important goal. We are trying to combine the streamline method and an efficient approach for modifying reservoir properties to realize the objective of interpreting tracer flow data as intelligently as possible.

4.1.5 REFERENCES

1. Abbaszadeh-Dehghani, M. and Brigham, W.E.: "Analysis of Unit Mobility Ratio Well-to-Well Tracer Flow to Determine Reservoir Heterogeneity," SUPRI TR-36 (February 1983) [DOE/ET/12056-36].

2. Batycky, R.P., Blunt, M.J. and Thiele, M.R.: "A 3D Field Scale Streamline Simulator with Gravity and Changing Well Conditions," SPE (October 1996).

3. Datta-Gupta, Akill, Lake, L.W., Pope, G.A. and King, M.J.: "A Type-Curve Approach to Analyzing Two-Well Tracer Tests," SPE (March 1994).

4. Datta-Gupta, A., Vasco, D.W. and Long, J.C.: "Detailed Characterization of a Fractured Limestone Formation Using Stochastic Inverse Approaches," SPE (April 1994) 71-86.

5. Goldberg, D.E.: "Genetic Algorithms in Search, Optimization, and Machine Learning," Addison-Wesley, 1989.

6. Thiele, M.R., Batycky, R.P., Blunt, M.J. and Orr, F.M., Jr.: "Simulating Flow in Heterogeneous Systems Using Streamtubes and Streamlines," SPERE (February 1996), 5-12.

Task 63 - Intevep shall provide DOE with information on studies to optimize heavy oil field exploitation using horizontal wells. The research is to reach conclusions about bore hole stability, pressure test interpretation and drainage pattern optimization when horizontal wells are applied to Venezuelan heavy oil reservoirs.

Stability Analysis of Horizontal Wells in Orinoco Belt, Venezuela

Prepared by

Rodríguez, Héctor A.
Silva, Ramón J.

INTEVEP, S. A.
Los Teques - Venezuela
October, 1997

Abstract

Hamaca MFB-53 heavy oil reservoir from Venezuela's Orinoco Belt has 175 wells, 56 of them being horizontal with high rate production. One of the horizontal well, has a completion problem and another one has sand production problems. The goal of this study is to asses the geomechanical stability conditions of these two wells and to determine possible remedial strategies, as well as procedures to avoid similar problems in the future.

The first well was completed in the closest sand to the basement with an approximately horizontal drilled section of 2000 feet. The diameter of the wellbore is 1.4 times the slotted liner attempted to complete the well. However, it was only possible to complete half of the well's horizontal planned section length. Due to the fact that the sand is unconsolidated and the well was drilled along the maximum horizontal stress direction, borehole failures may have occurred after drilling, leading to an unsuccessful completion of the well over the planned length.

The second well was completed in an upper sand which is composed of fine grains, containing also a high clay concentration of about 8-9 percent. The diameter of the wellbore is 1.75 times the slotted liner attempted to complete the well, and there was no problem completing it. Nevertheless, the well was plagued by sand production almost immediately after the start-up.

The behavior of these two wells was used to analyze the geomechanical stability problems under drilling and production conditions.

Although the reservoir is unconsolidated, the simulation results indicate that drilling a horizontal well in this reservoir using an overbalance condition is generally stable.

To produce a failure condition for the first well, it is necessary to apply an instantaneous drawdown of 200 psi or higher, which is more severe than letting the well to reach this drawdown slowly. Hence, no borehole failure should have been expected since such drawdown has not yet been applied. Therefore the inability to complete the well over its entire length might be attributed to the borehole trajectory.

To reach a failure condition for the second well, the bottom hole pressure must be reduced instantaneously just a few psi below the reservoir pressure. Given the fact that higher drawdown are needed to maintain well profitability, then a pre-packed liner or finer mesh slotted liner should be considered to prevent sand production.

The differences in geomechanical behavior of the formation are due to the lower sand having higher stress resistance as well as larger grain size than the upper sand. It seems that openhole completion in the lower sand can be stable if the well is initially

drawdowned slowly to avoid an abrupt pressure gradient development. Once the steady-state production is achieved, a 200 psi pressure drawdown can be sustained without sand production problems.

The stability of the horizontal wellbore during drilling is azimuth insensitive within the horizontal stress ratio measured for this formation.

Introduction

The reservoir has more than 150 wells with 40 of them being horizontal. Of these twenty wells, one had completion problems while another has presented sand production problems. The purpose of this work is to analyze geomechanical stability conditions for these wells and determine a possible remedial strategy as well as procedures for avoiding similar problems in the future.

This paper reflects the importance of the role that geomechanical reservoir simulation models can play in the optimization of field production practices, as well as in understanding important geomechanical effects on the observed reservoir response.

Description of the Geomechanical Simulator

In this study, an elastoplastic geomechanical simulator is developed for the stability analysis. The advantage of the elastoplastic approach over the nonlinear elastic or hyperelastic model is that the elastoplastic model can address important deformational phenomena such as yielding, failure, strain hardening and softening in order to describe inelastic material behavior. Typically, the theory of plasticity uses the concept of failure or yield surfaces in conjuction with a flow rule in order to describe yield and plastic deformation. The Mohr-Coulomb yield criterion tends to fit experimental results well. However, due to the discontinuity of stress derivates for certain loading conditions on this yield surface, other yield surfaces such as the simpler Drucker-Prager yield surface and the more elaborate Matsuoka-Nakai[1] yield surface are implemented. These yield surfaces provide a close approximation to the Mohr-Coulomb yield surface and have continuous derivatives throughout. A view of these yield surfaces is shown in Figure 1a and 1b. A detailed description of the geomechanical model can be found in Fung and Wan[2,3]. A brief overview is included in the following paragraphs.

Numerical stability analysis for unconstrained horizontal boreholes in unconsolidated reservoirs poses stringent demands on the robustness of the geomechanical simulator. As such, the classical approach to calculating the elastoplastic stiffness matrix as outlined by Owen and Hinton[4] is not suitable. In this work, a rigorous approach using implicit integration of constitutive equations and the consistent

linearization of the non-linear equilibrium equations similar to that discussed in Simo and Taylor [5] is applied. It may be noted that within the framework of the consistent tangent operators and stress return algorithms, a quadratic rate of convergence is achieved for both the shear and the tensile failure modes.In the determination of failure condition, plastic yielding alone is not a good failure criterion as the formation can be under plastic yielding but remain reasonably competent in its load carrying capacity. However, when the material reaches a tensile state due to wellbore unloading, dangerous near-well collapse can occur with substantial sand production or loss of well. On the other hand, when the accumulated plastic strains become large, the borehole will be reduced and spalling can develop. Therefore, in the context of the following analysis, the wellbore is deemed to have failed if the tensile regime is approached or if large plasticity has developed as indicated by the accumulated plastic strain. This model is applied to the geomechanical well analysis of Hamaca reservoir.

Prognosis

The first well was completed in the lower sand at a depth of 3241 feet, 9 feet above basement. Horizontal drilled length is 1800 feet, having a wellbore diameter of 9.625". Reservoir pressure is about 1100 psi. and in-situ oil viscosity is about 700 cp. Oil is saturated with gas at this condition and foamy oil is created in-situ when pressure drawdown occurs around the well. Estimated average permeability is 14 Darcy. Reservoir is made of an unconsolidated clean coarse sand with median grain size of 0.40 mm. Well was attempted to be completed using a slotted liner having 7" diameter and slot size of 0.020". However, it was only possible to complete half of the well length. The sand being unconsolidated, it was speculated that failure might have occurred after drilling impeding total well completion. This then leads to the inability to complete the wellbore over the entire length.

The second well was completed in the upper sand at a depth of 3185 feet. This is fine grained sand with median diameter of 0.28 mm and shale content of about 8-9 percent. The wellbore diameter is 9.625". and was successfully completed over it entire length with a slotted liner of 5.5" diameter and slot size of 0.018". However, the well was plagued by sand production almost immediately after the startup. Electrical pumps were initially used to lift production fluid. Once electrical pumps seemed to have deficiencies, well stimulation was applied to improve productivity but it was unsuccessful. After the electrical pump system failed two times in a row, production was then switched to a rod pump. The rod pump was quickly filled with sand. Later, a screw pump was used but producing fluids contain an unacceptable amount of sand. It is then proposed to analyze this well, under production conditions, and determine well stability state.

Geomechanical analysis: First well

INTEVEP's geomechanical model was used to analyze the stability of first well during drilling. For the upper sand, the material parameters are E=2.25E+5 psi, υ=0.27, c=14.7 psi, and f=40°. The reported range of mud specific gravity was 1.03 - 1.09. The in-situ total stress is estimated to be σ_V=2943.3 psi, σ_H=2153 psi and σ_h= 1959.2 psi. The direction of the wellbore is along the maximum horizontal stress. A cylindrical grid as shown in Figure 2 was used for the analysis. At the wellbore, boundary pressure was provided by the mud weight. The simulation also assumed that a mudcake was formed and no pore pressure build-up occurred in the formation. Using these conditions, it was found that the well is stable (no plastic nor tensile failure). The maximum and minimum effective stresses around the wellbore as well as the x and y displacement for this case are plotted in Figures 3 to 6. Because of stress anisotropy, maximum tangential stress occurs at the sides and minimum stress occurs at the roof of the wellbore (see Figures 3 and 4). The displacement plots of Figures 5 and 6 show that the deformation of the borehole is elliptical with major axis in the horizontal direction.

To produce sand failure, it is necessary to apply an instantaneous drawdown of 200 psi or higher, which is more severe than letting the well reaches this drawdown slowly. The simulated results are plotted in Figures 7 to 11. Comparing Figures 3, 7 and 4, 8, at this failure state, the stress distribution is similar to the previous case except that the maximum and minimum stresses are more severe. Comparing the displacement plot of Figure 5 and 9, the plastic yielding in the horizontal direction has caused significant shear dilation in the high stress region. The vertical displacement for the failure case is twice as large as can be seen in Figure 6 and 10.

Figure 11 shows the failure map, the highest tensile failure zone is at the roof of the well, and the most intense plastic failure is on the side. As this bottom hole pressure is lower than what we would expect during drilling, it is inferred that there was no borehole failure in this case. It is speculated that the inability to complete the well over its entire length is due to the borehole trajectory not being straight. The slotted liner would be stopped because it would not be able to negotiate a bend somewhere in the middle of the borehole. Also note that the liner diameter (7") is quite large compared to the borehole diameter (8.625").

Second well

The sands are dipping in the north direction at an average of 2-5 degrees. Since the second well site is 1.6 km to the north of first well, it is expected that the same sand unit to be about 180 feet deeper. Since the TVD of second well is 3185 feet, it was completed in the upper sand instead of the lower sand. The upper sand has a finer grain (D50 = 0.28mm), higher shale content and lower permeability. We suspect that

this sand has lower strength than the lower sand. Hence, for the simulation, the material parameters E=2.25E+5 psi, υ=0.27, c=14.7 psi, and f=35° were considered. The well direction is easterly with an angle of 42° degree from the minimum stress direction. The in-situ total stress for this well was estimated to be σ_V=2898 psi, σ_H=2020 psi and σ_h= 2020 psi. The slotted liner diameter is 5.5", while the borehole is 8.625". Effectively, this is an openhole completion. The mud weight used for drilling this well is the same as before, in the range of 1.03 to 1.09. For these mud weights, numerical simulation shows that well was stable during drilling.

To produce a failure condition for this well, the bottom-hole pressure was set to 998 psi, taking the pessimistic case of no formation pressure decline initially. Because this pressure is close to the reservoir pressure, it indicates that a bottom hole pressure drawdown can easily initiate sand production for this well. Bottom hole pressure history was analyzed and the values registered on 02-26-95 are shown in Table 1. It can be seen that bottom hole pressure fluctuated over a wide range and was as low as 100 psi at one point. This indicates that well was unable to produce fluid and some slugging was occurring in the well. The pressure changes could induce further instability in mobilizing sand. It is likely that in order to prevent sand production, completion using pre-packed liner or finer mesh slotted liner need to be considered.

Chemical treatment of this well provides data indicating that to inject fluid at 0.78 bbl/ min requires a pressure of 2600 psi. Using a formation fluid viscosity of 700 cp, the estimated kh for this well is 440 Darcy-ft. Because the formation average permeability is 10 Darcy, the effective well length should be about 44 feet. A neighbor well which is producing 2500 bbl/day with a drawdown of about 200 psi is estimated to have a kh of 7800 Darcy-ft. The effective well length should be 780 ft. Therefore, the trouble well has less than 5 percent effectiveness at the time of chemical treatment. It is likely that the damage is not of a chemical nature. The borehole cavity might have collapsed, hence the slotted liner may be ineffective in preventing sand from entering the wellbore. Well effectiveness is much lower because it was filled with sand.

The stress distribution and displacements during drilling are similar to the results of first well. These are shown in Figures 3-6. Although some plastic yielding exists, the borehole is stable. The simulation result at the failure state are plotted in Figures 12-16. As shown in Figures 12 and 13, there is a distinct low stress region around the wellbore where sand mobilization can occur. Figures 14 and 15 show that the displacement is generally directed towards the wellbore and vertical displacement near the roof to be the largest. Tensile zone develops around the entire perimeter of the wellbore and a large plastic region behind it. These failure zones are detailed in Figure 16.

Conclusions

Although the reservoir is unconsolidated, the simulation results indicate that drilling horizontal well in this reservoir using a mud weight of 1.03 to 1.09 is generally stable.

The lower sand is more resistant than the upper sand and has larger grain, it seems that openhole completion in the lower sand can be stable if the well is drawdown slowly initially to avoid abrupt pressure gradient development. Once steady-state production is achieved, a 200 psi pressure drawdown can be sustained without sand production problems. However, the upper sand is finer and has less strength, simulation results suggest that more stable completion strategy will be required to avoid sand production and keep the borehole stable.

Using the horizontal stress ratio of about 0.91, simulation results indicate that stability of horizontal well during drilling in Hamaca is orientation insensitive.

References

1. Matsuoka, H. and Nakai, T., "A New Failure Criterion for Soils in Three-Dimensional Stresses", IUTAM Conference on Deformation and Failure of Granular Materials, Delft, pp. 253-263.

2. Fung, L.S.K, and Wan, R.G., "Wellbore Stability Simulation for Vertical and Horizontal Well - Project 1", CMG Report to INTEVEP, Mar. 1995, 88p.

3. Fung, L.S.K, and Wan, R.G., "Wellbore Stability Simulation for Vertical and Horizontal Well - Project 2", CMG Report to INTEVEP, Dec. 1995, 83p.

4. Owen, D.R.J. and Hinton, E., "Finite Element in Plasticity", Pineridge Press, Swansea, U.K., 1980, 549p.

5. Simo, J.C. and Taylor, R.L., "A Consistent Tangent Operators for Rate-Independent Elastoplasticity", Comp. Meth. Appl. Mech. Engg., Vol. 48, 1985, pp.101-118.

Nomenclature

c	cohesion (psi)
E	Young's modulus (psi)
f	friction angle (degree)
υ	Poisson's ratio (dimensionless)
σ_v	Vertical stress (psi)
σ_H	Maximum horizontal stress (psi)
σ_h	Minimum horizontal stress (psi)

TABLE 1

Bottomhole Pressure for Second Well on 02-26-1995

Fluid Density	62.8 lb/ft3
Pressure Gradient	0.438 psi/ft.
Pump Depth	3145 ft.
Well Depth	3185 ft.

Time	Fluid Level (ft)	Fluid Column Above Well (ft)	BHP (psi)
10:52:58	2585	600	263
12:30:33	2671	514	225
12:41:07	2679	506	222
13:46:48	2020	1165	510
14:26:27	1778	1407	616
15:19:17	2141	1044	457
16:20:15	2920	265	116
16:37:03	2957	228	100
17:15:00	2487	698	306
17:45:58	2309	876	384

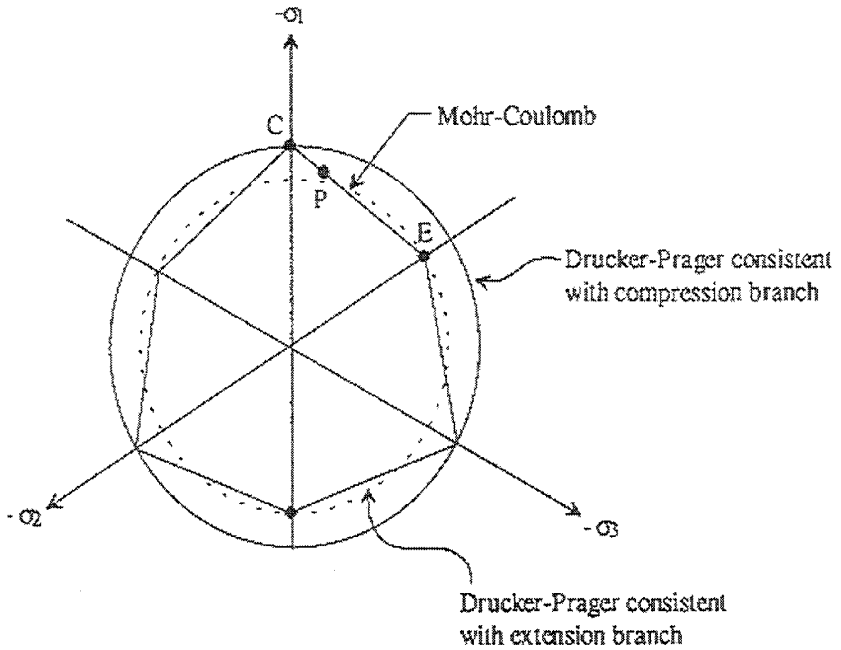

(1a) Mohr-Coulomb and Drucker-Prager Yield Surface Comparison

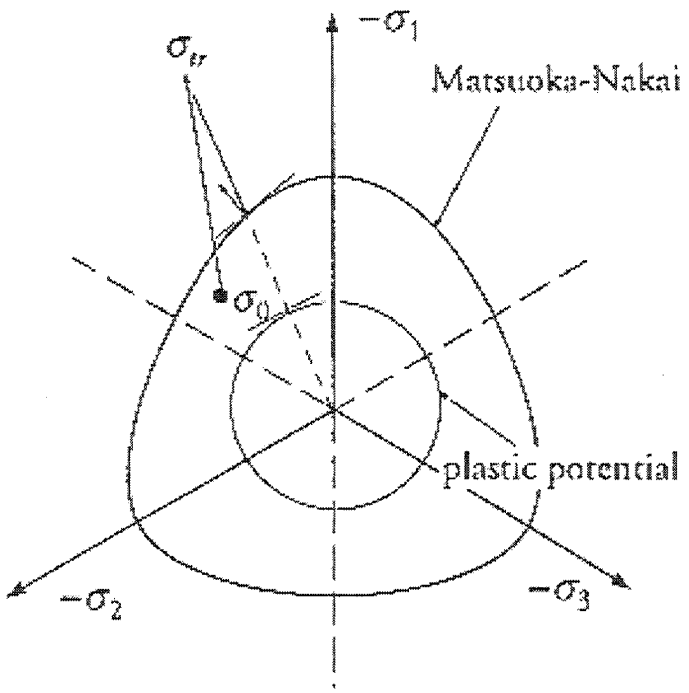

(1b) Matsuoka-Nakai Yield Surface

Figure: 1 Deviatoric View of Yield Surfaces

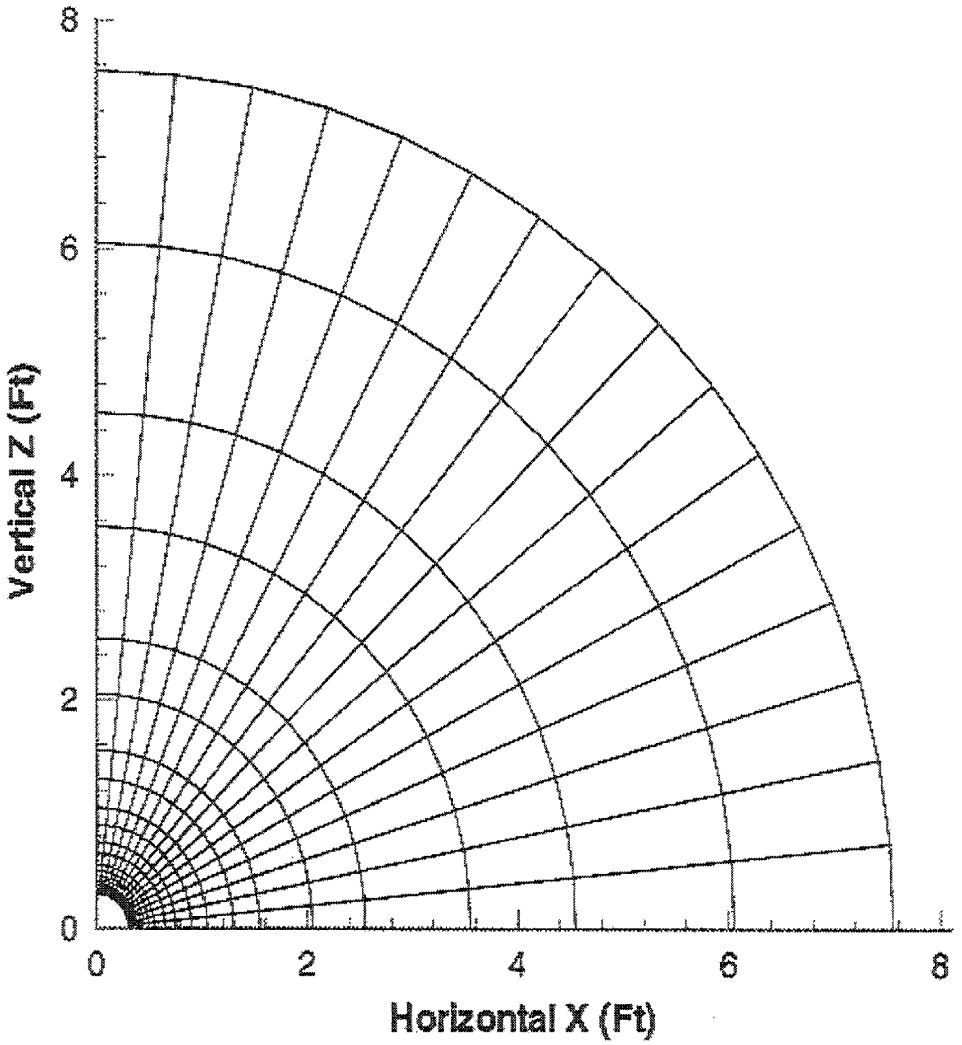

Figure 2: Grid for Horizontal Wells Geomechanical Studies

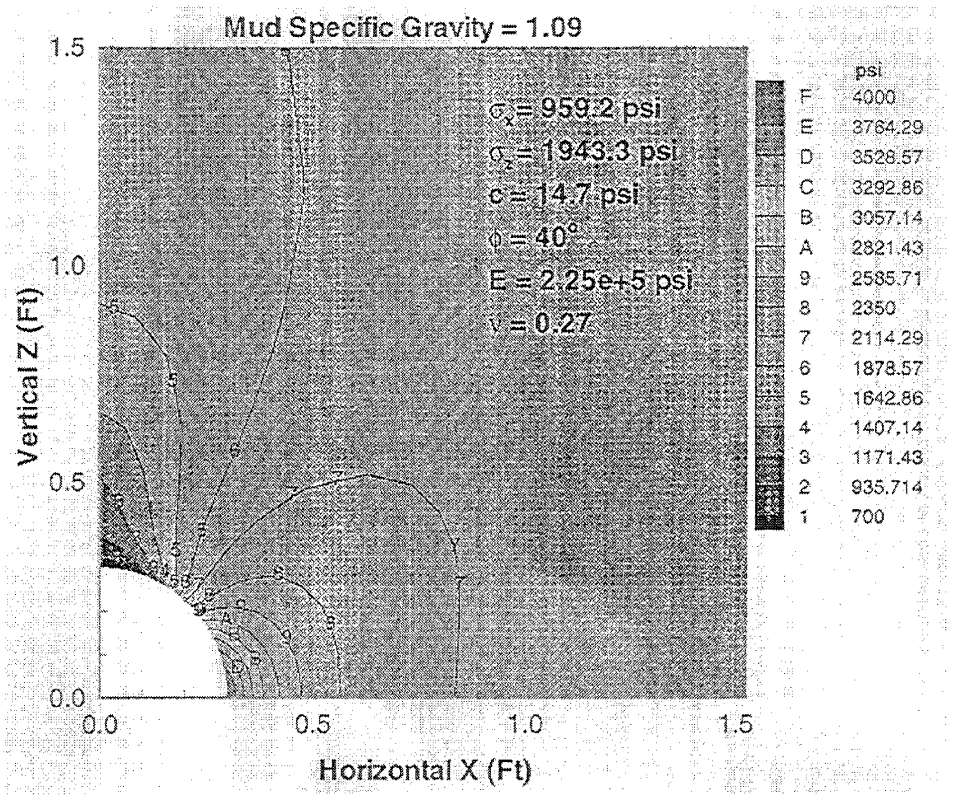

Figure 3: Maximum Effective Stress at First Well during Drilling

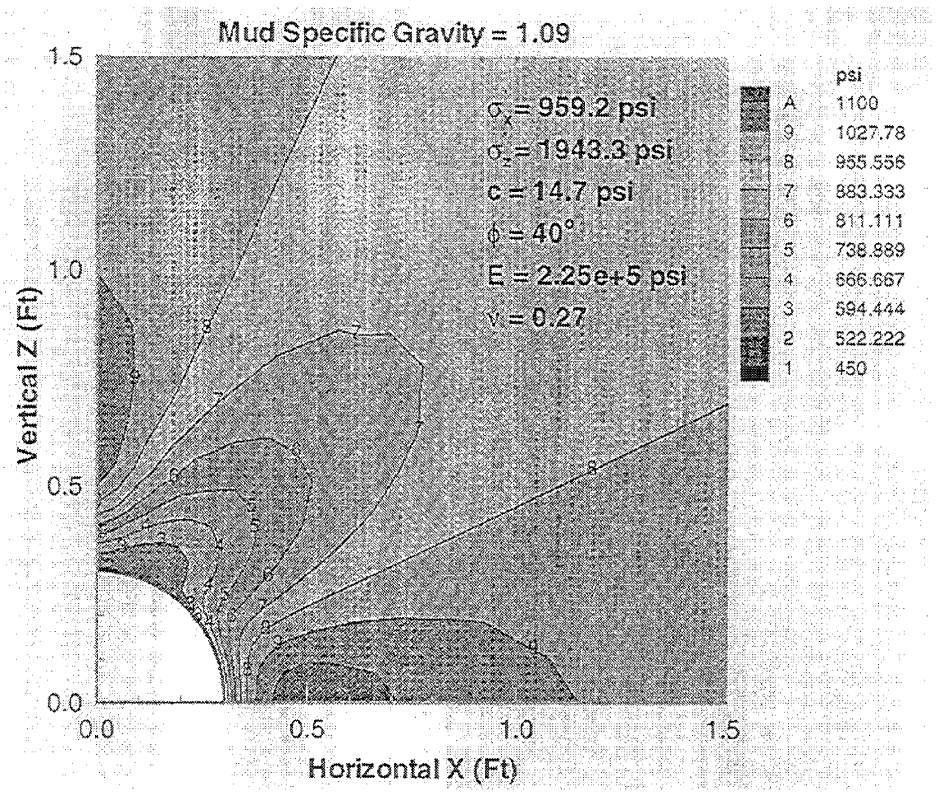

Figure 4: Minimum Effective Stress at First Well during Drilling

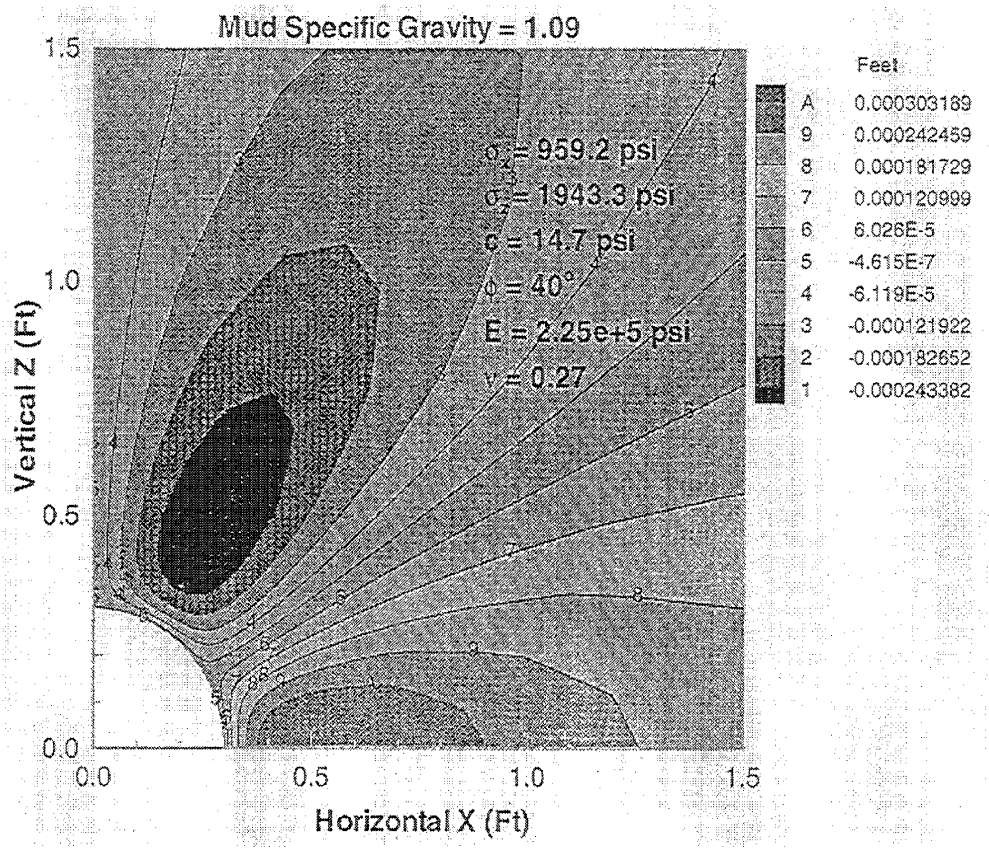

Figure 5: X Direction Displacement at First Well during Drilling

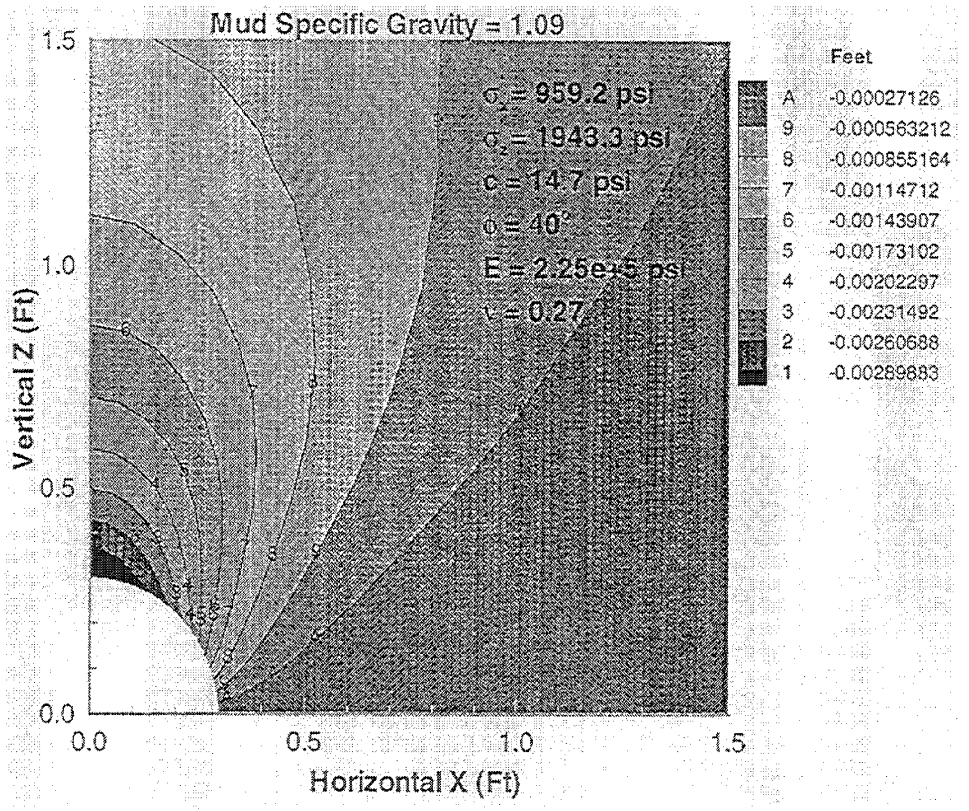

Figure 6: Z Direction Displacement at First Well During Drilling

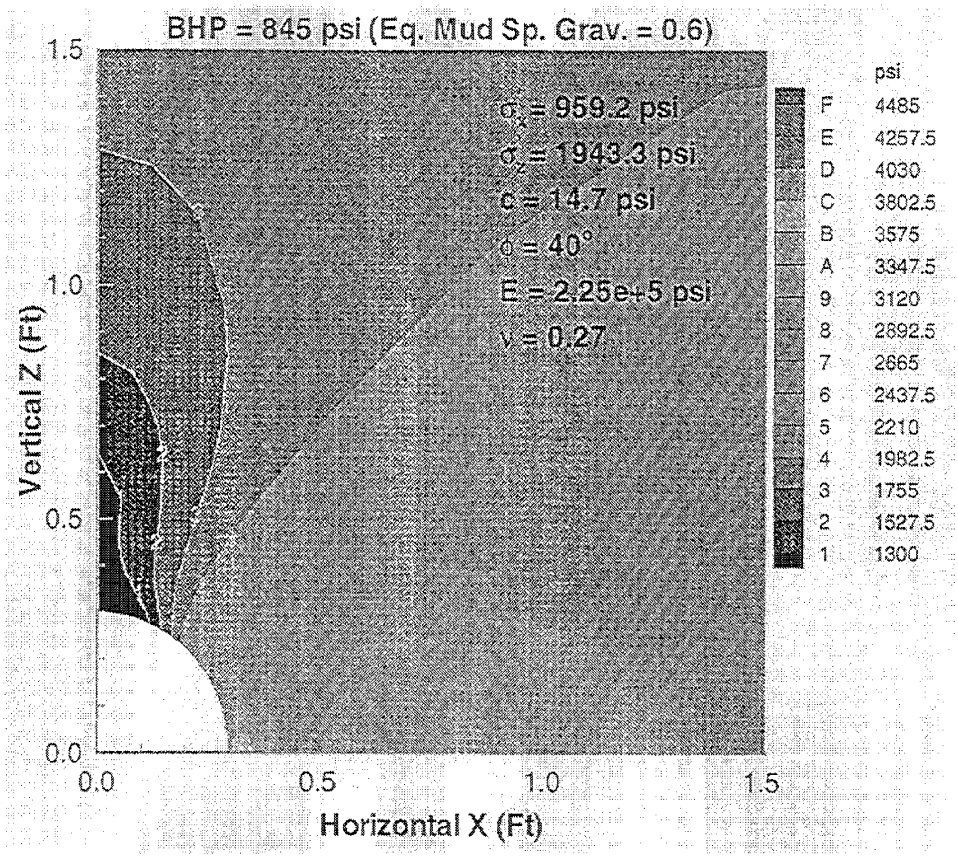

Figure 7: Maximum Effective Stress at First Well During Production

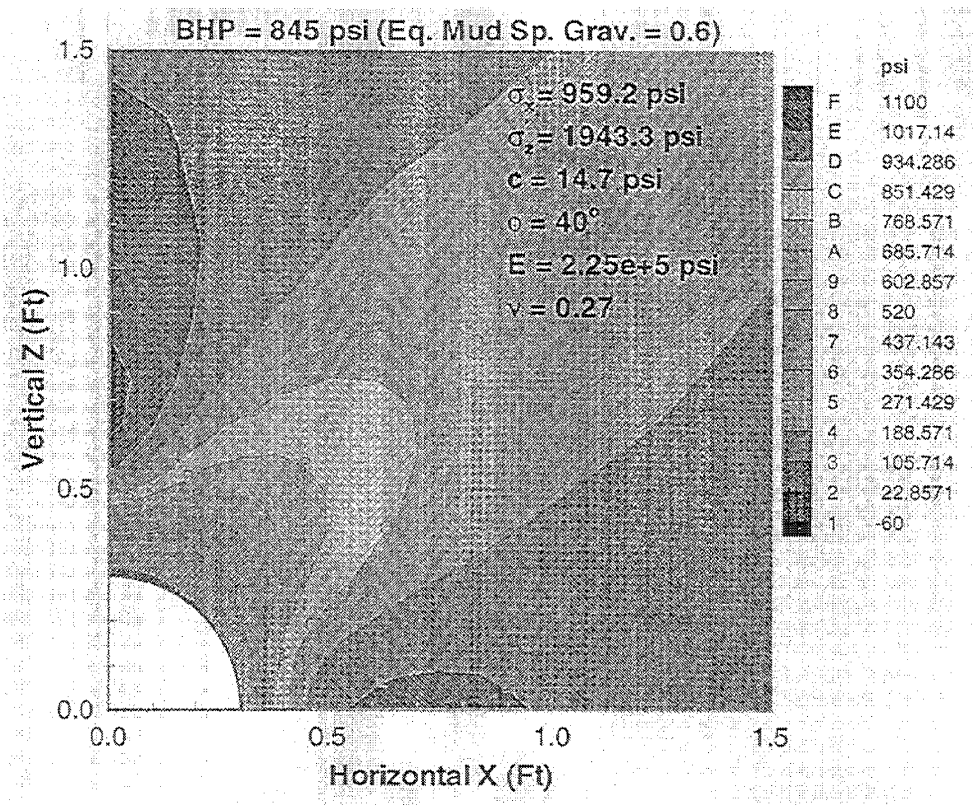

Figure 8: Minimum Effective Stress at First Well During Production

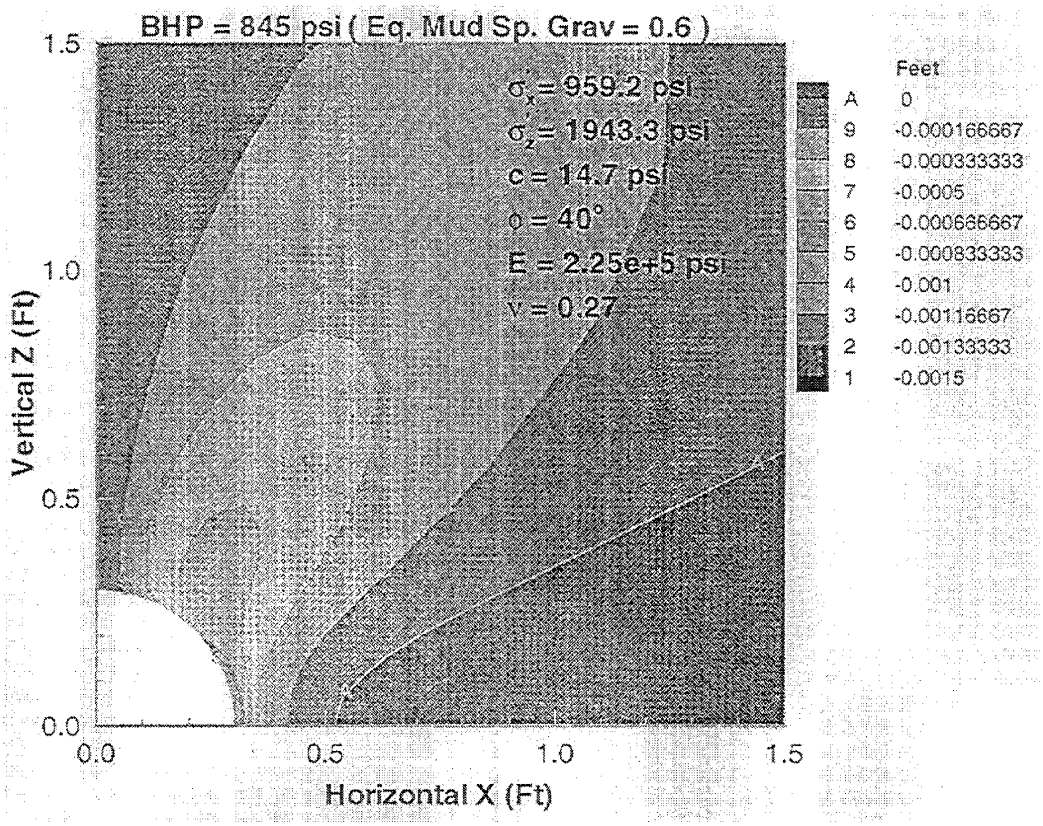

Figure 9: X Direction Displacement at First Well During Production

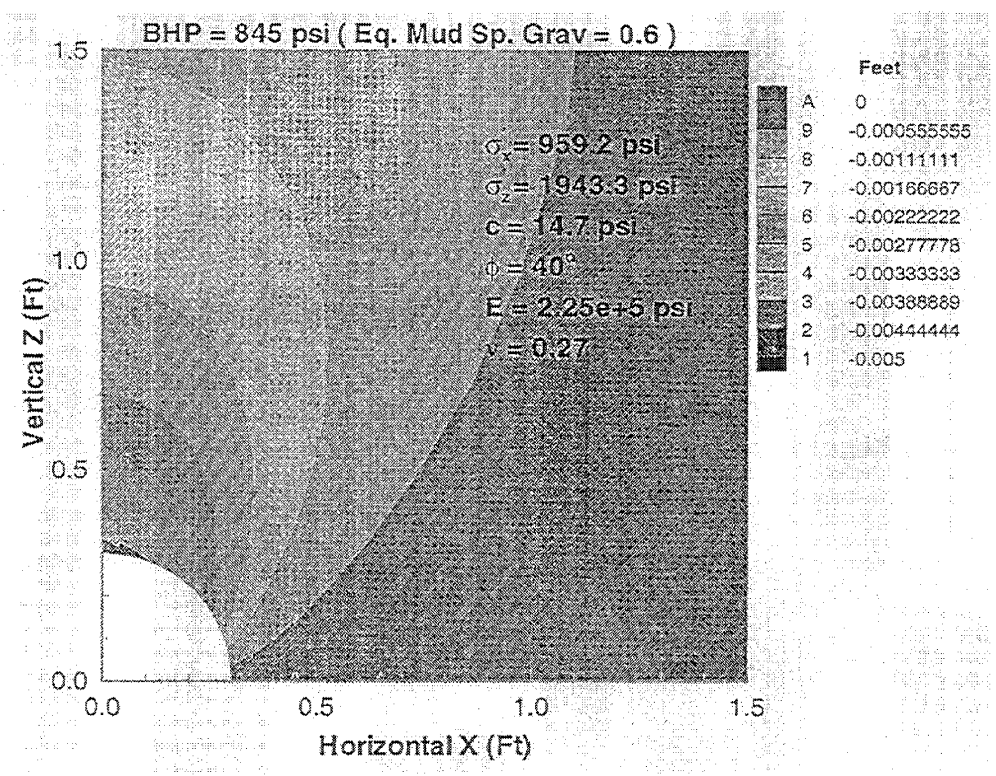

Figure 10: Z Direction Displacement at First Well During Production

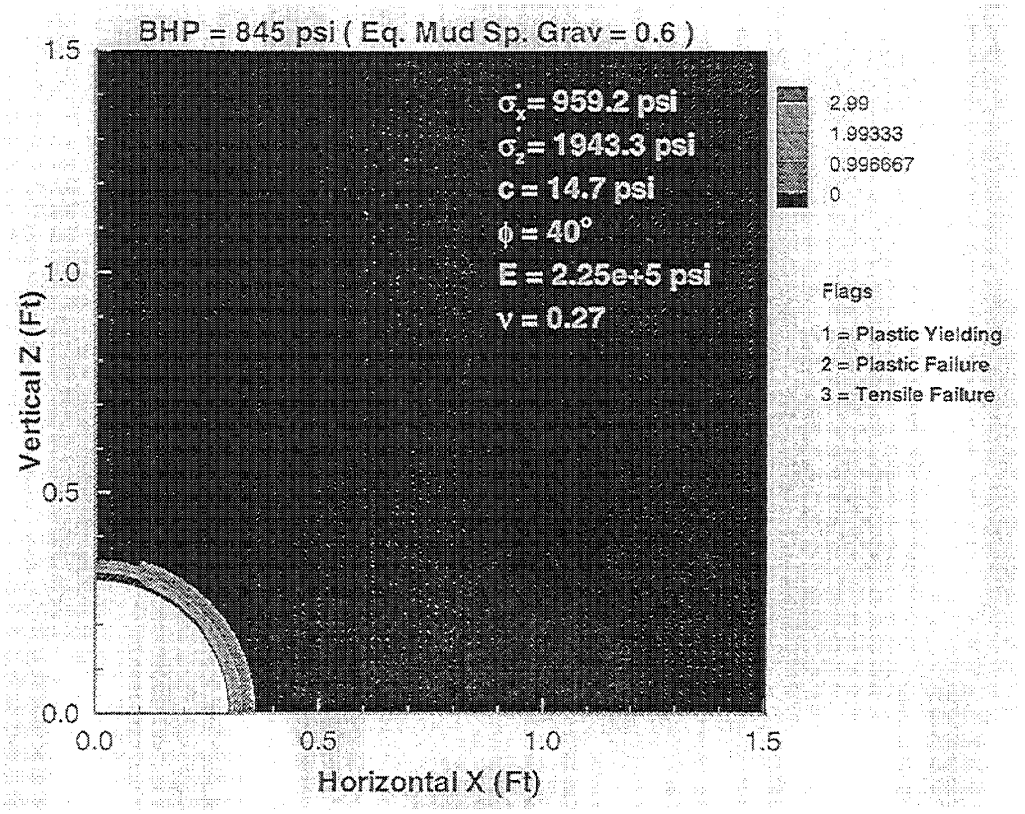

Figure 11: Failure Flags at First Well during Production

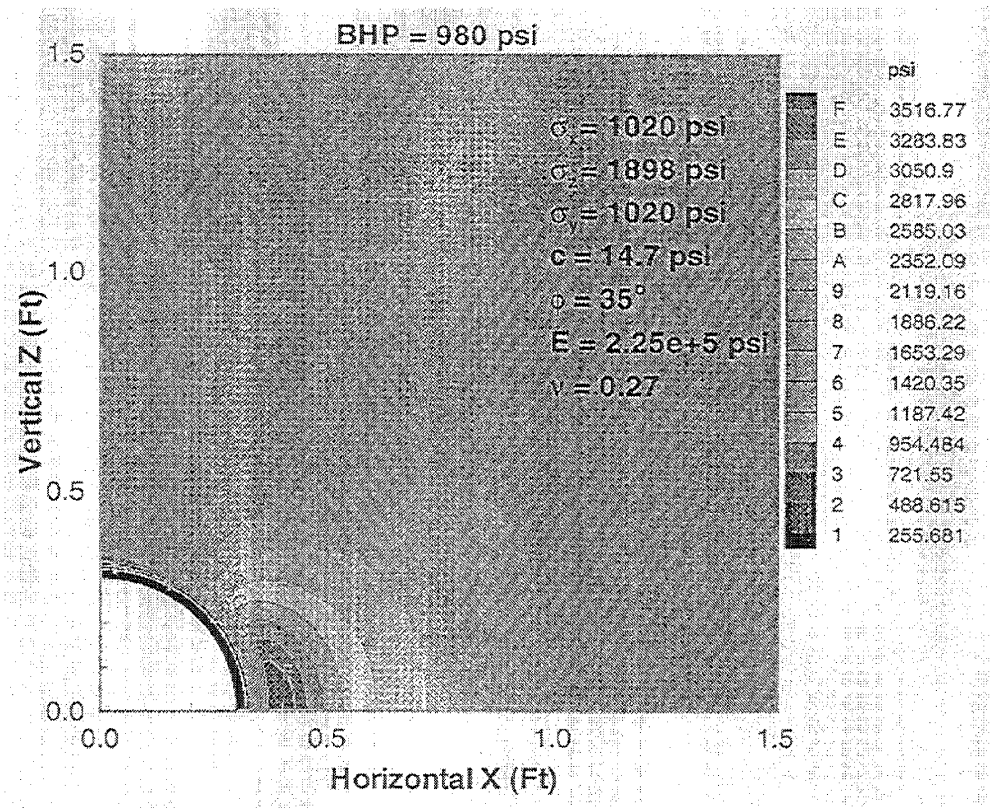

Figure 12: Maximum Effective Stress at Second Well During Production

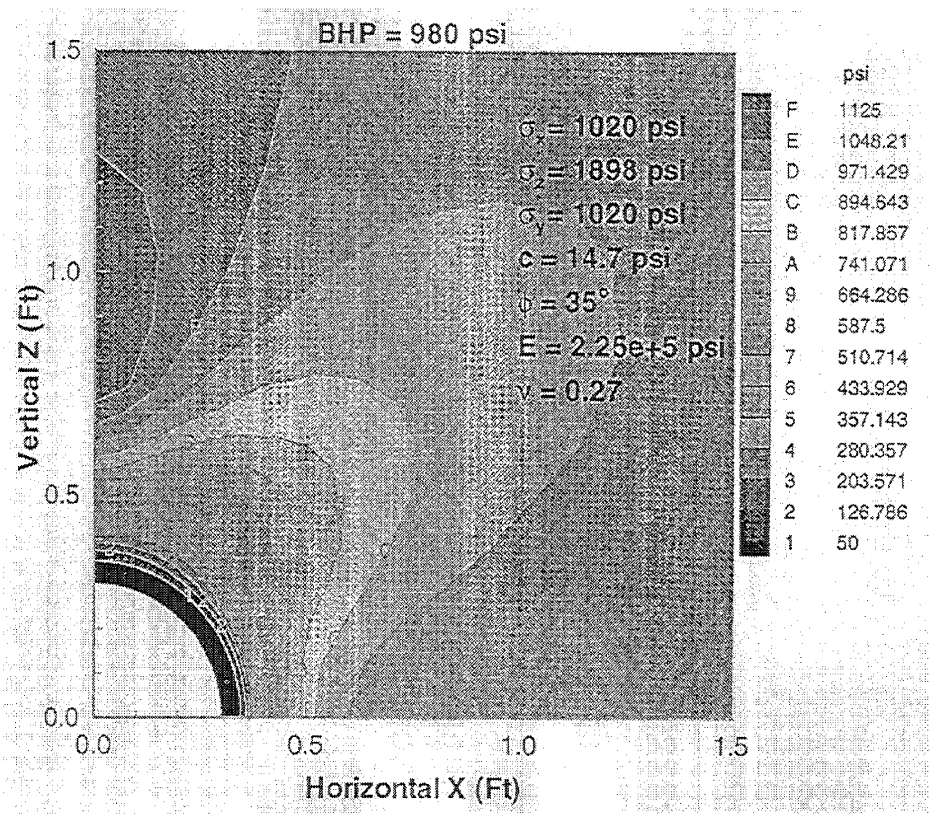

Figure 13: Minimum Effective Stress at Second Well During Production

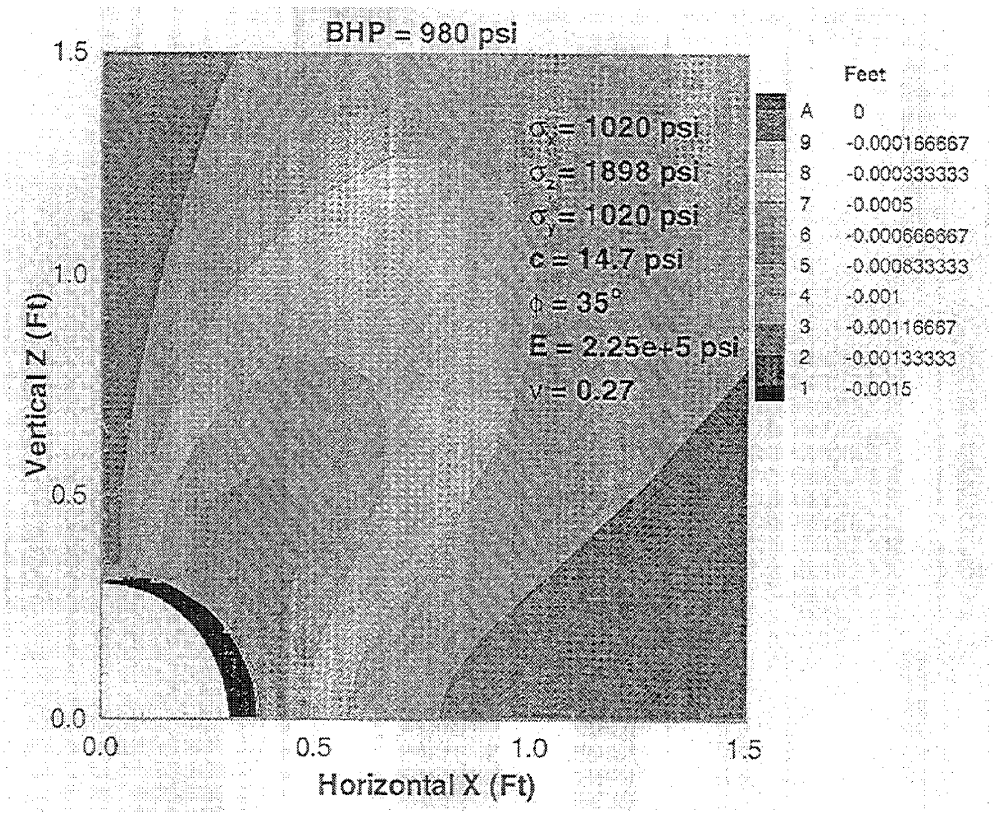

Figure 14: X Direction Displacement at Second Well During Production

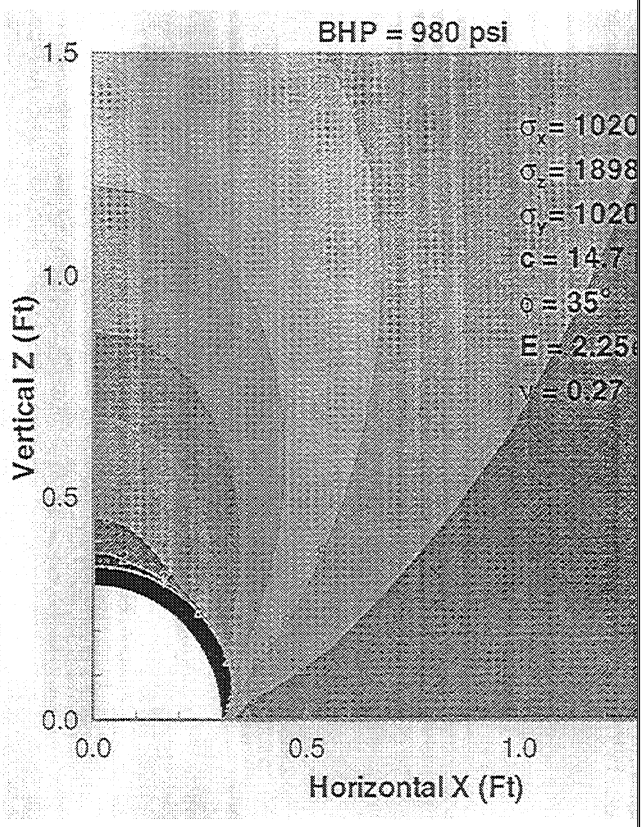

Figure 15: Z Direction Displacement at Second W

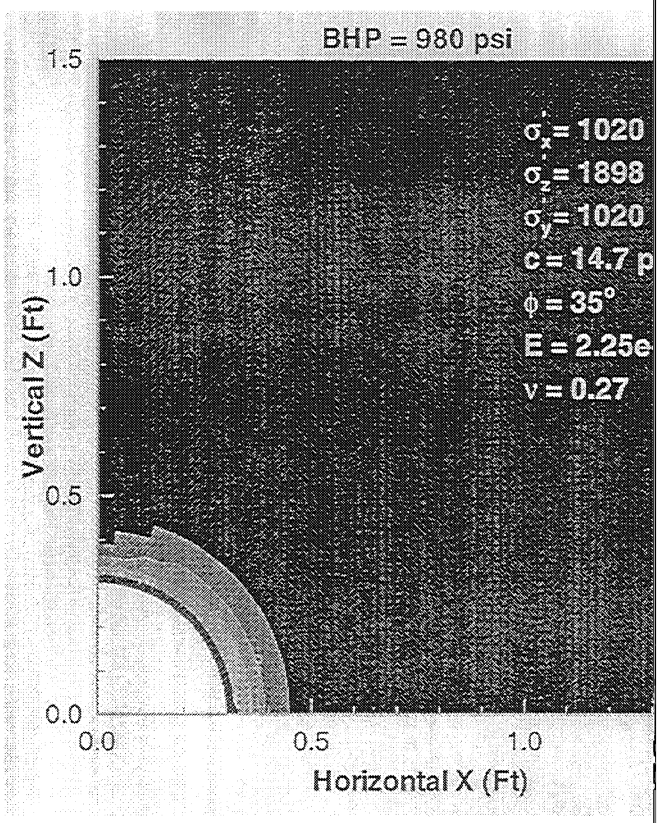

Figure 16: Failure Flags at Second Well During Pr

PRODUCTION IMPROVEMENT STRATEGY FOR HAMACA HEAVY CRUDE OIL RESERVOIRS

Prepared by

Rodríguez, Héctor
González, Oscar
Linares, Ignacio
Silva, Ramón

INTEVEP, S.A.
Los Teques - Venezuela
October, 1997

ABSTRACT

The purpose of this work is to show production improvement strategies for Bare extra-heavy crude oil reservoir, located in the north Hamaca area of the Orinoco Belt in Eastern Venezuela. This study was conducted by a multidisciplinary team for the development of a 3D numerical simulation model.

The generation of high-probability production profile has been obtained successfully by new understanding of foamy behavior and using emerging technologies for artificial lift systems such as Electric submersible pumps in horizontal wells.

Hamaca crude oil behavior modeling has permitted the understanding of the high productivity observed in wells from this reservoir, especially in horizontal wells. With this, a primary recovery factor greater than 10% and an increase in oil reserves of approximately 30% is obtained. These results were included in the development of a 3D numerical simulation model.

Matching field experience through 3D Simulation and Geomechanical models provided the definition of new drilling, completion scenarios and an optimum exploitation scheme.

From this study, it was clear that preliminary cold production with horizontal wells should be used prior to secondary recovery processes, allowing for 30% savings in the overall project cost.

INTRODUCTION

The study area is located in the Bare Block northeast of the Hamaca area, within the Orinoco Belt (Fig. I). Reservoir exploitation (U sands) began in 1982. It has an extension of 165 km^2 and an original oil in place (OOIP) of 2500 MMBLS. The largest extra-heavy crude oil recoverable reserves (250 MMBLS) discovered in North Hamaca belong to this area.

As of October 1997, 175 wells have been drilled (56 horizontal and 119 vertical), with an accumulated production of 115 MMBLS (4.6% of OOIP). Reservoir performance has been improved through the use of horizontal wells with an initial production of up to 3000 B/D and an average production of 1500 B/D [1]. Reservoir average pressure has decreased only 120 psi from an original pressure of 1220 psi.

Due to the high productivity index (7 to 12 BLS/psi) of horizontal wells, high volume lifting equipment was required in order to handle the produced fluids. Electric submersible pumps have been used successfully, and 65 MB/D of the reservoir

production are tied to this lifting method.

It is important to mention that Hamaca heavy/extra heavy oil production forecast is 270 MB/D for the year 2005, more than double the current production of 145 MB/D [2]. The development of the 3D model backs up the growing potential of Hamaca's expansion program. The main objective of this study is the definition of a production improvement strategy for Hamaca Crude Heavy/Extra Heavy Oil reservoirs in Orinoco Belt, Venezuela.

SCOPE

The scope of the working plan included analyzing, evaluating and realizing the following macro activities:

1. Detailed characterization of the reservoir
2. Establishment of production mechanisms
3. Development of predictive field behavior capabilities
4. Optimization of artificial lift methods and
5. Evaluation of optimum exploitation scenarios.

To reach the objective, a fastrack team approach in geology and reservoir engineering was implemented, applying novel technologies for the definition and construction of the geological model, research lab work on the special behavior of reservoir fluids, and finally the development of a three dimensional dynamic simulation model.

PRODUCTION MECHANISMS ANALYSIS

The production mechanisms identified in this reservoir are solution gas drive, a weak aquifer activity. Steam injection processes have also been applied. No evidence of compaction/subsidence has been detected. Reservoir and fluid properties are showed in Table 1.

This reservoir showed good pressure maintenance performance through 12 years of production history (Fig. 2), unexpected initial cold production rates of 500 B/D (vertical wells) and an initial average rate of 2500 B/D in horizontal wells (Fig. 3). It has been produced by using an average spacing of 1476 ft. (450 m). According to these analyses, high uncertainty was found when trying to match the reservoir pressure behavior which indicated that the high gas retention shown by the crude oil could not be evaluated by conventional techniques.

In consequence, to understand the acting production mechanisms in this reservoir, a

sequence of activities including experimental tests, production behavior analysis, compaction and subsidence status was developed[1,3].

A compaction/subsidence evaluation was made, where a recovery factor due to this mechanism was estimated to be in the range of 0.3% to 6% OOIP, depending on the threshold pressure[4].

Also, a mathematical model was developed to understand the flow process and quantify the impact of foamy crude oil on recovery[3,5]. The research strategy focused on evaluating and validating the numerical simulation models with laboratory data, scaling the analysis at field level.

As a consequence of all laboratory results, an evaluation study of the oil reserves in the reservoir was done. This analysis determined an updating of the total oil recovery factor to 14% OOIP (10% by primary recovery factor, 3% by compaction and l% by thermal activity) which represents in terms of reserves, an increment of 30%. The primary production mechanism seems to be controlled by the in situ formation of a non-aqueous oil foam under solution gas drive conditions.

The laboratory experience also revealed that at pressures lower than the pseudo bubble point (1000-900 psi), large quantities of gas are produced (Figs. 4,5). As a consequence, a decrease of pump efficiency is expected. It was possible to corroborate this critical behavior at well level, since the high capacity artificial lift systems (ESP) currently employed in horizontal wells allowed monitoring of these pressure levels [6] (Fig.6).

SIMULATION MODEL

Well-known state of the art numerical simulation techniques, adapted to account for foamy oil behavior, have been evaluated with the purpose of analyzing the possible acting production mechanisms in this area, their impact on the recovery factor and development of high probability production profile.

The evaluation of numerical simulators for foamy crude oil modeling was made by the following models:

- Conventional Solution Gas Drive;
- Pseudo-Bubble Point,
- Modified Pseudo-Bubble Point (Intevep),
- Non-Equilibrium Model, and
- LVM (Low viscosity model) [7].

Based on all these analyses (simulation efforts and laboratory tests), the foamy nature of the crude oil as a production mechanism has been determined to be of high impact. This approach and field experiences were incorporated in the construction phase of the three-dimensional simulation model discussed below.

For the predictive model of field behavior, a three dimensional compositional simulator model (STARS) was used applying the control-volume finite-element method (CVFEM) to optimize the numerical and computational calculations. It was possible, then to generate a grid independent from the preferential flow directions, adjusted to the boundaries of each one of the structures or layers of the reservoir, and to the actual location of the wells. In this manner, the number of cells to be used in a conventional grid of finite or Cartesian differences was reduced (2000 cells, Fig. 7).

The definition of two pseudo-components (dead crude oil and solution gas), was derived from the fluids molecular composition at reservoir level, and the characteristics of the fluid at surface conditions.

The relative permeability curves for the water-oil and liquid-gas systems were derived from displacement tests performed under transient conditions and at a stationary state. As a first step, a foamy oil behavior under primary recovery conditions, was considered, using the results obtained from laboratory tests.

History matching of fluids production and reservoir pressures was achieved (Figs. 8,9), considering production/ injection pressure of 175 wells, 113 hot wells (steam soak) and 72 cold wells, (56 horizontal wells). The technique employed for the history match considered the foamy effects of the crude oil observed in field as well as in the laboratory. It was used a critical gas saturation of 2% and was considered an entrained gas volume factor (Fig. 10).

During this process, the results obtained in field and laboratory level were matched from displacement test in vertical cells (Fig. 11,12) as well as in horizontal (Fig. 5, 13). The critical gas production behavior observed at horizontal well level (Fig. 6) could be reduced if an optimum draw-down is applied. It depend on the average pressure around the well and the oil rate. As the oil rate increases, the pressure around the well decreases and the fluid velocity increases, increasing the possibility that gas may liberate in the well and arrive at pump intake. On the contrary, upon reducing the rate the gas separated in the reservoir, by gravity effects the gas move towards the upper part of the reservoir, without affecting pumping efficiency. The simulations showed this effect, when different scenarios (rate control) were evaluated (Fig. 14,15).

Additionally, sand production is another field problem which must be considered in the simulation profile, because of the pump efficiency is affected. However, a geomechanical model which determined a critical draw-down in these horizontal

wells[8], was recently developed. Basically, it depends on the grain size in the U sands. Two sets were identified, U1 and U2,3. The probability of sand production is higher in U1 than U2,3. This observation was confirmed in the field.

EXPLOITATION STRATEGIES

Different exploitation scenarios were evaluated and production forecasts in cold conditions were constructed until the year 2070 (at an averages reservoir pressure of 450 lpc). For this period, a recovery factor of 15% to 19.8% of OOIP, was determined, depending on the critical rate. In the faster rate case, a primary recovery factor of 13% and 6,8% by others mechanisms, was estimated.

For economic analysis purposes (20 years), the recovery factor oscillated between 13,6% and 16%, at an averages reservoir pressure of 600 lpc (Fig. 15,16). In this case, the more relevant exploitation strategies as follows:

- Scenario 1: Maintenance strategy. To continue with the current production rate. Maintenance of 57 MBD by five (5) years and a recovery factor of 13.6% was achieved.

- Scenario 2: Development strategy by rate control. This case takes into account an increase initial production rate up to 75 MB/D, with the incorporation of 18 new horizontal rate controlled wells (Horizontal wells at 1100 B/D and Vertical wells at 300 B/D). A recovery factor of the 15% was obtained.

- Scenario 3: Maximum improvement strategy: Maximum production rate of 240 MB/D for less than six (6) months (Horizontal wells at 3500 B/D and Vertical wells at 1500 B/D). The following critical behavior were identified: Drastic increase of gas production. Severe probability of sand production and substantial decrease of the artificial lift systems efficiency. High operational cost. A recovery factor of the 16% was obtained.

- Scenario 4: Development of the reservoir with horizontal wells: The production oil rate reached 62 MB/D with 18 new wells, and existing horizontal wells (38 at 1100 B/D) without vertical wells. A recovery factor of the 14.6% was achieved.

All the analyzed scenarios considered the use of three different artificial lift systems for new horizontal wells, such as. ESP, PCP and RP and current lifting system for existing wells (RP, PCP, ESP). A minimum oil production rate of 1000 B/D in horizontal wells, was considered for change of the lifting system.

ECONOMICS ANALYSIS

20 years were considered for the analysis. The most relevant economic indicators are described in the following table:

SCENARIO	INV, MM$	NPV, MM$	MIRR,%	INVEST. EFF
1	-	250	-	-
2	21.2	273	26.3	12.9
3	50.4	410	23.6	8.1
4	21.2	258	26	12.2

Based on this results, the most attractive option is the exploitation of the reservoir with the existing wells and new horizontal producing at a controlled rate (scenario 2). In this case, it was identified an optimum production strategies in the horizontal wells of 1100 B/D and 300 B/D in vertical wells (maximum production rate). From the point of investment efficiency, it was concluded scenario 2 is the best also, with an efficiency of 12.9. It was observed that if the maximum production oil rate is considered in the reservoir, high operation cost will be found due to the gas and sand presence, causing a decrease in the investment efficiency (8.13).

Other interesting point was sensitivity of the economic analysis when considering the use of different methods in the artificial lift. Taking as example scenario 3, it can be observed that differences are marginal:

CASE	INV, MM$	NPV, MM$	MIRR,%
ESP	25,6	256	24,8
CPP	21,1	258	26
RP	22,7	259	25,6

Concluding then, particularly in this reservoir the lifting system does not appear to affect the project economics. ESP's appear to be the best choice, due to its ability to handle higher production rates.

Finally and according to the results, ¡t was confirmed that a cold production stage with horizontal wells before beginning with secondary recovery processes (i.e. gas injection and/or thermal activity) improves the overall oil recovery.

CONCLUSIONS

A production improvement strategy for Hamaca extra-heavy crude oil reservoir was achieved by using Horizontal wells in cold conditions. It is suggested that IOR processes, such as Horizontal Well Steaming and or SAGD, be implemented after

depletion by effect of the foamy oil mechanism.

An optimum production strategy, including new horizontal wells of 1100 BD and 300 BD in vertical wells (production rate controlled) in order to improve the recovery of the reservoir and the profitability of the same (a 30% saving in the overall project cost), was identified.

The critical areas to optimize are the production of gas and sand in this reservoir. The critical gas and sand production behavior at horizontal well level could be reduced if an optimum draw-down is applied. Drawdown depends on the grain size in the U sands, the average pressure around the well and the oil rate.

A 3D model considering a foamy crude oil mathematical formulation, has validated a major drive mechanism in the Hamaca area leading to a primary recovery factor up to 13% and 6,8% for another secondary mechanism (at an average reservoir pressure of 450 lpc).

For Hamaca reservoirs, it was determined that the lifting system has very little effect project economics. The improvement of ESP designs, will extend the life of the equipment and increase the profitability of the project, however.

NOMENCLATURE

BLS	=	Barrels of Oil
BHP	=	Bottom Hole Pressure
CPP	=	Cavity progressive Pump
ESP	=	Electric Submersible Plump
INV	=	Investment
IOR	=	Improved Oil Recovery
GOR	=	Gas O¡) Ratio
MIRR	=	Modified Internal Rate of Return
NPV	=	Net Present Value
OOIP	=	Original Oil in Place
RB	=	Reservoir Barrels Of Oil
RP	=	Rod pump
RCF	=	Reservoir Cubic Feet of Gas
SCF	=	Standard Cubic Feet
STB	=	Stock Tank Barrels
SAGD	=	Steam-assisted Gravity-drainage

REFERENCES

1. Mirabal, M. et al.: "Integrated Study for the Characterization and Development of the MFB-53 Reservoir, North Hamaca, Orinoco Belt, Venezuela". SPE 36095, IV LACPEC. Trinidad & Tobago, April 1996.

2. Figueredo, C. and Gordillo, R.: "An Overview of Corpoven S.A. Heavy and Extra Heavy Crude Oil Upstream Business". Page 790. IV LACPEC. Trinidad & Tobago, April 1996.

3. Mirabal, M, et al.: "Impact of Foamy Oil Mechanism on the Hamaca Oil Reserves Orinoco Belt-Venezuela". SPE 36140, IV LACPEC. Trinidad & Tobago, April 1996.

4. Prats, M.: "Compaction in the U-sands of the Hamaca Area and Others Parts of the OB". Internal Note. TCA-Intevep. December 1994.

5. Huerta, M., et al,: "Understanding Foamy Oil Mechanisms for Heavy Oil Reservoir During Primary Production". SPE36749. Annual Technical Conference and Exhibition. Denver-Colorado. October 1996.

6. Gonzalez, R., and C.Bruning.: "Influence of Increased Pump Frecuency in the Production of the Orinoco Belt Foamy Extra Heavy Crude Oil". Electric Summersible Pump Workshop. Houston, Texas. May 1996.

7. Claridge, E, and Prats, M.- "A Proposed Model and Mechanism For Anomalous Foamy Heavy Oil Behavior" SPE 29243. International Heavy Oil Symposium-Calgary-Canada.June 1995.

8. Rodriguez, H., et. al.: "Stability Analysis of Horizontal Wells in Orinoco Belt, Venezuela". SPE 36076, IV LACPEC. Trinidad & Tobago, April 1996.

TABLE 1. - Reservoir and fluid properties Bare Field, Orinoco Belt

Oil Gravity, ^{o}API	9.1
Original Oil In Place, MMBLS	2500
Average Depth, ft.	3500
Net Pay, ft.	100
Average Porosity,%	30
Average Permeability, Darcy	10
Reservoir Temperature, ^{o}F	137
Original Reservoir Pressure, psi	1220
Original GOR, SCF/STB	96
Original Formation Volume Factor, RB/STB	1.088
Dead Oil Viscosity at Reservoir Temperature, cp	3000

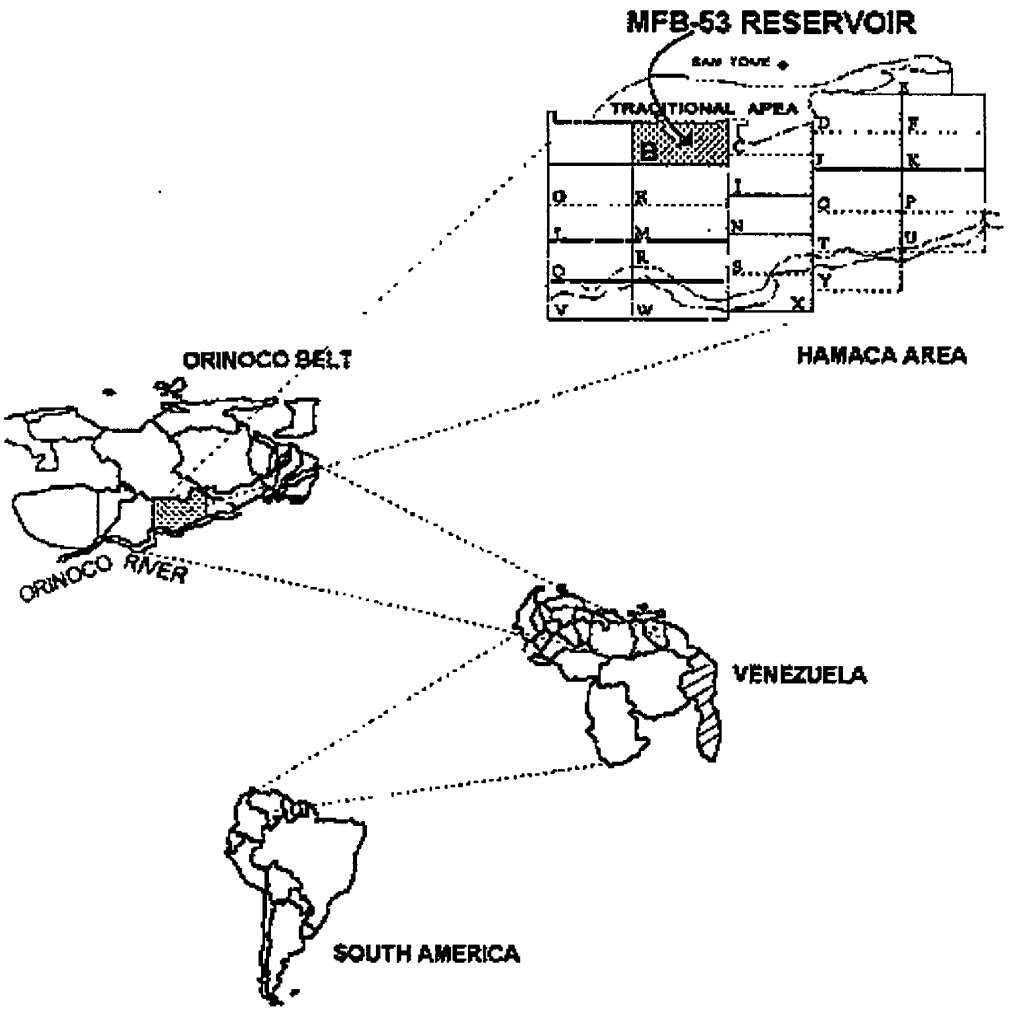

Fig.1- MFB-53 Reservoir Location Map

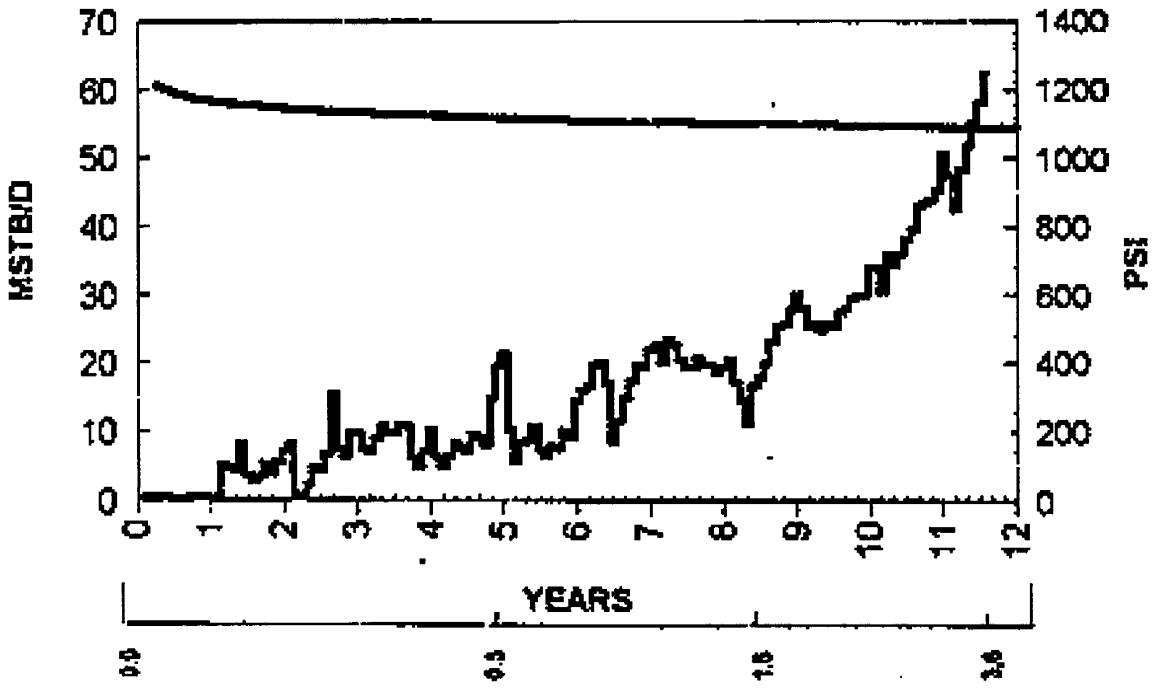

Fig. 2 - Reservoir Pressure and Production Behavior of MFB-53 Reservoir

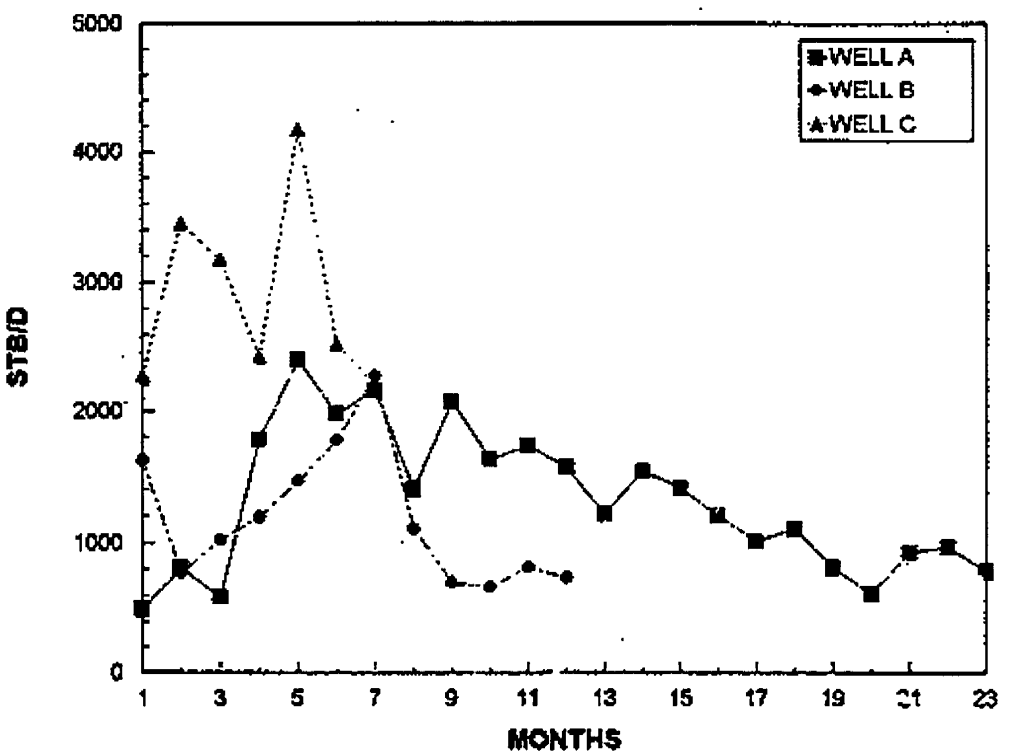

Fig. 3 - Horizontal Wells Production History, MFB-53 Reservoir

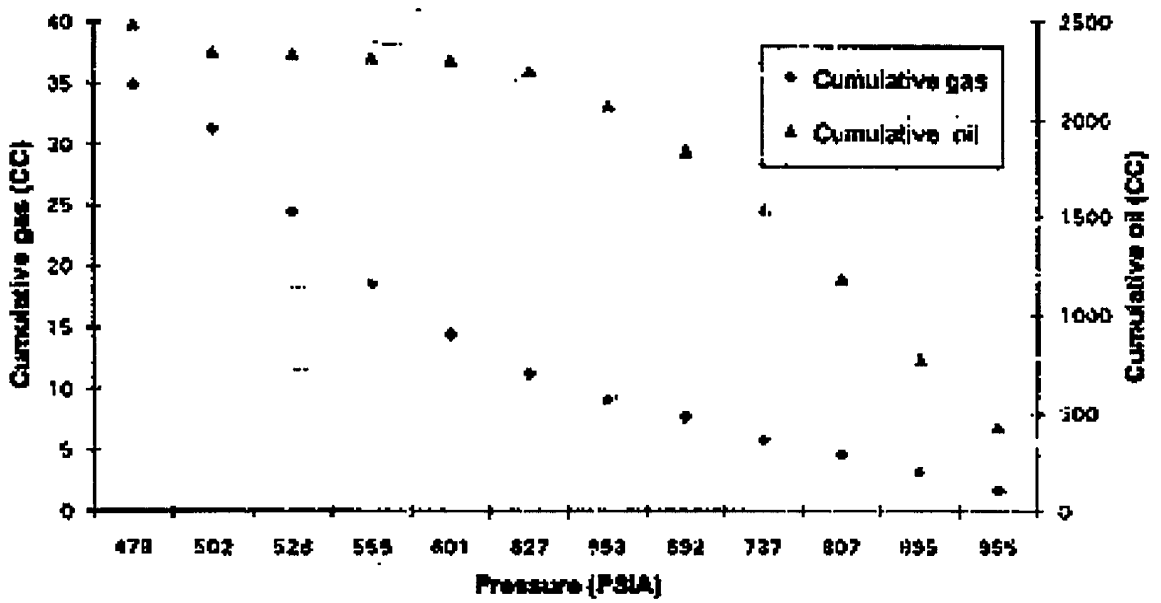

Fig. 4 - Production Profile during the Natural Depletion Test.

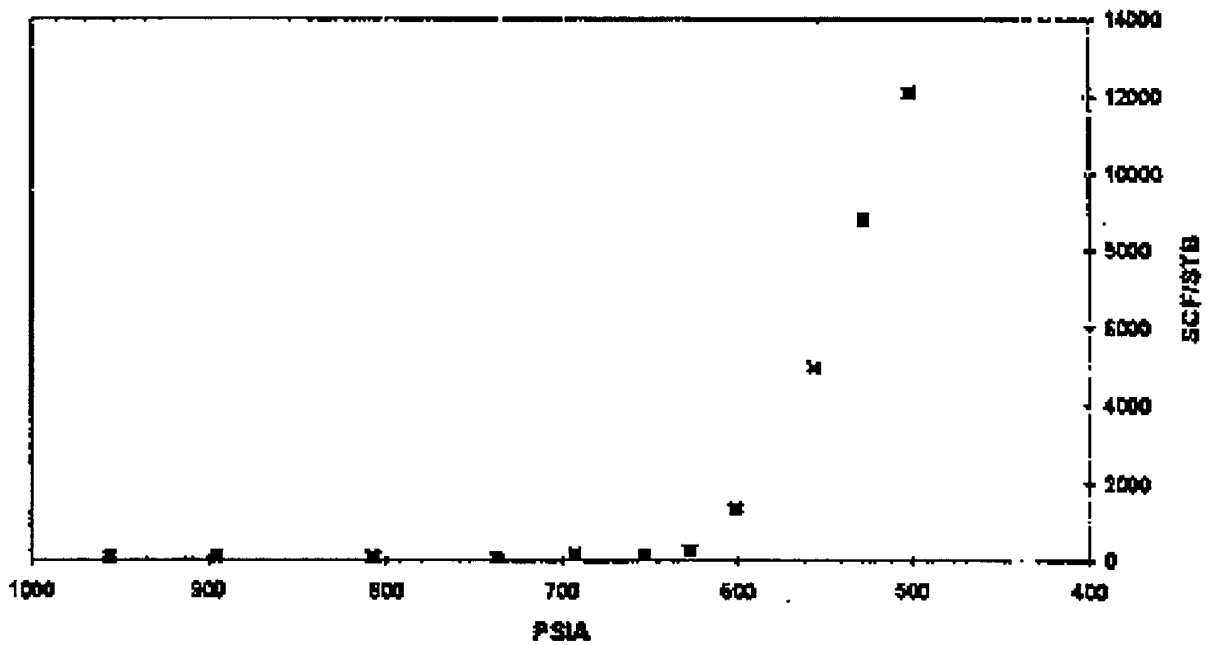

Fig. 5 - Production GOR vs. Pressure

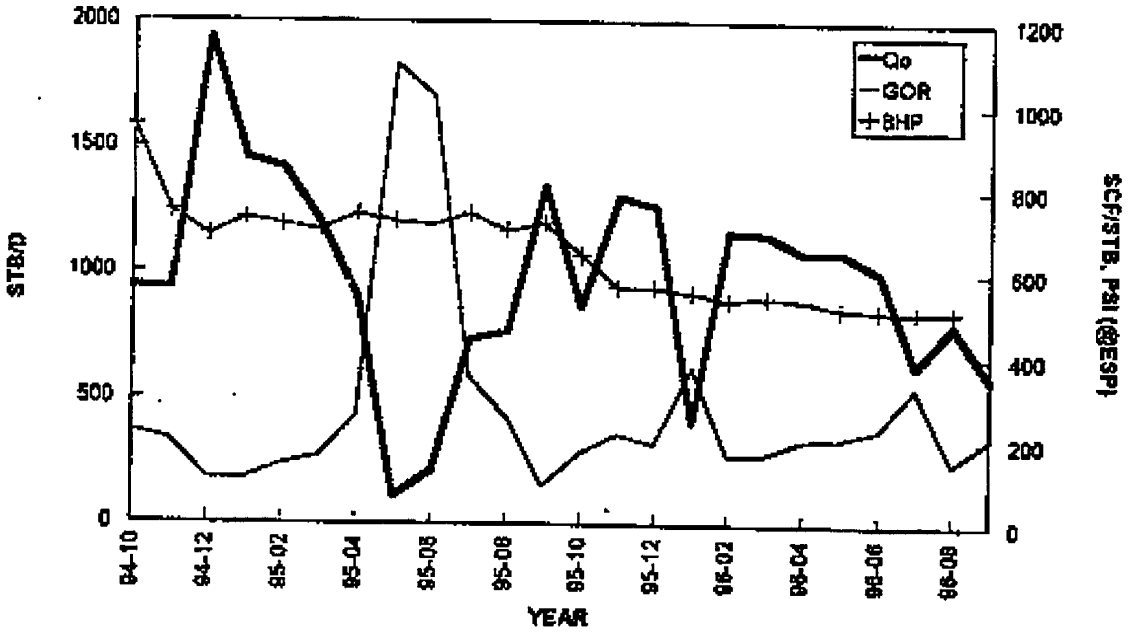

Fig. 6 - Critical Horizontal Well Behavior.

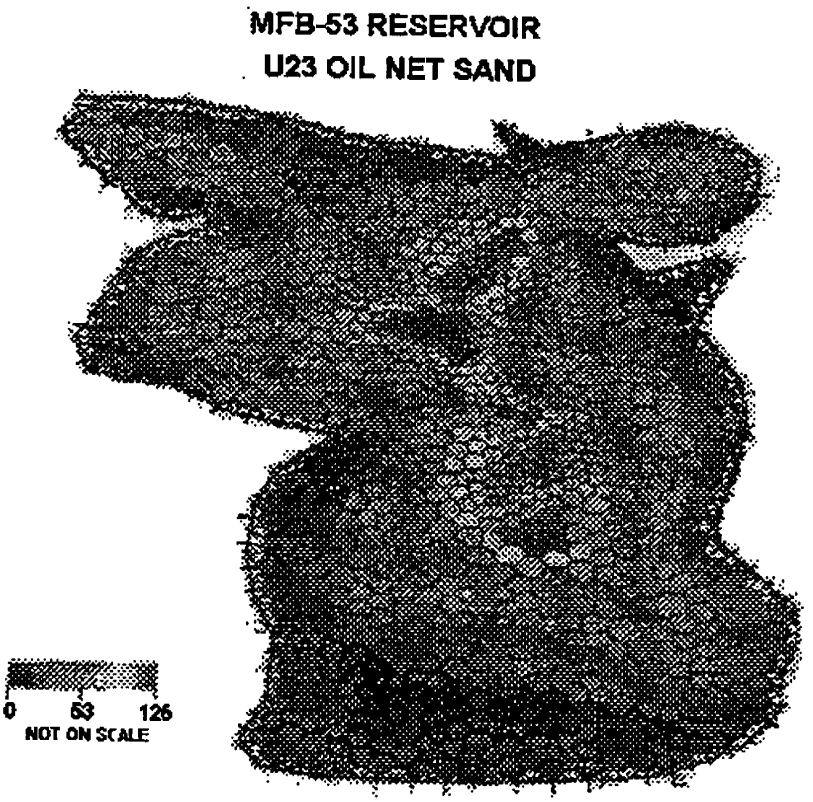

Fig. 7 - Simulation Grid

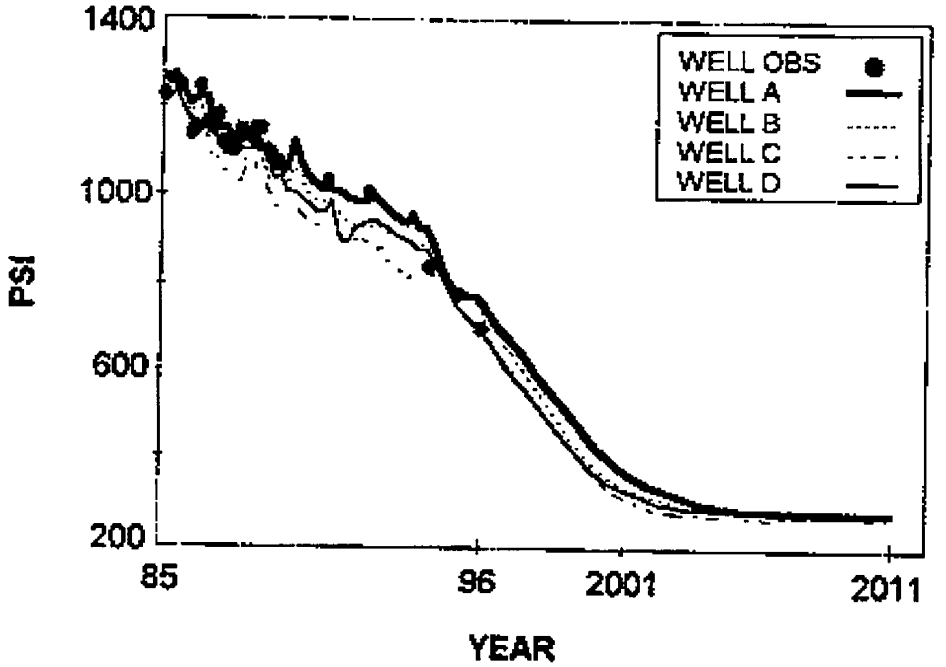

Fig. 8 - Pressure History Match - Cluster

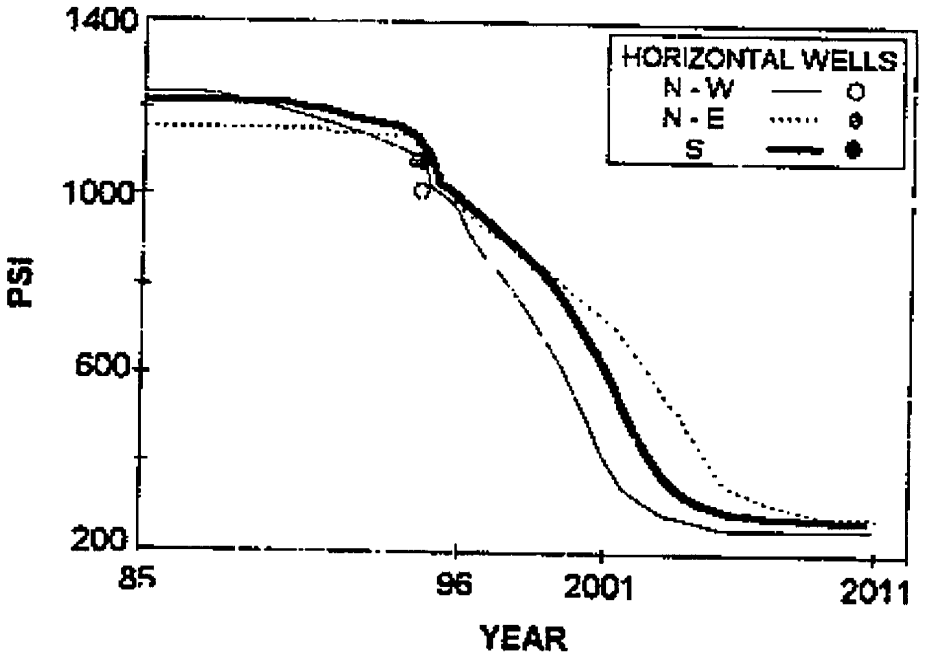

Fig. 9 - Pressure History Match - Horizontal Wells

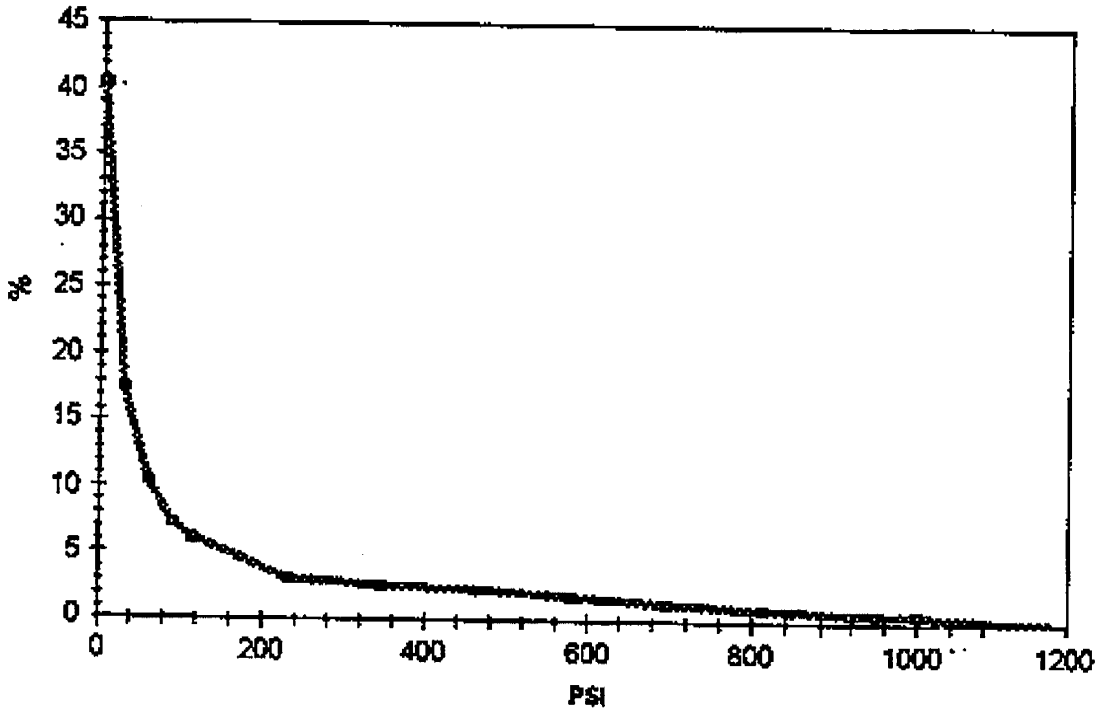

Fig. 10 - Entrained Gas Volume Factor vs. Pressure

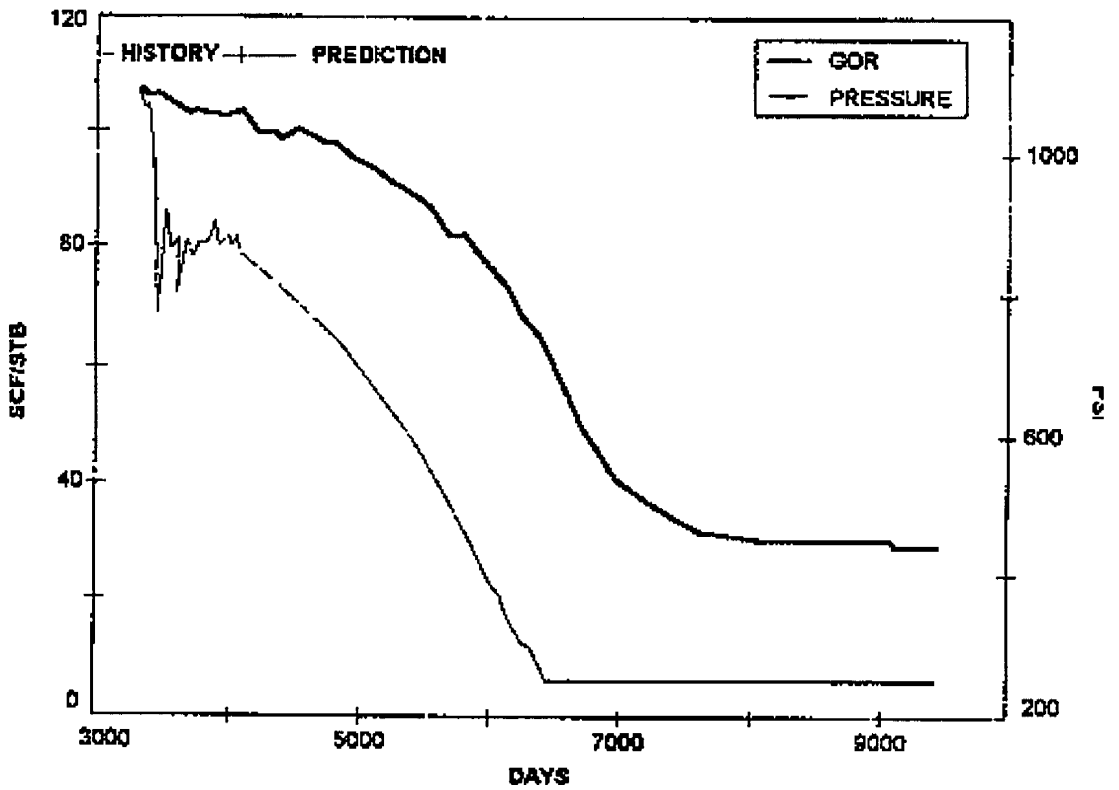

Fig. 11 - Horizontal Well. Production Profile

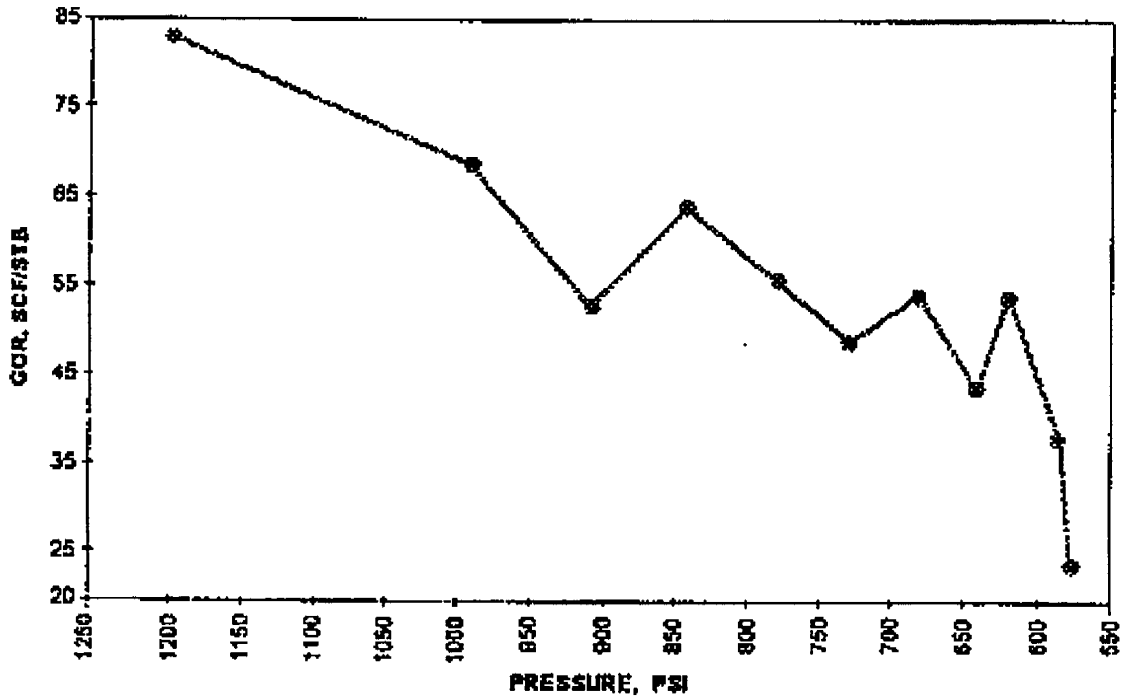

Fig. 12 - Natural Displacement Test - Vertical Cell

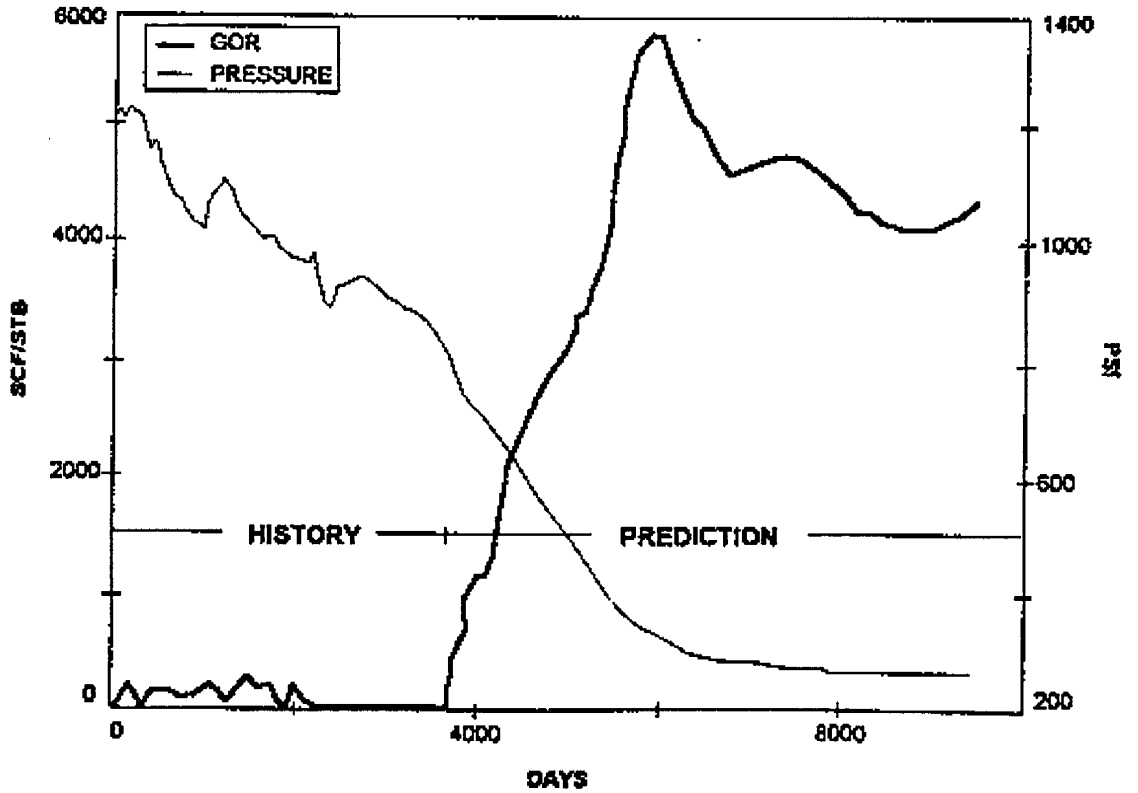

Fig. 13 - Vertical Well. Production Profile

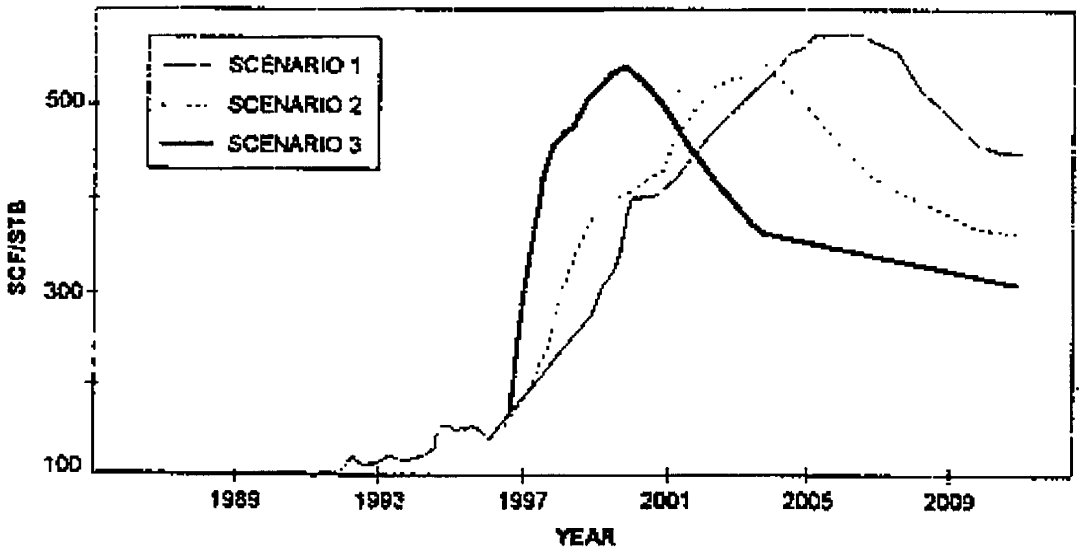

Fig. 14 - Production GOR Profile. Exploitation Strategies.

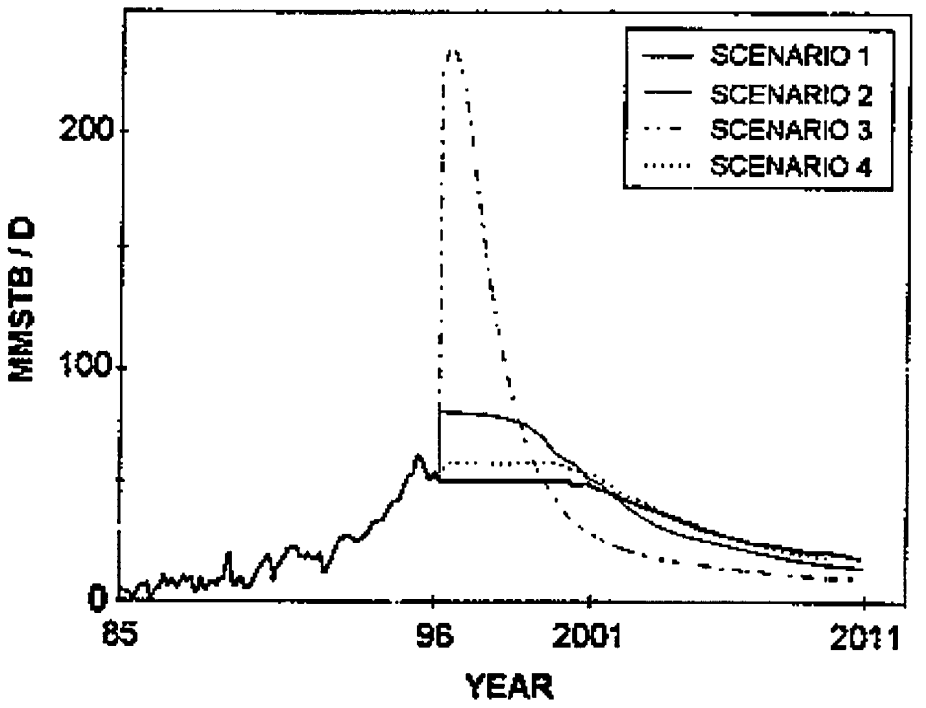

Fig. 15 - Oil Rate. Exploitation Strategies.

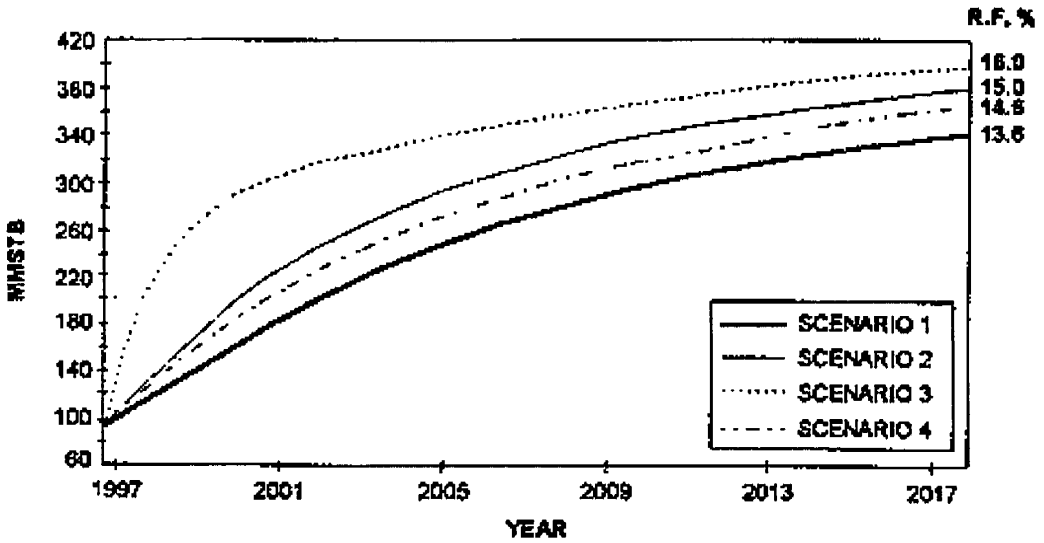

Fig. 16 - Cumulative Oil Production, Recovery Factor. Exploitation Strategies.

Task 64

DOE shall provide INTEVEP with information on the results of NIPER's thermal light oil program. This work deals with tracking the progress of DOE's light oil steamflood at Naval Petroleum Reserve # 3, Teapot Dome Field, Wyoming, and laboratory research on light oil steamflooding of oil-wet dolomitic reservoirs that contain high pour point waxy crudes.

REVIEW OF TEN YEARS STEAM FLOOD OPERATION AT NAVAL PETROLEUM RESERVE No. 3, TEAPOT DOME FIELD, WYOMING: A TIGHT, HIGHLY FRACTURED, SHALLOW, HETEROGENEOUS LIGHT OIL RESERVOIR

by

David K. Olsen

Abstract

The United States has two light oil steamflood pilots with 10 years operating experience in low permeability consolidated formations. Results of steamflood field tests in the hydraulically fractured diatomite's in the San Jaoquin Valley of California have been the subject of a number of Society of Petroleum Engineers publications since 1992 and covering 10 years operation. In contrast, this paper highlights the results of 10 years operation of the light-oil (32-34° API gravity) steamflood in a highly heterogeneous, consolidated, tight (average 37 mD), faulted, and extensively fractured Shannon sandstone at Naval Petroleum Reserve No. 3, (NPR-3) Teapot Dome field, Wyoming.

To date (1996)the Shannon steamflood has produced over 2 million barrels at a steam/oil ratio (SOR) of nearly 10. The progressive flood has steamed over 250 acres, 90 acres of which is currently being steamed with three of the five 50 MMBtu/hr steam generators. The high oil price for Wyoming sweet crude produced by the steamflood has permitted operation despite of the high SOR. Continuous improvement and modification of operation have reduced operating expense and improved profitability. These also led to better environmental compatibility. The design, operation, and performance of the steamflood is reviewed in light of the dominant role that the reservoir's complex geology plays, since both injection and production wells are greatly influenced by the localized, highly heterogeneous geology of the consolidated, tight, faulted, and extensively fractured sandstone composing the Upper and Lower Shannon. Optimization of the steamflood has depended upon accumulating and using information from pattern-specific operations.

1. Introduction

The United States has two light-oil steamflood pilots with 10 years of operating experience in low-permeability consolidated formations. Results of steam-drive field tests in hydraulically fractured diatomites in the San Jaoquin Valley of California have been the subject of a number of Society of Petroleum Engineers publications since 1992 and cover 10 years of operation. The diatomite resource in the San Joaquin Valley are estimated to contain more than 10 billion barrels of oil in place. Typical porosity of these diatomite reservoirs range from 25 to 65% and the original oil saturation varies from 35 to 70%. The large porosity and oil saturation, combined with formation thickness up to 1,000 ft and areal extents of fields up to a few square miles, yield estimates of the original oil in place (OOIP) that exceed 1×10^7 barrels (B) of oil. This oil volume is roughly comparable to the OOIP of Prudhoe Bay field, Alaska. However, diatomites are low-permeability formations (0.01–10 mD). Portions of the diatomite have been developed by hydrofracturing the reservoir and waterflood on 1-1/4 and 5/8 acre patterns. Included in the bibliography at the end of this paper are references to select publications from the petroleum literature discussing the diatomite resource, geologic setting, recovery processes that have been implemented, and results of the two thermal light-oil steamflood pilots (phase I and II) conducted by Shell Western E & P (Cal Resources) in the diatomite in South Belridge field. The diatomite lies under the very prolific Potter and Tulare unconsolidated heavy oil sands of South Belridge field. Phase I used two separate, noncommunicating hydrofractures in the lower half of the diatomite column (350 ft), where steam was injected in one well and production was from the lower half of the offset well (first 5 years of pilot operation). Phase II which operated during the second five-year period used two separate, noncommunicating hydrofractures for steam injection over the entire diatomite column (800 ft). A limited interval (300 ft) producer was located 40 ft east of the injectors, whereas a full interval producer covering the entire diatomite column (800 ft) was locate 130 ft east of the injectors. Both pilots extensively used monitoring wells to assist in tracking steam performance and fracture extension, and to provide valuable data for numerical simulation of the steamflood. Based on performance of the two pilots, engineering data, and simulation, a test of the economics of pattern flooding the diatomite could be justified. Phase III is in progress; results should be available in about 1998.

This Annex IV paper highlights the results of 10 years of operation of the light-oil (32–34° API gravity) steamflood in the highly heterogeneous, consolidated, tight (average 37 mD), faulted, and extensively fractured Shannon sandstone at Naval Petroleum Reserve No. 3 (NPR-3), Teapot Dome field, Wyoming. The target resource is much smaller, only 144 million barrels (MMB) of OOIP at the start of the steamflood. The intent of this paper is to highlight some of the lessons learned from ten years of operation of the light-oil steamflood at NPR-3. The lessons learned from this steamflood may be useful to other operators who may be considering development of other pressure-depleted,

consolidated, tight, fractured (natural or induced), or heterogeneous light-oil reservoirs. In the United States, potential light-oil steamfloodable reservoirs include not only the diatomite and Monterey shale reservoirs of California, but also many of the shallow pressure-depleted, fractured, or oil-wet reservoirs of the Mid-Continent and Appalachian basins. This paper provides a brief description of NPR-3's steamflood field geology, project history, pattern design, spacing, completions, operational problems, and performance, and a brief economic analysis.

This paper updates data and trends, but is largely based on SPE paper 30286, "An Update of Steam Injection Operations at Naval Petroleum Reserve No. 3, Teapot Dome Field, Wyoming: A Shallow Heterogeneous Light Oil Reservoir" (Doll et al., 1995).

2. Background and History

Naval Petroleum Reserve No. 3, also known as the Teapot Dome field, is a federally owned oil field, located 35 miles north of Casper, Wyoming (Fig. 1). The reserve, established by executive order of President Wilson in 1915, was at the center of the Teapot Dome scandal of the early 1920s, when much of the pressure was depleted and wells were produced at maximum rate (Curry, 1977). In the mid-1920s, the field was set aside as a petroleum reserve. The reserve was activated during World War II (1942–1945), and again produced during 1958–1976 (to mitigate loss of oil from the reserve due to development along the lease line east of the reserve). Full production was initiated in 1976 under the mandate of producing at the maximum efficient rate (Naval Petroleum and Oil Shale Reserves, 1993).

The field is about 7 miles long and 2 miles wide, with the bulk of the Shannon sandstone occurring in Sections 3 and 10. The Shannon is the shallowest of nine producing formations in the Teapot Dome anticline (Fig. 2). Development wells for all other formations are drilled through the Shannon. The Shannon is fully developed for primary production on 10-acre spacing. The Shannon reservoir has the highest productive potential of all the reservoirs in the field, 144 MMB OOIP, and currently accounts for 65% of total field production of 1,800 barrels per day (B/D). The Shannon was deposited 80 million years ago as a Cretaceous offshore bar composed of bar margin and bioturbated shelf sandstone. The upper Shannon is more areally extensive and is separated from the lower Shannon (Figs. 3 and 4) by a nonproductive siltstone. The Shannon's light-oil (32–34° API gravity) steamflood averages nearly 800 B/D, or approximately 45% of total production. Total floodable acreage in the steamflood (presence of both upper and lower Shannon) is approximately 750 acres, 250 acres of which has been or is currently (1996) being steamed using three of the five available 50 MMBtu/hour steam generators that are distributed across Sections 3 and 10.

A screening of potential methods to recover more of the Shannon's oil was begun in early 1980 (Chappelle et al., 1986). The Shannon steamflood began in 1985 as a result of the favorable production response to steam preheating in the in-situ combustion pilot carried out in the early 1980s (Sarathi et al., 1995). Favorable but mixed success of two 10-acre steamflood pilots led to commercial scale operation in 1987. Within the field (Fig. 5), each of the five 50-MMBtu/hr generators typically services a 30-acre pattern containing 25 producing wells and 10 or 12 injection wells (five or six injection pairs of wells, each injecting into a separate layer of the Shannon). Figure 5 shows the location of patterns and major fault blocks across the Teapot Dome anticline. The composite oil saturation (thousands of barrels per 10-acre block) map for both upper and lower Shannon combined is shown in Figure 6. Isopach maps of the average permeability (in mD) are shown for the lower Shannon (Fig. 7) and the upper Shannon (Figs. 7 and 8). The development of the steamflood has targeted some of the thicker, higher oil saturation blocks common to both the Upper and Lower Shannon.

3. Geologic Characterization

3.1 Geologic Setting:

Teapot Dome field is located on a small, asymmetrical, doubly plunging anticline bounded by a reverse fault and syncline to the west and the Powder River basin to the east. To the north, separated by a saddle, lies the larger Salt Creek anticline. To the south lies a structural ridge of decreasing magnitude containing the Sage Spring Creek and Cole Creek oil fields.

Steamflood operations in Teapot Dome field are in the Shannon sandstone member of the Cretaceous Steele shale formation. Locally, the Shannon consists of two stacked, heterogeneous, coarsening-upwards sandstone intervals separated by shaly nonproductive siltstone, (see Fig. 4). The lower and upper Shannon were deposited as linear, north-south–trending shelf sand ridges 200 miles from shore on the western edge of the Western Interior Seaway (Martinsen and Tilliman, 1984). The sand was transported by storm-driven, longshore currents southward along the shelf. The lower and upper Shannon in Teapot Dome field are primarily bar margin and bioturbated shelf sandstone (little or no central bar is present). Reservoir quality is highest in the central bar and declines through the transition of bar margin to interbar to saturated shelf sandstone, as shown in Figure 9.

The Shannon reservoir has an areal extent of about 3,500 acres. Another 1,600 acres of the reservoir are in East Teapot field adjacent to NPR-3. The reservoir is very asymmetrical (Fig. 5). It produces oil from depths of 200 ft on the anticlinal axis to nearly 1,500 ft about 10,000 ft east of the axis. West of the anticlinal axis, oil production extends to only 700 ft in depth, or about 1,500 ft downdip.

The tilted or asymmetrical appearance of the Shannon reservoir appears to restrict fluid migration. Migration west of the axis is restricted by a reverse fault. It is restricted in the north by a 150-ft normal fault and in the south by poor sand quality. Updip migration from the Powder River basin

to the east is the only available direction for fluid migration. Throughout the reservoir, there is no waterdrive and only minimal solution-gas drive.

Net pay sections of each sand are 10–50 ft thick with averages in the 30 to 40 ft range. Higher porosity and permeability extend north-northwest to south-southeast in both the upper and lower Shannon. Each sand has an abrupt decrease in porosity and permeability in both east and west directions (see Figs. 7 and 8). Average matrix permeability through the net pay section ranges from 10 mD to as high as 500 mD in small, localized areas. The average permeability is about 40–200 mD through the steamflood areas but is highly variable (see Fig. 4) (Jackson et al., 1987, 1992).

A 200-mD permeability area runs the length of the Shannon reservoir or about 15,000 ft. However, it is only about 1,500 ft wide at its widest section. Oil saturation is generally highest in the high-permeability areas. The high oil saturation trend runs north-south, coincident with the high permeability.

The oil saturation (Fig. 6) and trends of the mathematical average permeability (Figs. 7 and 8) do not follow the axial trend of the Teapot Dome structure. Generally, the domal axis runs northwest to southeast with easterly offsets due to normal, right lateral faulting. In the steamflood area, the structural axis turns to a more north-south direction. It lies just to the west of the high-permeability and oil-saturation trend. Primary recovery ranges from 28% of OOIP in the deeper, lower oil saturation areas in the east, to 5–6% OOIP in the shallower, high oil-saturation areas near the crest of the domal axis. Steamflood oil production as a percentage of OOIP is highest where permeability and OOIP are highest. Areas west of the anticlinal axis have the lowest oil production. Containment and recovery of injected fluids are difficult in the area west of the anticlinal axis.

3.2 Impact of the Fracture System

A doubly plunging, asymmetrical anticline like Teapot Dome typically shows faulting and fracturing in three directions: perpendicular to the axis, about 120–130° offset from the primary direction, and a tertiary direction parallel to the axis. The secondary and tertiary sets are hard to locate and measure. Each has little offset. Oil production from the underlying shale indicates their presence.

The largest offset or primary faults run N 65°E across Teapot Dome (see Fig. 5). These faults and associated fracture trends are spaced about 600–1,000 ft apart. Vertical displacement generally ranges from about 5 ft to 75 ft. The faults are nearly parallel in direction. Primary oil production from wells near these faults is two to four times that of wells away from the faults. During steamflooding, wells near faults do not show higher oil production, as they did during primary production. Steamflood wells are enhanced in secondary and tertiary directions, independent of fault proximity.

To measure the importance of the fault-fracture directions in steamflooding, injection-to-production vectors were drawn to determine oil response and water breakthrough directions (Figs. 10–12). Mapping

response to individual units (upper or lower Shannon) was not possible due to commingling of production; thus, a composite of the two units is used. Response was compared and mapped using three criteria: two by time response of three months or less (see Fig. 10 for oil and Fig. 12 for water) and the third by cumulative production (see Fig. 11). Time responses for wells with a 10 B/D production increase and wells with a produced water cut greater than 80% were each mapped. Wells with a cumulative oil production of over 20,000 stock tank barrels (STB) were also mapped. Vectors from each nearby injection well to producer were drawn, and their directions listed. The directions were plotted as 180° Rose diagrams. Injector-to-producing well direction was equated with producing well–to-injector direction.

The secondary fault-fracture direction, N65°W, was found to be the most important direction for both rapid oil and, more important, water response (Fig. 10). The reverse and downdip (S65°E) direction is equally important, overcoming a normal updip steam migratory direction. The tertiary fault-fracture direction (north-south) was the most important direction for cumulative production. It was also the second most important for oil response time. This direction nearly aligns with permeability and depositional strike.

Other response directions are also important. Water production had a secondary and tertiary response direction of nearly east-west and north-south, respectively. Oil production response by time and cumulative production had unusual directional responses of N25°E and N40°E, for which there is no explanation. Response along the primary fault direction, N65°E appears to be unimportant in the steamflood area. However, no steam injectors have been placed near a primary fault for fear of excessive channeling and poor sweep efficiency.

Present well location strategy has north-south pattern trends, injector placement N65°W of each other, and producing wells north and south, N30°E, and east-west of injectors. Design of steamflood patterns 1C, 1D, 2B, 3A, 4A, and 5A made use of these directions to varying degrees. Design of patterns 1A, 1B, and 2A ignored faulting and stratigraphy. Design of patterns 1C, 1D, and 2B are oriented north-south across primary faulting and parallel to permeability. Patterns 3A, 4A, and 5A are located parallel to primary faulting and perpendicular to permeability. The western portions of patterns 2A, 4A, the northern portion of 1A, and the southern portion of 5A are located in lower permeability areas. Patterns 1B, 2A, and 4A lie west of the anticlinal axis where the permeability is lower, formation recharge is less, and fluid migration can be extensive.

4. Analysis of Steamflood Performance

4.1 Recovery Mechanisms and the Target Oil

Major mechanisms of oil recovery in this light-oil steamflood are believed to be steam distillation, repressurization, thermal expansion of the oil, imbibition, oil viscosity reduction and alteration in oil relative permeability, and dry heat distillation (Olsen et al., 1993). Performance of the steamflood pilot has redefined the resource base which originally was believed to be only the bar margin facies of

the upper Shannon (Lawrence-Allison & Associates West, Inc., 1989). The redefined resource base for the upper and lower Shannon was established by taking into account the performance of the steamdrive pilot and by using "porosity × oil saturation" as the limiting factor (Olsen et al., 1993). A summary of the Shannon's steamfloods' performance is shown in Table 1.

4.2 Shannon Steamflood Operating Strategies

Efforts during the last few years have focused on determining the optimum economic methodology for oil production. Early steam injection strategies in the upper and lower layers of the Shannon consisted of high injection rates of 100 gallons/minute or 3,400 barrels of cold water equivalent per day (BCWE/D) per pattern of 80% steam quality per generator (measured at the exit of the steam generator). This typically resulted in quick oil production responses that peaked in 3–10 months, followed by 3–9 months of flat oil production, which then declined sharply (see Table 1 and Figs. 13 and 14 for production history of steamflood patterns). By mid-1995, cumulative steam injection of 19.6 MMBCWE had netted 1.96 MMB oil, for a cumulative SOR of 10. In contrast to the SORs of many of the steamflood projects operating in the heavy oil fields of California, annual average SORs of approximately 4 were common in 1985 but, due to better heat management, a number of operators reduced this to 2.5 in 1995 (Hong and Use, 1996). The Duri steamflood in Indonesia, the world's largest enhanced oil recovery (EOR) project, produces over 300,000 B/D. This shallow light-oil steamflood is in an unconsolidated/friable sand with 2–5 D permeability. The combination of reservoir and oil properties along with good engineering and heat management permits operation at a SOR of less than 2.5 (Kumar et al., 1996; Primadi et al., 1996). Direct costs associated with the operation of the Shannon steamflood have historically averaged between $11 and $12/B of oil produced, nearly half attributed to the cost of natural gas to fire steam generators (Olsen et al., 1993). This cost per barrel to produce oil from the steamflood is two to three times higher than Duri or many of the heavy oil steamfloods in California.

Operation of a steamflood is very cost intensive and operates much like a commercial bank. The operator supplies heat in the form of steam (the investment). But there is constant heat loss to the overburden (bank charges that never stop) and losses through produced fluids (daily carrying charges for money transactions), but there is oil that is produced (interest on the investment). The bank levies significant carrying charges and, if not enough heat is supplied, all the investment can be consumed in bank charges without producing any interest or even recovering the original investment. Unlike waterflooding or other forms of EOR, delays in producing oil by not injecting enough heat (steam quality × injection rate), having wells shut in, or having steam generators that are not functioning, constantly consumes the money in the bank. Steam breakthrough from an injector to a producing well, contributes to ineffective heat use and has to be addressed immediately or it is like throwing money out the window of the bank. Heat management, like money management, is critical to the economics of a steamflood. The investment that the bank holds is heat, and heat has to be managed to produce any interest (oil).

In early 1993, oil prices were $19/B which provided a positive operating margin. Improvements to reduce overall costs were continually being made. As oil prices declined in late 1993 to levels approaching $13.50/B, injection plans had to be significantly altered to accommodate revised budgetary requirements. Starting in October 1993, steam injection strategy changed to lower steam injection rates at moderate volumes levels of 2,400 BCWE/D (70% quality in October 1993) per pattern. Due to economic constraints of lower oil prices and reduced project funding, the rate and quality were again reduced in January 1994 to 2,050 BCWE/D of 51% quality steam. The objective was to reduce premature breakthrough and possibly improve sweep efficiency while adhering to budgetary constraints. By the end of 1993, steamflood oil production had dropped precipitously from 819 B/D to 660 B/D over a three-month period, and there were indications that the decline would continue. This decline masked increased production response from two new patterns (1D and 2B), which began receiving steam injection in July and August 1993, respectively. It was clear that the reduction in the amount of heat being injected (whether by a decrease in steam quality or injection rate) caused oil production to falter.

4.3 Project Review

To determine the variable(s) primarily responsible for the production decrease, a panel of EOR experts having experience in thermal operations was convened in June 1994 to provide assistance in trying to reverse declining oil production. Members of the panel and operations personnel reviewed the depositional environment and diagenesis that lead to the heterogeneities present in the Shannon, and examined the effect these have had upon historical injection/production response. The team believed that not only was heat management critical, but that the geology of the reservoir was a major factor controlling the economics of the project. Since both injection and production wells are greatly influenced by the localized, highly heterogeneous geology of the consolidated, tight, faulted, and extensively fractured sandstone composing the upper and lower Shannon, optimization of the steamflood has to depended upon accumulating and using information from pattern-specific operations. Some team member supported the proposition that comparison of pattern performance (pattern 1A with 2A) may not be as definitive as in some of the more homogeneous unconsolidated heavy-oil reservoirs of California.

Within the limitations of the 1994 steamflood budget, a consensus recommendation of the team was to test the hypothesis on steam quality and increase the steam quality in one pattern while holding the injection rate constant. Because steam generator pattern 5A was newer and physically isolated from the remainder of the steamflood (Fig. 5), the pattern was chosen to test the hypothesis that heat injection was the major driving force for oil production in the Shannon steamflood. The increase in steam quality and higher cost for steam generation were allocated within the revised steamflood budget.

4.4 Patterns 1B, 1C, 2A, 3A

Expansion floods with the first two steam generators serviced patterns 1B, 1C, and 2A. Steam generator 2 was shut down from December 1992 to August 1993 due to tube failure, and then was permanently shut down in December 1993, abandoning pattern 2A after it reached its economic limit. The influence of each patterns development on adjacent patterns is shown in Figure 13 and the individual performance of each pattern is shown in Figures 14 and 15.

Steam generator 3 provided injection into pattern 3A starting in February 1991, followed by generator 4 with injection into pattern 4A during June 1991. Steam injection from generator 5 started into pattern 5A in January 1993 after three months of water injection. Steam generator 3 provided steam injection for pattern 2B in August 1993, with steam injection ceasing into pattern 3A during April 1994. Steam generator 1 provided ongoing steam injection into patterns 1B and 1C until November 1994, when both patterns were shut in. Steam generator 1 provided steam injection for pattern 1D starting July 1993.

4.5 Changing Steam Injection Strategy

The original three steam generators servicing patterns 1A, 1B, 1C, 2A, 3A, and (initially) 4A injected using the philosophy of high cold-water-equivalent rate (340 BCWE/D per injector) at high steam quality (80% quality). Oil production response to this high injection rate and high-quality steam was rapid oil production that was relatively short lived, with resultant oil recovery falling below original estimates. With further steamflood expansion into steam generator 4A and 5A patterns, injection volumes were reduced to 200 BCWE/D per injector at approximately 50% quality steam. This change in injection philosophy was a result of production side response driven by economic factors of escalating operating costs, and reduced oil price which had to meet the profitability requirement.

4.6 Pattern 5A and Response to High Steam Quality

Evaluation of the steamflood by a panel of thermal experts during June 1994 resulted in changes in philosophy/mode of operation. Prior operations suggested steam distillation and repressurization were believed to be the most important recovery mechanisms of this light-oil steamflood. Based on historic performance in each pattern, the panel recommended increasing heat injection by increasing steam quality. Pattern 5A was selected on the basis of geology, production performance to date, and injection parameters. This pattern's geographic location in relation to the others and the higher water and steam injection pressures indicated an isolated and confined to test the hypothesis of heat injection is the major economic force in the steamflood. Operations monitored the injection and production of the pattern prior to and after steam quality increase. Steam generator pattern 5A injection and production data are presented in Figure 15 and Table 2.

Increased production response was noted from pattern 5A wells within the first month of increased steam quality injection. Over seven months of increased steam quality the pattern oil production

increased from 119 B/D to 163 B/D, for a 44 B/D average increase. Return on investment (ROI) for costs associated with increased fuel gas consumption and revenue based on pattern wide oil response is 2.53 during the first seven months of increased steam quality injection. In November 1994, steam quality was increased at steam generators 1, 3, and 4 as a result of the favorable oil production response observed when the steam quality was increased in pattern 5A.

Oil production response due to increased heat was most dramatic in pattern 1D is shown in Figure 14. Pattern 2B oil production has been under response to steam injection since September 1993, which masked the response to the November 1994 steam quality increase at steam generator 3. However, in all patterns, production response to increased steam quality injection is strongly influenced by the pattern-specific geologic complexity, injection rate, and pressure, and the economics associated with increased fuel gas consumption.

4.7 Pattern 1D

Steam generator 1 expansion pattern 1D, located east of prior expansion patterns 1B and 1C, had been slow to respond to steam injection. Steam injection began in July 1993 with 10 injection wells. Injection volume in pattern 1D was influenced by the requirement to have steam generator 1 supply the eight additional wells in patterns 1B and 1C.

Production response has been delayed longer than experienced in other patterns due to the low CEW injection volume. Oil and water production response during the first half of 1993 was the result of the drilling and completion of pattern 1D producers and reflects primary production. With steam injection in July 1993, water production continued to increase while oil production remained constant. Dramatic increase in oil response was noted in January 1995 due to the increase in heat injection that started in November 1994. Patterns 1B and 1C were shut in during November 1994, allowing full steam generator output to the 1D pattern.

4.8 Pattern Tailout

The petroleum literature contain numerous references to the tailout (shutdown) of steamfloods (recent publications include Hong, 1994, 1985; Ault et al., 1985; DeFrancisco et al., 1985; and Sarathi and Olsen, 1992). Most references are to steam tailout in thick, high-permeability unconsolidated sandstone reservoirs where the principal oil displacement mechanism is oil viscosity reduction. Four approaches to steam tailout are usually discussed: reduction in steam quality at the same injection rate, reduction in rate but at the same quality, simultaneous reduction in both quality and rate, and various adaptations to water alternating steam. Each have been attempted by various operators with mixed success and sometimes devastating effects, as evidenced by operators responding to low heavy-oil prices in 1986. The 1992 tailout of pattern 2A used the approach of injecting one month of water and then one month of steam. Oil production dropped sharply after the second cycle and the experiment was terminated.

Other approaches to tailout in the Shannon including a cold water waterflood in other patterns, but assessment of performance and adoption of a standard technique is incomplete.

4.9 *Production Operations*

Wells that are influenced by the steamflood require a higher maintenance compared to the field's wells producing on primary) and some innovative techniques. Scale deposition in areas where pressure drops occur have been a continuing problem. A high-temperature scale inhibition program was initiated in November 1987 (Doll et al., 1992). This program greatly reduced the scaling problem, but has not eliminated it. Soft calcium-carbonate scale is deposited in the perforations, on strainers of rod pumps, and in the top three joints of tubing. This scale has caused very erratic well tests and significant loss of production due to inoperative wells that are not pumped.

Several types of acid jobs were performed with varying concentrations of hydrochloric acid (HCl) and various additives. It was concluded that an effective acid treatment program could be applied with small amounts of acid injected by NPR-3's chemical truck and personnel. The average treatment is 10 barrels of 5% HCl displaced to the top of the perforations. The well is shut in for eight hours and then returned to production. This treatment costs is $500 and is approximately 90% effective in preventing pulling pump jobs if it is done before the pump becomes stuck. Approximately 50% of these small acid jobs actually increased the oil production rate an average of 50%. The increase gradually declines over the following 45 days. Scale squeezes are performed on the wells that responded best to acid. These squeeze treatments have been successful in inhibiting scale buildup for 2–4 months. The average payout for these acid jobs is 19 days based on $16/B oil, not including the cost avoidance for preventing pump pulling jobs.

Using pump-off controllers in the steamflood has greatly enhanced the ability to detect and mitigate the negative effects from scale buildup. By having continuous downhole surveillance, scale deposition in the pump can be detected at an early stage and treated before it causes downtime and wear on the pump. The pump-off controllers are one of the most cost-effective/cost-saving devices in the field.

4.10 *Operating Cost Reductions*

The water treatment facility operating costs have been reduced by lowering salt and chemical costs by improved surveillance of water softening operations and a reduction in water-treating chemicals (Fig. 16). Savings of $180,000 in one fiscal year (12 months) was the result of reduction in salt consumption due to brine reuse during the softener resin bead regeneration and the substitution of a commodity purchased pH control agents rather than additional cost savings.

During 1995 and 1996, biotreatment of produced water from the steamflood (6,000 B/D) has reduced water disposal costs by as much as $1.50/B. The biotreatment combines the steamflood-produced water with 30,000 B/D of low-salinity produced water obtained from Tensleep oil production. Produced water

is gravity fed to a large lagoon and settling pond (surface biotreatment facility), aerated, and discharged to a marsh filled with cattails. This alternate water disposal method has significantly reduced chemical treatment costs on water disposal wells, eliminated some pumps that had been used for subsurface water disposal, and provides a badly needed consistent water source for downstream grazing of animals.

5. Future Direction of Program

The future direction of the Shannon light-oil steamflood depends on several technical, economic, and operational factors. The following is a brief summary of the current and planned activity associated with the Shannon steamflood.

5.1 Infill Drilling

Drilling on the periphery of the steamflood patterns is common practice in an attempt to modify original patterns to capture mobilized oil moving off pattern. The current drilling program focuses on oil production in the fractured shale (Steele and Niobrara formations) underlying the Shannon. If the shale is not productive, then cement plugs are set to complete the well as a Shannon producer. Several shale wells were recompleted in the Shannon in 1995–1996. Initial oil production rates have been in the range of 30 B/D plus 150 B/D of water, reflecting the influence of the steamflood.

5.2 Drilling/ Completion Costs

Drilling costs associated with the Shannon steamflood are relatively low due to the reservoirs shallow depth (250–750 ft from surface). Some costs are incurred due to the dual layer nature of the Shannon, with each layer being perforated and stimulated (small hydraulic fracture) separately. The total cost of a new producer, including completion, flowline, pumping unit, and labor, is approximately $78,000. Perforation and stimulation costs accounting for more than one-third of the producers total cost. The cost of a new injector is approximately $50,000, which includes the wellhead assembly, chokes, and meter run. The injection wells are completed in either upper or lower Shannon with limited stimulation.

5.3 New Patterns or Expansion of Existing Patterns

There are no scheduled plans for expansion patterns of the Shannon steamflood. Expansion in future years may be limited to individual sets of injectors surrounded by two or more new producers, with other existing wells used to fill out unflooded portions of a pattern. The economics of mini-expansion appear to be favorable; however, the success of this investment is particularly sensitive to oil price, gas purchase price, and drilling cost. Volatility in oil price has been the greatest obstacle to expansion. Future plans will focus upon smaller capital investments that take advantage of existing well location and oil production response.

5.4 Fuel Gas Purchase Price

The purchase of natural gas to fire the steam generators is the largest operating expense of the Shannon steamflood. The 1995 purchase price is approximately $1.80/MMBtu (long-term contract price). Current spot prices for natural gas purchase are significantly lower than the current contract price, and efforts are being made to reduce the fuel gas price even further.

5.5 Network Steam Generator Distribution Lines

During 1995, the design of surface steam injection lines was completed. This allows for networking the steam distribution system to insure that temporary loss of a steam generator does not interrupt steam injection in a pattern. Patterns 4A and 1D, and 2B and 1D have been combined. By reducing the number of operating steam generators from the original five to two by the end of calendar year 1996 will also reduce fuel gas consumption. This network strategy could eliminate the disastrous effects previously observed in individual steamflood patterns when steam generators are incapacitated for weeks or months. Cyclic steam injection by pattern and/or within patterns is under consideration.

6. Summary

1. Knowledge of optimum injection strategies in each pattern is needed and must be applied if the steamflood is to remain economic. Because pattern step out is dominated by geologic and reservoir conditions, adjustments in injection rate and steam quality and the drilling of properly placed infill wells are needed to maximize pattern economics.
2. Production response is tied closely to heat injected. Increasing steam quality in the generator 5A pattern from 52% to 75%, while holding injection rate constant, resulted in an incremental production increase of 44 B/D of oil. An average 153 MCF/D in additional fuel gas purchase was needed for the quality increase which provided a 2.53 return on the investment in additional gas.
3. In general, a moderate rate (205 BCWE/D per well)/high quality (75%) steam injection strategy appears to be a more-optimum method of maximizing economic Shannon steamflood operations. This theory should be substantiated after acquiring another year of production information.
4. Since 1985, cumulative steam injection (through mid-1995) was 19.6 MMBCWE, resulting in 1.96 MMB of oil, for a cumulative SOR of 10.0. Higher sweet-oil prices make the Shannon steamflood economic, but the SOR must be reduced to remain economically competitive.
5. Innovative cost reductions, and environmentally responsive surface disposal of produced water have helped reduce direct operating costs to less than $9.50/B of oil.
6. The use of pump-off controllers on producers provides immediate information in monitoring injection/production operations, instead of relying on weekly or monthly test information. Acid treatments to reduce carbonate scale in producing wells can now be scheduled sooner, in addition to

optimizing the frequency of well-testing operations. This information enhances the operation of the steamflood.

7. Acknowledgment

The author thanks the U.S. Department of Energy Naval Petroleum and Oil Shale Reserve—Colorado, Utah, Wyoming and its contractor, Fluor Daniel NPOSR, for providing data and the opportunity to work on this project analysis. The author also thanks the coauthors of SPE papers 25786, 30286, and 37565, which provided a background for this report.

8. Bibliography

Ault, J. W., W. M. Johnson, and G. N. Kamilos, 1985. Conversion of Mature Steamfloods to Low-Quality Steam and/or Hot-Water Injection Projects, SPE paper 13604 presented at the 1985 California Regional Meeting, Bakersfield, CA, (March 27–29).

Chappelle, H. H., G. P. Emsurak Jr., and S. L. Obernyer, 1986. Screening and Evaluation of Enhanced Oil Recovery at Teapot Dome in the Shannon Sandstone: A Shallow, Heterogeneous Light-Oil Reservoir, SPE/DOE paper 14918 presented at the 1986 SPE/DOE Fifth Symposium on Enhanced Oil Recovery, Tulsa, OK, (April 20–23).

Curry, W. H., 1977. Teapot Dome—Past, Present and Future, *AAPG Bulletin*, (May): 61: 671–697.

DeFrancisco, S. T., S. J. Stanford, and K. C. Hong, 1985. Utilizing WASP and Hot Waterflood to Maximize the Value of a Thermally Mature Steam Drive in the West Coalinga Field, SPE paper 29665 presented at the 1985 California Regional Meeting, Bakersfield, CA, (March 27–29).

Doll, T. E., M. L. Tyler, and R. E. Dutton, 1992. Shallow, High-Gravity-Steamflood Economics Improved by New Application of High-Temperature Scale Inhibitor, SPE paper 24338, presented at the 1992 Rocky Mountain Regional Meeting, Casper, WY, (May 18–21).

Doll, T. E., D. K. Luers, G. R. Strong, R. K. Schulte, P. S. Sarathi, D. K. Olsen, and M. L. Hendricks, 1995. An Update of Steam Injection Operations at Naval Petroleum Reserve No. 3, Teapot Dome Field, Wyoming: A Shallow Heterogeneous Light Oil Reservoir, SPE paper 30286 presented at the International Heavy Oil Symposium, Calgary, Alberta, Canada, (June 19-21).

Hong, K. C., 1985. Guidelines for Converting Steamflood to Waterflood, SPE paper 13605 presented at the 1985 California Regional Meeting, Bakersfield, CA, (March 27–29).

Hong, K. C., 1994. Effects of Steam Quality and Injection Rate on Steamflood Performance, Society of Petroleum Engineers Reservoir Engineering, (November): 290–296.

Hong, K. C., and D. J. Use, 1996. Economic Potential and Optimum Steamflood Strategies for Trough Reservoirs of San Joaquin Valley, California, paper presented at the 1996 AAPG Annual Meeting, San Diego, CA (May 19-22).

Jackson, S. J., M. M. Chang, and D. K. Olsen, 1992. Synthesis of Available Structural Data and Analysis of Injection/Production Data in Steam Generator Pattern 3A Area, Shannon Sandstone, Naval Petroleum Reserve No. 3, Teapot Dome field, Wyoming, Department of Energy Report NIPER-602, (June).

Jackson, S., M. Szpakiewicz, and L. Tomutsa, 1987. Geological Characterization and Statistical Comparison of Outcrop and Subsurface Facies: Shannon Shelf Sand Ridges, U.S. Department of Energy Report NIPER-214, (September).

Kumar, M., A. A. Reed, M. E. Smith, D. S. Mims, E. J. Hanzlik, and S. J. Gross. 1996. Strategic Recovery Processes for Rindu Development, paper presented at the 1996 AAPG Annual Meeting, San Diego, CA (May 19-22).

Lawrence-Allison & Associates West, Inc. Wyoming Division, 1989. Shannon Reservoir Steamflood Economic Assessment, U.S. Department of Energy internal report, (March).

Martinsen, R. S., and R. W. Tilliman, 1984. The Shannon Shelf-Ridge Complex, Salt Creek Anticline Area, Powder River Basin, Wyoming, SEPM Special Publication No. 34, Tulsa, OK, (May): 85–142.

Naval Petroleum and Oil Shale Reserves, Annual Report of Operations Fiscal Year 1993. U. S. Department of Energy Report DOE/FE-0300.

Olsen, D. K., P. S. Sarathi, M. L. Hendricks, R. K. Schulte, and L. A. Giangiacomo, 1993. Case History of Steam Injection Operations at Naval Petroleum Reserve No. 3, Teapot Dome Oilfield, Wyoming: A Shallow Heterogeneous Light-Oil Reservoir, SPE paper 25786 presented at the 1993 SPE International Thermal Operations Symposium, Bakersfield, CA, (February 8–10).

Olsen, D. K., P. S. Sarathi, T. E. Doll, K. K. Yung, S. C. Knudson, L. Callaway, and M. L. Hendricks, 1997. Review of 10 Years Steam Flood Operation at Naval Petroleum Reserve No. 3, Teapot Dome Oilfield, Wyoming: A Tight, Highly Fractured, Shallow Heterogeneous Light-Oil Reservoir, SPE paper 37565 to be presented at the 1997 SPE International Thermal Operations and Heavy Oil Symposium, Bakersfield, CA, (February 10–12).

Primadi, H., W. D. Jackson, G. J. Mcnaboe, L. Bamahry, H. Semimbar, A. Desman, B. Setiydai, H. Dedi, M. Djamaludin, and I. Z. Batubara, 1996. Geologic Input to Work Processes at Duri Field, Indonesia, paper presented at the 1996 AAPG Annual Meeting, San Diego, CA (May 19-22)

Sarathi, P. S., D. K. Olsen, and C. R. Williams, 1995. Naval Petroleum Reserve No. 3 (NPR-3), Teapot Dome Oilfield, Wyoming: Case History of the In Situ Combustion Pilot Operations, Paper ISC-13 in Proceedings of Symposium on Field Application of In Situ Combustion—Past Performance/Future Application, April 21-22, 1994, Tulsa, OK. Edited by P. Sarathi and D. Olsen, U.S. Department of Energy Report NIPER/BDM-0086, (January): 179–202.

Sarathi, P. S., and D. K. Olsen, 1992. Practical Aspects of Steam Injection Processes—A Handbook for Independent Operators, U.S. Department of Energy Report NIPER-580, DE92001070, (October).

Select References to Steaming California Diatomite Reservoirs:

Dale, B. A., G. M. Narahara, and R. M. Stevens, 1996. A Case History of Reservoir Subsidence and Wellbore Damage Management in the South Belride Diatomite Field, SPE paper 35658 presented at the 1996 SPE Western Regional Meeting, Anchorage, AK, (May 22-24).

de Rouffignac, E. P., P. L. Bondor, J. M. Karanikas, and S. K. Hara, 1995. Subsidence and Well Failure in the South Belridge Diatomite Field, SPE paper 29626 presented at the 1995 SPE Western Regional Meeting, Bakersfield, CA, (March 8–10).

Johnson, R. M., and G. T. Shahlin, 1995. Interpretation of Steam Drive Pilots in the Belridge Diatomite, SPE paper 29621 presented at the 1995 SPE Western Regional Meeting, Bakersfield, CA, (March 8–10).

Kovscek, A. R., R. M. Johnson, and T. W. Patzek, 1995. Evaluation of Rock/Fracture Interactions During Steam Injection Through Vertical Hydrofractures, SPE paper 29622 presented at the 1995 SPE Western Regional Meeting, Bakersfield, CA, (March 8–10).

Kumar, M., and F. D. Beatty, 1995. Cyclic Steaming of Heavy Oil Diatomite, SPE paper 29623 presented at the 1995 SPE Western Regional Meeting, Bakersfield, CA, (March 8–10).

Patzek, T. W., 1992. Surveillance of South Belridge Diatomite, SPE paper 24040 presented at the 1992 SPE Western Regional Meeting, Bakersfield, CA, (March 30-April 1).

Shahlin, G. T., and R. M. Johnson 1995. Imaging Hydraulic Fractures Using Temperature Transients in the Belridge Diatomite, SPE paper 29624 presented at the 1995 SPE Western Regional Meeting, Bakersfield, CA, (March 8–10).

Stosur, J. J., and A. David, "Petrophysical Evaluation of the Diatomite Formation of the Lost Hill Field, California," Journal of Petroleum Technology, Oct. 1976, v. 28, no. 10 , 1138-1144.

TABLE 1

Shannon Steamflood Pattern Description and Performance as of January 1, 1995

Description	Pilot	Pilot								
Generator, pattern name	1A-N	1A-S	1B	1C	1D	2A	2B	3A	4A	5A
Size, acres	10	10	15	15	30	30	30	30	30	30
Pattern alignment, geometry	Inv 9-spot	Inv 5-spot	E-W line drive	N-S line drive	N-S line drive	E-W line drive	N-S line drive	Fault block line drive	Fault block line drive	NW-SE line drive
Pattern orientation[1]	Exp	Exp	Exp	Exp	Exp	Exp	Exp	Exp	Exp	Exp
Injectors, wells (pairs)	2 (1)	2 (1)	6 (3)	6 (3)	10 (5)	10 (5)	10 (5)	10 (5)	10 (5)	10 (5)
Producers, well	[2]17		22	23	19	31	22	24	24	24
Temperature monitor, wells	1	4	0	0	0	0	0	0	0	0
Infill wells drilled after stm inj	4	-	2	2	0	8	0	4	3	0
Start of steam injection, date	10/85	10/85	12/88	8/89	7/93	1/89	8/93	2/91	7/91	1/93
End of steam injection, date			11/94	11/94	--	12/93	--	8/93	--	--
Prod. well frac size, lb sand			6,000 +	12,000	12,000	12,000 +	12,000 +	12,000 +	12,000 +	12,000 +
Cumulative oil, B			261,482	268,603	71,839	310,356	100,548	216,425	228,328	128,602
Cumulative steam, B			2,460,789	2,439,225	722,447	3,781,769	909,051	2,697,739	2,736,050	1,496,268
Steam quality at generator, %	80	80	80	80	[3]Var	80	[3]Var	80	80	[3]Var
Steam rate, BCWE/D/Inj	340	340	283	283	[3]Var	340	[3]Var	340	340	[4]Var
Start of Tailout, month			6/93	6/93		4/93	4	2/93	6/93	
Dec. 1994 production, B/D			42	74	109	17	242	42	76	163
Estimated OOIP, B			740,800	740,800	1,461,650	1,461,650	1,481,650	1,481,650	1,461,650	1,461,650
Recovery of OOIP to date, %			35	36		21		14.6	15.6	8.8
Performance Assessment	Good	Poor	Good	Good	[6]TET	Fair	Good	Fair	Fair	Good

[1] Pattern Design 1A, 1B, and 2A ignored faulting and stratigraphy; 1C, 1D, and 2B oriented N-S across primary fault and parallel to permeability; and 3A, 4A, and 5A are located parallel to primary faulting and perpendicular to permeability.

[2] Total 17 producing wells for pattern 1A (5 Upper Shannon, 4 Lower Shannon, 4 original 10-acre wells, 4 infill intercept wells).

[3] Var = Variable steam quality 70% at 2,400 BCWE/D/pattern from startup, reduced to 51% quality at 2,050 BCWE/D/pattern starting January 1994, increased to 70% quality at 2,050 BCWE/D starting November 1994.

[4] Pattern 5A started 10/92 as hot water. Steam quality averaged 52% at 2,053 BCWE/D; increased to 75% quality at 1,895 BCWE/D starting July 1994.

[5] WASP = Water-alternating-steam as tailout. Alternating one month of water then one month of steam injection.

TABLE 2

Steam Generator Pattern 5A
Injection and Production Data

	Prior to Quality Increase	Post Quality Increase
Wells on Production	23	23
Oil Production, B/D	119	163
Water Production, B/D	1974	2291
Wells on Injection	10	10
Injection, BCWE/D/well	205.3	189.5
Steam Quality, %	52.4	75.3
Generator Discharge Pressure, psi	927	1087
Generator Steam Temperature, °F	551	556
Generator On-line, hr/D	23.95	23.80
Fuel Gas Consumption, MCF/D	595	748

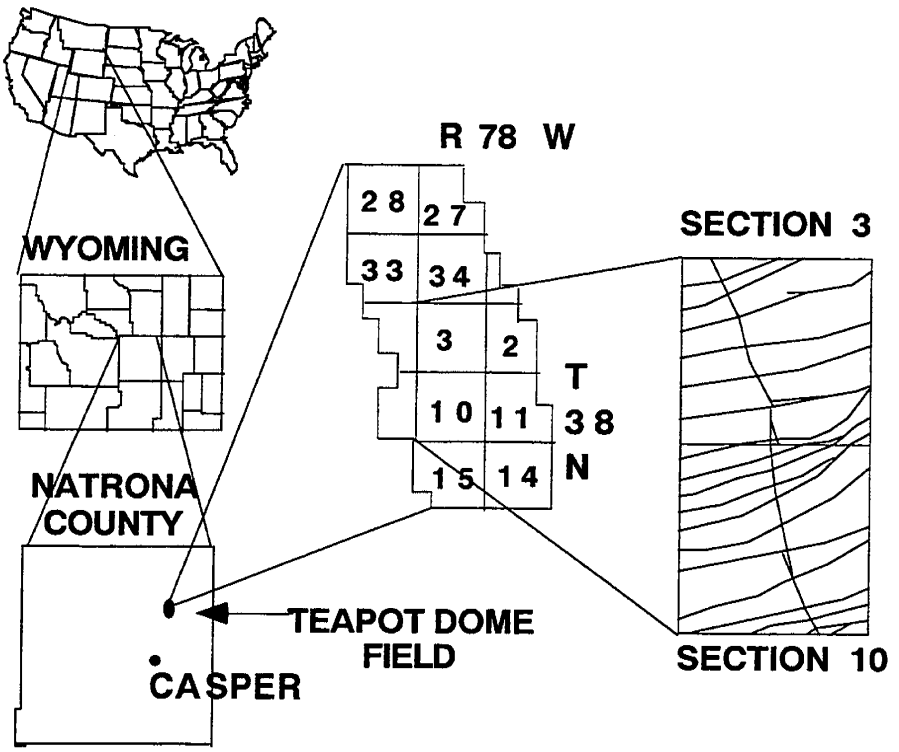

Fig. 1. Location of Teapot Dome Field Natrona County, Wyoming, showing the outline of the field and major faults within Sections 3 and 10, location of the Shannon steamflood.

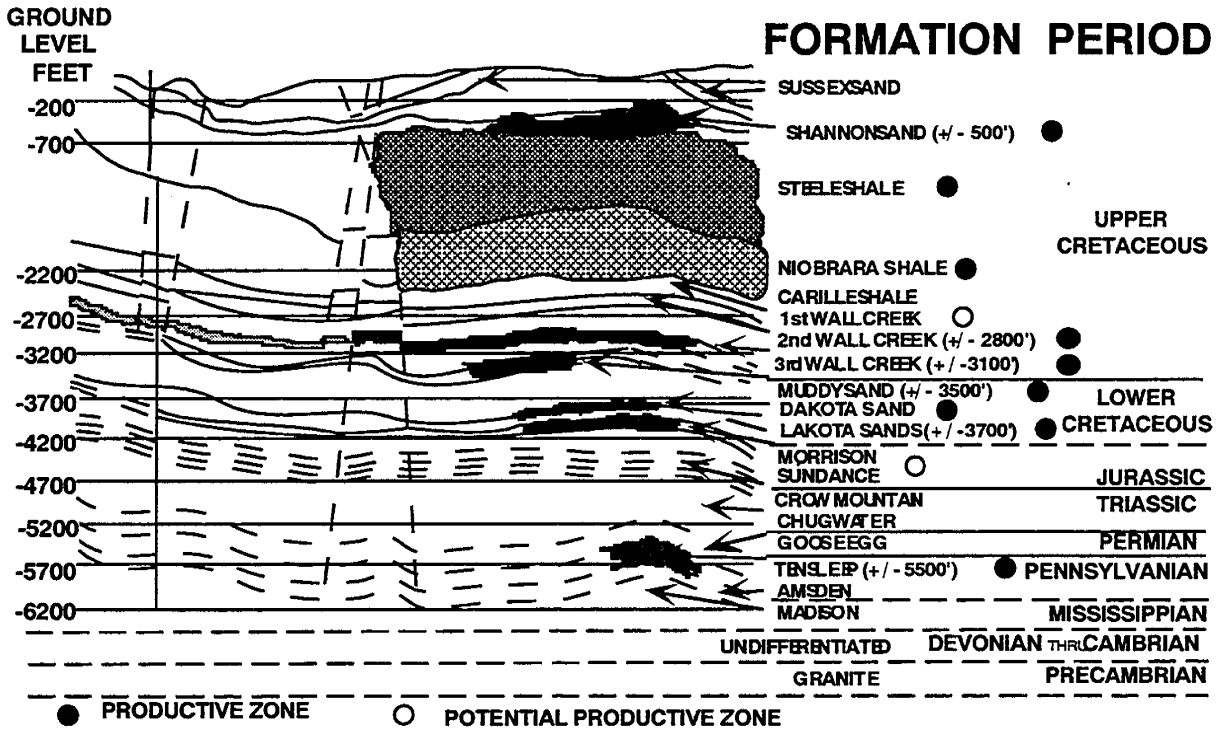

Fig. 2. Geologic column at Teapot Dome Field.

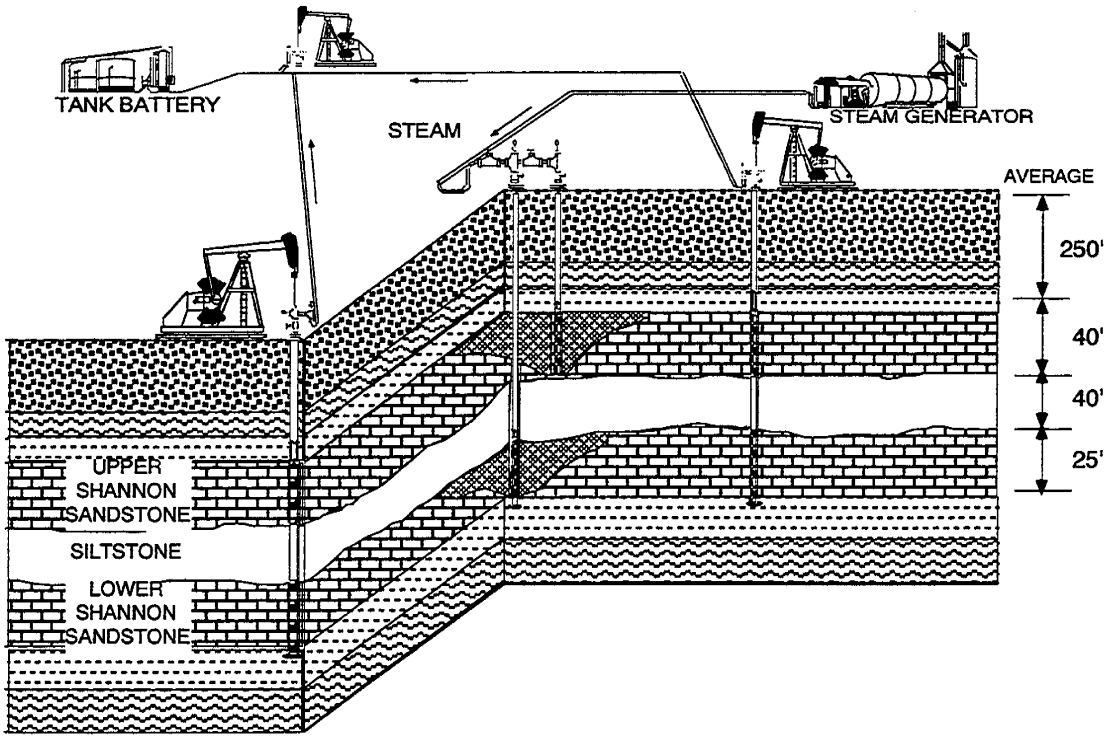

Fig 3. Schematic of Shannon steamflood showing dual steam injectors. Steam is injected into the Upper or Lower Shannon and production is comingled.

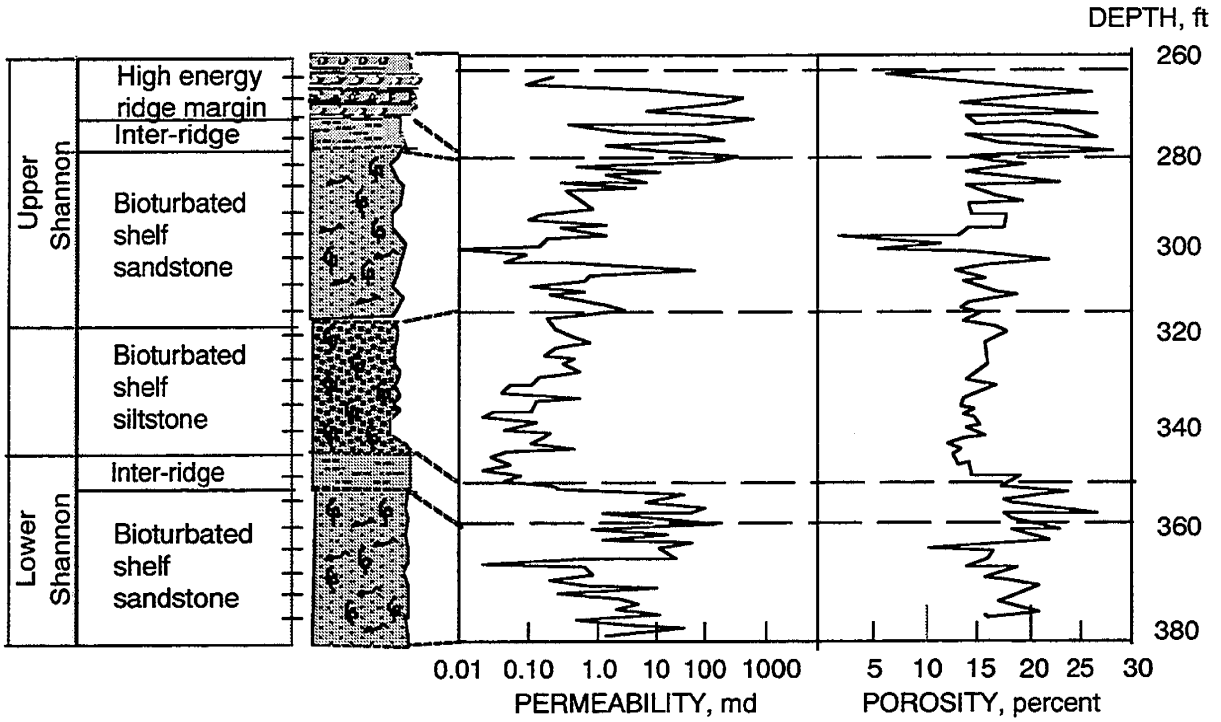

Fig 4. Limited lithology of Upper and Lower Shannon showing permeability and porosity profiles for well 5566 SX3-FP in the in situ combustion pilot (Jackson et al., 1987).

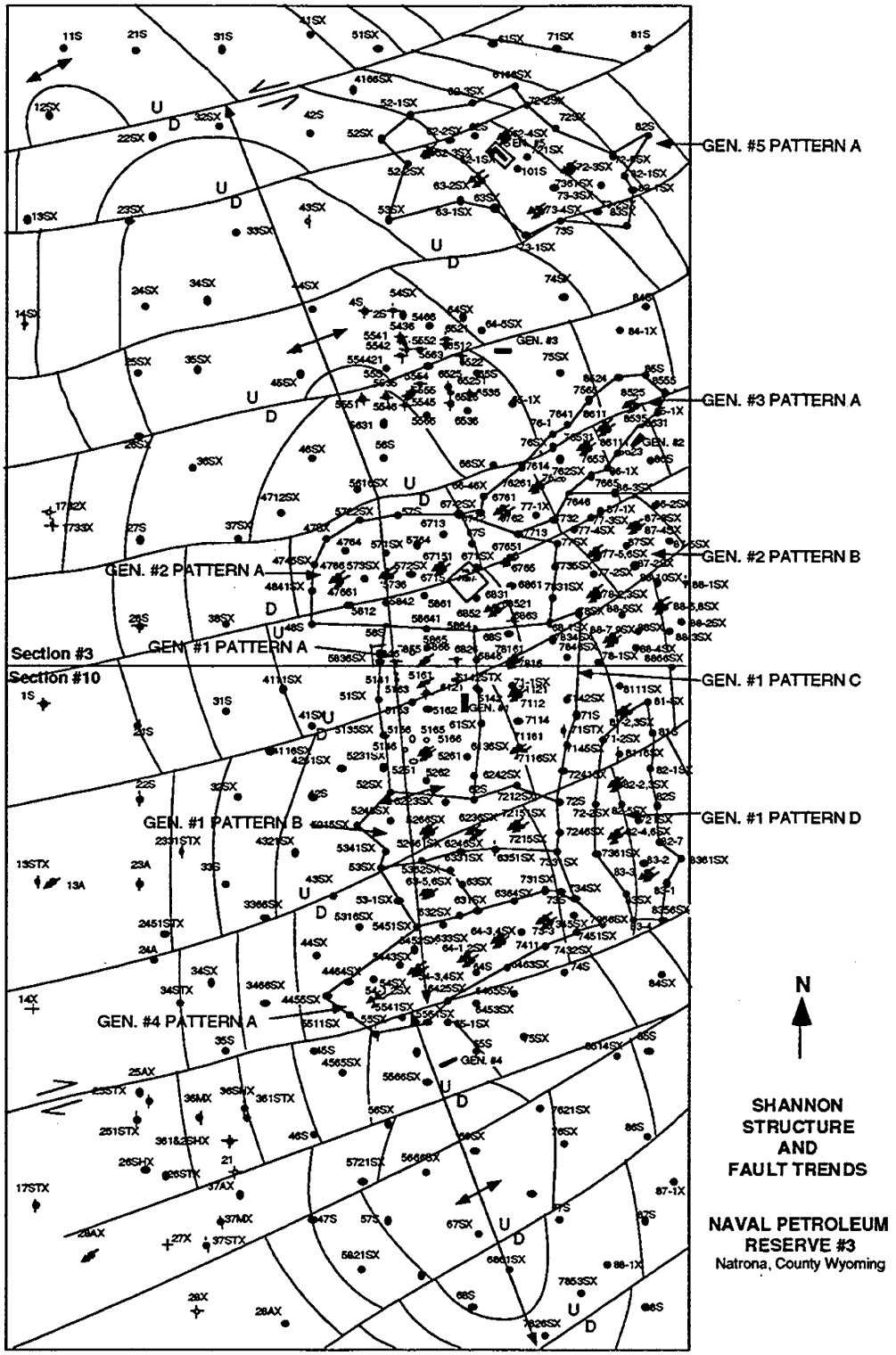

Fig 5. Shannon structure and faults in Sections 3 and 10 of Teapot Dome field. Steam generators, the water treatment plant and steamflood pattern are listed.

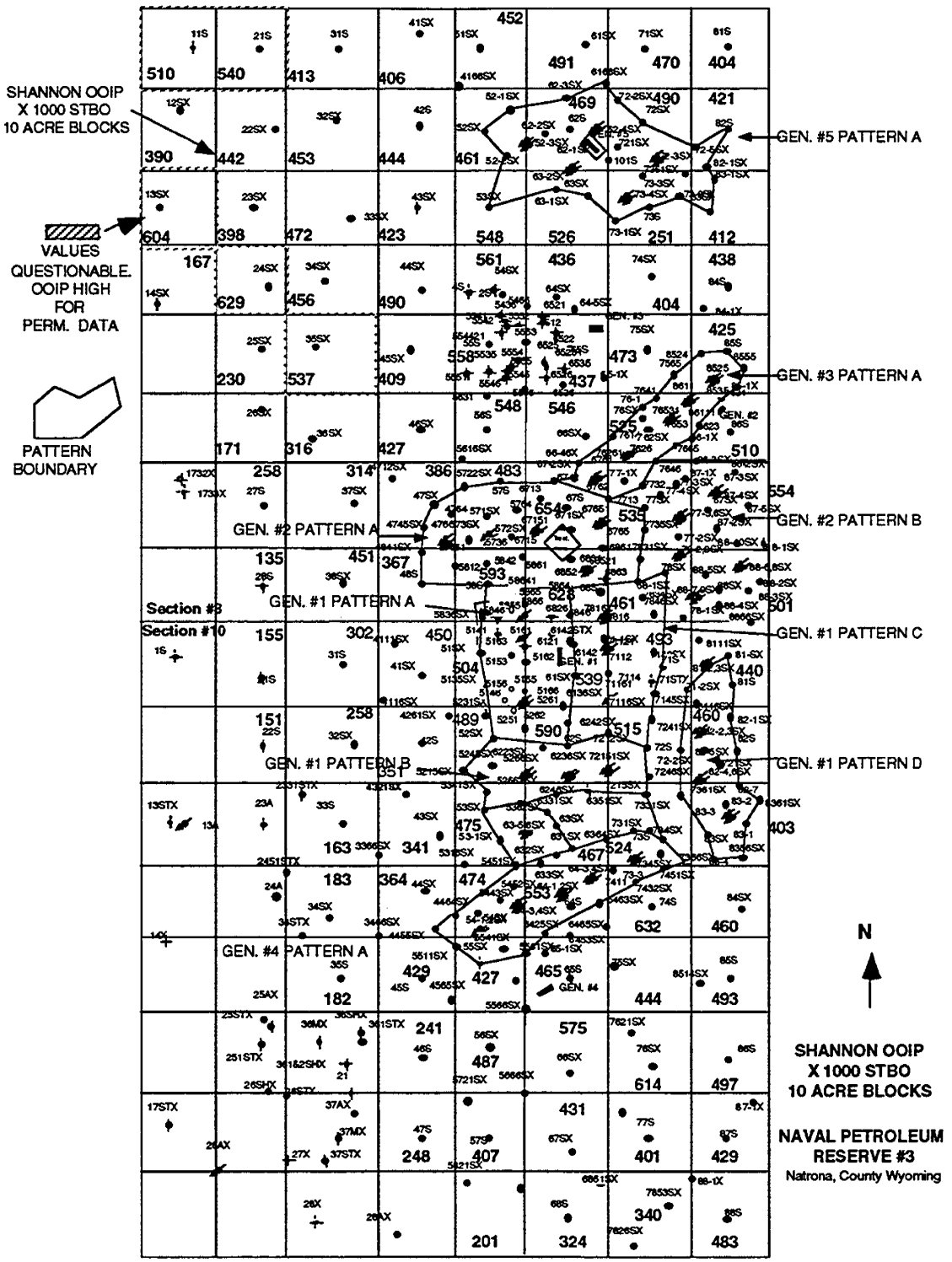

Fig 6. Map of composite oil saturation (Upper and Lower Shannon) determined for every 10 acres (volume in thousands of barrels).

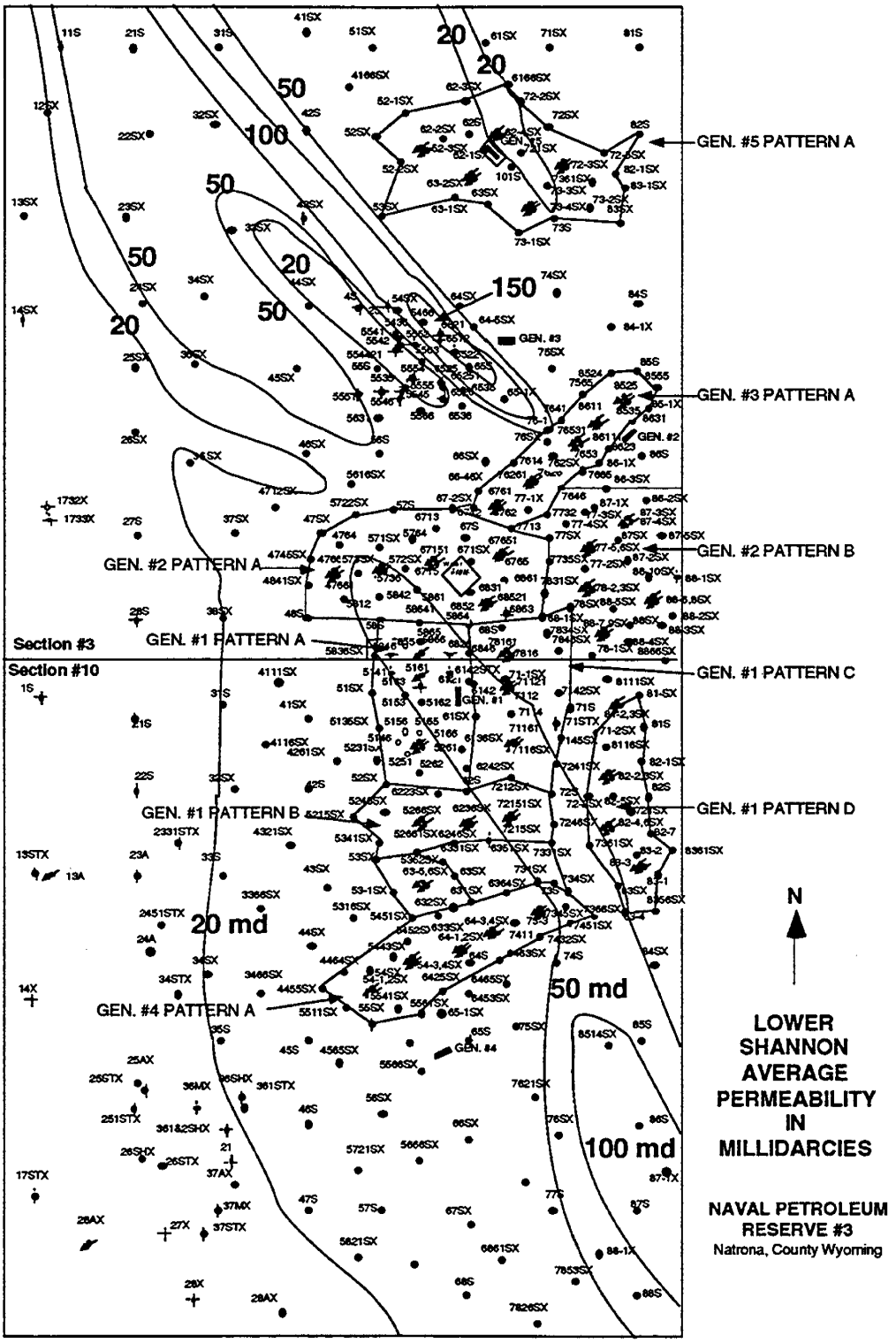

Fig. 7. Isopach map of Lower Shannon's average permeability (mD).

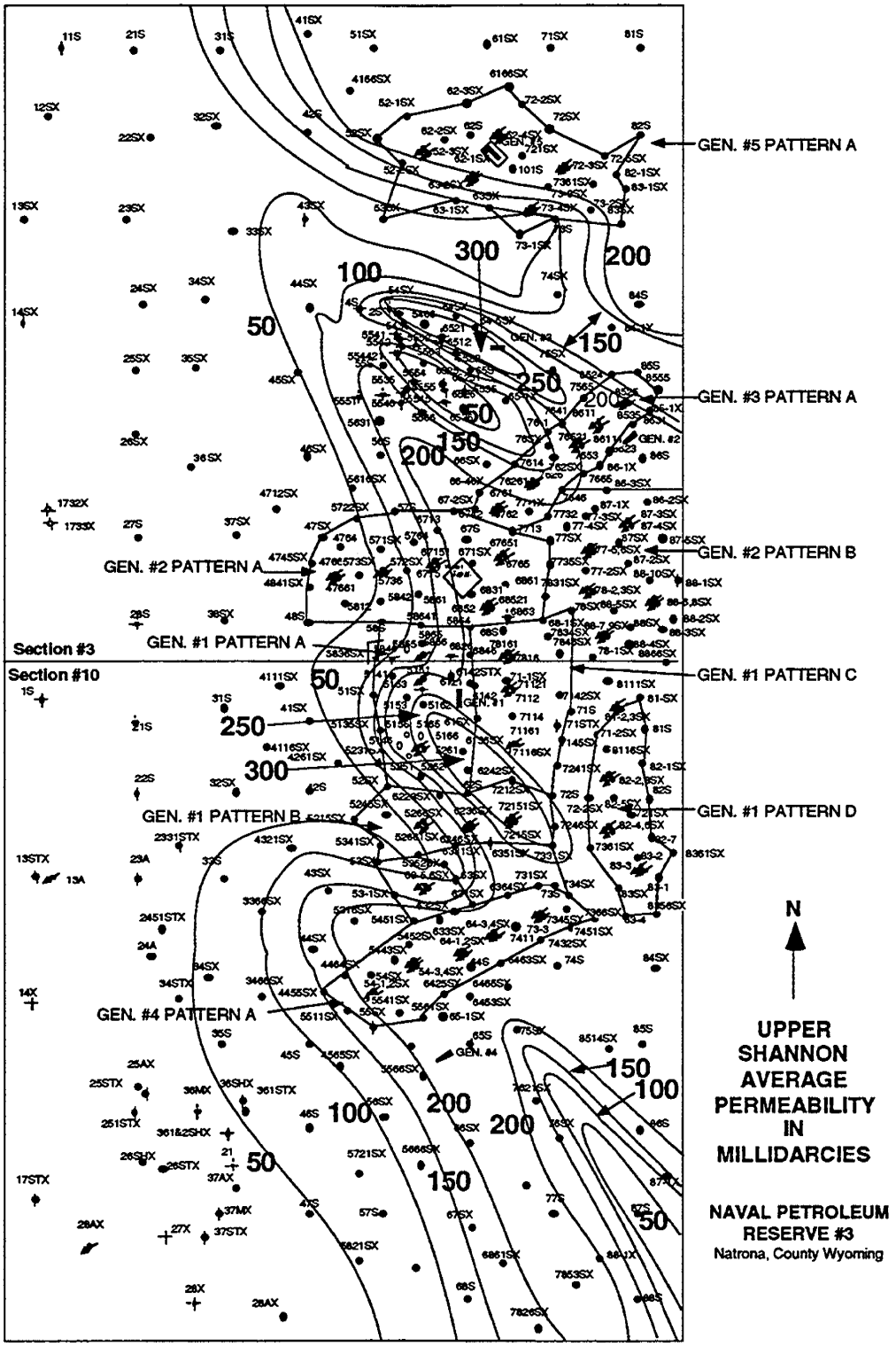

Fig 8. Isopach map of Upper Shannon's average permeability (mD).

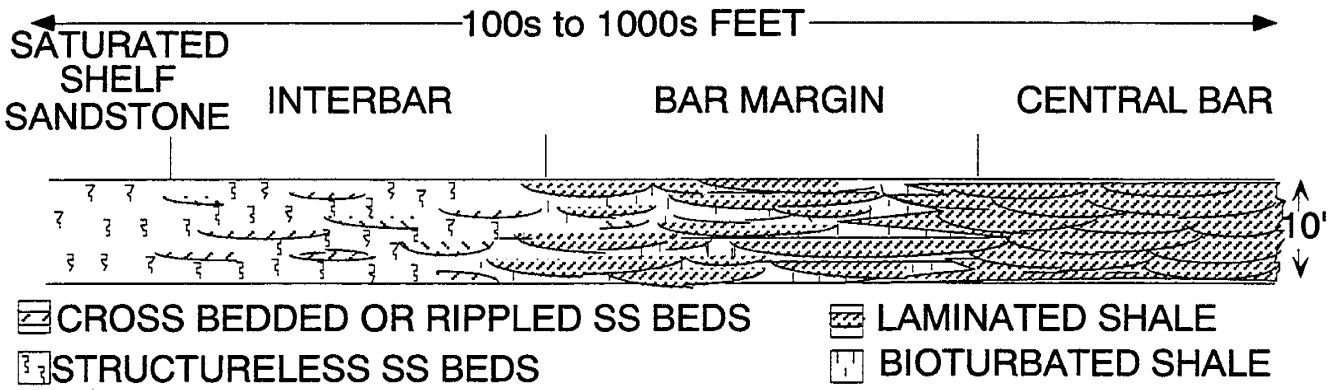

Fig 9. Schematic of depositional environment of offshore barrier bar such as Upper and Lower Shannon at Teapot Dome field.

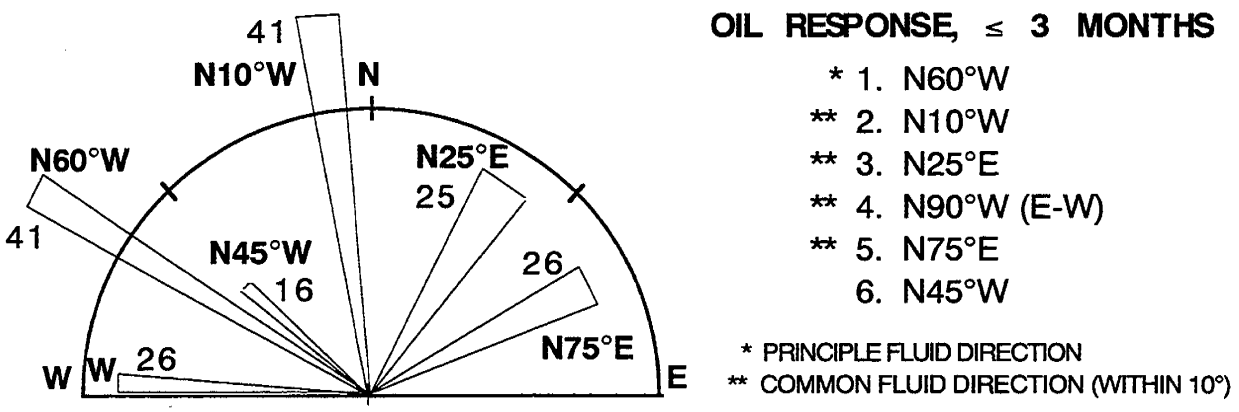

Fig 10. Rose diagram of principle direction and magnitude of oil response by time, < 3 months.

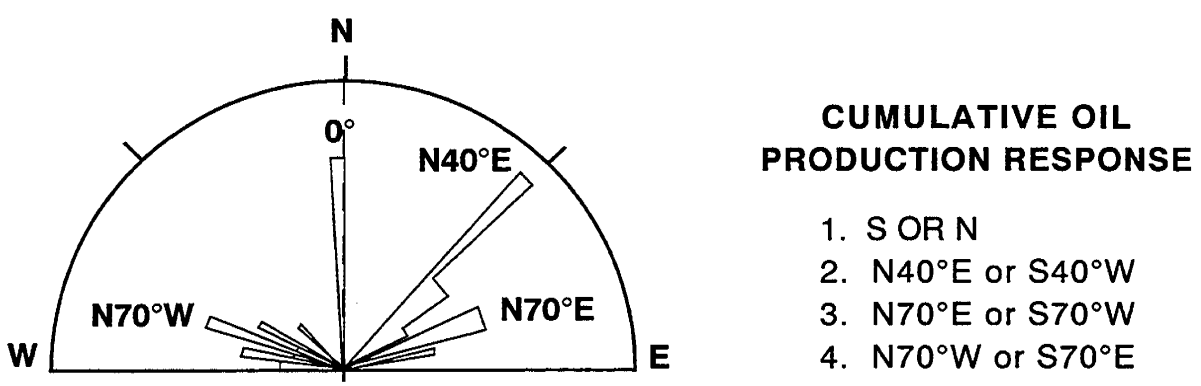

Fig 11. Rose diagram of cumulative oil production response (direction and magnitude from steam injection wells) for wells with >20,000 barrels of oil production since start of injection.

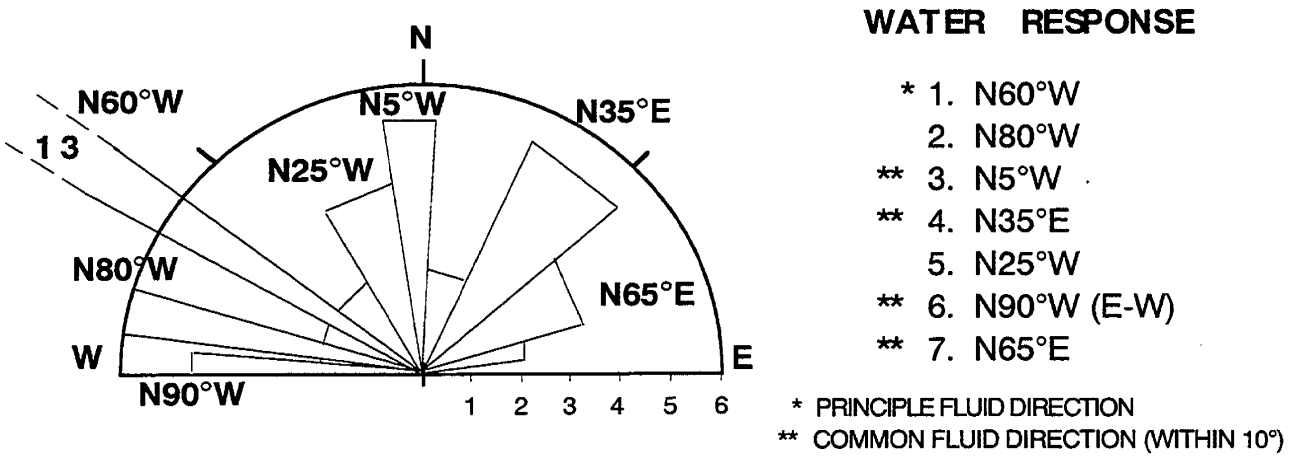

Fig 12. Rose diagram of principal direction and magnitude of water production (WOR >80%) in < 3 months.

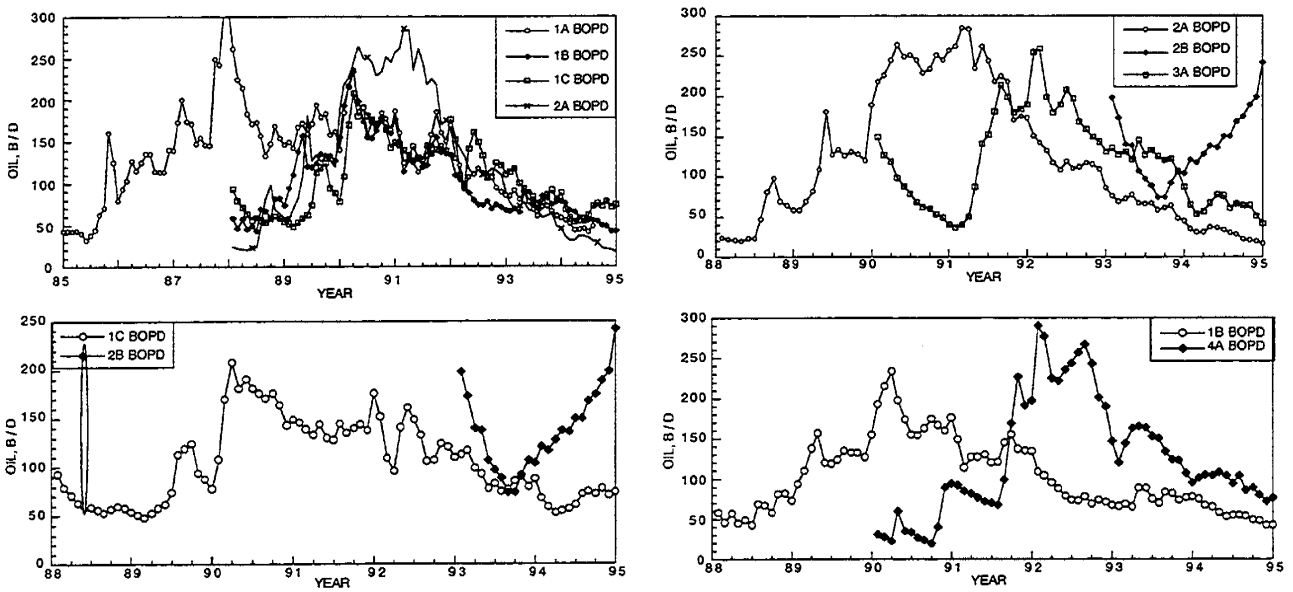

Fig. 13. Shannon steamflood pattern performance.

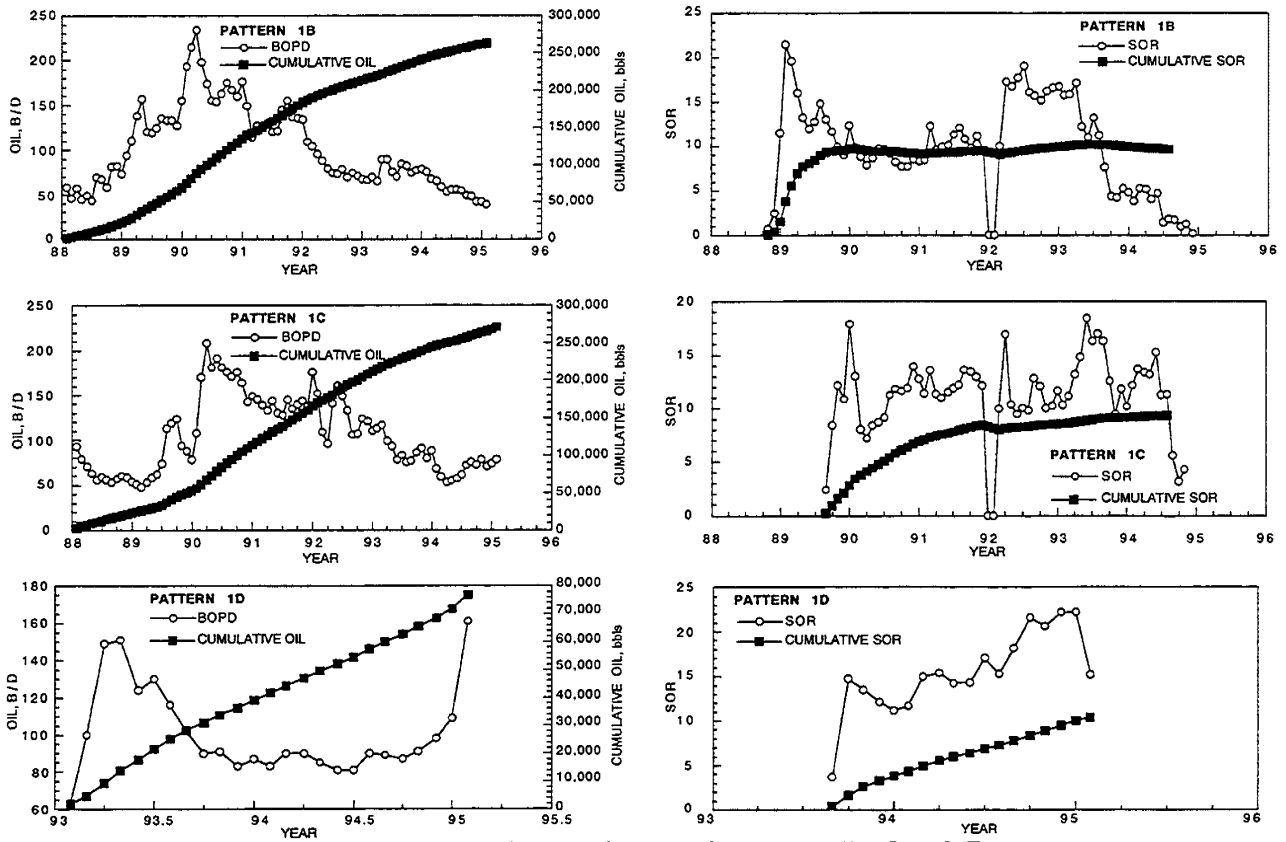

Fig 14. Shannon steamflood performance for patterns 1B, 1C, and 1D.

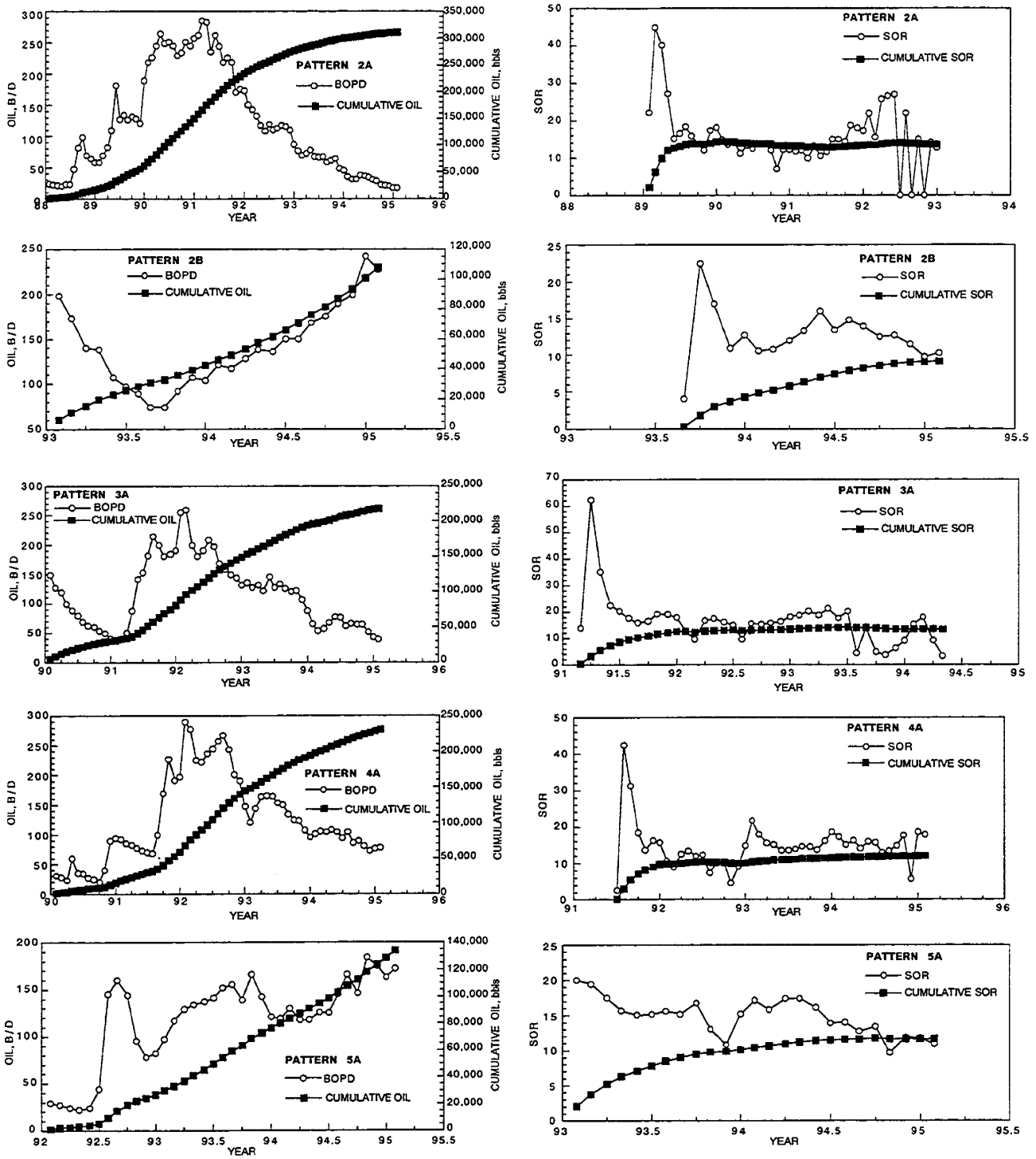

Fig 15. Shannon steamflood performance for patterns 2A, 2B, 3A, 4A and 5A.

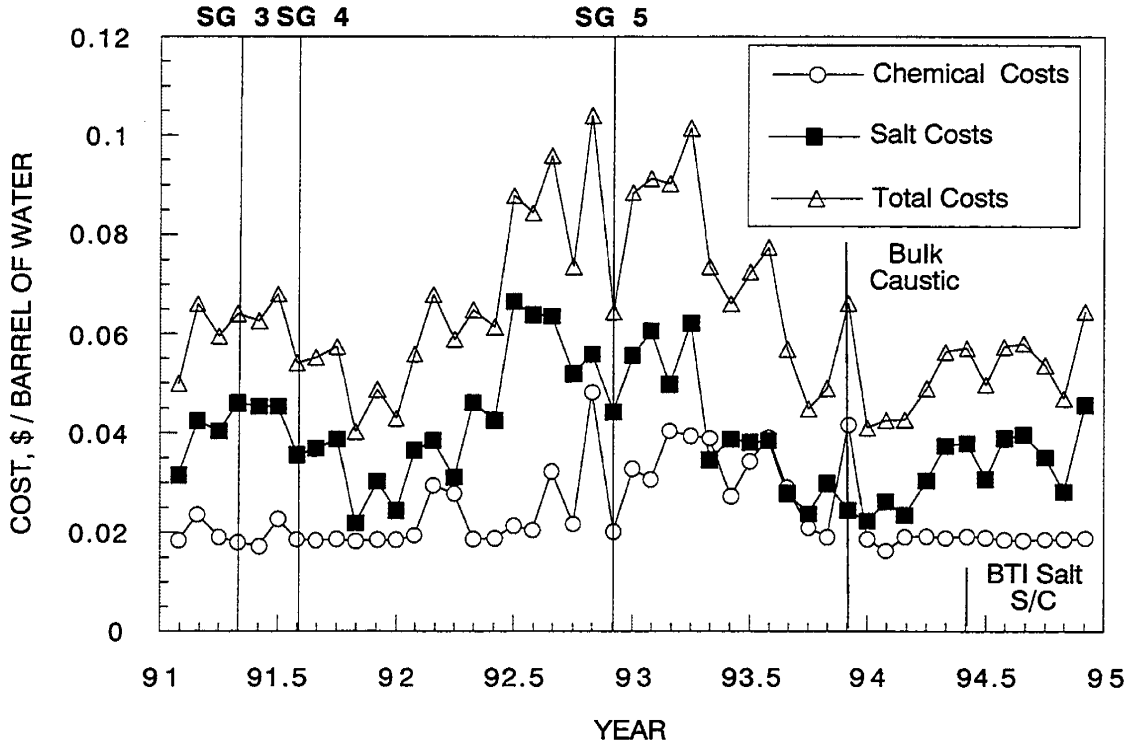

Fig 16. Chemical costs for Shannon steamflood showing startup dates of steam generators SG3, SG4 and SG5.

Task 65- INTEVEP shall provide DOE with information on the Modeling of Thermal Processes. The effort will include the application of Analytical Models to predict the production performance of steam stimulated wells.

Model for Predicting the Production Rate of Well under Cyclic Steam Injection Process.

by

Saúl Buitrago, (INTEVEP, S.A.)

ABSTRACT

In this work we present a methodology for matching and predicting the production rate behavior in time, for wells stimulated by cycle steam inyection.

The production rate is given by the transient solution of the equation of the flow of a slightly compressible fluid in an infinite radial aquifer in a porous media. Also, expressions for the effective compressibility and permeability, based on experimental studies and production rate behavior from field data, are proposed.

A function which gives the error between the production rate generated by the transient analytical model and the field production rate is presented. This function depends on the parameters associated to the expressions for the effective compressibility and permeability. A non linear global optimization technique to minimize the error function is presented in order to determine those parameters. The optimization technique combines a stochastic exploration of the domain of the error function and a heuristic calculation of a descent direction, in order to avoid stopping the algorithm at a local minimum.

The methodology was used to match the production rate behavior of several wells which have been cycle steamed in Costa Bolivar. In all the cases an excelent match with errors below 10% and similar parameters for the set of wells were achived.

1. Transient analytical model

Steam stimulation aids oil production through several mechanisms: oil viscosity reduction, thermal expansion of reservoir fluids, reduction in residual saturation, reduction of interfacial tension and capillary forces. The injected steam also imparts expulsive energy through compression of formation fluids.

The objective of this work is to develop an analytical model of cyclic steam injection, which integrates conventional energy balances with solutions of the equations of flow in radial geometry to predict process performance during the production period.

None of the models developed so far have been completely satisfactory to predict the behavior of cyclic steam processes. All the models use the steady state or semi-steady state solutions.

Moreover, none of the models include the effects of pressure drop and reservoir depletion due to the production and/or injection of fluids.

The reservoir is considered to be homogeneous with constant thickness. The reservoir will be a semi-infinite volume divided into two concentric cylinders around the wellbore (see Fig.1). The inner cylinder, which extends from the wellbore radius (R_w) to the heated radius (R_H), is called the hot zone (H). The outer cylinder, from the heated radius to the drainage radius (R_e), is called the cold zone (C). The real extension of the equivalent heated zone around the injection well is determined using Marx-Langenheim equations [1]. The heated zone radius is considered constant during the cycle. Boberg and Lantz equations are used to calculate the average instantaneous temperature for a given time t in the hot zone, which is assumed to be constant along the radius, and to decrease with time due to heated losses by conduction to the adjacent formations and to heat lost with the producing fluids. The temperature of the cold zone is the initial temperature of the reservoir.

The production rate is given by the solution of the equation of unsteady state of a slighly compressible fluid in an infinite radial aquifer in a porous media [2].

Following Rivas et al. [3], the steady state solution is valid in the hot zone since mobility in here is much greater than in the cold zone, while the unsteady state solution applies to the cold zone.

Thus,

Zone H: $$P_H - P_w = \frac{q_H}{2\pi h_t (K_{ef} / \mu)_H} \ln(\frac{R_H}{R_w} + S_H) \qquad (1)$$

Zone C: $$P_o - P_H = \frac{q_C}{2\pi h_t (K_{ef} / \mu)_C} \frac{1}{2} F(t_H, R_H) \qquad (2)$$

where P_H refers to the pressure in the outer boundary of the hot zone (R_H), q_H and q_C are the volumetric flow rates of the fluids leaving the hot zone and cold zones respectively, K_{ef} the effective permeability and $F(t,R)$ are defined below.

Since $q_H = q_C = q$, adding equations (1) and (2) follows

$$q = \frac{2\pi h_t (P_o - P_w)}{(\frac{\mu}{K_{efF}})_H \ln(\frac{R_H}{R_w} + S_H) + (\frac{\mu}{K_{ef}})_C \frac{1}{2} F(t_H, R_H)} \qquad (3)$$

where

$$F(t,R) = 2(1-\exp(\frac{-2}{\pi\sqrt{D(t,R)}})) + \ln(1+0.93D(t,R)),\ D(t,R) = (\frac{K_{ef}}{\mu})_C \frac{t}{c_{ef}\phi R^2},$$

c_{ef} is the fluids compressibility and t_H is the equivalent time of heated production at which it is desired to calculate the production rate q. The equivalent time t_H will be the time needed for a larger well (radius R_H) to produce the same accumulative total fluid volume as the smaller well (radius R_w) had been producing since it was initially put into production. To determine the equivalent time t_H for a first and subsequent cycles, see [3].

An analysis carried out, based on experimental studies and production rate behavior from field data, gives the following relationships for the effective compressibility and effective permeability for the cold and hot zones

$$c_{ef} = comp(x_1 \exp(-x_2 t)) \quad (5)$$

$$(K_{ef})_C = K_{efoil}(-x_3 t + x_4) \quad (6)$$

$$(K_{ef})_H = K_{efoil}(x_5 \exp(-x_6 t)) \quad (7)$$

where *comp* is the fluid compressibility before stimulation, K_{efoil} is the oil effective permeability, and $x_1,...,x_6$ are parameters to be estimated.

Now, the transient analytical model is conformed by the relationships (5) to (7) for the effective compressibility and permeability, and the formula (3) for the production rate q.

2. Estimation of the transient analytical model parameters.

The problem could be formulated as:

Given the production rate behavior in time $\tilde{q}(t)$, find the parameters $x_1,...,x_6$ $(x=(x_1,...,x_6))$ such that the answer $q(x,t)$ given by the transient analytical model and the production rate $\tilde{q}(t)$ are closed, that is, given $T>0$, find $x_{\min} \in \Omega$ such that

$$f(x_{min}) = \text{global } \min_{x\in\Omega} f(x)$$

where $f:\Omega \subset R^6 \to R$ is defined by

$$f(x) = f(x_1,\ldots,x_6) = \int_0^T (q(t)-\tilde{q}(x,t))^2 dt$$

and $\Omega = \prod_{i=1}^{6}[a_i,b_i]$.

f represents the error between the production rate generated by the transient analytical model and the field production rate. It is important to point out that it is possible to find more than on set of parameters which satisfy the minimality condition required and related to the size of Ω.

The method proposed in this work, the Exterior-Interior algorithm (Ex-In from now on), is a multistart type algorithm that combine a stochastic exploration of the domain Ω and a heuristic calculation of a descent direction, in order to avoid stopping the algorithm at a local minimum (see[4-5]).

Let n be the number of parameters, the main steps of the algorithm are as follows:

P1. Generate the set I of $N > n$ points separated among them at least the distance

$$\frac{1}{2}\left[\frac{\prod_{i=1}^{n}(b_i - a_i)}{N}\right]^{\frac{1}{n}}\alpha, \text{ with } \alpha > 1.$$

The idea is to cover the domain with a finite number of points in order to get the largest possible information of the objective function.

Evaluate the objective function f at x_i for all x_i in I, and denote this set of pairs $(x_i, f_i) = (x_i, f(x_i))$ by C_0. Set $k = 0$.

P2. Determine the point (x_m, f_m) in C_k that has the highest function value.

P3. Determine a new point (x_i, f_i) where x_i belongs to Ω and f_i is lower than f_m.

P4. Replace the point (x_m, f_m) in C_k by the new point (x_i, f_i)

P5. If the stopping criteria is satisfied, stop, otherwise increase k and return to step P2.

Selection of (x_i, f_i) in P3.

If n is the dimension of the space, $n+1$ points are chosen at random from the set C_k. Let $R_i = (x_i, f_i)$, $i = 1,\ldots,n+1$, be those points after been numbering in ascending order, i.e. $f_1 \le f_2 \le \ldots \le f_{n+1}$. If all f_i, are almost equal follow P3.1, otherwise P3.2.

P3.1. Calculate the point (x_i, f_i), where $x_i = \dfrac{(x_g + x_{n+1})}{2}$ and x_g is the centroid of the points $x_i, \ldots, x_n$.

P3.2. Calculate the point (x_i, f_i), where $x_i = 2x_g - x_{n+1}$ and x_g is the centroid of the points $x_i, \ldots, x_n$. (x_i is the mirror point of x_{n+1} with respect to x_g).

This step is repeated until a point x_i in Ω with $f_i < f_m$ is obtained, where (x_m, f_m) is the point calculated in P2.

The stopping criteria in P5.

The natural criteria taken into account are: how close are the points of the last two iterations and the number of performed iterations. In adition, for each iteration calculate the saturation of all possible clusters and stop the algorithm only if the saturation of all the clusters exceeds a threshold.

3. Results

The methodology hereby described, implemented for a SUN workstation, was applied to two wells in Lake Maracaibo. A comparison between the results given by the transient analytical model and the field data are presented in Fig.2 and 3.

4. Conclusions

- A transient analytical model for cyclic steam injection was developed whose predictions are qualitative correct and quantitative acceptable.
- The model can be calibrated to specific conditions by adjusting the effective compressibitity and permeability of the system.
- A novel optimization technique was developed to estimate the model parameters which provide the closest match between the production rate generated by the transient analytical model and the field production rate.

Nomenclature

c_{ef}	effective compressibility
h_t	net oil sand thickness
K_{ef}	effective permeability
K_{efoil}	oil effective permeability
P_H	pressure in the outer boundary of the hot zone
P_o	original reservoir pressure
P_w	downhole flowing pressure
q_C	cold production flow rate
q_H	hot production flow rate
R_e	drainage radius
R_H	radius of the hot zone
R_w	wellbore radius
S_H	hot skin factor
t_H	equivalent time of heated production
μ	viscosity

REFERENCES

1. Marx, J.W.; Langenheim, R.H. Reservoir heating by hot fluid inyection. Trans. AIME, Vol.216, pp.312-315, 1959.
2. Collins, R.E. Flow of fluids through porous materials. The Petroleum Publishing Co., Tulsa, 1976.
3. Rivas, O.; Boccardo, G. Transient analytical modeling of cyclic steam inyection. Latin American and Caribbean Petroleum Engineering Conference on Improving Oil and Gas Recovery within Sustainable Development, 3th, SPE 27060, Buenos Aires, April 26-29, 1994.
4. Buitrago, S; Gedler, G; Rodriguez, E. Determining the optimum location of a production well in oil reservoirs. Proceeding of the 4th European Conference on the Mathematics of Oil Recovery. Topic E: History Match and Recovery Optimization. Roros, Norway, June 1994.
5. Buitrago, S.; Gedler, G. Automatic Optimization Parameters in Horizontal Well Test Analysis. SPE 37070. International Conference on Horizontal Well Technology Proceedings, Calgary, Canada, November 1996.
6. Torn, A.; Zilinskas, A. Global optimization. Lectures Notes in Computer Science. Vol.350. Springer-Verlag, 1989.
7. Prats, M. Procesos termicos de extracion de petroleo. Intevep, S.A., Los Teques, 1987.

LIST OF FIGURES

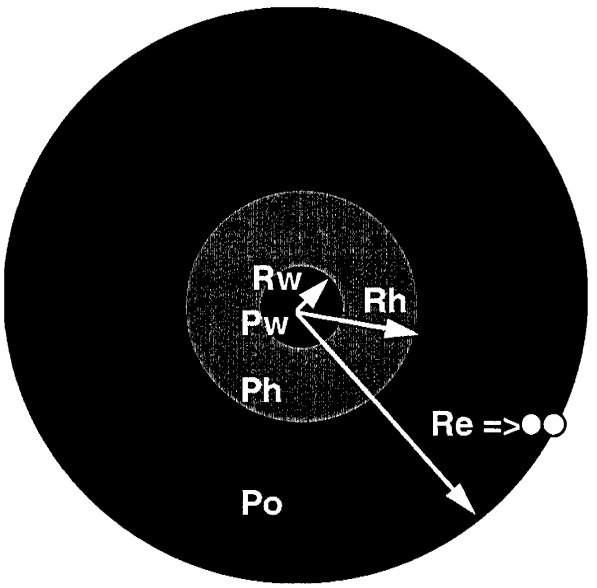

Fig.1. Schematic representation of a steam injected reservoir

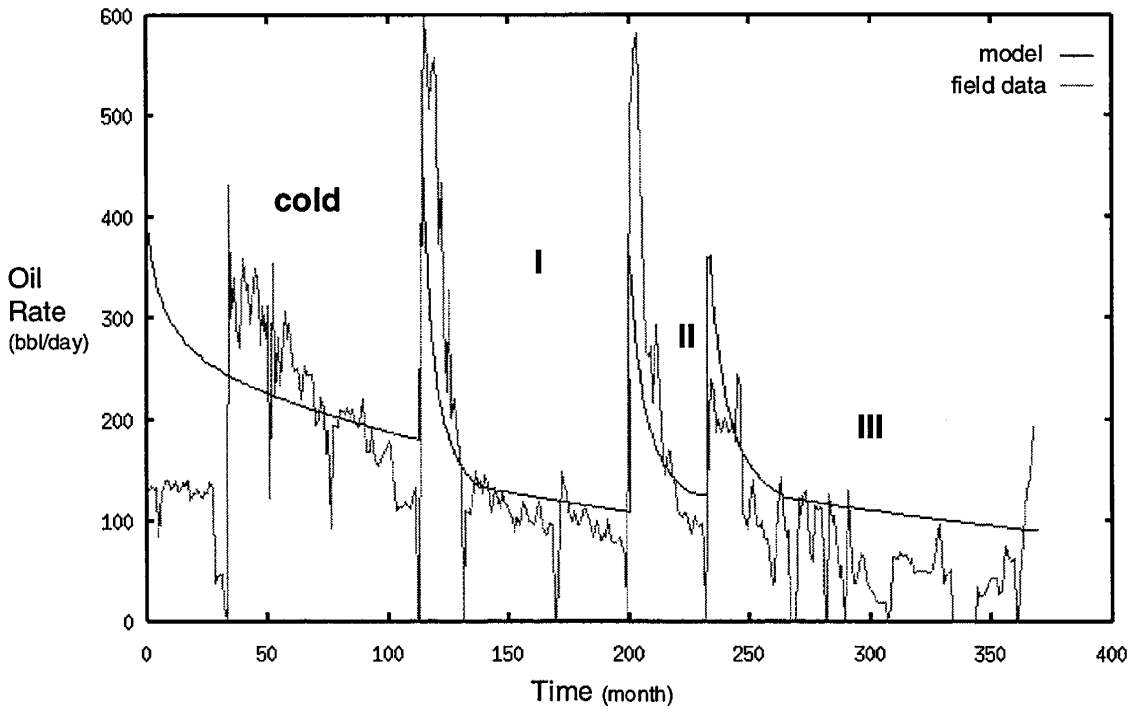

Fig.2. Production behavior of well 1 (Lake Maracaibo)

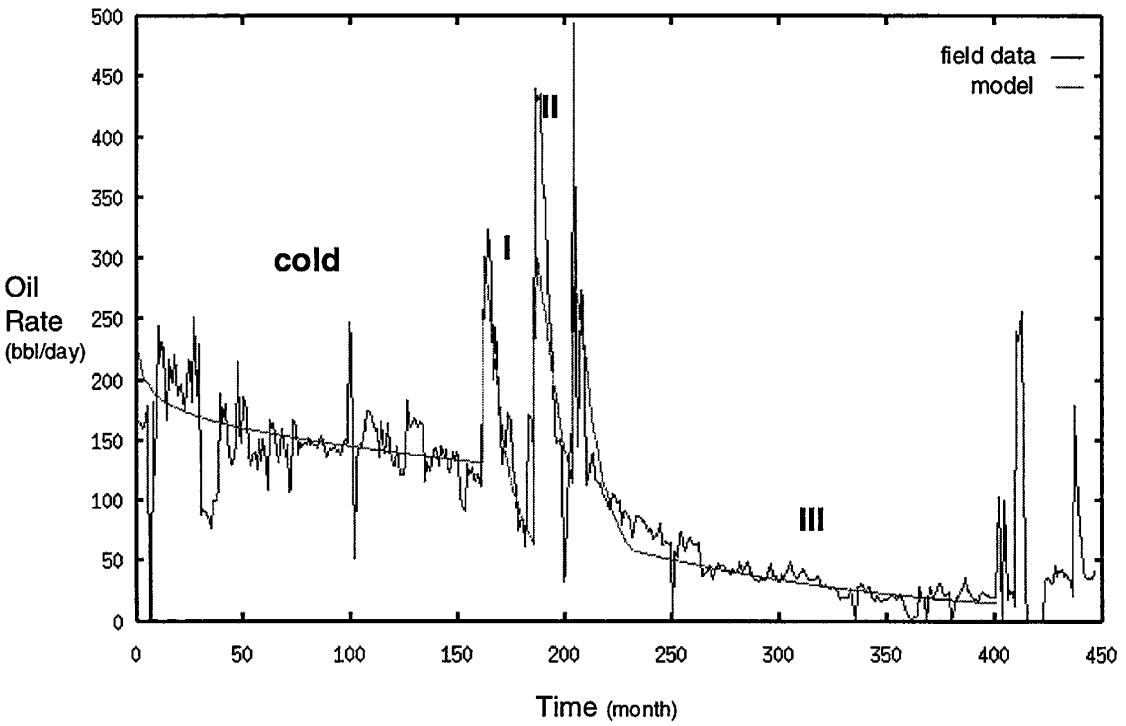

Fig.3. Production behavior of well 2 (Lake Maracaibo)

Crosshole EM for Oil Field Characterization and EOR Monitoring: Field Examples from Lost Hills, California

Michael Wilt and Clifford Schenkel
Lawrence Livermore National Laboratory

Michael Wratcher and Ilia Lambert
Mobil Development and Production U.S.

Carlos Torres-Verdin
Schlumberger-Doll Research

Hung-Wen Tseng
University of California at Berkeley

Abstract

A steamflood recently initiated by Mobil Development and Production U.S. at the Lost Hills #3 oil field in California is notable for its shallow depth and the application of electromagnetic (EM) geophysical techniques to monitor the subsurface steam flow. Steam was injected into three stacked eastward-dipping unconsolidated oil sands at depths from 60 to 120 m; the plume is expected to develop as an ellipsoid aligned with the regional northwest–southeast strike. Because of the shallow depth of the sands and the high viscosity of the heavy oil, it is important to track the steam in the unconsolidated sediments for both economic and safety reasons.

Crosshole and surface-to-borehole electromagnetic imaging were applied for reservoir characterization and steamflood monitoring. The crosshole EM data were collected to map the interwell distribution of the high-resistivity oil sands and to track the injected steam and hot water. Measurements were made in two fiberglass-cased observation wells straddling the steam injector on a northeast–southwest profile. Field data were collected before the steam drive, to map the distribution of the oil sands, and then 6 and 10 months after steam was injected, to monitor the expansion of the steam chest. Resistivity images derived from the collected data clearly delineated the distribution and dipping structure of the target oil sands. Difference images from data collected before and during steamflooding indicate that the steam chest has developed only in the middle and lower oil sands, and it has preferentially migrated westward in the middle oil sand and eastward in the deeper sand.

Surface-to-borehole field data sets at Lost Hills were responsive to the large-scale subsurface structure but insufficiently sensitive to model steam chest development in the middle and lower oil sands. As the steam chest develops further, these data will be of more use for process monitoring.

Introduction

For a number of years, heavy oil has been produced with the aid of steam injection from shallow unconsolidated sands in the San Joaquin Valley of central California. Although most thermal enhanced oil recovery (EOR) projects have been economically successful, many have problems of steam override, steam bypass, and inefficient sweep as a result of channeling. Thus, developing low-cost geophysical monitoring methods for EOR has been a priority of operating companies for some time. Seismic techniques have been applied to EOR monitoring with good success, but the high cost of drilling dedicated observation wells and doing surveys deters many developers (Eastwood et al., 1994). Lower-cost alternative techniques are continually being sought to make further use of observation wells and allow greater sensitivity to produced and injected fluids.

Electromagnetic techniques, which are sensitive to the subsurface electrical resistivity, are responsive to changes in the rock pore fluids. This contrasts with the seismic techniques, which have higher sensitivity to the rock matrix. EM techniques are therefore ideal for monitoring EOR processes because of the large-scale fluid and heat flow. Traditionally, however, EM techniques have been employed only in borehole logging. Only recently have instrumentation and interpretation techniques become available for crosshole and surface-to-borehole EM configurations.

Borehole induction logging measurements in oil fields undergoing EOR confirm the high sensitivity of electrical resistivity to changes in subsurface temperature and pore fluid. Published reports have shown that the resistivity typically decreases from 35 to more than 80% after steam injection (Mansure and Meldau, 1990; Ranganayaki et al., 1992; Spies and Greaves, 1990). This decrease occurs because temperature increases and because the high-resistivity oil is replaced by the lower-resistivity steam and water injectate mixture. If the resistivity distribution can be determined between wells, then the field engineer would have a powerful tool for tracking injected fluids and thereby controlling the recovery process.

This short case history illustrates the application of crosshole and surface-to-borehole EM methods for reservoir characterization and EOR monitoring at the Lost Hills oil field in central California. The Tulare 3T steamflood at Lost Hills is among the shallowest on record; steam injection occurs at depths of less than 60 m. It is therefore most important to monitor the flow for safety as well as economic reasons. The EM method was chosen as a pilot technology to monitor the steamflood because of the high sensitivity of measurements to regions affected by underground steam.

This project was initiated from discussions between Ranga Ranganayki at Mobil Research and Michael Wilt at Lawrence Livermore National Laboratory (LLNL) in 1990. The field operators at Mobil Lost Hills became involved with the onset of field activities in 1991. Much of the technical work was accomplished through the crosshole EM

consortium, which includes Mobil, Schlumberger-Doll Research, LLNL, Lawrence Berkeley National Laboratory (LBNL), and the University of California at Berkeley.

Geologic Setting

The Lost Hills oil field is located along the crest of the Lost Hills anticline in California's San Joaquin Valley. This anticline is the southernmost segment of a northwest-trending segmented antiform that includes the Kettleman Hills anticlines and the Coalinga anticline to the north. It is located on the western margin of the San Joaquin Basin and roughly parallels the trace of the San Andreas fault zone 20 miles to the west (Figure 1). The San Andreas system is thought to be the dominant control for structure in the western San Joaquin Valley oil fields (Miller et al., 1990).

The Lost Hills oil field was discovered in 1911, although substantial production did not occur until the mid to late 60s. Presently, oil is produced via steam and water flooding from a series of stacked oil sands ranging from the Miocene Monterey shales and diatomites to the Pleistocene Tulare sands.

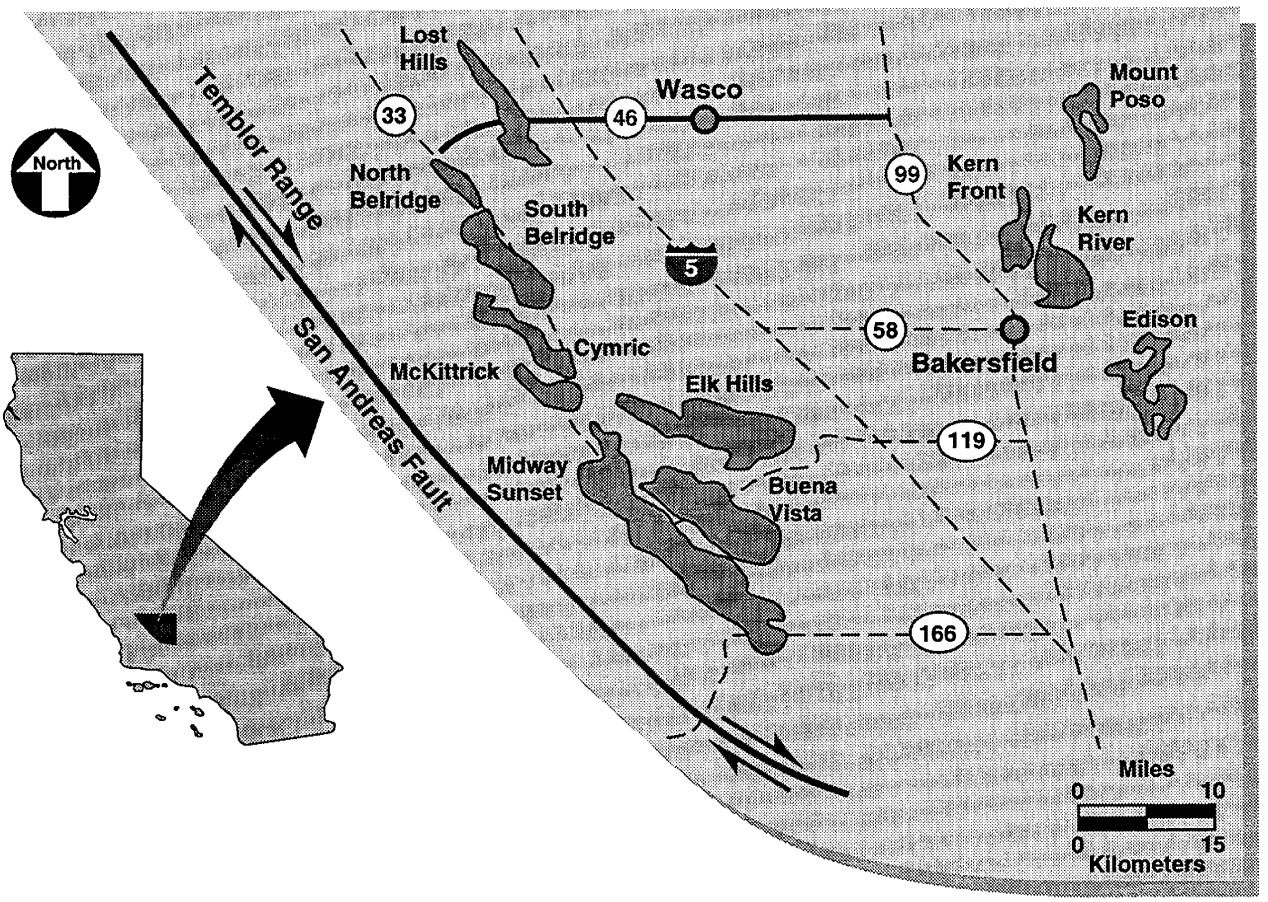

Figure 1. Site location map for the Lost Hills oil field.

The Tulare Formation records the Pleistocene history of basin filling in the present-day San Joaquin Valley. It is the first nonmarine deposit to be preserved, unconformably overlying the marine Pliocene/Miocene Etchegoin Formation (Figure 2). The unconformity at the base of the Tulare is angular and therefore at least in part tectonic in nature. Although the underlying units contain numerous normal faults, the Tulare is largely unfaulted and has apparently filled in the older faulted eroded surface.

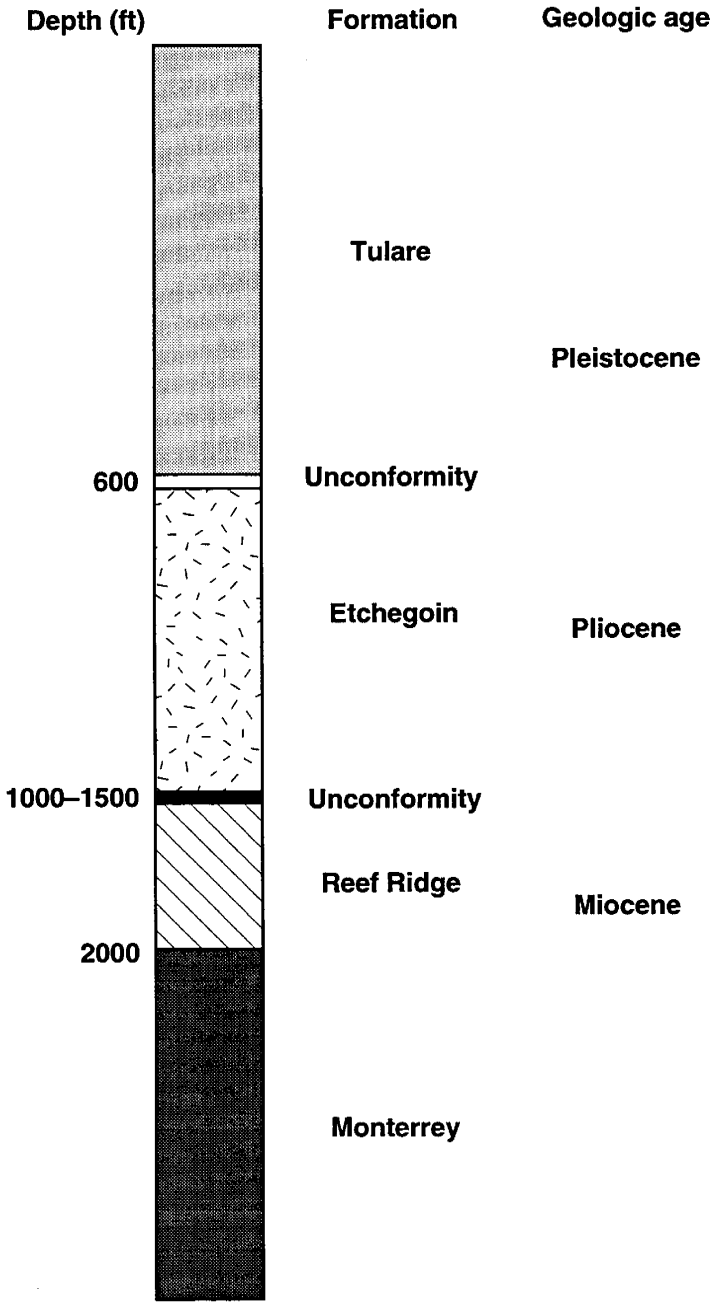

Figure 2. Composite stratigraphic column for the Lost Hills field.

The Tulare records small- to medium-sized streams depositing loads in lacustrine delta complexes at the western margin of Pleistocene Lake Corcoran. Because of the system's high energy, there are abundant clean sands throughout the field. Clay content is highly variable, depending on the facies type. Sand geometry is complicated but can generally be thought of as a series of discontinuous sheets and troughs. Well correlations must take into account the highly transitory depositional environment. Also, sedimentary packages can change dramatically within one steam pattern with a large resulting impact on fluid flow.

Permeabilities range from a few hundred millidarcies in muddy sands to between 1000 and 3000 millidarcies in the clean sands. The total porosity ranges from 38 to 42% and displays little variability. Oil saturations range between 35 and 75% with a weighted average of 65%. The oil produced from Tulare sands is biodegraded and water washed; it ranges from 10 to 13 API gravity (Miller et al., 1990).

Steamflood Design

Initial steamflooding activities at Lost Hills #3 were targeted in the Etchegoin sands, with a line-drive steamflood in the late 1980s. The shallow Tulare section was targeted in the 1991 steamflood development termed the 3T. With a structural dip of approximately 5 degrees and an initial reservoir pressure of 35 psig, the Tulare has minimal reservoir energy to drive production. Recovery via primary and cyclic steam depletion in adjacent properties is 12% of the oil in place (OOIP). In contrast, steamflooding is expected to increase the ultimate recovery to 55% OOIP.

The 3T steamflood was designed using the nearby 3B Tulare steamflood, with 4-acre (16 km^2) inverted 7 spot patterns, as a model for optimization (Figure 3). The 3T design incorporates the same number of wells per pattern to deplete a larger area, approximately 5 acres (20 km^2). By using a larger spatial pattern, we hoped to reduce the capital investment required for the project. What was not foreseen is that a low allowable injection pressure (0.6 psi/ft) coupled with shallow injection depths (50 m average) restricts injectivity to rates below what is required for efficient recovery on this larger pattern.

Yet another critical challenge at 3T is the existence of undersaturated zones (air gaps) within the oil column. These regions act as "thief" zones, transporting injected steam into other patterns or to overlying air sands. The 3T steamflood is located just eastward from known Tulare undersaturated zones. While this location prevents initial thieving of heat, if the steam chest connects to the existing undersaturated zones, it will migrate preferentially westward and much of the pressure will be lost.

The Tulare is divided into the upper, middle, and lower flow units. The units are accessed via limited entry injectors, designed to flood each with 1.15 bspd/net acre-ft. Although the steamflood was initiated in 1991, initial steam injectivity was very low

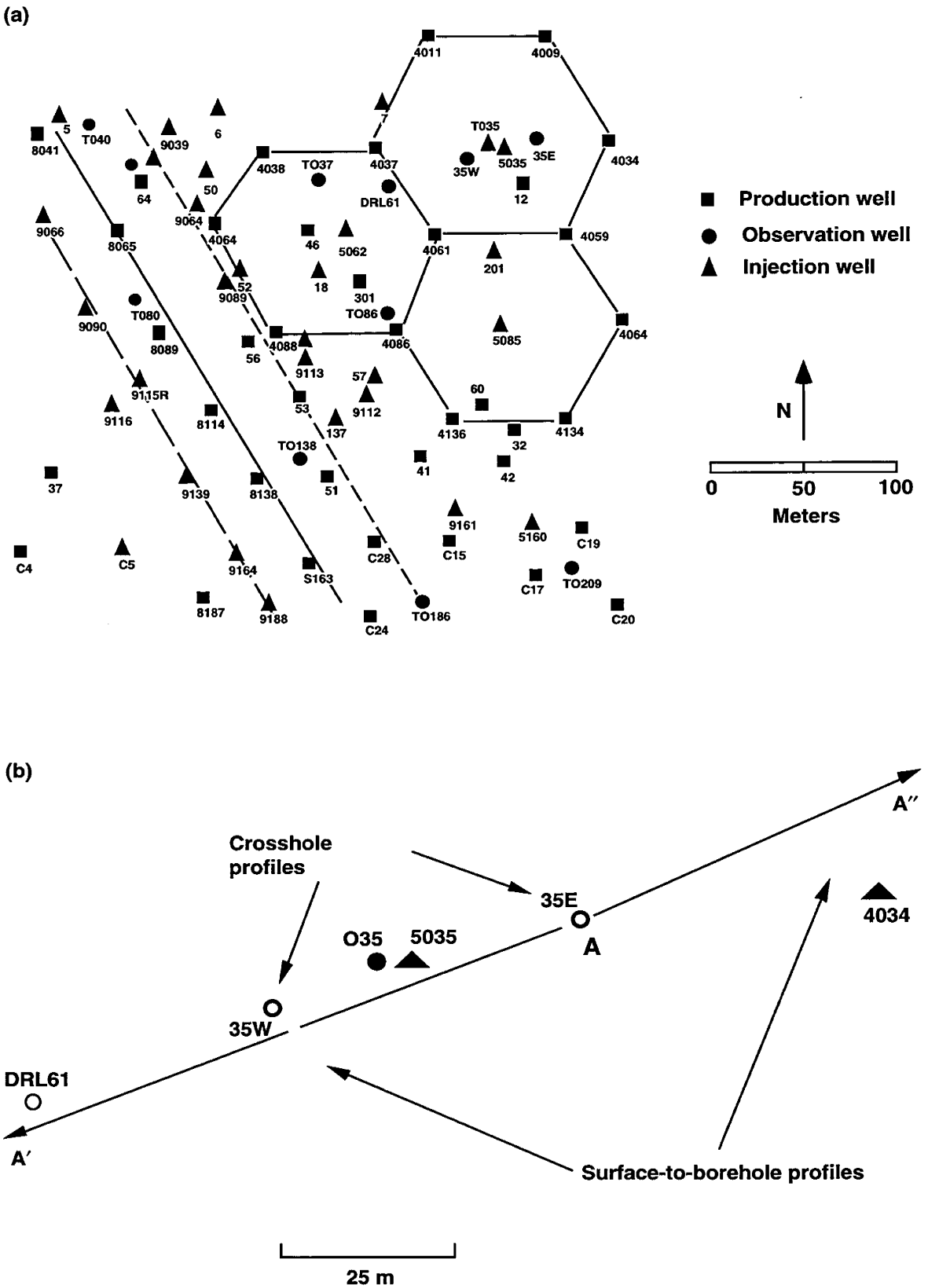

Figure 3. Site map for the EM project at the Lost Hills 3T steamflood.

because of the high oil saturations with low mobility (cold oil). Intense producer cyclic steaming has been required to supplement pattern heat.

The pattern under EM surveillance is one of two surviving patterns. It, too, has had continuous injection into the upper Tulare via injector #5035 since 1991, but at very low rates. In late 1993, we increased the injection rate by steam fracturing #5035 and by recompleting a nearby service well, TO-35, into an injector for the middle and lower Tulare zone. At present, 450 bbl/day is injected into the primary and secondary steam-injection wells. Production response to the steam injection occurred, finally, in February 1995.

Objectives of the EM Surveillance

The northeastern most of four 3T pilot patterns was selected for monitoring with crosshole and surface-to-borehole EM. We wanted to determine if the EM measurements were effective in locating steam-saturated zones and if they could provide information on steam flow before the temperature fronts arrived at observation or production wells. In addition, we wanted to determine the value of interpreted EM sections in defining sand body continuity.

The crosshole surveys are designed to examine flow in the plane between the boreholes and to track sand-bed continuity. This method is quite sensitive to subsurface flow in individual layers. The surface-to-borehole surveys were designed to investigate upward-moving steam flow and flow outside the plane between observation wells 35E and 35W. We expect that these measurements will have a lower resolution than the crosshole data and may not have sufficient sensitivity to detect deep-seated resistivity changes due to steam flow. The advantages of this method are that it does not require two boreholes and that the images are not limited to the plane between wells.

Basic Principles of Crosshole EM

A simplified EM system consists of a transmitting magnetic dipole (loop) antenna broadcasting a sinusoidal signal and a corresponding receiving antenna located some distance away. The transmitting antenna generates an electromagnetic field in the electrically conducting earth around the borehole, thereby inducing secondary (induced) currents to flow in the formation. At the receiver end, the measured field includes both primary (generated) and secondary (induced) field components. If the primary field is subtracted from the data, the remaining field (secondary) is a direct indicator of the subsurface electrical conductivity between the source and receiver antennas.

If the antennas are located close together, as is the case in a single-hole logging devise, the tool investigates a relatively small region that is centered adjacent to the borehole (approximately 0.5 m). In this region, it is usually safe to assume that the electrical

conductivity is uniform. The measurements are then converted from electromagnetic field to electrical conductivity using a simple formula for a homogeneous earth.

The cross-borehole technique uses the same principle as the borehole induction log, but the source and receiver antennas are located in separate boreholes. Under these conditions, the measurements are sensitive to the region between the wells. The analysis of collected data is substantially more complex, however, since we cannot assume that the earth is uniform between the boreholes. Data are interpreted using complex numerical models and imaging techniques

If only one borehole is available or if wells are widely separated, then we may apply electromagnetic induction techniques in a surface-to-borehole configuration. With this method, a series of surface-installed loop transmitters are employed together with borehole receiver antennas. In general, the surface-to-borehole method is less sensitive to detailed subsurface conductivity structure than single hole or cross-borehole techniques, but it is more sensitive than surface-based methods.

LLNL/LBNL Field System

The LLNL/LBNL EM field system was developed in 1990 for oil-field characterization and process monitoring (Wilt et al., 1995). It may be deployed in crosshole, surface-to-borehole, and surface configurations and has proven effective from boreholes up to 500 m apart (Figure 4). As with any tomographic system, data are collected by positioning transmitter and receiver tools at several levels that encompass the area of interest between the boreholes. A typical data set consists of several thousand measurements.

The transmitter station generates high-power ac signals at the surface and sends them down standard logging cable to be broadcast using a vertical-axis coil antenna. The transmitter coil consists of a magnetically permeable rod (mu-metal or ferrite) wrapped with several hundreds turns of wire and tuned with capacitors to broadcast a single frequency. Typically the core rod is 2 to 3 m long and 3 to 4 cm in diameter; the strength of the transmitter is proportional to the volume of this core. We can change the frequency by changing the number of turns (inductance) and/or capacitor in the tool. A surface-based loop transmitter is used for the surface-to-borehole system. This transmitter is operated in the same manner as the borehole source (i.e., tuned with capacitors), but because of the large surface area, it is 10 to 100 times more powerful.

Vertical magnetic fields are detected at the receiver borehole with a commercial borehole receiver coil, and the signal is amplified and transmitted up the logging cable for measurement with a lock-in amplifier. The lock-in amplifier operates by measuring magnetic fields that are synchronous with an external phase reference, in this case the transmitter signal. This phase reference is carried from the transmitter to the receiver using an

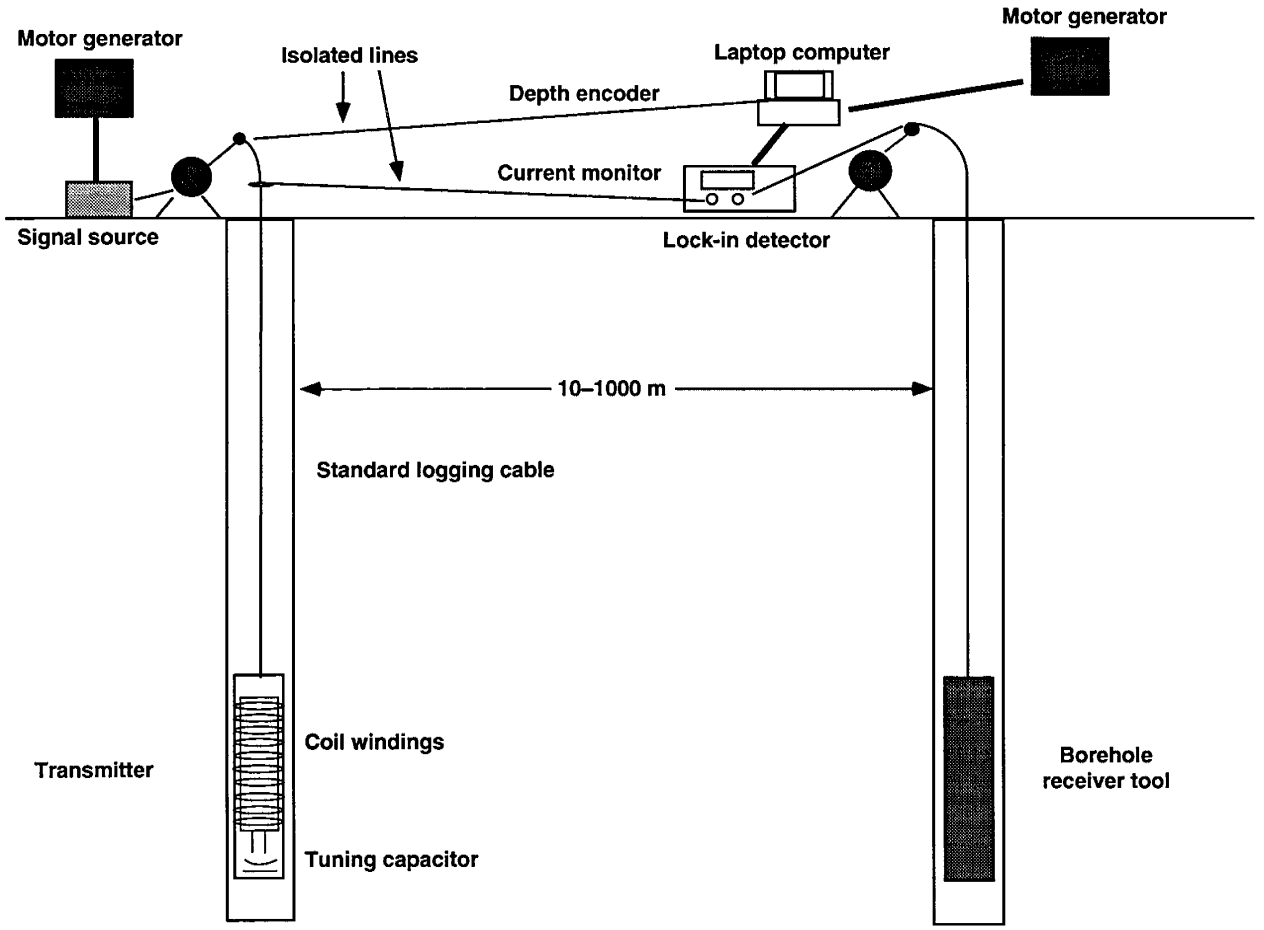

Figure 4. Schematic diagram for the LLNL/LBNL EM system.

optically isolated line. Wheel-type encoders are used to track tool depths, and a portable computer is used to log the data.

With these simple analog systems, we have collected high-quality data at a variety of field sites at borehole separations from 10 to 300 m using frequencies from 100 Hz to 100 kHz (Wilt et al., 1991). Data are typically repeatable and reciprocal to 1%. We believe that the high quality of the data is due to careful attention to isolation and local grounding of the transmitter and receiver sections. Each unit has a separate generator for power supply and a local common ground. The transmitter and receiver modules are connected for phase reference and depth control, using optically isolated cables.

Field data are interpreted using numerical models and regression analysis (inversion) that fit the EM fields to a two- or three-dimensional resistivity distribution. We use a two-dimensional rectangular mesh code, developed at Schlumberger-Doll Research (Torres-Verdin and Habashy, 1993), and a three-dimensional rectangular mesh code developed by Ki Hu Lee of Lawrence Berkeley National Laboratory. Because of the complexity of the

electromagnetic field in a discontinuous medium, a typical data inversion requires more than 12 hours for the two-dimensional solution to more than one day for the three-dimensional code on a fast computer workstation.

For the surface-to-borehole data, we use only a one-dimensional solution at present and piece together the best-fit layered models. Interpretation of these data using two- and three-dimensional models is presently impractical because of the large volumetric coverage. This coverage requires enormous meshes for the numerical models to adequately resolve the subsurface resistivity structure. Numerical codes for interpreting these data are being developed.

Field Plan

Figure 4 is a schematic map of steam pattern 2 at the Lost Hills #3 oil field where we are applying crosshole EM as a pilot test. Two fiberglass-cased observation wells 35W and 35E were drilled along a northeast–southwest profile straddling steam injector #5035. The wells were drilled for the combined purposes of crosshole EM surveys and repeated temperature and induction (resistivity) logging. Steam was injected at depths of 65, 90, and 120 m into upper, middle, and lower members of the Tulare Formation heavy oil sand. Subsurface steam flow is expected to follow the natural northwest–southeast regional strike, with the plume developing as an ellipse having its major axis aligned with the natural fractures. The monitoring wells are positioned orthogonal to the regional strike direction so that the crosshole EM data roughly follow the assumption of a two-dimensional rectangular geometry.

A cross section derived from borehole induction resistivity logs shows that the higher-resistivity intervals (10–100 ohm-m) typically represent the oil sands; the lower-resistivity units (2–10 ohm-m) are associated with confining silts and shales (Figure 5). The target sands extend from 60 to 120 m in three separate intervals. The upper sand is the thickest and most continuous of the three. It lies at a depth of 60 m, has a thickness of up to 20 m, and dips gently eastward at about 6 degrees. The middle and lower members are thinner and less continuous. The middle member is 3 to 6 m thick and is centered at a depth of approximately 90 m. This unit seems to pinch out near well 35W and becomes a water sand somewhere between 35E and borehole 4034. The lower Tulare, centered at a depth of 110 m, is continuous throughout this portion of the field and dips eastward at about 8 degrees. The water table lies at a depth of 160 m, or just below the bottom of these wells.

EM Field Surveys

Crosshole and surface-to-borehole EM data were collected three times: in November 1993, before steam injection began; in April 1994, 6 months after steam injection; and in September 1994, 10 months after injection. Crosshole data were collected at 5 and 20 kHz

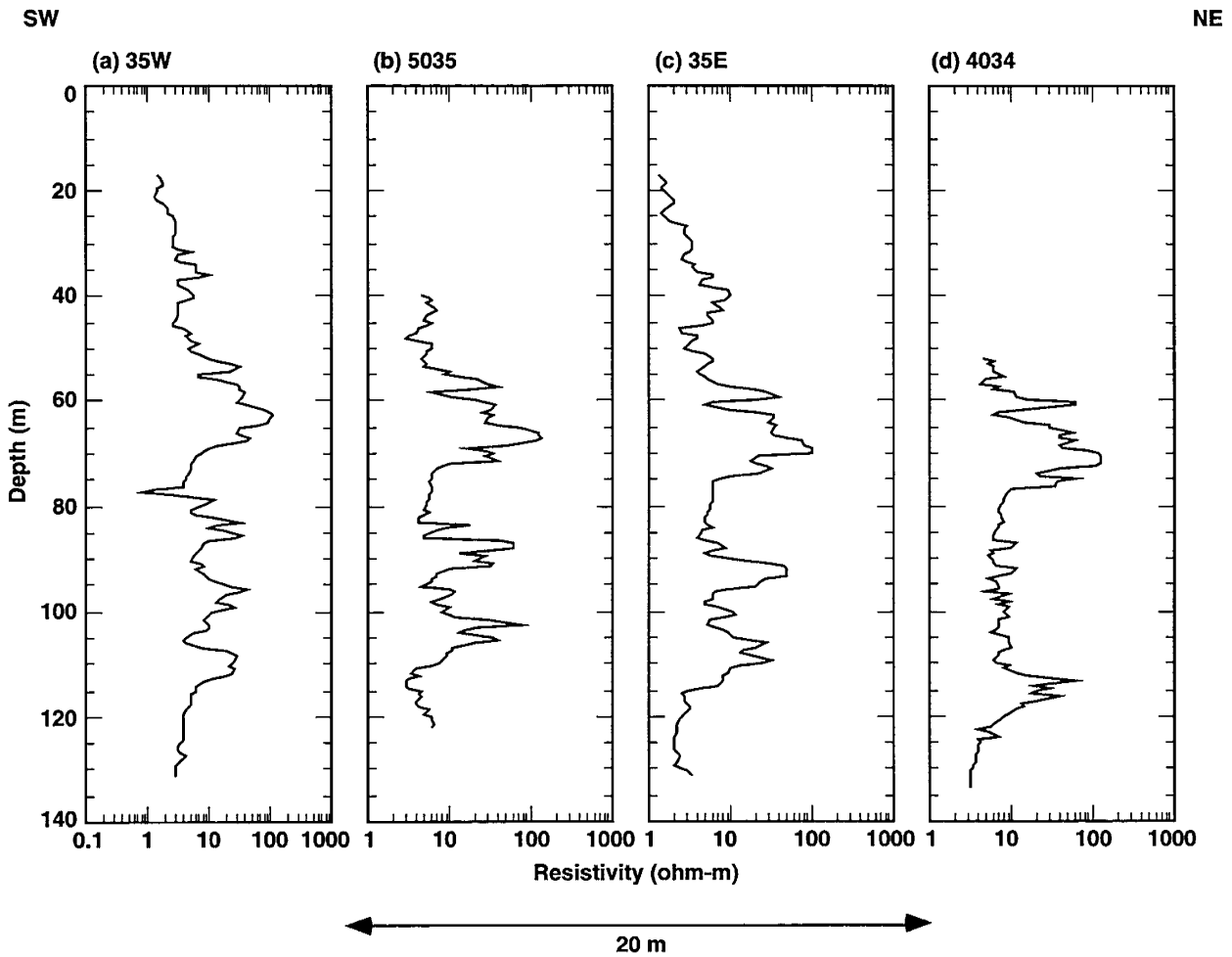

Figure 5. Induction logs along profile A′–A″.

using borehole 35W for the transmitter and 35E for the receiver tool. Receivers were spaced 4 or 8 m apart in borehole 35E, and EM data were collected continuously as the transmitter moved between 130 and 30 m in borehole 35W. A typical crosshole profile required approximately one hour to measure. A typical field survey, which consisted of 18 to 22 profiles, required 20 hours to complete for each frequency.

Surface-to-borehole EM data were collected along profile A′–A″, using 10- × 10-m surface loop transmitting antennas and a borehole receiver antenna. The surface loops are spaced along profile A′–A″ at 10- to 20-m intervals, to a maximum distance of 125 m from the receiver borehole, 35E. For each transmitter, vertical magnetic field data were collected at 6-m intervals at depths from 10 to 140 m using frequencies of 1 and 5 kHz. Individual surface-to-borehole profiles required about one hour; the collection of 16 profiles on line A–A′ required two days for both frequencies.

Crosshole EM Results

Figure 6 shows a sample crosshole EM profile. The profile is measured using a fixed receiver, located within the upper oil sand at a depth of 60 m, and a continuously moving transmitter. Measurements were made at 1-m intervals. At first glance, the amplitude data reflect the relative positions of the source and receiver coils; the fields become larger as the source and receiver coils approach the same level and fall off in proportion to the borehole tool separation. The phase data are considerably more sensitive to the resistivity

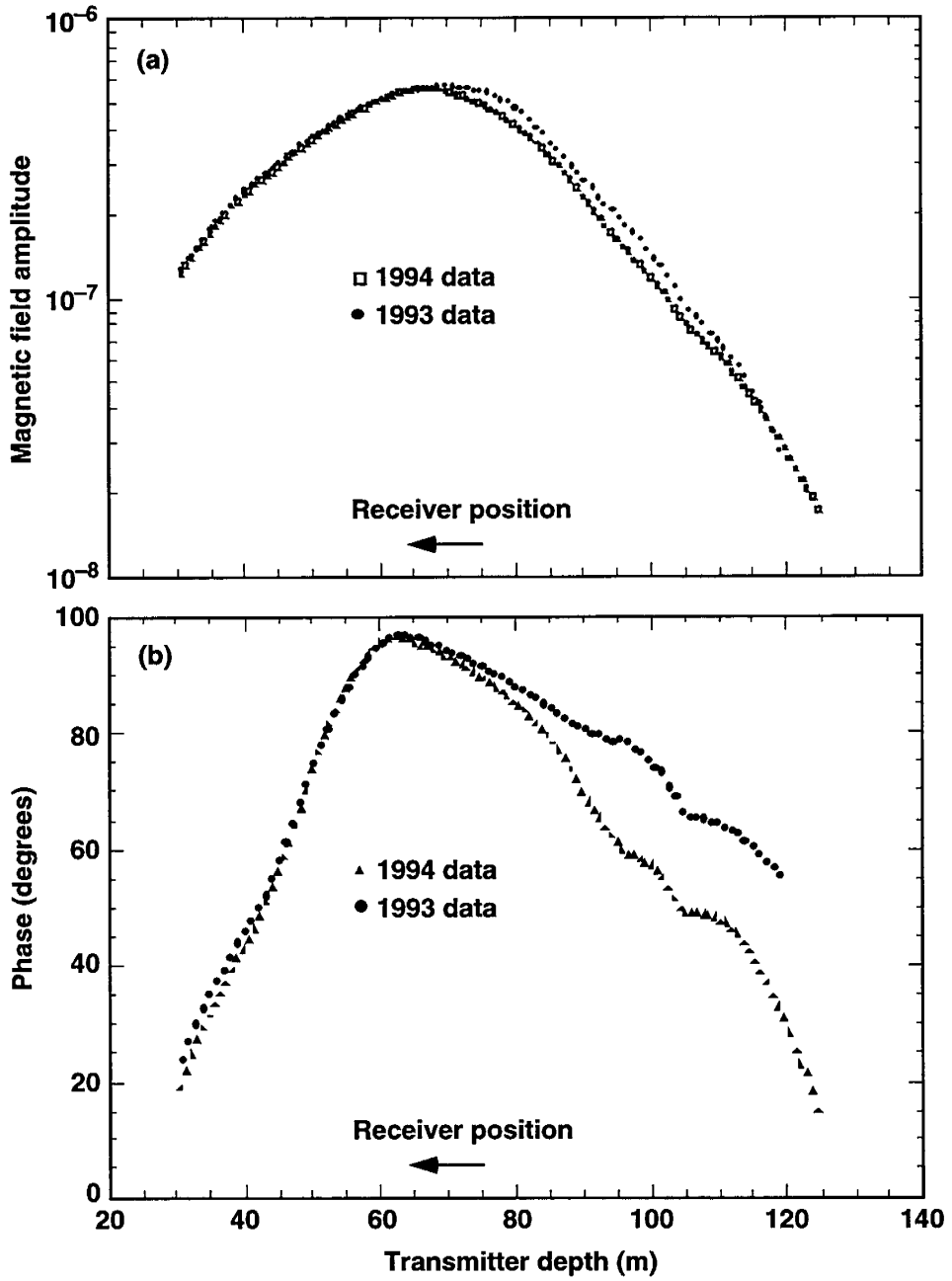

Figure 6. Sample crosshole 5-kHz EM data profiles collected between boreholes 35W and 35E.

distribution. For example, the phases are higher within the higher-resistivity oil strata but show pronounced rotation in the lower-resistivity shale beds above and below the oil sands. The crosshole field data are repeatable to within 2%; we use Figure 6 in estimating data uncertainty during interpretation.

In Figure 7, we show the 5-kHz amplitude and phase data in contoured form for surveys collected before (November 1993) and after (April 1994) steam injection. In general, the contour plots have the same characteristics as the individual profiles; that is, the amplitude data generally reflect the geometric spacing between the borehole tools, while the phase data are maximum in the higher-resistivity oil sands between 60 and 110 m and lower in the low-resistivity silts. Notice that although the data collected in 1993 and 1994 are remarkably similar for tool depths above 60 m, they are quite different below this depth. The data collected in April 1994 show a systematic reduction in both amplitude and phase at depths from 60 to 120 m compared with the November 1993 data. More than a 40% decline in the field amplitude is observed together with a change in the measured phase of more than 20 degrees. We attribute this to decreases in electrical resistivity as a result of the steamflooding. The observed difference in the crosshole data is considerably greater than it is in the surface-to-borehole observations. This is primarily because the crosshole tools are closer to the steamed zone and because a higher frequency is applied in the crosshole surveys.

Crosshole EM data were interpreted using the two-dimensional code described above. We use a smoothed version of the induction resistivity logs in boreholes 35W and 35E as a starting estimate for the inversion, and the computer changed the interwell conductivity distribution until the observed field data match the calculated data to within the observed field error of 2%. For each data set, the code required 20 iterations and approximately 20 hours on an IBM model 590-600 computer workstation to reach a final model.

Figure 8 shows the interpreted subsurface resistivity distribution between boreholes 35E and 35W before and after steam injection. These images represent an interpretation of the three individual data sets collected in 1993 and 1994. The arrows show the steam-injection intervals in injection borehole 5035 and O35. The darker sections of the images represent higher-resistivity zones associated with heavy-oil sands; the lighter areas are lower-resistivity silts and confining shale beds of 2 to 6 ohm-m. The pre-injection image in Figure 8a shows the upper oil sand to be a thick, continuous unit dipping gently eastward. The middle and lower sands are thinner and more discontinuous between the wells. Note that there is a certain amount of blurring in these layers; we believe this blurring is primarily caused by the coarseness of the numerical grid (2×2 m). The images in Figures 8b and 8c are visibly different only at depths below 80 m in the region below the injection borehole. In this portion of the figure, the resistivity has decreased significantly because of the steam injection. In all other parts of the image, the before and after data agree to within a few percent.

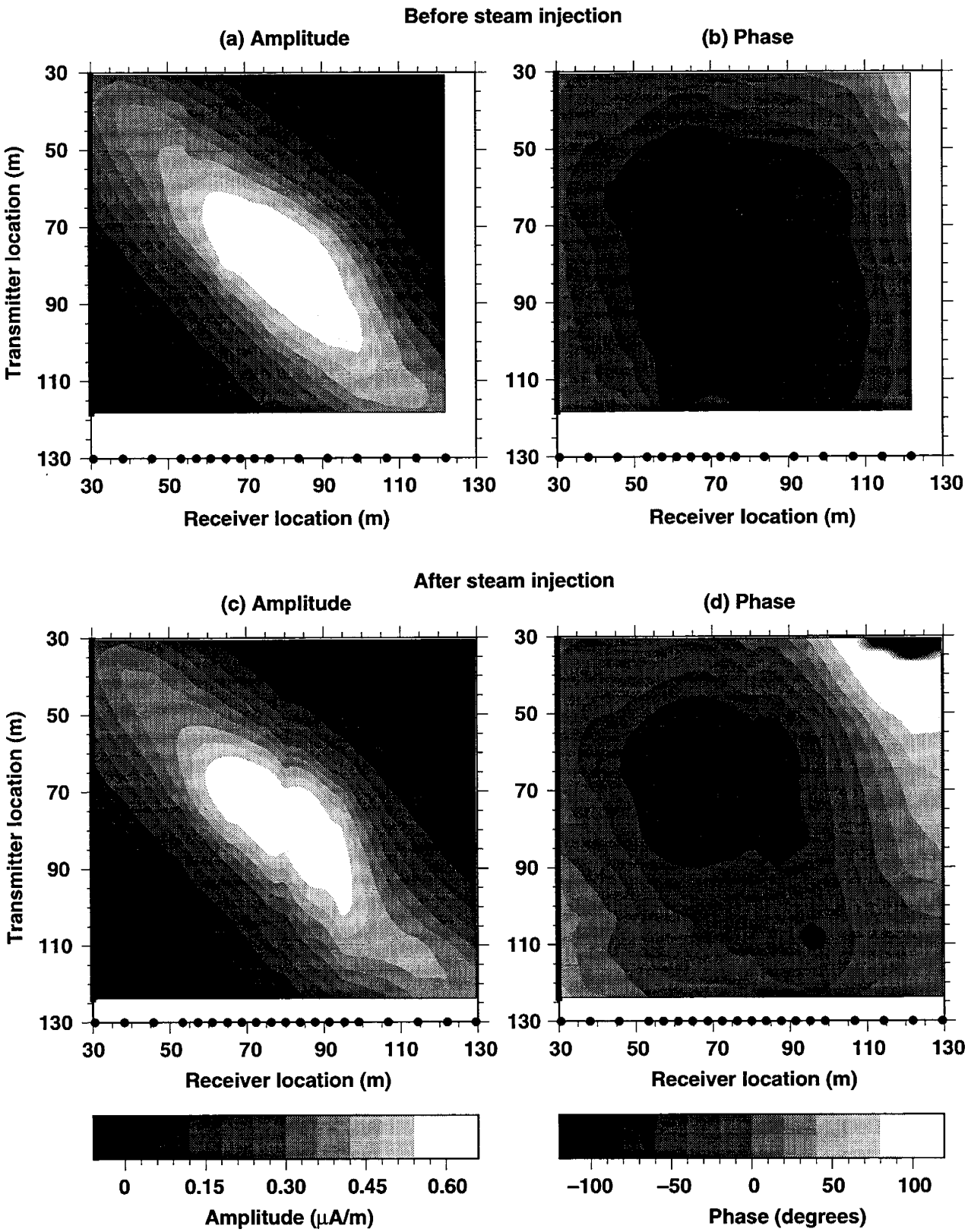

Figure 7. Combined 5-kHz crosshole data set before and six months after steam injection.

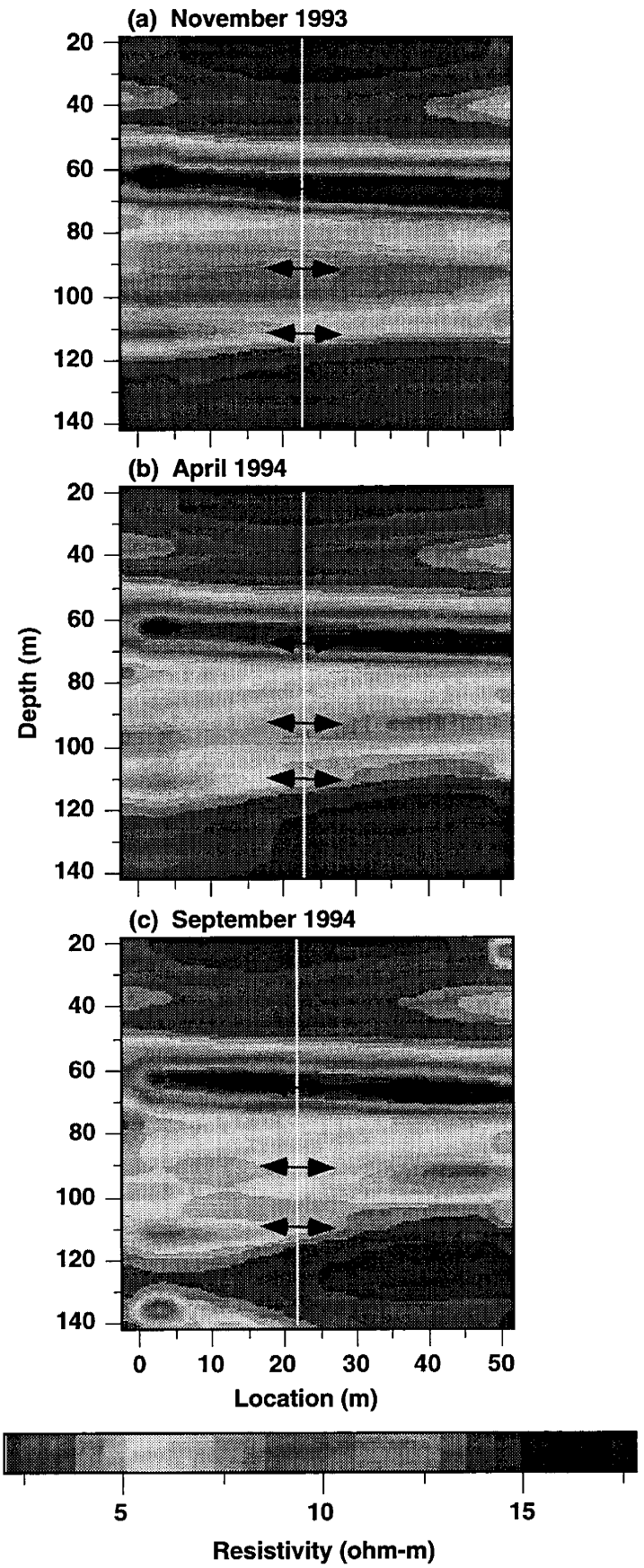

Figure 8. Resistivity images derived from crosshole EM data (a) before steam-flooding, (b) 6 months after flooding, and (c) 10 months after flooding.

In Figure 9, we show two difference images, made by subtracting the baseline images from the two post-steamflood images; again, the arrows represent the steam-injection intervals. The darker portions of these difference images indicate substantial decreases in the subsurface resistivity as a result of the steam injection; the greatest difference is a decrease of more than 35% in the region surrounding the injection hole at depths below 80 m. These images indicate that a substantial steam chest has formed in the middle and lower sands, and almost none of the steam has gone into the upper oil sand. The difference images also show that the injected steam is preferentially moving eastward in the lower oil sand but westward in the middle sand. We note that nearby producer 4034 was not completed in the middle oil sand because on this well site, at the eastern margin of the field, the middle sand is water saturated. The well is therefore providing no eastward pull to the steam, thereby leaving it to respond only to the pressure gradients from the other producers to the west, north, and south. We explain the eastward movement of the steam in the lower Tulare by better stratigraphic connection as noted in the borehole logs shown in Figure 5.

Since steam injection logs in well 5035 show that a considerable amount of steam penetrates in the upper perforated zone, it is unknown why there is no evidence of steam chest formation in the EM results. This may be because the colder and more viscous oil in the thicker upper Tulare sand is responding much more slowly to the steam injection. If so, the steam plume will develop later. Alternatively, there may be a connection from the upper to the lower Tulare sands via natural or man-made fractures. Such a connection would redirect the steam into these lower units. The worst case is that the steam could be filling an upper air-filled sand, which would pose a safety hazard. Since no evidence of this is manifest in the well data or in the surface-to-borehole EM results, our results suggest that, to date, the steam is confined to the oil-bearing strata.

Note that Figure 9 provides only a two-dimensional picture of subsurface steam flow perpendicular to the prevailing northwest–southeast geologic strike. The steam plume is clearly a three-dimensional structure, and in fact, we expect that most of the steam flow will be along geologic strike. If, for example, the plume in the upper oil sand is developing as a very narrow ellipsoid, parallel to geologic strike, it may not be evident on the cross-hole data.

In February 1995, Mobil contracted for repeat induction resistivity and temperature logs in borehole 35W to determine if steam breakthrough had occurred; we show these logs together with similar logs made before injection in Figure 10. The temperature logs in Figure 10 confirm that steamflooding has been restricted to the lower two Tulare sands and that the flooding is associated with a substantial resistivity decrease in the high-temperature zones. Well-log resistivity decreased by 30 to 50% in the middle oil sand and the associated confining silts; this decrease is in accord with predictions from the cross-hole EM surveys. These changes are in close agreement with observed changes in the South Belridge Tulare sands after steamflooding (Ranganayaki et al., 1992).

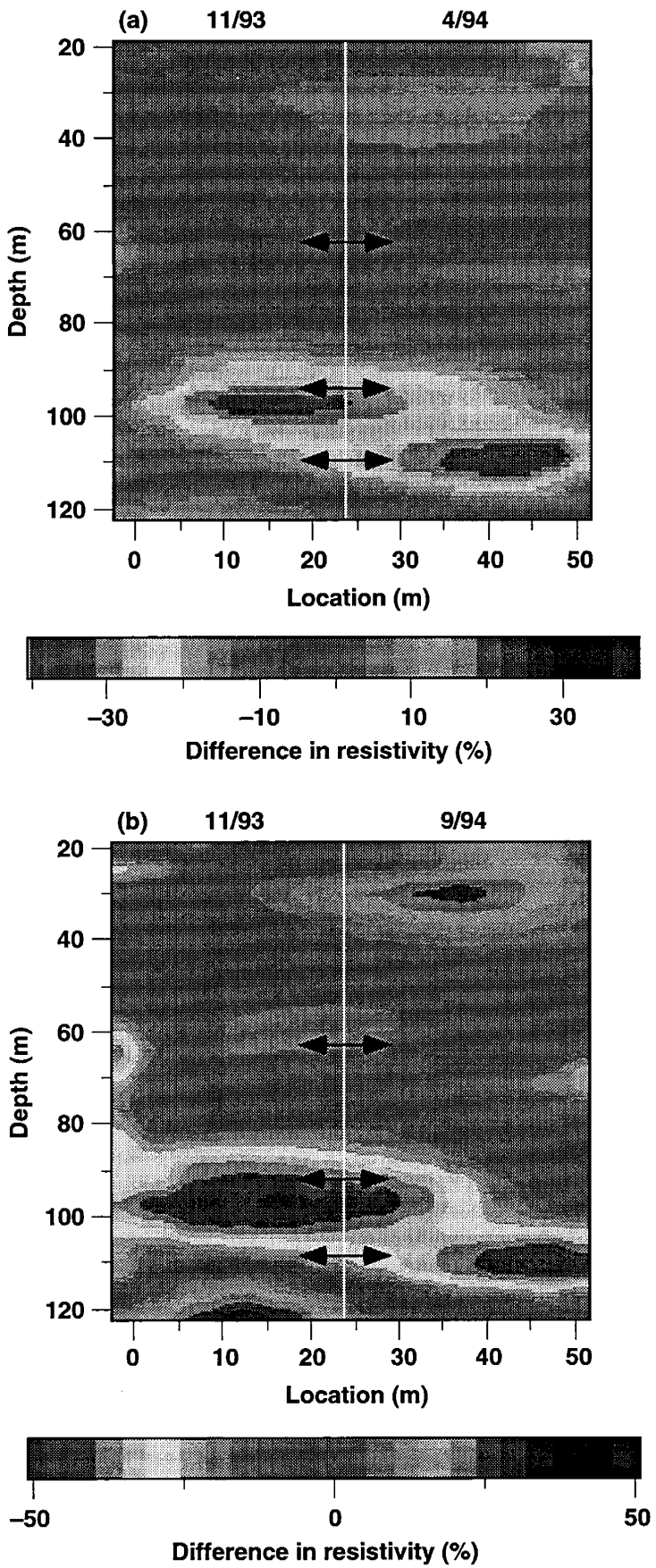

Figure 9. Resistivity difference images of crosshole EM data before steamflooding, 6 months after flooding, and 10 months after flooding. Differences were made by subtracting the baseline image from the postflood images of Figure 8.

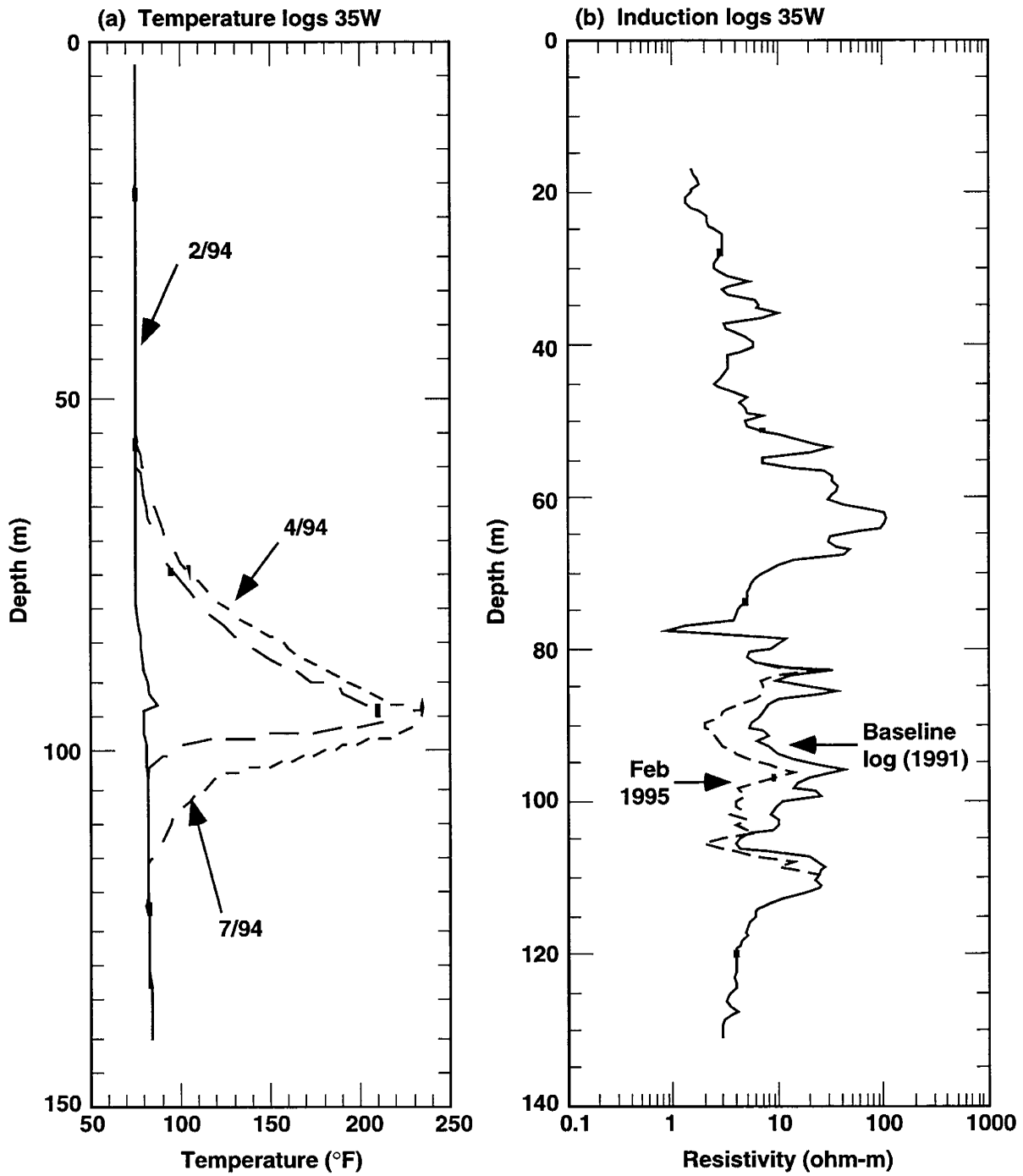

Figure 10. Temperature and induction resistivity well logs collected in borehole 35E before and after steamflooding.

Note that the reduction in resistivity is in accord with expected changes due to temperature alone (Keller, 1988). This is not obvious because the resistivity of sedimentary rock is a complex function of porosity, clay content, fluid type, salinity, and saturation as well as temperature. An earlier analysis of a similar steamflood showed that, although

steam injection results in measureable changes in saturation and fluid salinity, these affects seem to cancel each other and the combined affects on the resistivity of the rock is often quite small (Newmark and Wilt, 1992). In fact, in sands and clays the resistivity changes can be predicted within 10% on the basis of temperature.

Surface-to-Borehole Results

Figure 11 shows a sample surface-to-borehole profile with the fit from the one-dimensional model. The profile shows the 1-kHz EM field amplitude as a function of depth in borehole 35E using a surface loop transmitter located 25 m from the well. The 11-layer, one-dimensional model is made by initially assuming that the earth consists of 12 layers of equal resistivity each 10 m thick. The resistivity of the layers (but not the thicknesses)

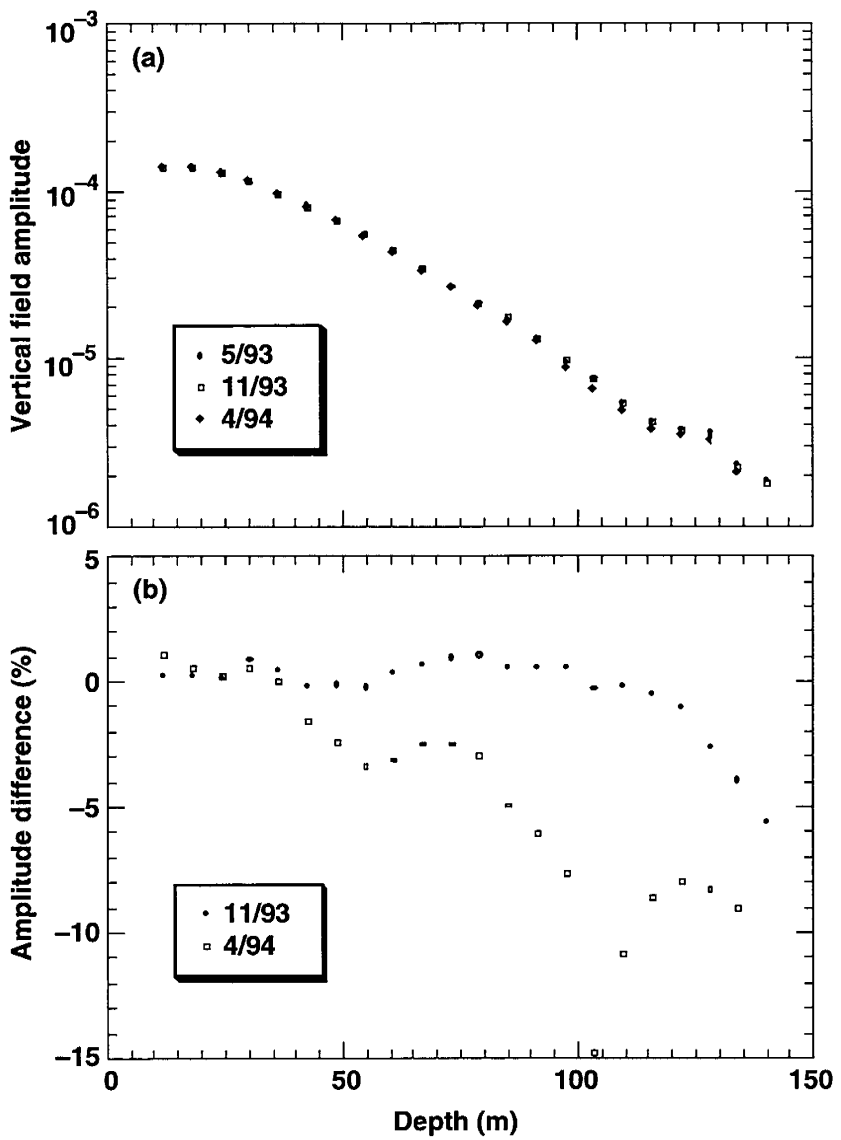

Figure 11. Sample surface-to-borehole data plot.

was then adjusted by the computer until the observed and calculated data match. A similar plot is produced from each of the 16 loop transmitter sites. The layered models derived from the surface-to-borehole data agree well with the borehole induction log, but the lateral structure may not be obtained from the layered models.

In general, the surface-to-borehole data quality was good, with most individual profiles repeating over time from 1–2% for shallow receiver depths to 2–5% for greater depths. The plot in Figure 12 is typical of difference in observed data collected over long time intervals. Notice that the amplitude profiles collected before and after steaming are quite similar at shallow depths but begin to diverge in the lower 20 to 30 m of the well. The later measurements are lower in amplitude, which typically indicates a decrease in resistivity. Although we can reasonably attribute this change as the effects of subsurface steam flow, we found that the observed change is too small and the data were not sufficiently accurate for use in detailed modeling. As the steamflood develops further over time, we expect it to be more visible to these data, but at present, it is difficult to delineate. At the three transmitter sites adjacent to the steam injection well, some of the data show obvious signal contamination probably because of the nearby steam pipes and well casings.

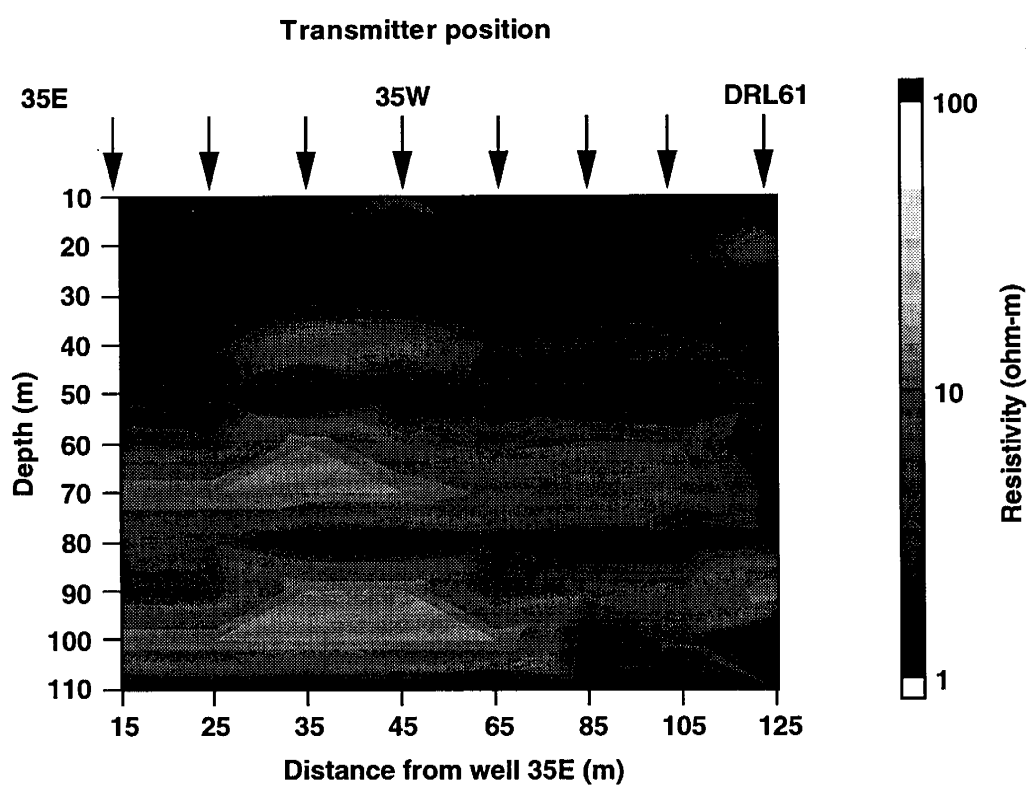

Figure 12. Pieced-together one-dimensional inversion of surface-to-borehole data along A′–A″.

As the steamflood develops further, we expect the surface-to-borehole results to become more and more sensitive to subsurface changes. This is especially true if the steam begins to flow in the shallower upper Tulare sand. Then the technique will offer significant advantages in that we are not restricted to the plane between boreholes and we may deploy our system along any arbitrary profile.

Although data interpretation is at present in a primitive state, several interpretational tools are being developed. The interpretation problem for this configuration is much more difficult than the crosshole case because of the surface layer and because a much greater volume of rock is affected by the measurements.

Discussion and Conclusions

Since it is a pilot for the development of almost 5 million barrels of oil, this project has been given every opportunity to succeed. However, in October 1994, after three years of continuous steam injection, the two western patterns were shut-in due to lack of response. In addition, the shallow steamflood has had eight incidences of steam breaching the ground surface, each resulting in extended periods of non-injection, subsequent steam restrictions, and ultimately, the closure of one pattern.

The upper oil sand is clearly having some difficulty accepting steam, at least in the initial phase of steamflooding. We expect that this unit will also develop a substantial steam chest but it will require more time. We plan to collect crosshole and surface-to-borehole EM data in this area at 6-month to 1-year intervals, so we can continue to monitor the movement of the underground stream. Our modeling results indicate that when substantial steam flow occurs in the upper oil sand, both crosshole and surface-to-borehole data should be able to detect it.

Results from this project have demonstrated that crosshole EM can be a powerful tool in reservoir characterization and process monitoring. This finding is particularly encouraging because the technology is relatively young. We can therefore expect significant improvements in data collection and image definition to be forthcoming. In addition, the method is well suited for joint interpretation with seismic and other data types.

The practical challenge is to incorporate technologies such as crosshole EM and seismics in field monitoring in a cost-effective manner. These technologies serve to improve the knowledge of reservoir geometry and to allow the engineer more control of secondary and tertiary recovery processes.

Acknowledgments

This project was funded by the U.S. Department of Energy through Fossil Energy research under Contract W-7405-Eng-48. We thank project manager Tom Reid for his continued support. We also thank Mike Deets, at Mobil in Bakersfield and Kim Halbert at Lost Hills for their cooperation and support throughout this project. Field technicians Don Lippert and Jim Dougherty, from the Geophysical Measurement Facility at Lawrence Berkeley National Laboratory were instrumental in the data collection.

References

Eastwood, J.; Lebel, P.; Dilay, A.; and Blakeslee, S. (1994), "Seismic Monitoring of Steam-Based Recovery of Bitumen," *The Leading Edge* **13**(4), 242–251.

Keller, G. V. (1988), "Rock and Mineral Properties," in *Electromagnetic Methods in Applied Geophysics, Vol. 1, Theory.* Investigations in Geophysics Series, No. 3 (Society of Exploration Geophysicists, Tulsa, OK), pp. 13–51.

Mansure, A. J.; and Meldau, R. F. (1990), "Steam-Zone Electrical; Characteristics for Geodiagnostic Evaluation of Steamflood Performance," *Soc. Petrol. Eng. Formation Evaluation* September, pp. 241–247.

Miller, D.; McPherson, J. G.; and Covington, T. E. (1990), "Fluvio-Deltaic Reservoir, South Belridge Field, San Joaquin Valley, California," in Barwis, J. H.; McPherson, J. G.; and Studlick, J. R. (Eds.), *Sandstone Petroleum Reservoir* (Springer-Verlag, New York, NY), pp. 109–130.

Newmark, R., and Wilt, M. J. (1992), "Changes in Formation Electrical Properties during Steam Flooding," *Expanded Abstacts, Soc. Explor. Geophys. Annual Meeting* (New Orleans, LA), pp. 488–491.

Ranganayaki, R. P.; Akturk, S. E.; and Fryer, S. M. (1992), "Formation Resistivity Variation due to Steam Flooding: A Log Study," *Geophys.* **57**(3), 488–494.

Spies, B. R.; and Greaves, R. J. (1990), "Numerical Modeling of Surface-to-Borehole Electromagnetic Surveys for Monitoring Thermal Enhanced Oil Recovery," *Geoexploration* **60**(9).

Torres-Verdin, C.; and Habashy, T. (1993), "An Approach to Nonlinear Inversion with Application to Cross-Well EM Tomography," in *Extended Abstracts Society of Exploration Geophysicists Annual Meeting,* pp. 351–354.

Wilt, M. J.; Morrison, H. F.; Becker, A.; and Lee, K. H. (1991), *Cross-Borehole and Surface-to-Borehole Electromagnetic Induction for Reservoir Characterization,* U.S. Department of Energy, Washington, DC, DOE/BC/91002253.

Wilt, M. J.; Alumbaugh, D. L.; Morrison, H. F.; Becker, A.; Lee, K. H.; and Dezcz-Pan, M. (1995), "Crosswell Electromagnetic Tomography: System Design Considerations and Field Results," *Geophys.* **60**(3), 871–885.

Task 67 - INTEVEP shall provide DOE with information on research about H_2S inhibition during steam injection. The research will provide field data on H_2S generation during the application of controlling methods.

Technical Evaluation of the H_2S inhibition process related to steam injection. Bachaquero Field, Project LL-4.

by

R.E. Campos, (INTEVEP, S.A.)

T.E. Vásquez, (INTEVEP, S.A.)

E. Añez, (MARAVEN, S.A.)

INTRODUCTION

It has been determined that during the extraction process of light, medium, heavy, and extraheavy crudes, the gas associated to each of the reservoirs presents concentrations of hydrogen sulphur (H_2S) and carbon dioxide (CO_2), which are sometimes significant.

In reservoirs containing heavy and/or extraheavy crudes, the H_2S and CO_2 concentrations abruptly increase during the application of thermal processes (steam injection). For instance, in the steam drive process, concentrations between 10,000 and 100,000 ppm of H_2S and up to 10% (v/v) of CO_2 have been found, as in the case of Project M-6 in the Costa Bolívar and Jobo in the eastern part of Venezuela.

Similarly, in the cyclic steam injection processes, the increase in the concentrations of H_2S and CO_2 is also abrupt but temporal, that is, H_2S concentrations reach limits of up to 30,000 - 32,000 ppm within the first days after opening the well for production, decreasing subsequently with crude production. In several cases the maximum production of H_2S has been detected to occur between the first 2 to 15 days of production of the stimulated well. Subsequently, with time, the concentration of H_2S decreases exponentially thus returning to levels of 10 to 30 ppm (cold production) in approximately 200 to 400 days.

In the past, and with the purpose of minimizing or neutralizing H_2S production, caustic solutions (NaOH), which partially remove the H_2S content, have been employed at field level, showing poor results. This type of treatment produced negative collateral effects, such as: reduction of porosity, destruction of the porous medium cementation, and decrease of porous media permeability. Hence, this treatment has not been and is not at present an integral solution to the problem, since the damage caused to the well has brought greater consequences than the problem to be solved. There is no doubt that the production of these gases (H_2S and CO_2) has limited the exploitation of heavy crude reservoirs associated with steam injection projects.

In view of this fact, INTEVEP, S.A. proposed to MARAVEN, S.A., within the context of the Project 5102 (Recovery Processes for Heavy and Extraheavy Crudes), an H_2S inhibition process related to steam injection, by using a urea and ammonium chloride-based chemical formulation. This formulation, tested at an experimental level, offered highly satisfactory results in the reduction and/or inhibition of H_2S, without disturbing the well's productive stage.

ABSTRACT

A description of the technical evaluation of the H_2S inhibition process related to cyclic steam injection is presented. This process was introduced in the Bachaquero Field, Project LL-4, MM-5, MM-6 geographical blocks, operated by MARAVEN, S.A. and put into practice between December 1994 and March 1995.

The type of process introduced, its stages, the selection of the area, and the results obtained from the project are also detailed. The control and follow-up of the H_2S concentrations in each of the wells included in the project made it possible, in the first place, to define a clear trend of the H_2S concentrations in the steam injected wells in a second cycle of production in the selected area, Bachaquero. Secondly, it was posible to test a state-of-the-art technology, which will make it possible to position the application of thermal processes in a significant economical advantage, and, finally, to propose improvements in the exploitation scheme of Bachaquero's crude.

The efficiency of the process introduced is over 90% reduction of the H_2S generated by the stimulation of wells in the area of the above mentioned project. Its effectiveness in the reduction of the H_2S generated is immediate and the cost of treatment per well is not higher than 950 Mbs. (2.0 MUS$), out of which 60% corresponds to the injection service.

BACKGROUND

One of the most interesting phenomena observed in the steam injection projects (steam drive or cyclic injection) is the production of gases having high contents of H2S. In the case of MARAVEN'S M-6 steam drive project, the concentration of this gas increased with time as the reservoir began to heat up.

In 1981, out of 130 active wells, 53 wells (41%) showed an H_2S concentration range from 1,000 to 10,000 ppm, 38 wells (29%) from 100 to 1,000 ppm, 29 wells from 1 to 100 ppm, and the remaining 10 wells from 10,000 to 100,000 ppm [1].
In the specific case of the Bare Field, Hamaca reservoir Orinoco Belt, H_2S concentrations between 12 and 15 ppm were detected in cold wells. In steam stimulated wells, at first, second and/or third cycle, concentrations of up to 1,800 ppm were found during the first day of production, and 160 ppm after 200 days of production [2].

For each of the cases mentioned above, plenty of information is available; however, only few technical reports are published on this matter as well as on the control and systematic follow-up of H_2S concentrations in wells, locations and/or fields, after stimulation. In most of PDVSA'S Operating Affiliates, corrective measures aimed at preventing this effect have been mainly directed towards the handling of this gas through production facilities, establishing dispersion in the atmosphere as the ideal method to minimize the concentrations of this gas in the environment.

In most cases of recently steam-injected wells, in which high H_2S concentration levels are detected, the immediate action to be taken is to connect the well's casing to its flow line, so as to allow the associated gas to flow towards the station,

where, once separated from the crude, it is released to the atmosphere through 20 to 40-m high smokestacks.

However, in Costa Bolívar, MARAVEN exploits a lot of its heavy crude reservoirs keeping the casing open to the atmosphere, thus contributing to the increase of H_2S concentration in areas near the well, which are, in most of the cases, highly populated. This kind of problems has not only environmental connotations, but also produces delays in the injection programs, deferring of production in fields having huge oil reserves, substantial investments in the flow stations in order to handle the problem, irreparable damages in flow lines due to the corrosive effect of these gases in the presence of water (H_2S, CO_2), as well as in the design of well completion.

Once the magnitude of the problem was established, INTEVEP and MARAVEN decided to carry out a project which would make it possible to reduce the H_2S levels related to the process of cyclic steam injection in the Bachaquero field, Project LL-4, using an urea/ammonium chloride solution under different injection schemes and steam cycles.

SELECTION OF THE PROSPECT AREA

The selection of the prospect area was mainly related to the evidence of H_2S generation present in the central area of the Bachaquero field, Project LL-4, and specifically those wells concentrated in the MM5 and MM6 geographical blocks, near the MM-6 steam plant.

In the Bachaquero field there is no regular program to measure H_2S concentrations in steam-stimulated wells; however, there is written evidence reporting concentrations in a variable range of 1,000 and 5,600 ppm of H_2S in the MM-6 block, well LB-607A, and in well LB-2090 which was completed in 1992 and steam-stimulated in August 1993. This well reached levels of 5,000 ppm 60 days after being opened to production, and 2,000 ppm after 212 days, which made it necessary to direct it to the MM-5 flow station and to build a 20 meters high disposal smokestack.

Based on this information, it was decided to focus the study on wells located in the MM5 and MM6 blocks, near the MM-6 steam plant and well LB-2090, and with few steam cycles.

The test was defined by conforming two concentric hexagons. The vertices of the external hexagon are wells LB-440, 1781, 593, 1512, 356 and 494. The internal hexagon is limited by wells LB-442, 512A, 515, 1808, 517, and 603. The study area with the limits mentioned represented the area of the H_2S inhibition project in Bachaquero (see Figure 1).

SELECTION OF WELLS

The selection of wells was based on the following characteristics:

1.- Optimal mechanical conditions.

2.- Sand variable thickness (170 < ONS > 90).

3.- Reference wells, both of first and second cycle.

4.- 7" casing. 51/2" lining; preferably with gas anchor.

5.- Steam injection conventional process.

Wells having such characteristics were: LB-1809, 442, 593, 1718, 494, 353, 1808, and 2090. This last well, was chosen due to its high H_2S concentrations, in order to perform a post-treatment.

TYPE OF PROCESS IMPLEMENTED

The process implemented was related to the passivation of the catalytically-active areas of the rock, the increase of the medium ionic strength, and the conformation of an aqueous medium with a pH = 7.5 - 8.0. One of the main objectives of the process was to prevent the ionic exchange of the clays and their subsequent transformation.

STAGES OF THE PROCESS

Pretreatments of the porous medium, with a combination of organic and inorganic additives, before and during the steam injection process were proposed. In those wells having oil net sand (ONS) ranges under 90 feet the pre-injection of an additive aqueous solution "plug" was proposed. In the case of wells showing superior ranges (ONS>100 feet) it was proposed to increase the addition of the additive "plug" when reaching half the tonnage per well and at the end of the process (see Figure 2).

ADDITIVES OF THE PROCESS

The additives that, according to the objectives of the project, showed the abovementioned activity are: urea and ammonium chloride. Both compounds are soluble and completely hydrolyze in water, which guarantees that the suspended solids concentration is null. The hydrolysis of both compounds is total. The components of this mixture are harmless and do not represent any risk if contact with the skin is produced.

DESIGN OF THE PROCESS

A database was required for the implementation and put into operation of the process. This database contained: physical characteristics of the reservoir, wells, production data, core analysis, fluids analysis, general characteristics of the steam injection process, production behavior of the wells, petrophysical data, clays volume (Vsh), records (flowmeter) of the selected or surrounding wells.

The analysis of this information made it possible to obtain some variables which had to be kept constant during the design of the process, in order to explain deviations which were characteristic of the process or of its operational conditions. The preliminary analysis of the information obtained is presented next.

STEAM-INJECTED WELLS

The analysis of the steam-injected wells showed that there was no correspondence between the tons of steam injected and the feet of stimulated net sand (steam ton per well/sand foot), nor there was a sole injection rate. A first summary of this analysis is presented in Table 1.

During the process both net sand tons/feet and injection rate (ton/day) are characteristics that should be maintained in a nearly similar range for test wells, so as to have a better control of the process, and not interfere in the expected production of each well; otherwise, the process or the additives added may be considered responsible of such situation.

In the summary table it can be observed how the amount of steam has varied from 4,438 to 6,087 tons. It may also be observed how the injection rate varied from 164 to 380 tons/day, the highest rates being present, in some cases, during the lowest thickness of net sand (ONS).

CRUDE ANALYSIS

Crudes from the selected wells - LB-356 and 1718 - will be, in this study, the reference of the typical characteristics of the area. Table 2 shows that water production in the area is between 6.8 and 7.9; similarly, we infer that asphaltenes concentration is 7.9 to 8.4%, and that the standard kinematic viscosity at 100 °F is near 1,300 - 1,560 cSt, which is observed in the cold wells LB-356, 1718, and 442 (after two years of production).

When comparing crudes viscosity values in wells 517 and 521, stimulated respectively on May, 1993 and February, 1992, we found kinematic viscosities of up to two and four times the original value of crude viscosity in this area. Analyses demonstrate that the former shows a viscosity of 4,379.8 at 100 °F, and the latter 2,100.2 cSt, values which could be related to high-viscosity W/O emulsions. Table 2 presents a sumary of the above mentioned characteristics and some production data.

According to the average range of asphaltenes taken as a reference, 7.9-8.4%, in wells injected in a first cycle such as 2,090, and 494 in a second cycle, asphaltenes contents are higher (9.18%, 9.27%) than the average range established.

Consequently, it may be inferred that this steam-stimulated crude varied in its chemical composition, becoming, after the stimulation, heavier than that originally contained in the reservoir. Hence, changes in its fractions (saturates, aromatics,

resins, and asphaltenes) are expected to occur. In this way, the production of fluids in these wells will be partly a function of the motive power necessary to move a heavier crude with a trend to be strongly retained in the formation due to the polar characteristics of heavy fractions (resins/asphaltenes).

GAS ANALYSES

No information was obtained about the composition of the gas associated to these wells, before and after the steam injection process. This information would have made it possible to verify and validate the extent of the crude's physicochemical reactions (distillation, cracking, etc.) at those steam temperatures, thus allowing to clarify the above point.

PROCESS CONDITIONS

After the analysis performed it was necessary to set some of the important operational conditions in the steam injection process in Bachaquero, and unify the selection of wells in order to evaluate the proposed process under similar conditions. Thus,

1. Wells LB-494 and 1808 were eliminated from the project, since the former has a lead plug in the bottom, and the latter presented a significant amount of repairs, as well as obstruction of the line (fish) as of December 1994.

2. An average of 36 - 37 steam ton/net sand foot was maintained in the selected wells.

3. A steam injection rate range of 350 - 360 ton/day was maintained. In other cases and depending on the well injectivity the injection rate was maintained in ranges of 300 tons/day.

4. Flowmeter runs were programmed in order to verify the amount of stimulated sand. The rate was between 200-250 ton/day.

5. The planned injection sequence in the area was taken into consideration in order to include in the project as many first and second-cycle reference wells as possible. The initially planned scheme was modified as shown in Figure 5 and Annex B.

BASES FOR THE DESIGN OF TREATMENT

The information on reservoirs (physical properties) necessary to design the process was obtained from the Projects Report, Fields: Lagunilla and Bachaquero, volume 2, September, 1993, by MARAVEN, S.A. A listing of this information is shown in Table 3.

With the purpose of facilitating treatment calculations, an Excel spread sheet was prepared, which allwos to introduce the basic values of the reservoir, the penetration radius to be considered, and the optimal Urea/NH4HCl ratio to be used. The additives concentration can be calculated based on the volume operatively feasible to be injected in field.

For practical purposes of the design it is considered that:

1. The steam contacts the formation in a homogeneous and uniform way. It is considered to be a radial type distribution.

2. Clays concentration is uniformly distributed in the penetration radius considered.

3. The total amount of clays contained is highly reactive to the steam injection process conditions.

4. There are changes in the saturation of crude per steam injection cycle, which influences the displacement volume to be used

CONTROL AND FOLLOW-UP OF THE PROCESS

Control and follow-up of the process were introduced during the initial stages of additives injection, steam injection, flow recording until its pumping condition, and consisted in gas (H_2S and CO_2) quantification per well in the casing and the tubing. In the tubing a gas-crude separation (flash) was performed in the areas near the well.

Gas quantification was performed from the Well's Natural Rate condition, flow at pressures and temperatures of the steam injection process, until the Well at Pump Introduction condition, pumping condition and mechanical lifting. A follow-up was performed during 120 days of production both to reference and treated wells.

Additionally, fluids analyses were carried out in order to interpret physical and chemical changes in the crude, such as viscosity, water content and sediments (% A and S), content of asphaltenes, metals, nitrogen and sulfur, and gases composition.

RESULTS

The dynamics of production operations and the accelerated changes in the steam injection programs and/or sequences, made it necessary to perform slight modifications to the project, such as:

1. Incorporation to the project of the wells LB-316, 436 (II cycles), recently injected.

2. Impossibility of incorporating first cycle additional wells. The high concentrations of H_2S found in the well LB-1718 did not allow measurement and control, since it was closed by the proximities of the MM-6 steam plant, and due to protests made by the staff adscribed to it.

3. Deferring of the post-treatment scheme to well LB-2090. For March 1995 this well was waiting for repair, and the concentrations of H2S in the casing were 20 ppm 9 months after being injected with steam.

Figures 4 and 5 show the results of the H_2S measurement performed on the second-cycle reference wells (II C) LB-316 and 436, in the tubing and casing respectively. As it may be noticed in Figure 4, H_2S concentrations in the tubing

start from values over 10,000 ppm few days after opening the well to production, and begin to decrease after 50 days of production to mean values of 500 ppm. From 60 days on, the concentrations stabilized until 103 days in mean values of 400 ppm. As regards to measurements performed in the casing the same curve trend can be observed, but with higher levels than in the tubing (see Figure 5). The explanations to these significant differences are related to the gas anchor function, which allows to increase the volumetric efficiency of the pump, producing and instant flash of production fluids, thus separating a significant part of gas in solution which emerges through the casing. Similarly, from 60 to 103 days of production, H2S concentrations stabilize in values of 400-500 ppm.

Figures 6 and 7 show the H_2S concentration behavior with respect to the time of the II cycle well LB-1809, compared to the behavior of the reference wells, both in the tubing and casing respectively. Measurements performed in the tubing show that the H_2S maximum concentrations after 4 days of well production are 300-350 ppm; decreasing after 20 days to concentrations under 10 ppm, and remaining stable in a range of 10 to 20 ppm, which indicates mean reductions of 96%, with respect to the concentrations of the model curve (see Figure 6). In the case of the H_2S concentrations contained in the gas flowing through the casing, the maximum value found was 40 ppm after 15 days, which was then stable in the range of 10 ppm in 103 days. This fact demonstrate the effective action of addivites and the efficiency of the treatment.

Figures 8 and 9 show the behavior of the H_2S concentration obtained in the II cycle well LB-442, both in the tubing and in the casing. In this case the H_2S concentrations in the tubing (see Figure 8) are between 300-350 ppm during 30 days; there is then a decrease, as in the case of the well LB-1809, to values of 10 ppm. Observing Figure 9, behavior in the casing, the H_2S concentrations begin in levels of 30 ppm until reaching values of 400 ppm, and begin to decrease to 10-20 ppm after 10 days of production. These behaviors seem contradictory, that is, when concentrations in the tubing are high or low, those found in the casing respectively decrease or increase. This can be explained based on oil production and the efficiency of the gas anchor. Implicitly the former of the two mentioned factors is related to the heated areal volume.

Figures 11 and 12 show the behavior of the H_2S concentrations based on a production time of 103 days of the first cycle well (I C) LB-353. The impossibility of building a reference well model behavior in a first cycle, due to the high concentrations of this harmful gas in the well production stage, was stated at the beginning of this section, which makes it possible to assert the success of the treatment in wells of a first steam cycle. Nevertheless, only for comparative purposes, we have drawn in both Figures the trend curve shown by the II cycle reference wells. Similar to what is observed in the tubing of the 2nd. cycle well LB-442, at the beginning of the production, concentrations of up to 700 ppm are obtained, which in 30 days fall to levels under 100 ppm, and after 50 days of

production become constant between 10-20 ppm. This situation is different in the casing; the efficiency of the separation increases, the gas maintains H_2S concentrations around 100 ppm until 80 days of production, and then falls under 10 ppm. If H_2S concentration values would have been obtained in 1st. cycle wells, the process would have been highly efficient. However, and comparing the reference model curve of 2nd cycle wells the reduction efficiency is above 80% values, in average.

CONCLUSIONS

1. A well treatment process which makes it possible to reduce and/or inhibit H_2S concentrations, associated with cyclic steam injection processes was introduced.

2. The efficiency and effectiveness of urea/NH4Cl in the treatment of wells involved in stimulation activities was proved through cyclic steam injection. The global efficiency of the process in the reduction of H_2S is over 90% in II cycle wells, and over 80% in I cycle wells.

3. The efficiency and effectiveness of urea/NH4Cl in the treatment of wells with 12% clay contents was proved.

4. For Bachaquero field, Project LL-4, Blocks MM-5 and MM-6, a reference and/or model curve of the H_2S concentrations contained in the gas associated with the steam injected wells in a second cycle was obtained. This curve was not previously available.

5. It was demonstrated that the high concentrations of H_2S in the cyclic steam injection projects in Bachaquero, maintain levels of 20,000 - 10,000 ppm during the first 10 days of well production; fluctuant concentrations between 8,000 - 1,000 ppm from 15 to 70 days and a stabilization of up to 600 ppm, even 103 days after. This fact denies the existing arguments that the H_2S concentrations in the gas of wells treated with steam injection, are only present few days after opening the well to production.

LIST OF TABLES

TABLE 1

Production and steam injection characteristics in wells from Bachaquero Field, Project LL-4, Blocks MM-5, MM-6

Well	Accumulated Production (cold)	Net sand	Ton steam	Injection pressure	Rate	Accumulated production	Ton /ONS
	(MBP)	(ONS)	(ton)	(psi)	(ton/day)	(in cycle)	(ton/feet)
LB-517	714.6	70	4438	825	164	4.3	63.4
LB-521	333.7	90	5005	1150	294	18.7	55.6
LB-593	482.9	90	4939	1100	235	35.2	54.9
LB-2090	0.73	122	4479	660	118	3.0	36.7
LB-494	1319.6	170	6087	900	380	68.5	35.8
LB-442	1581.6	160	5758	825	360	72.6	36.0

TABLE 2

Production characteristics and properties of the crudes from Bachaquero Field.

Project LL-4, Blocks MM-5, MM-6

Condition /	Sediments	Water	Asphaltenes	Kinematic viscosity	
Well	**(%w/w)**	**(%w/w)**	**(%w/w)**	**100 °F**	**150 °F**
Going to cycle I					
LB-356	0.2	6.8	7.9	1338	215
LB-1718	0.1	7.9	8.33	1556.6	228
Going to Cycle II					
LB-442	0	4.4	8.24	1339.8	218
LB-494	0.05	3.4	9.27	1675.4	210
LB-593	0.05	8.0	8.04	1360.6	
In cycle I					
LB-2090	0.05	7.0	9.18	1880.3	259
LB-517	0.8	66.6	7.36	4379.8	599
LB-521	0.05	28.0	6.18	2100.2	217

TABLE 3

Physical characteristics of the Bachaquero Field, Project LL-4

Property	Value
Porosity (%)	34
Reservoir temperature (°F)	130
Water initial saturation (%)	14.8
Petroleum initial saturation (%)	85.2
Present pressure (psi)	500
Clays average content (%)	12-15
Sand density (kg/l)	2.07
Net sand (ONS/feet)	44-160

LIST OF FIGURES

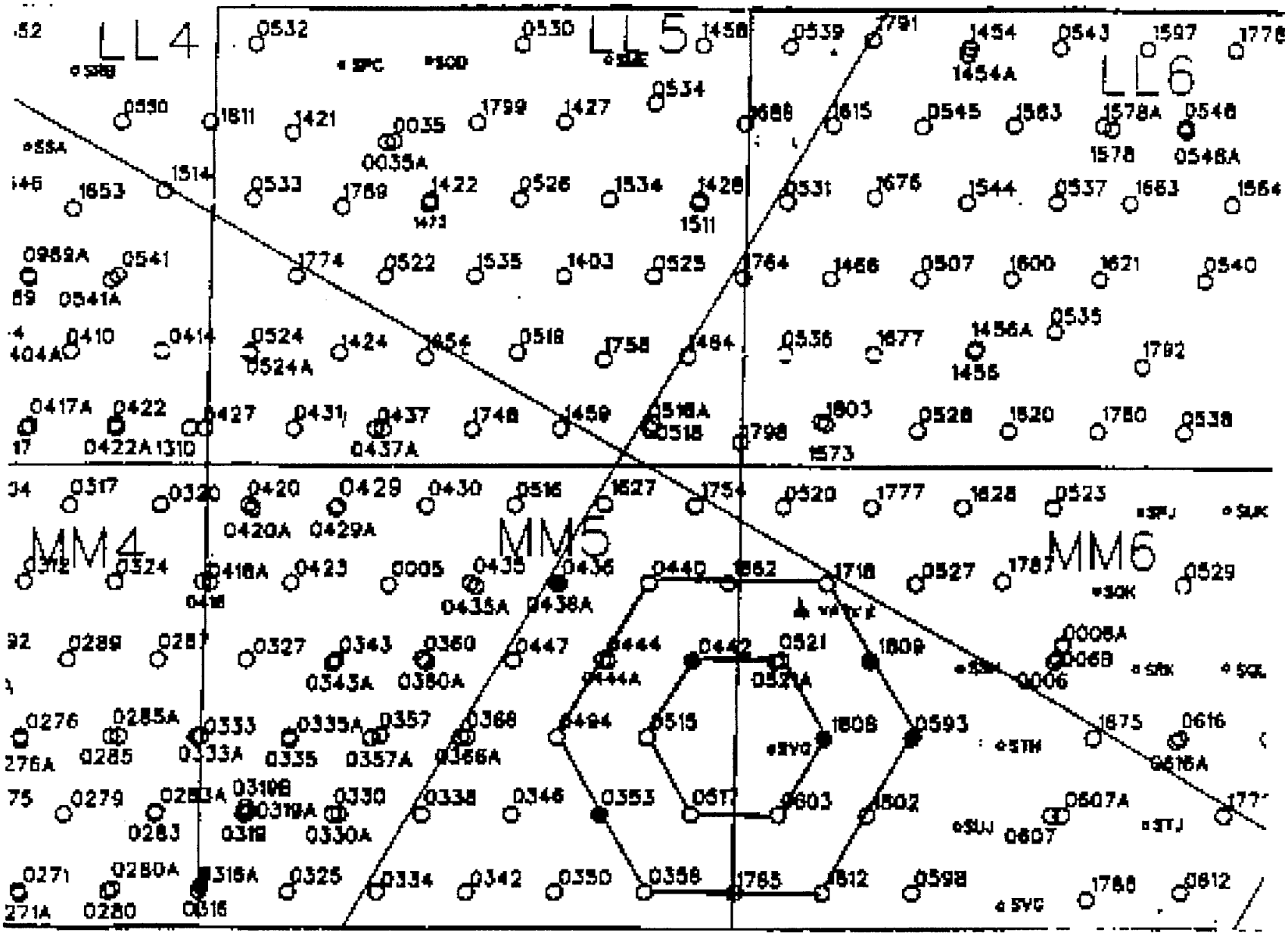

Fig. 1 SELECTED BACHAQUERO AREA

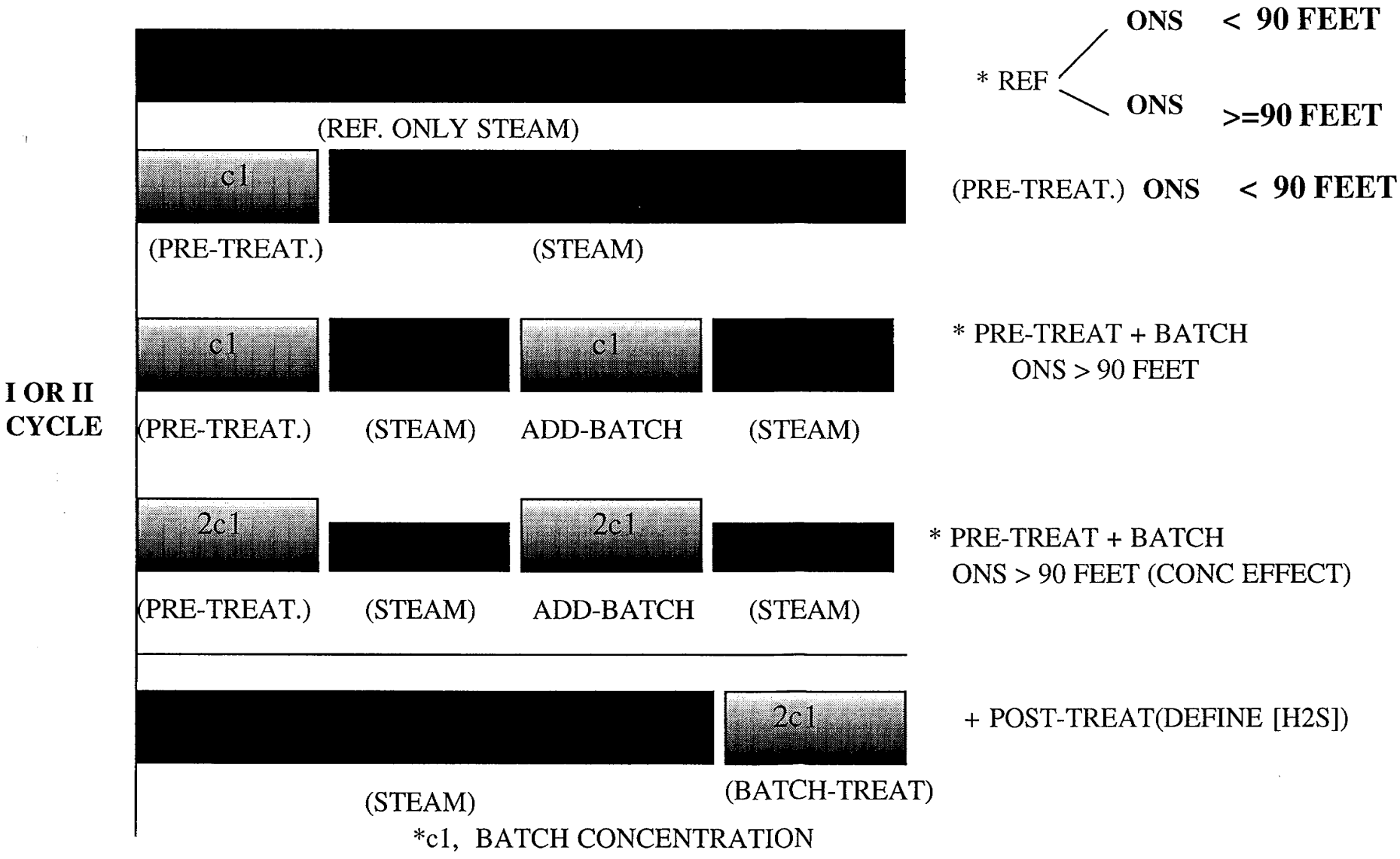

FIGURE 2. SCHEMES USED IN BACHAQUERO

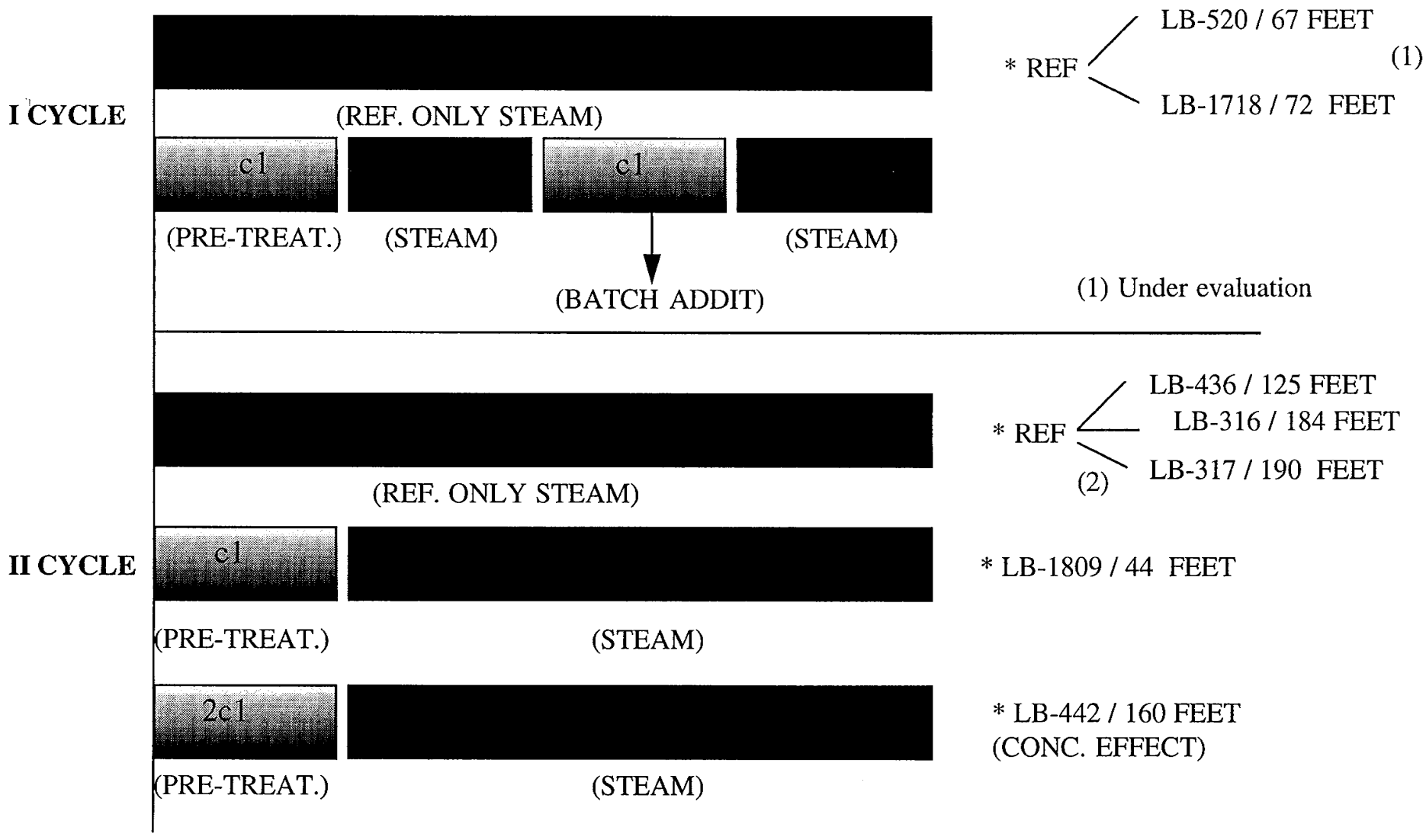

FIGURE 3. INJECTION SCHEMES USED IN BACHAQUERO (ONS/WELLS)

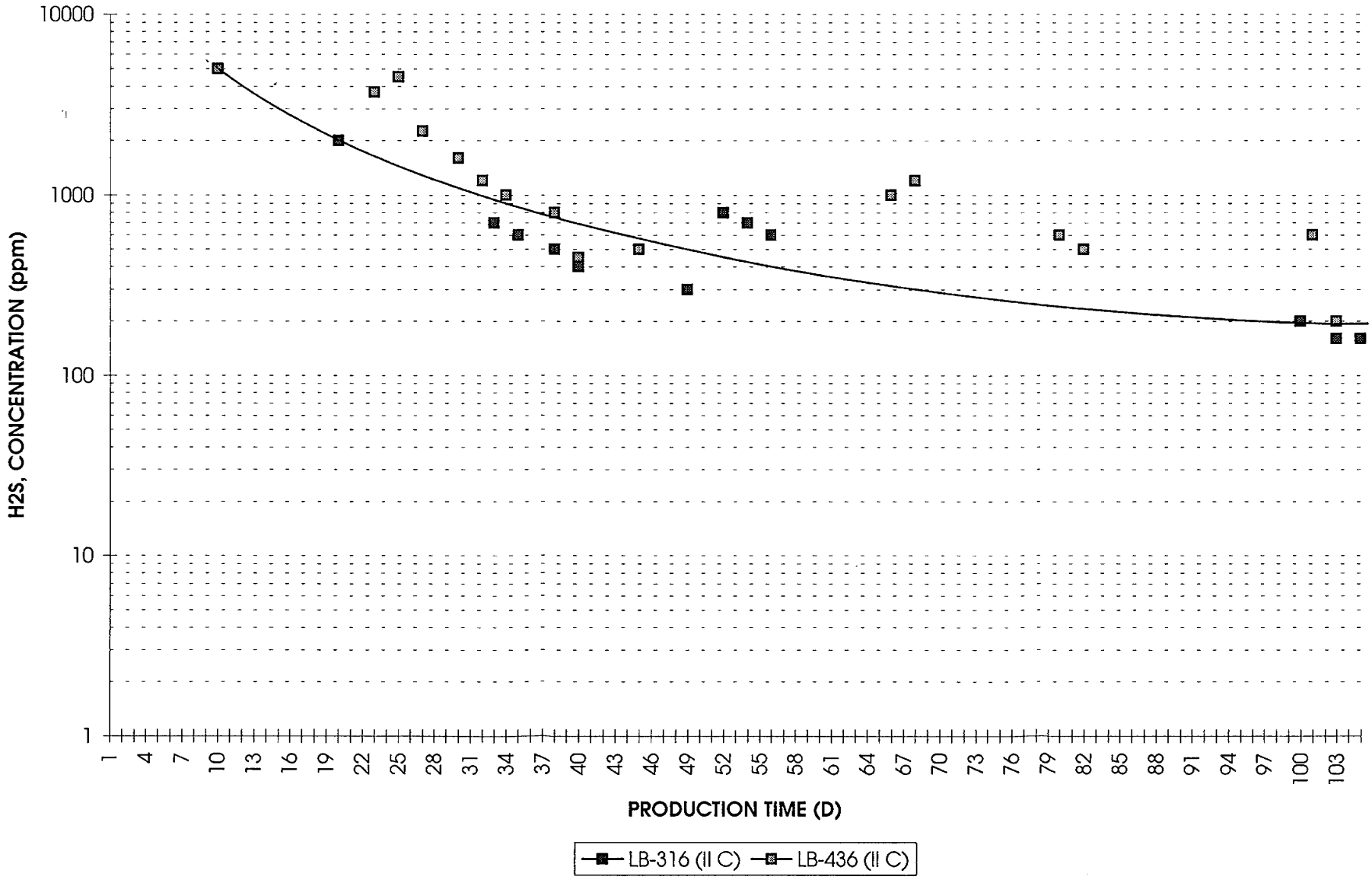

Fig. 4.- H2S Concentrations in References wells LB-316 y LB-436.
Tubing Level, II cycles.

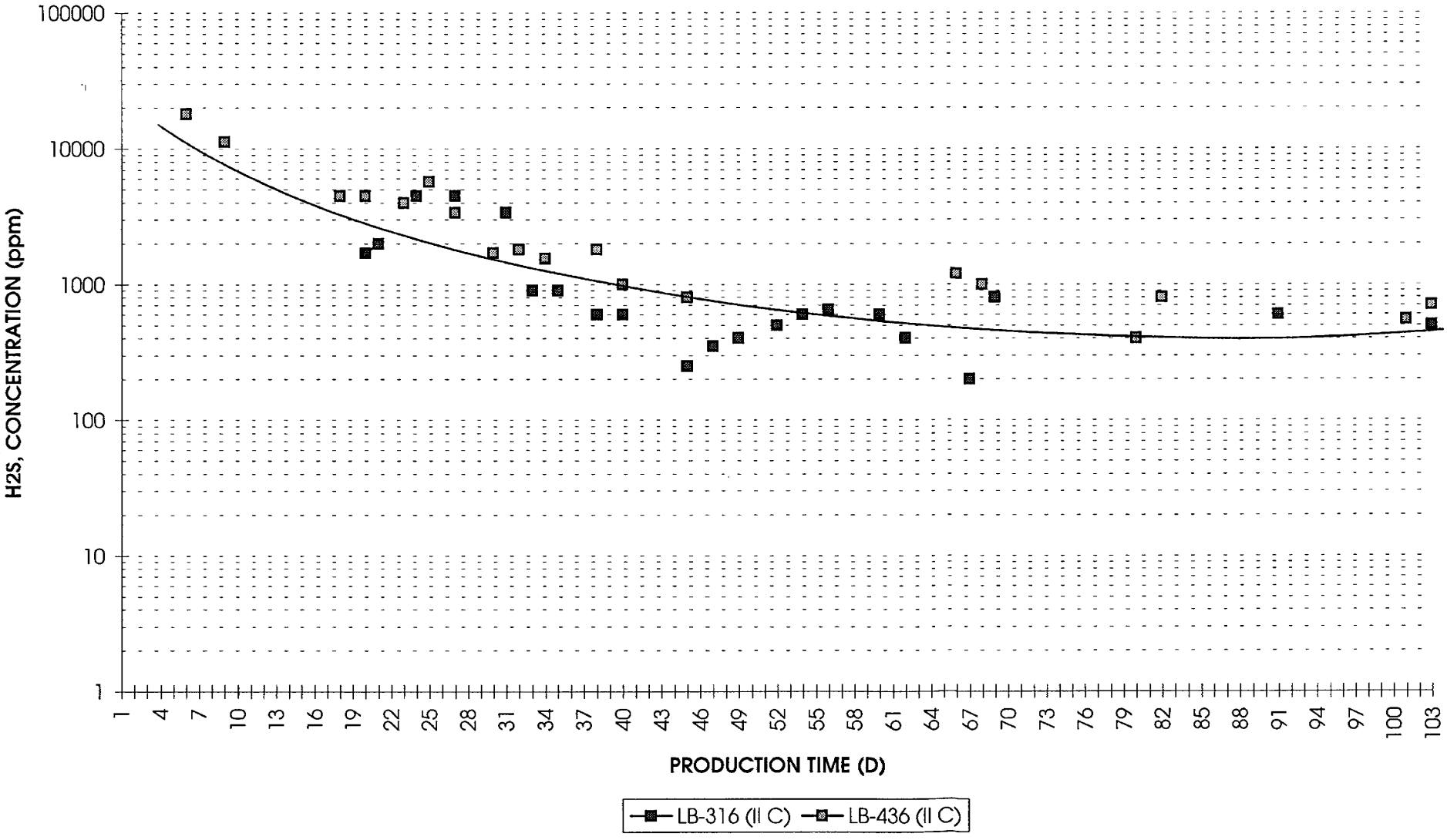

Fig. 5.- H2S Concentrations in Reference Well LB-316 y LB-436.
Casing Level, II Cycles

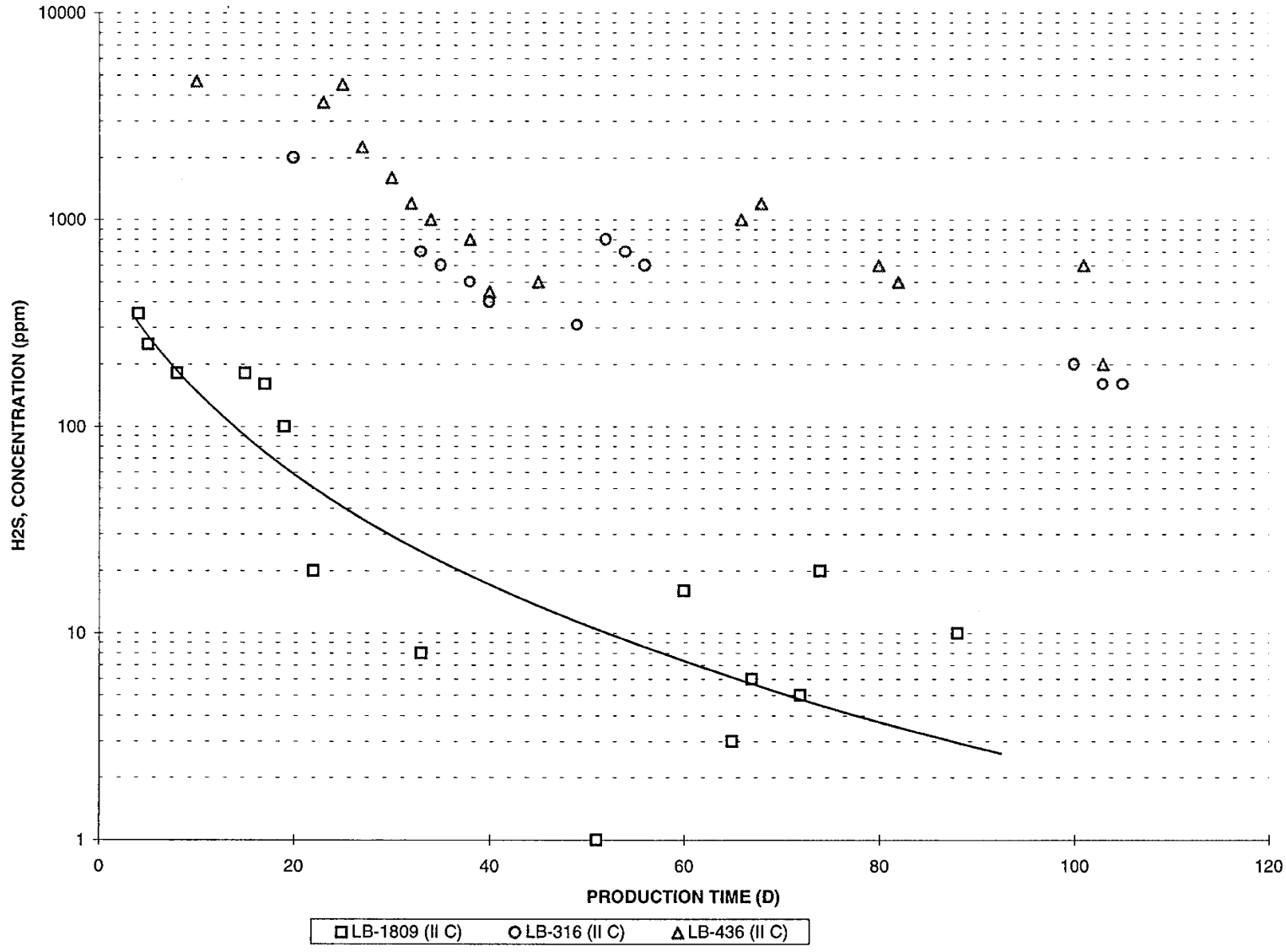

Fig. 6.- H2S Concentrations in the LB-1809 Treated Well vs Reference Wells LB-316 and LB-436. Tubing Level, II Cycle.

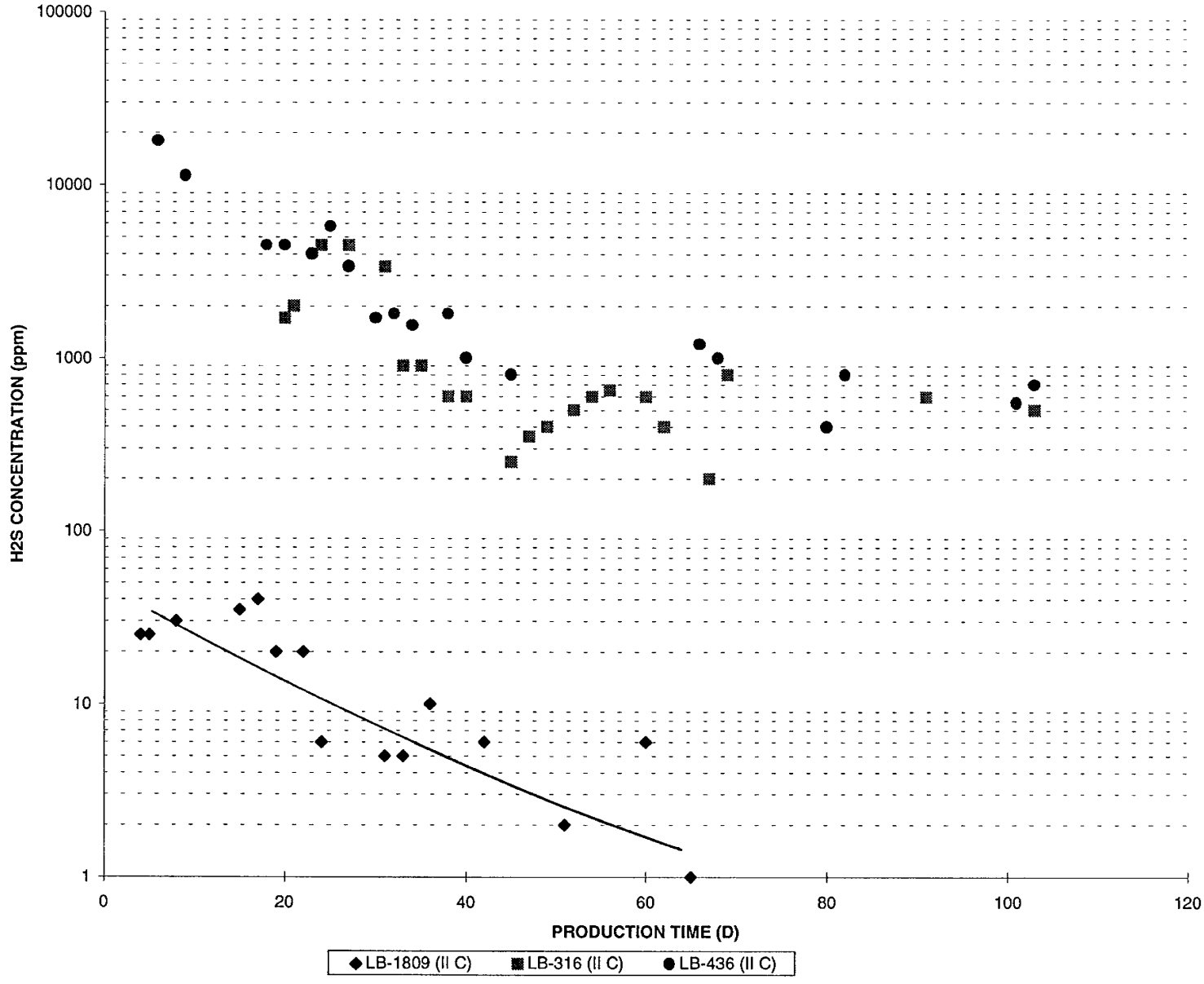

Fig. 7.- H2S Concentrations in the LB-1809 Treated Well vs Reference Wells LB-316 and LB-436. Casing Level, II Cycle.

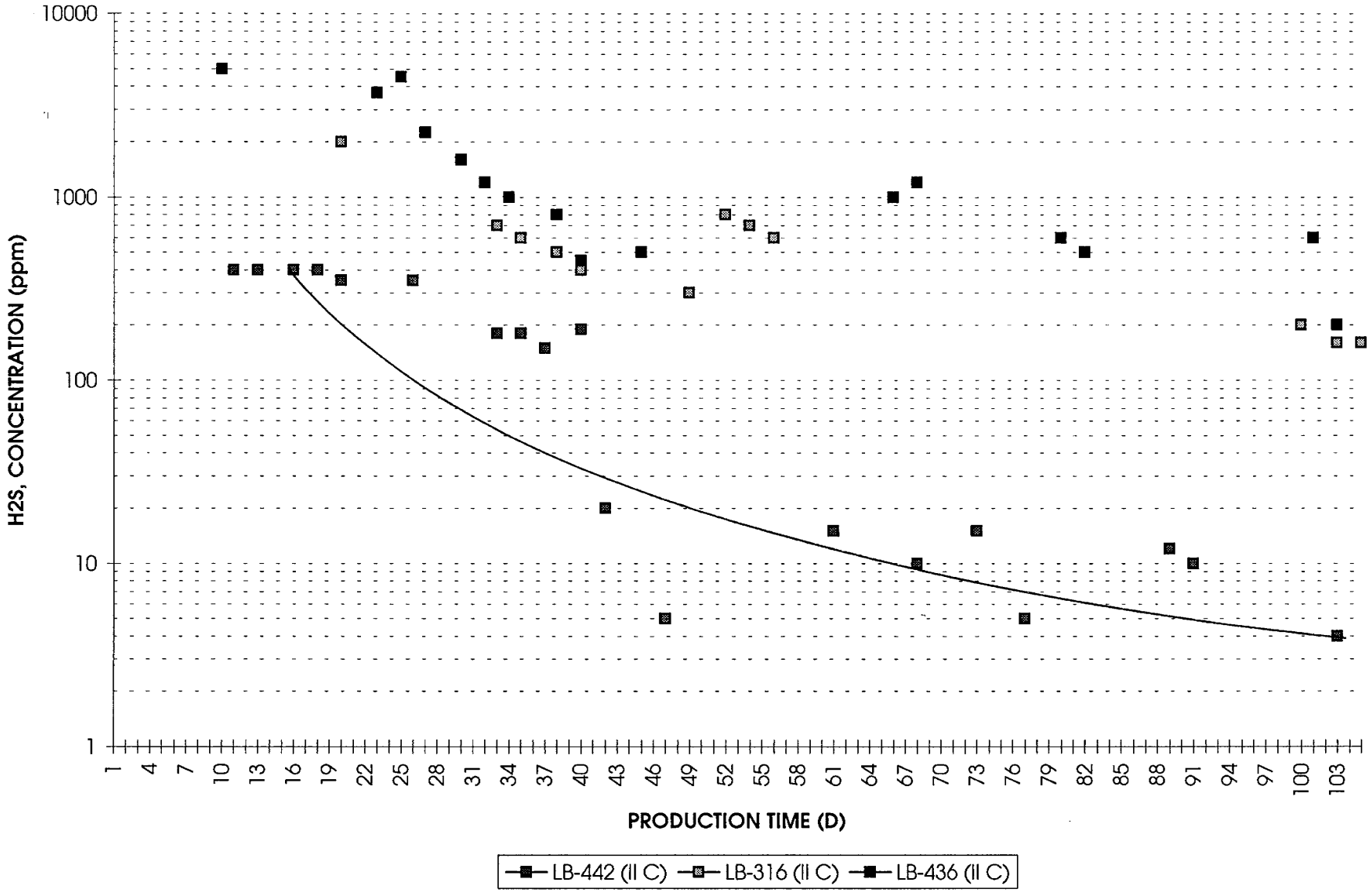

Fig. 8.- H2S Concentrations in the LB-442 Treated Well vs Reference wells LB-316 y LB-436.
Tubing Level, II Cycle.

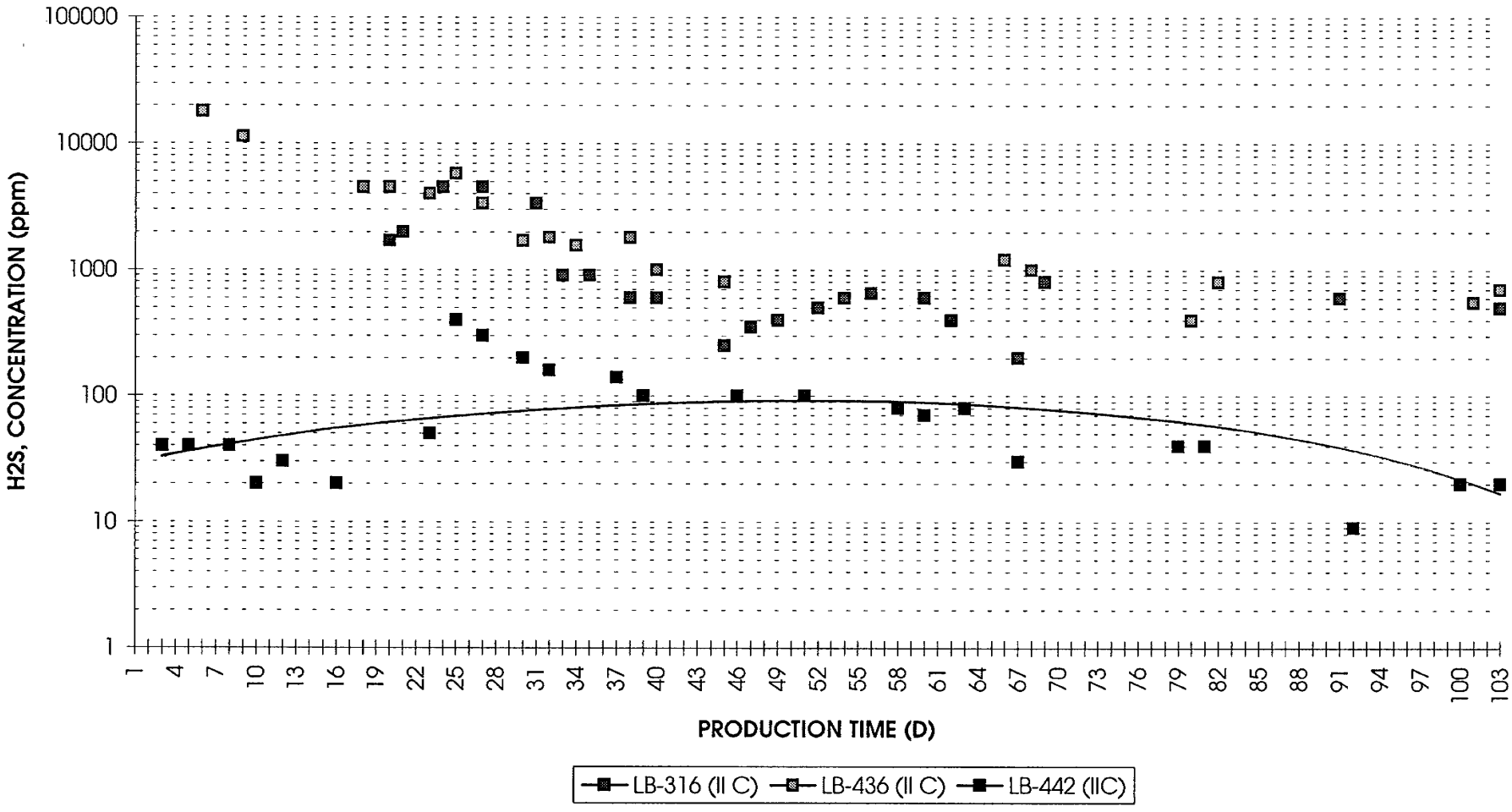

Fig. 9.- H2S Concentrations in the LB-442 Treated Well vs. Reference Wells LB-316 y LB-436. Casing Level, II Cycle.

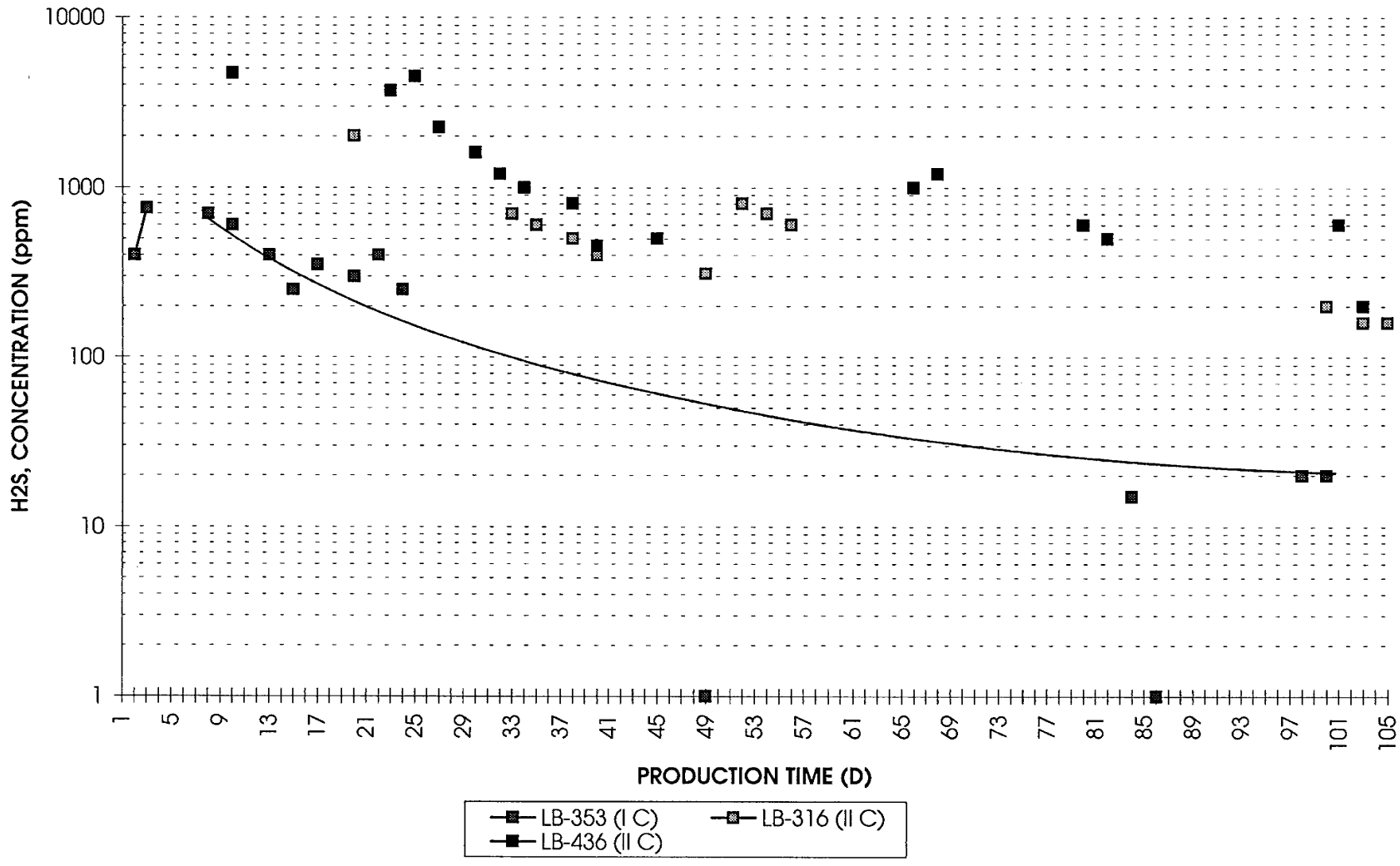

Fig. 10.- H2S Concentration in the LB-353 (I Cycle) vs. Reference Wells LB-316 y LB-436.
Tubing Level, II Cycle.

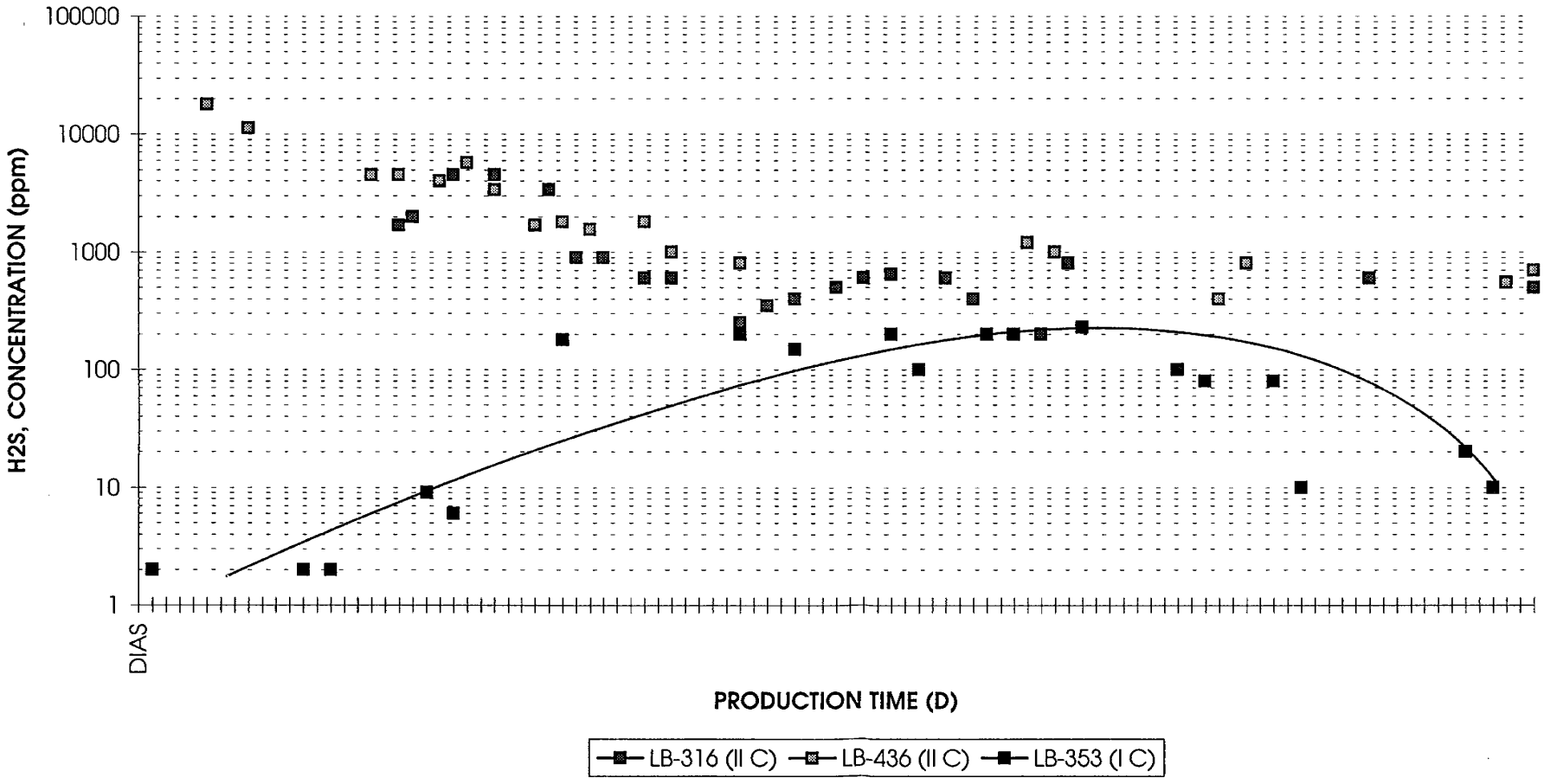

Fig. 11.- H2S Concentrations in the LB-353 (I Cycle) Treated Well vs. Reference Wells LB-316 y LB-436 (II Cycle). Casing Level

REFERENCES

1. Portillo, F.; Dórazio, F. *"Análisis del comportamiento de producción de H_2S en el proyecto de Inyección contínua de vapor en M-6"*. Informe Técnico IT-9239. Maraven, Sept. 1982

2. Campos, R. E., ; Ramirez, J. W.; Vásquez T. *"Laboratory and Field Research on H_2S. Generation in Steam Processes. EOR Thermal Processes"*, Venezuela-MEM/USA-DOE, Fossil Energy Report IV-9, March, 1995.

APPENDIX A

Full text of the "Ninth Amendment and Extension of Implementing Agreement IV Between the Department of Energy of the United States of America and the Ministry of Energy and Mines of the Republic of Venezuela in the Area of Enhanced Oil Recovery Thermal Processes."

NINTH AMENDMENT TO AND EXTENSION OF

IMPLEMENTING AGREEMENT NO. IV

BETWEEN

THE DEPARTMENT OF ENERGY OF THE UNITED STATES OF AMERICA

AND

THE MINISTRY OF ENERGY AND MINES OF THE REPUBLIC OF VENEZUELA

IN THE AREA OF

ENHANCED OIL RECOVERY THERMAL PROCESSES

WHEREAS, the United States Department of Energy (hereinafter referred to as DOE) and the Ministry of Energy and Mines of Venezuela (hereinafter referred to as MEMV) entered into an Agreement in the field of Energy Research and Development signed March 6, 1980 (hereinafter referred to as the Agreement);

WHEREAS, the Agreement has been extended to include the period through September 8, 1998;

WHEREAS, in furtherance of their mutual interests, DOE and MEMV on 29 September 1980, entered into Implementing Agreement IV for cooperation in the area of Enhanced Oil Recovery Thermal Processes (hereinafter referred to as the Implementing Agreement);

WHEREAS, DOE and MEMV have previously agreed to the First, Second, Third, Fourth, Fifth, Sixth, Seventh, and Eighth Amendments to and Extensions of the Implementing Agreement;

WHEREAS, DOE and MEMV have discharged their principal obligations and duties under the Implementing Agreement and the First, Second, Third, Fourth, Fifth, Sixth, Seventh, and Eighth Amendments and Extensions to their mutual satisfaction and benefit;

WHEREAS, DOE and MEMV now desire to further extend ongoing cooperative efforts and further desire to initiate and pursue new and additional cooperative activities;

WHEREAS, the need exists to increase the recovery efficiency of steam injection methods for the recovery of heavy oil, and the use of additives continues to be an attractive method of potentially increasing recovery efficiency;

WHEREAS, DOE and MEMV desire to cooperate in the application of in-situ combustion for the recovery of heavy oil;

WHEREAS, DOE and MEMV desire to further cooperative efforts on the understanding of the thermal processes and the reservoir and its fluids where these processes are conducted;

IT IS AGREED AS FOLLOWS:

ARTICLE 1

In accordance with Articles 5 and 7 of the Agreement, DOE and MEMV hereby further amend and extend the Implementing Agreement as hereinafter provided.

ARTICLE 2

Article 1 of the Implementing Agreement and all other articles and provisions not herein amended are extended as written. The Parties named hereafter are the same Parties identified in Article 1 of the Implementing Agreement.

ARTICLE 3

Article 2 of the Implementing Agreement is amended by adding the following Tasks 62 through 67:

Task 62 - DOE shall provide INTEVEP with results from the SUPRI research on heavy oil recovery mechanisms. This task includes experiments on flow properties, in-situ combustion, steam injection, and computerized X ray tomography. Mathematical and simulation results on the same topics as well as formation evaluation methods such as well testing or tracer surveys will be included.

Task 63 - INTEVEP shall provide DOE with information on studies to optimize heavy oil field exploitation using horizontal wells. The research is to reach conclusions about bore hole stability, pressure test interpretation and drainage pattern optimization when horizontal wells are applied to Venezuelan heavy oil reservoirs.

Task 64 - DOE shall provide INTEVEP with information on the results of NIPER's thermal light oil program. This work deals with tracking the progress of DOE's light oil steamflood at Naval Petroleum Reserve #3, Teapot Dome Field, Wyoming and laboratory research on light oil steamflooding of oil-wet dolomitic reservoirs that contain high pour point waxy crudes.

Task 65 - INTEVEP shall provide DOE with information on the Modeling of Thermal Processes. The effort will include the application of Analytical Models to predict the production performance of steam stimulated wells.

Task 66 - DOE shall provide INTEVEP with information on electrical imaging from cross-borehole and surface-to-hole electromagnetic induction using research conducted by Lawrence Livermore National Laboratory. The research is designed to extend the borehole induction logs to the region between wells for better reservoir characterization and control of EOR processes. LLNL will provide information on instrumentation and interpretation of data and show field examples where this technology has been applied in operating oil fields.

Task 67 - INTEVEP shall provide DOE with information on research about H_2S inhibition during steam injection. The research will provide field data on H_2S generation during the application of controlling methods.

ARTICLE 4

The Implementing Agreement shall hereafter consist of the Implementing Agreement as amended by the First, Second, Third, Fourth, Fifth, Sixth, Seventh, Eighth, and Ninth Amendments and Extensions.

ARTICLE 5

This Ninth Amendment and Extension shall become effective when signed by the DOE and MEMV Project Managers of Annex IV or their designated representatives. The Implementing Agreement, as amended, shall remain in effect until September 30, 1996, or until terminated by written notice as provided in Article 8 of the Implementing Agreement.

Done in Caracas, Venezuela and Bartlesville, Oklahoma.

On behalf of DOE

Thomas S Reid

Project Mgr - Thomas Reid

September 30, 1994

Date

On behalf of INTEVEP

Project Mgr - Manuel Estrada

September 30, 1994.

Date

APPENDIX B

Full text of the extension to the "Agreement Between the Department of Energy of the United States of America and the Ministry of Energy and Mines of the Republic of Venezuela in the Field of Energy Research and Development."

Signed on September 8, 1993 extending the Agreement for five years to September 7, 1998.

AGREEMENT
BETWEEN
THE DEPARTMENT OF ENERGY OF THE UNITED STATES OF AMERICA
AND
THE MINISTRY OF ENERGY AND MINES OF THE REPUBLIC OF VENEZUELA
IN THE FIELD OF ENERGY RESEARCH AND DEVELOPMENT

Whereas the Government of the United States of America and the Government of the Republic of Venezuela are Parties to an Agreement for Scientific and Technological Cooperation, with Annex, of December 8, 1990;

Whereas the United States Department of Energy (hereinafter "DOE") and the Ministry of Energy and Mines of the Republic of Venezuela (hereinafter "MEM") (hereinafter "the Parties") concluded an Agreement in the Field of Energy Research and Development of March 6, 1980, (hereinafter "the 1980 Agreement");

Whereas the Parties believe that the cooperative activities in the field of energy research and development undertaken pursuant to the 1980 Agreement were mutually beneficial to both Parties;

Whereas the Parties have a common interest in continuing certain Implementing Agreements under the 1980 Agreement and in undertaking new cooperative activities in the field of energy research by entering into a new Agreement;

Now therefore the Parties agree as follows:

ARTICLE I

The objective of cooperation under this Agreement is to continue, for the mutual benefit of the Parties, the balanced exchange of energy technology information related to petroleum, natural bitumen, solar energy, geothermal energy, hydroelectric energy, coal, and energy efficiency established by the 1980 Agreement and to conduct related joint research and development activities, which will be further defined in Project Annexes to this Agreement.

ARTICLE II

Cooperation under this Agreement may include, but is not limited to, the following:

1. Exchange of scientific and technical information, and results and methods of research and development on a periodic basis in a manner agreed to by the Joint Steering Committee (JSC) established by Article III;

2. Organization of seminars and other meetings on agreed topics of research and development in the areas enumerated in Article I in a manner agreed to by the JSC;

3. Survey visits by specialists to the energy research facilities of the other Party at the invitation of the host institution;

4. Exchange of materials, instruments, components, and equipment for testing;

5. Exchange of personnel for participation in agreed research, development, analysis, design and experimental activities;

6. Joint projects in the form of experiments, tests, design analysis, or other technical collaborative activity;

7. Joint funding of specific research and development projects which may be undertaken in connection with other qualified organizations or persons in a manner agreed to by the JSC; and

8. Other such forms of cooperation as may be jointly agreed in writing by the Parties and approved by the JSC.

ARTICLE III

1. A Joint Steering Committee (JSC) shall be established with each Party designating three officials to serve as Coordinators, to supervise the implementation of this Agreement. As mutually agreed, the JSC shall meet to evaluate all aspects of the cooperation under this Agreement. These meetings shall be held alternately in the United States and Venezuela.

2. The JSC shall approve and monitor all cooperative activities to be carried out under this Agreement.

3. At its meetings, the JSC shall review and evaluate any newly proposed activities and the status of cooperation under this Agreement. The JSC also shall give appropriate guidance and direction to subcommittees and the project managers of activities established under this Agreement. If so requested, the JSC may give advice to the Parties regarding the progress and future of the cooperative activities established under this Agreement.

4. Each Party shall nominate one person to act on its behalf, during periods between meetings of the JSC, in all matters concerning cooperation under this Agreement.

5. The JSC shall, as necessary and appropriate, establish separate subcommittees in each of the following areas: petroleum, natural bitumen, solar energy, geothermal energy, hydroelectric energy, coal, and energy efficiency to facilitate implementation of projects which may be undertaken in those areas.

ARTICLE IV

1. Proposals for cooperation under this Agreement may be presented by either Party or its designated representatives to the JSC for its approval.

2. Each cooperative activity which is approved by the JSC shall be described in writing in a Project Annex to this Agreement. Such Annexes shall contain detailed procedures for the implementation of the cooperative activity, including but not limited to the contributions by each Party (costs and cost-sharing), schedules, and responsibilities of each Party.

3. No cooperative activity shall be undertaken by the Parties until a Project Annex has been concluded by the Parties.

4. Each Project Annex concluded by the Parties thereof shall be subject to and refer to the provisions of this Agreement.

5. The following Implementing Agreements, which were entered into pursuant to the 1980 Agreement shall continue to apply until work undertaken is completed subject to the terms and conditions of this Agreement, or until this Agreement expires or is terminated in accordance with Article XIII:

A. Implementing Agreement I, Joint Characterization of Heavy Crude

B. Implementing Agreement II, Cooperation Supporting Research at Universities, Government Energy Technology Centers, and National Laboratories

C. Implementing Agreement III, Evaluate Past and Ongoing Enhanced Oil Recovery Projects in the United States and Venezuela

D. Implementing Agreement IV, Enhanced Oil Recovery Thermal Process

E. Implementing Agreement VIII, Coal Preparation, Combustion, and Related Analytical Technology at Universities, Government Energy Technology Centers, and National Laboratories

F. Implementing Agreement X, On-Site Training of Petroleum Engineers

G. Implementing Agreement XI, Energy Conservation

H. Implementing Agreement XII, Geochemistry

I. Implementing Agreement XIII, Microbial Enhanced Oil Recovery

J. Implementing Agreement XIV, Exchange of Energy Related Personnel

ARTICLE V

The following provisions shall apply concerning exchanges of equipment pursuant to this Agreement:

1. By mutual agreement, a Party may provide equipment to be utilized in a joint activity. In such cases, the sending Party shall supply, as soon as possible, a detailed list of the equipment to be provided together with the relevant specifications and appropriate technical informational documentation related to the use, maintenance, and repair of the equipment.

2. Title to the equipment and necessary spare parts supplied by the sending Party for use in joint activities shall remain in the sending Party, and the property shall be returned to the sending Party upon completion of the joint activity, unless otherwise agreed.

3. Equipment provided pursuant to this Agreement shall be brought into operation at the host establishment only by mutual agreement between the Parties.

4. The host establishment shall provide the necessary premises for the equipment, shall provide for utilities such as electric power, water, and gas, and normally shall provide materials to be tested, in accordance with the agreed technical requirements.

5. The responsibility and expenses for the transport of equipment and materials from the United States of America by plane or ship to an authorized port of entry in Venezuela convenient to the ultimate destination, and also responsibility for its safekeeping and insurance en route shall rest with DOE.

6. The responsibility and expenses for the transport of equipment and materials from Venezuela by plane or ship to an authorized port of entry in the United States of America convenient to the ultimate destination, and also responsibility for its safekeeping and insurance en route shall rest with MEM.

7. Equipment provided pursuant to this Agreement for use in joint activities shall be considered to be scientific, not having a commercial character, and each Party shall make its best effort to obtain duty free entry.

ARTICLE VI

The following provisions shall apply concerning exchanges of personnel under this Agreement:

1. Whenever an exchange of personnel is contemplated, each Party shall ensure the selection of adequate personnel with skills and competence necessary to conduct the activities planned under this Agreement. Each such exchange of personnel shall be mutually agreed in advance by an exchange of letters between the Parties, referencing this Agreement and its pertinent intellectual property provisions.

2. Each Party shall be responsible for the salaries, insurance, and allowances to be paid to its staff or its contractors.

3. Each Party shall pay for the travel and living expenses of its staff or its contractors when staying at the establishment of the host Party, unless otherwise agreed.

4. Each Party shall arrange for adequate accommodations for the other Party's staff or its contractors (and their families) on a mutually agreeable, reciprocal basis.

5. Each party shall provide all necessary assistance to the staff of the other Party or its contractors as regards administrative formalities.

6. The staff of each Party or its contractors shall conform to the general rules of work and safety regulations in force at the host establishment.

ARTICLE VII

1. The Parties shall ensure adequate and effective protection of intellectual property created or furnished under this Agreement and relevant annexes. The Parties agree to notify one another in a timely fashion of any inventions or copyrighted works arising under this Agreement and to seek protection for such intellectual property in a timely fashion. Rights to such intellectual property shall be allocated as provided in this Article.

2. SCOPE

   A. This Article is applicable to all cooperative activities undertaken pursuant to this Agreement, except as otherwise specifically agreed by the Parties or their designees.

   B. For purposes of this Agreement, "intellectual property" shall have the meaning found in Article 2 of the Convention Establishing the World Intellectual Property Organization, done at Stockholm, July 14, 1967.

   C. This Article addresses the allocation of rights and interests between the Parties. Each Party shall ensure that the other Party can obtain the rights to intellectual property allocated in accordance with this Article by obtaining those rights from its own participants through contracts or other legal means, if necessary. This Article does not otherwise alter or prejudice the allocation between a Party and its nationals, which shall be determined by that Party's laws and practices.

   D. Disputes concerning intellectual property arising under this Agreement should be resolved through discussions between the concerned participating institutions or, if

necessary, the Parties or their designees. Upon mutual agreement of the Parties, a dispute shall be submitted to an arbitral tribunal for binding arbitration in accordance with the applicable rules of international law. Unless the Parties or their designees agree otherwise in writing, the arbitration rules of UNCITRAL shall govern.

E. Termination or expiration of the Agreement shall not affect rights or obligations under this Article.

F. Cooperative activities will not be entered into where the purpose of the cooperative activity is to produce inventions in the following areas, or where there is a possibility of producing inventions in the following areas, until such time as inventions in these areas are considered patentable subject matter by both Parties:

1. drinks and food products for humans and animals;

2. medicines of all kinds; and

3. pharmaceuticals and chemical preparations, reactions and compounds.

3. ALLOCATION OF RIGHTS

A. Each Party shall be entitled to a non-exclusive, irrevocable, royalty-free license in all countries to translate, reproduce, and publicly distribute scientific and technical journal articles, reports, and books directly arising from cooperation under this Agreement. All publicly distributed copies of a copyrighted work prepared under this provision shall indicate the names of the authors of the work unless an author explicitly declines to be named.

B. Rights to all forms of intellectual property, other than those rights described in Section VII.3.A. above, shall be allocated as follows:

1. Visiting researchers, for example, scientists visiting in furtherance of their education, shall receive intellectual property rights under the policies of the host institution. In addition, each visiting researcher named as an inventor shall be entitled to national treatment with regard to awards, bonuses, benefits, or any other rewards, in accordance with the policies of the host institution.

2. (a) For intellectual property created during joint research, for example, when the Parties, participating institutions, or participating personnel have agreed in advance on the scope work, each Party shall be entitled to all rights and interests in its own territory. Rights and interests in third countries will be determined in implementing arrangements. If research is not designated a "joint research" in the relevant implementing arrangement, rights to intellectual property arising from the research will be allocated in accordance with paragraph VII.3.B.1. In addition, each person named as an inventor shall be entitled to national treatment with regard to awards, bonuses, benefits, or any other rewards, in accordance with the policies of the host institution.

(b) Notwithstanding paragraph VII.3.B.2.(a), if a type of intellectual property is available under the laws of one Party but not the other Party, the Party whose laws provide for this type of protection shall be entitled to all rights and interests worldwide. Persons named as inventors of the property shall nonetheless be entitled to awards, bonuses, benefits, or any other rewards as provided in paragraph VII.3.B.2.(a)

4. BUSINESS-CONFIDENTIAL INFORMATION

In the event that information identified in a timely fashion as business-confidential is furnished or created under this Agreement, each Party and its participants shall protect such information in accordance with applicable laws, regulations, and administrative practices. Information may be identified as "business-confidential" if a person having the information may derive an economic benefit from it or may obtain a competitive advantage over those who do not have it, or the information is not generally known or publicly available from other sources, and the owner has not previously made the information available without imposing in a timely manner an obligation to keep it confidential.

ARTICLE VIII

1. Unless otherwise agreed, all costs resulting from cooperation pursuant to this Agreement shall be the responsibility of the Party that incurs them.

2. Each Party shall conduct the activities provided for in this Agreement, and its Annexes subject to its applicable laws and regulations, and shall provide financial resources subject to the availability of appropriated funds.

3. Each Party shall use its best efforts to obtain all permits and licenses required by the applicable laws and regulations for the implementation of this Agreement and its Annexes.

ARTICLE IX

Both Parties agree that no information or equipment requiring protection in the interests of national defense or foreign relations of either Party and classified in accordance with the applicable national laws and regulations shall be provided under this Agreement. In the event that information or equipment which is known or believed to require such protection is identified in the course of cooperative activities undertaken pursuant to this Agreement, it shall be brought immediately to the attention of the appropriate officials and the Parties shall consult to identify appropriate security measures to be agreed upon by the Parties in writing and applied to this information and equipment and shall, if appropriate, amend this Agreement to incorporate such measures.

ARTICLE X

The transfer of unclassified export-controlled information or equipment between the Parties shall be in accordance with the relevant laws and regulations of each Party. If either Party deems it necessary, detailed provisions for the prevention of unauthorized transfer or retransfer of such information or equipment shall be incorporated into the contracts or implementing arrangements. Export-controlled information shall be marked to identify it as export-controlled and identify any restrictions on further use or transfer.

ARTICLE XI

All information or equipment transmitted by one Party to the other Party under this Agreement shall be appropriate and accurate to the best knowledge and belief of the transmitting Party, but the transmitting Party does not warrant the suitability of the information or equipment transmitted for any particular use or application by the receiving Party or by any third party. Information or equipment developed jointly by the Parties shall be appropriate and accurate to the best knowledge

and belief of both Parties. Neither Party warrants the accuracy of the jointly developed information or the appropriateness of equipment or its suitability for any particular use of application by either party or by any third party.

ARTICLE XII

All questions related to the interpretation or application of this Agreement shall be settled by the Parties by mutual agreement.

ARTICLE XIII

1. This Agreement shall enter into force upon signature by each Party and shall remain in force for five (5) years.

2. This Agreement may be amended or extended by mutual written agreement of the Parties. This Agreement may be terminated upon one (1) year's advance notification in writing by either Party. Such termination shall be without prejudice to any rights and interests which may have accrued under this Agreement to either Party up to the date of termination.

3. All joint efforts and experiments not completed at the expiration or termination of this Agreement may be continued until their completion under the terms of this Agreement.

Done at Caracas and Washington, in duplicate, in the English and Spanish languages, each text being equally authentic, this 8th day of September 1993.

FOR THE DEPARTMENT OF ENERGY OF THE UNITED STATES OF AMERICA

Signature

Jack S. Siegel
Acting Assistant Secretary
for Fossil Energy

Printed Name/Title

FOR THE MINISTRY OF ENERGY AND MINES OF THE REPUBLIC OF VENEZUELA

Signature

Rafael M. Guevara
General Director

Printed Name/Title

☆U.S. GOVERNMENT PRINTING OFFICE: 1995 - 660-029/20011